CARBON NANOMATERIAL FILLED POLYMER COMPOSITES FOR FUNCTIONAL APPLICATIONS: PROCESSING, STRUCTURE, AND PROPERTY RELATIONSHIP

EDITED BY: Dong Xiang, Eileen Harkin-Jones, Jiabin Shen and Dan Sun

PUBLISHED IN: Frontiers in Materials

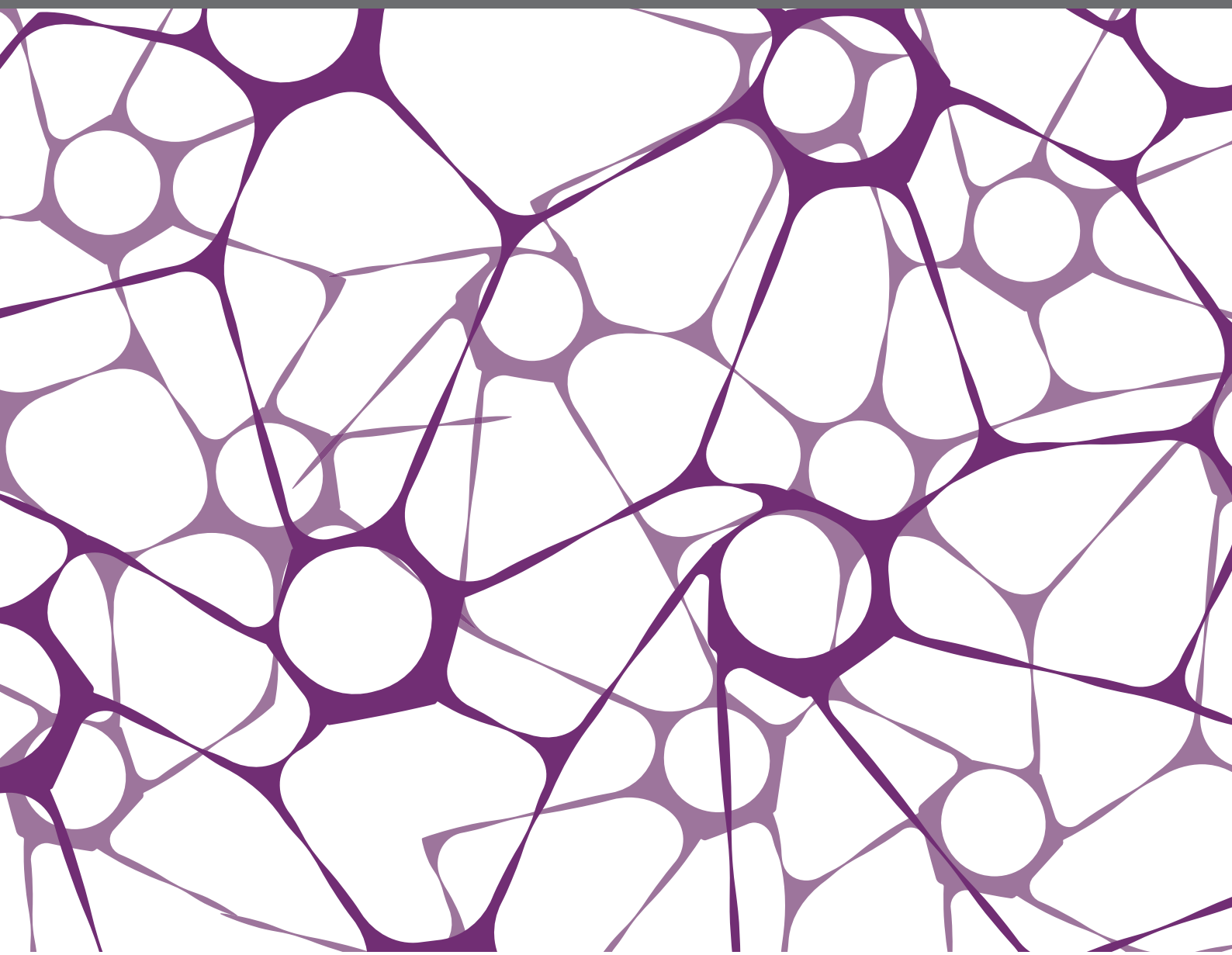

frontiers Research Topics

ISSN 1664-8714
ISBN 978-2-88974-649-1
DOI 10.3389/978-2-88974-649-1

About Frontiers

Frontiers is more than just an open-access publisher of scholarly articles: it is a pioneering approach to the world of academia, radically improving the way scholarly research is managed. The grand vision of Frontiers is a world where all people have an equal opportunity to seek, share and generate knowledge. Frontiers provides immediate and permanent online open access to all its publications, but this alone is not enough to realize our grand goals.

Frontiers Journal Series

The Frontiers Journal Series is a multi-tier and interdisciplinary set of open-access, online journals, promising a paradigm shift from the current review, selection and dissemination processes in academic publishing. All Frontiers journals are driven by researchers for researchers; therefore, they constitute a service to the scholarly community. At the same time, the Frontiers Journal Series operates on a revolutionary invention, the tiered publishing system, initially addressing specific communities of scholars, and gradually climbing up to broader public understanding, thus serving the interests of the lay society, too.

Dedication to Quality

Each Frontiers article is a landmark of the highest quality, thanks to genuinely collaborative interactions between authors and review editors, who include some of the world's best academicians. Research must be certified by peers before entering a stream of knowledge that may eventually reach the public - and shape society; therefore, Frontiers only applies the most rigorous and unbiased reviews.
Frontiers revolutionizes research publishing by freely delivering the most outstanding research, evaluated with no bias from both the academic and social point of view. By applying the most advanced information technologies, Frontiers is catapulting scholarly publishing into a new generation.

What are Frontiers Research Topics?

Frontiers Research Topics are very popular trademarks of the Frontiers Journals Series: they are collections of at least ten articles, all centered on a particular subject. With their unique mix of varied contributions from Original Research to Review Articles, Frontiers Research Topics unify the most influential researchers, the latest key findings and historical advances in a hot research area! Find out more on how to host your own Frontiers Research Topic or contribute to one as an author by contacting the Frontiers Editorial Office: frontiersin.org/about/contact

CARBON NANOMATERIAL FILLED POLYMER COMPOSITES FOR FUNCTIONAL APPLICATIONS: PROCESSING, STRUCTURE, AND PROPERTY RELATIONSHIP

Topic Editors:
Dong Xiang, Southwest Petroleum University, China
Eileen Harkin-Jones, Ulster University, United Kingdom
Jiabin Shen, Sichuan University, China
Dan Sun, Queen's University Belfast, United Kingdom

Citation: Xiang, D., Harkin-Jones, E., Shen, J., Sun, D., eds. (2022). Carbon Nanomaterial Filled Polymer Composites for Functional Applications: Processing, Structure, and Property Relationship. Lausanne: Frontiers Media SA.
doi: 10.3389/978-2-88974-649-1

Table of Contents

frontiers in Materials

EDITORIAL
published: 15 February 2022
doi: 10.3389/fmats.2022.843571

Editorial: Carbon Nanomaterial Filled Polymer Composites for Functional Applications: Processing, Structure, and Property Relationship

*Dong Xiang**

School of New Energy and Materials, Southwest Petroleum University, Chengdu, China

Keywords: carbon nanomaterials, polymer composites, functional nanocomposites, processing, structure, property relationship

Editorial on the Research Topic

Carbon Nanomaterial Filled Polymer Composites for Functional Applications: Processing, Structure, and Property Relationship

OPEN ACCESS

Edited by:
Guilherme Mariz de Oliveira Barra, Federal University of Santa Catarina, Brazil

Reviewed by:
Claudia Merlini, Federal University of Santa Catarina, Brazil

***Correspondence:**
Dong Xiang
dxiang01@hotmail.com

Specialty section:
This article was submitted to Polymeric and Composite Materials, a section of the journal Frontiers in Materials

Received: *26 December 2021*
Accepted: *27 January 2022*
Published: *15 February 2022*

Citation:
Xiang D (2022) Editorial: Carbon Nanomaterial Filled Polymer Composites for Functional Applications: Processing, Structure, and Property Relationship. Front. Mater. 9:843571. doi: 10.3389/fmats.2022.843571

BACKGROUND

Carbon nanomaterials, such as carbon nanotubes and graphene, are able to transfer their excellent thermal and electrical conductivity to polymers while retaining or even improving their original mechanical performance. Polymer/carbon nanomaterial composites are increasingly applied in aerospace, automotive and electronic industries for electromagnetic interference (EMI) shielding, electrostatic dissipation (ESD), sensors etc., when flexibility or light weight is required. Up to date, many researchers have conducted a lot of studies on the development of functional polymer/carbon nanomaterial composites. How processing affects the structuring and properties of these nanocomposites is usually ignored, while it is very significant to their applications. The aim of the current Research Topic is to cover novel research in the processing-structure-property relationship of functional polymer/carbon nanomaterial composites, including the property and structure tuning of nanocomposites in processing.

MAJOR HIGHLIGHTS OF THE CONTRIBUTIONS

In recent years, 3D printing (also called as additive manufacturing), as a rapid development method of no mold, low-cost, high-precision and rapid preparation in recent years, has attracted a lot of attention in carbon nanomaterials filled polymers based flexible strain sensors. To summarize the latest progress, Liu et al. presented a dedicated mini-review on high-performance flexible strain sensors of conductive polymer composites by employing different 3D printing technologies, involving Direct Ink Writing (DIW), Selective Laser Sintering (SLS), Fused Filament Fabrication (FFF) and Digital Light Processing (DLP) and printing materials in recent years. The authors also summarized the development direction of high-performance flexible strain sensor based on 3D printing. Golbang et al. made a comparative study on FFF and injection moulding of high-performance inorganic fullerene tungsten sulphide (IF-WS_2)/poly ether ether ketone (PEEK) composites, including dispersion, crystallinity and mechanical

properties. It was concluded that IF-WS_2 nanoparticles doped with PEEK can improve the mechanical properties of PEEK prepared by FDM.

Mokhtari et al. prepared antistatic, high-performance composites of PEEK and expanded graphite (EG) through twin-screw extrusion and injection molding. The morphological, rheological, electrical, mechanical, thermal and wear properties of the EG/PEEK composites were studied. The results indicated that the mechanical properties of the composites could be improved by annealing. The introduction of 5 vol% EG increased the flexural and tensile modulus of PEEK from 3.55 to 3.84 GPa to 4.40 and 4. 15 GPa, respectively. Compared with the neat PEEK, the wear resistance of the composite with 3 vol% EG was increased by 37%.

Biaxial stretching is also another effective method to prepare high-performance carbon nanomaterials filled polymer composites. In the mini-review by Chen et al., the influence of biaxial stretching on the structure and properties of nanocomposites containing different nanofillers was presented. In addition, their applications were summarized, and the future prospects and challenges of this technology were discussed. The reported work could promote future research for the development of high-performance polymer nanocomposites with high productivity. Mayoral et al. investigated the effects of biaxial stretching and graphene nanoplatelets (GNPs) loading on the bulk properties of polypropylene (PP)/GNP nanocomposites. It is shown that the electrically conductive composites were obtained with the addition of GNPs (>5 wt%) due to the generation of numerous conductive paths. The GNP resulted in enhanced modulus and strength and increased crystallinity of polymer. Biaxial stretching further enhanced the mechanical properties of nanocomposites wihle the electrical conductivity was slightly reduced.

The development of interlayer dielectric materials with low dielectric loss factor (Df) and dielectric constant (Dk) has attracted the attention of much researchers in order to achieve low delay and high fidelity characteristics in high-frequency signal transmission. The dielectric loss mechanism of polymer composites and the resins usually used in high-frequency copper-clad laminates were summarized by Wang et al. How to reduce the dielectric constant and dielectric loss of composites was discussed from the aspects of nanofiller selection and molecular structure design.

The out-of-plane mechanical performance of glass fiber reinforced polymer (GFRP) composites still need further improvement to achieve the practicability of GFRP in the field of oil and gas. Yao et al. fabricated GNP/GFRP composites by two methods combining either vacuum mixing or spray coating with vacuum-assisted resin infusion. A severe filtering effect was observed in the former method, where the GNPs were not uniformly dispersed in the resulted composite, whereas the latter led to a uniform GNP dispersion on the glass fabrics. The flexural strength and modulus of GFRP were respectively increased by 6.8 and 1.6% with an optimal content of 0.15 wt% GNPs.

Kyei-Manu et al. investigated the thermo-mechanical properties of carbon black filled natural and styrene butadiene rubbers under rapid adiabatic conditions. The results showed a strong correlation among the temperature rise, mechanical hysteresis, modulus and crystallinity of the rubbers measured in tensile extension with strain amplification factors. This highlighted the effect of matrix overstraining on microstructural evolution of the rubbers during extension. Analysis of the thermal measurements of the rubber compounds during extension and retraction and contrasting between non-crystallizing and crystallizing rubbers indicated that a substantial irreversible heat generation happened during the rubber compounds extension.

Carbon nanotube (CNT) composites are promising candidates for structural power composites due to their high surface area, mechanical and electrical properties. Koliolios et al. explored the nail penetration behaviors of supercapacitors with carbon nanotube-polyaniline (CNT/PANI) electrodes. It was shown that the wet cells with the electrolyte and the dry cells without electrolyte exhibited a piece-wise nonlinear relationship and a power law behavior, respectively. The cyclic voltammetry indicated the significant capacitance loss, resulting in the transition of cell behavior from capacitor to resistor-like manner.

Laser welding is a critical manufacturing technology for various plastic products including medical devices, automotive components and consumer goods. Determining a set of optimal parameters for laser transmission welding (LTW) technique of thermoplastics and composites could be quite challenging due to a higher heat density of the LTW. was used A 3D transient thermal model for LTW of isotactic polypropylene (iPP) and its composites with CB was built by Ali et al. using the finite element method (FEM)-based software COMSOL Multiphysics to investigate the effect of carbon black along other control parameters for high-speed welding. It was observed that the composites with 0.5 wt% and 1 wt% of CB were successfully welded with neat iPP.

AUTHOR CONTRIBUTIONS

DX Completed this editorial article.

ACKNOWLEDGMENTS

The author would like to thank all the reviewers and handling editors for every success in this Research Topic.

Conflict of Interest: The author declares that the research was conducted in the absence of any commercial or financial relationships that could be construed as a potential conflict of interest.

Publisher's Note: All claims expressed in this article are solely those of the authors and do not necessarily represent those of their affiliated organizations, or those of the publisher, the editors and the reviewers. Any product that may be evaluated in this article, or claim that may be made by its manufacturer, is not guaranteed or endorsed by the publisher.

frontiers in Materials

ORIGINAL RESEARCH
published: 28 June 2021
doi: 10.3389/fmats.2021.687282

Characterizing Biaxially Stretched Polypropylene / Graphene Nanoplatelet Composites

*B. Mayoral[1], G Menary[1], P Martin[1], G Garrett[1], B Millar[1], P Douglas[1], N. Khanam[2], M. A. AlMaadeed[2,3], M. Ouederni[4], A. Hamilton[1,5] and D. Sun[1]**

[1]School of Mechanical and Aerospace Engineering, Queen's University Belfast, Belfast, United Kingdom, [2]Center for Advanced Materials, Qatar University, Doha, Qatar, [3]Materials Science and Technology Program, Qatar University, Doha, Qatar, [4]Qatar Petrochemical Company, Doha, Qatar, [5]School of Engineering and the Environment, University of Southampton, Southampton, United Kingdom

In this work, polypropylene (PP) nanocomposites containing different weight concentration of graphene nanoplatelets (GNP) were prepared by melt-mixing using an industrial-scale, co-rotating, intermeshing, twin-screw extruder. The materials were then compression moulded into sheets, and biaxially stretched at different stretching ratios (SRs) below the PP melting temperature. The effects of GNP content and biaxial stretching on the bulk properties of unfilled PP and PP/GNP nanocomposites have been investigated in details. Results show that the addition of GNP (>5wt%) can lead to electrically conductive composites due to the formation of percolation network. The GNP have led to increased polymer crystallinity and enhanced materials stiffness and strength. Biaxial stretching process further enhances the materials mechanical properties but has slightly decreased the composites electrical conductivity. The PP/GNP nanocomposites were also processed into 3D demonstrator parts using vacuum forming, and the properties of which were comparable with biaxially stretched composites.

Keywords: polymer composites, graphene nanoplatelet, Bi-axial stretching, mechanical properties, thermal properties, electrical properties

OPEN ACCESS

Edited by:
Miroslav Slouf, Institute of Macromolecular Chemistry (ASCR), Czechia

Reviewed by:
Jose Antonio Covas, University of Minho, Portugal
John Zhanhu Guo, , University of Tennessee, United States

****Correspondence:***
D. Sun
d.sun@qub.ac.uk

Specialty section:
This article was submitted to Polymeric and Composite Materials, a section of the journal Frontiers in Materials

Received: *29 March 2021*
Accepted: *10 June 2021*
Published: *28 June 2021*

Citation:
Mayoral B, Menary G, Martin P, Garrett G, Millar B, Douglas P, Khanam N, AlMaadeed MA, Ouederni M, Hamilton A and Sun D (2021) Characterizing Biaxially Stretched Polypropylene / Graphene Nanoplatelet Composites. Front. Mater. 8:687282. doi: 10.3389/fmats.2021.687282

INTRODUCTION

Graphene possesses exceptional mechanical properties, excellent thermal/electrical conductivity as well as large specific surface area. Due to its outstanding multifunctional properties, graphene has received extensive research interests in recent years in multiple fields (Zhao et al., 2019; Jiang et al., 2020; Noorunnisa et al., 2016a; Noorunnisa et al., 2016b; Nidamanuri et al., 2020; Zhao et al., 2020; Zhou et al., 2021). Compared to single-layer graphene, large yield of graphene nanoplatelets (GNP) can be produced from natural graphite precursors at a lower cost (Noorunnisa et al., 2016a). Past literatures suggest the electrical conductivity and mechanical properties of polymers can be greatly enhanced by the addition of GNP due to its high electrical conductivity and excellent mechanical properties (modulus 1 TPa for graphene (Mayoral et al., 2015). For instance, GNP have been used to reinforce a range of polymers such as polyethylene (Noorunnisa et al., 2016b), polyethylene terephthalate (Zhang et al., 2010), polycarbonate (King et al., 2011), thermoplastic polyurethane (Yuan et al., 2017), polyether ether ketone (He et al., 2020; Zhu et al., 2021) and polyamide (Mayoral et al., 2015), etc, to obtain various nanocomposites with enhanced thermal, mechanical and electrical properties. Polypropylene (PP) is one of the commonly used matrix materials for polymer composites due to its availability and ease of processing (Maddah, 2016). PP has a low density

and high crystallinity in comparison with other engineering thermoplastics, allowing for potential weight reductions of the final products. Its excellent heat resistance, moisture barrier, and good optical properties also enable its wide industrial applications in packaging, laboratory equipment, automotive components and many others (Valentini et al., 2003; Xu et al., 2019; Tsai, 2020; Yan et al., 2020; Singh, 2021). In recent years, GNP reinforced PP nanocomposites have received increasing research interest. For instance, Liang and Du (2018) investigated the effect of GNP concentration on the melt flow behavior and flexural properties of reinforced PP composites. An optimum concentration of 0.4wt% has been reported for maximum mechanical resistance and a linear correlation between the melt shear viscosity and GNP weight fraction. Jun et al. (2018a) studied the effect of GNP size on PP nanocomposites processed by twin-screw extrusion and injection molding and found that smaller size GNP (<25 μm) are more effective in improving the composites tensile strength and thermal stabilities, due to their lower tendency to agglomeration. Jun et al. (2018b) also reported large sized GNP (>150 μm) can reduce the GNP percolation threshold and increase electrical conductivity of the melt compounded PP/GNP nanocomposite. Similar result was also reported by He et al. (2017a) in extruded and compression molded PP/GNP nanocomposites. He et al. (2017b) also reported that the residence time during extrusion plays an important role in dispersing GNP and better dispersion of GNP tends to increase the electrical and thermal conductivities of the resulting PP/GNP nanocomposites and significantly reduce the electrical percolation threshold.

From the literature, it can be seen that the processing route used to manufacture PP/GNP nanocomposites is likely to have a large impact on the dispersion and orientation of GNP, and consequently influence the properties of the resulting composite materials. In practical applications, polymer composites produced through primary processing (such as extrusion, injection molding) may require secondary processing in order to be made into final products. During secondary processes such as thermoforming and blow molding, heated polymer materials are subjected to rapid biaxial deformation as they are drawn into the shape of a mold (Martin et al., 2005). The effects of the biaxial stretching action and the presence of the filler materials on the resulting structure and properties of stretched PP/GNP composites is yet to be explored. In the present work, PP/GNP nanocomposites were prepared *via* melt-mixing using an industrial co-rotating, intermeshing extruder with custom-designed twin-screw. Compression moulded PP/GNP sheets were subsequently subjected to bi-axial stretching and the effects of GNP addition and different biaxial stretching ratios on the resulting composites properties have been investigated. Demonstrator parts were produced using vacuum forming process and the properties of the biaxially stretched material and the demonstrator parts have been compared.

METHODS

Materials

Moplen HP500N grade Polypropylene (Homopolymer, Melt Flow Rate (230°C/2.16 kg) = 12 g/10 min, density = 0.90 g/cm^3) was supplied by Basell. Grade M xGNP® GNP are made through a proprietary manufacturing process, and were supplied by XG Sciences. The technical specifications for the xGNP® grade M GNP are detailed in **Table 1**.

Melt-Mixing of PP/GNP

In order to obtain better GNP dispersion in the polymer matrix, the as purchased PP pellets were cryogenically ground into micron scale fine powder using a Wedco SE-12 UR pilot plant grinding mill at 7,000 rpm and a gap size of 400 μm. Liquid nitrogen was used for temperature regulation in order to prevent shear heating and degradation of the materials. PP and GNP, both in powder form were mixed using a Thermo Scientific Prism Pilot three High Speed Mixer at 2000rpm for 2 min.

The melt-mixing process was performed using a co-rotating intermeshing twin-screw extruder (Collin GmbH) with a screw diameter of 25 mm and a barrel length of 750 mm (L/D = 30). A bespoke screw configuration designed in-house (Mayoral et al., 2014) was used to enhance the nanoparticle dispersion into the polymer matrix. The detailed configuration of the twin-screw extruder can be found in (Mayoral et al., 2015). In brief, this configuration consists of forward conveying and forward kneading block elements with the addition of a toothed mixing element into the mixing zone and a reverse conveying element after the mixing zone. On exiting the capillary die, the extrudate was drawn through a cooled water bath at a constant haul off rate and pressure. The extrudate was dried by passing through an air ring and then pelletized using a Collin Pelletiser. The process parameters for PP/GNP twin-screw extrusion are: feeding rate = 2.5 kg/h, screw speed = 150 rpm, residence time = 1 min 30 s. Additional process parameters can be found in **Table 2**. According to the published literature, electrical percolation network within PP/GNP composite can be achieved at 5–10wt% GNP concentration (He et al., 2017). Given the bi-axial stretching process may potentially increase the mean distance between conductive filler materials (Feng and Jiang, 2014) and increase the percolation threshold, GNP weight concentrations of 0, 5, 10, 15, and 20wt% were deployed and the resulting composites were named as PP unfilled, PP/5%M-5, PP/10%M-5, PP/15%M-5, PP/20%M-5, respectively.

Compression Molding

The extruded pellets were dried in an oven at 80°C for 4 h before compression molding. Materials were compression moulded at 200°C at 150bars for 3 min using a Rondol platen press. Square samples with dimension of 12 mm × 12 mm × 1 mm were prepared for subsequent biaxial stretching tests.

Biaxial Stretching of PP/GNP Composites

The as purchased PP has a narrow softening temperature in the range 145–155°C. Trials show that the addition of GNP modified the PP thermal properties and that 147°C was the optimum temperature required for stretching the nanocomposite specimens. Test specimens were cut into 75 mm squares and were clamped using 24 nitrogen-driven pneumatic clamps of the biaxial stretching machine. More detailed configuration of the biaxial stretching machine can be found in (Martin et al., 2005;

TABLE 1 | XG Sciences xGNP® grade M GNP technical specifications.

Grade	Product	# Layers	Thickness (nm)	Diameter (μm)	Surf. Area (m^2/g)
M	M-5	18–24	6–8	5	120–150

TABLE 2 | Process parameters set for PP/GNP twin-screw extrusion.

PP/GNP	GNP	Pressure	Motor arrest	T_m
	wt (%)	Bar	Amp	°C
PP/M-5	5	3.2	13	218
	10	3.3	16	225
	15	3.5	17	227
	20	3.9	19	228

Zhang et al., 2020). It was found that only unfilled PP and PP/5wt % GNP can be successfully biaxially stretched to SR2. It was not possible to find a softening temperature suitable for stretching composite containing >10% GNP. This can be due to the higher GNP content has led to a high thermal conductivity of the PP/GNP composites, which rapidly dissipated the thermal energy, accelerated the crystallization process, and caused the very rapid cooling before it is possible to stretch the polymer (Martin et al., 2005). It is also found that the addition of GNP to PP limited the achievable strain rate to lower values and the best results were obtained for strain rate 2 s^{-1}. Therefore, a constant strain rate of 2 s^{-1} and stretch ratio (SR) of 1.5 and 2 was used to biaxially stretch the samples whenever possible and the true stress and nominal strain data were recorded.

Demonstrator Parts

Demonstrator products were developed for the targeted potential applications, such as enclosures with good mechanical robustness and electrostatic dissipation capabilities. Vacuum forming (C. R. Clarke 1820 Vacuum Former) was selected as the manufacturing process for producing 3D demonstrator prototypes. Optimized parameters used for vacuum molding were: 150°C/100 s for unfilled PP sheet and 150°C/76 s for PP/GNP composites sheet. Materials for static dissipation applications require an electrical resistivity of approximately 10^8 to 10^3 ohm-cm (King et al, 1999). The range of conductivity of the composites, and their ability to withstand biaxial deformation was first determined and the results were used to inform the formulation and dimension of the demonstrator parts. The thermal forming process and the resulting demonstrator parts are shown in **Supplementary Figures S2, S3**. The range of properties exhibited by the demonstrator parts were subsequently compared to those of the biaxially stretched materials, to evaluate the effectiveness of using biaxial stretching for product property prediction.

Mechanical Analysis

Tensile tests were carried out at room temperature following BS EN ISO 527–1: 1996 and using an Instron 5,564 universal Tester with a clip-on extensometer and a 2 kN load cell. Dumbbell-shaped samples (type 1BA) were cut from the compression moulded samples using a stamping press. For modulus measurement, nominal strain was determined using data from the extensometer, which was attached to the narrow portion of the dumb-bell samples, and at a crosshead speed of 1 mm/min. The elastic modulus was determined from the slope of the regression of the stress-strain data between 0.05–0.25% strain. For strength and elongation, the nominal strain was derived from the grip displacement at a crosshead speed of 50 mm/min.

Thermal Analysis

Differential scanning calorimetry (DSC) was performed to study the melting and crystallization behavior of unfilled PP and PP/GNP composites using a Perkin–Elmer DSC model six under an inert nitrogen atmosphere and a heating and cooling rate of 10 K/min, in a temperature range from 30 to 275°C. In all cases the samples were held at 275°C for 3 min, cooled to 30°C and reheated to 275°C to ensure complete melting of the crystalline fraction of PP and to remove thermal history. The apparent crystalline content of the PP composites was determined using a value of 148 J/g for the enthalpy of fusion for a theoretically 100% crystalline PP (Kaszonyiová et al., 2018).

Electrical Properties

Volume resistivity measurements were performed in accordance with ASTM D-257 on compression moulded and stretched specimens using a Keithley electrometer (Model 6517A) equipped with an 8,009 test fixture. Circular samples (Φ = 60 mm, t = 1 mm) was used. The sample was placed between two circular electrodes and the volume resistivity was measured by applying a DC voltage across opposite sides of the sample and measuring the resultant current through the sample.

Microstructural Analysis

The morphology and the degree of dispersion of GNPs in the polymer matrix were investigated using Scanning Electron Microscopy (SEM). Samples for SEM analysis were plasma

TABLE 3 | Effect of GNP addition on the thermal properties of unfilled PP and PP/GNP composites.

Material	First heating			Cooling		Second heating		
	Tm (°C)	X_c (%)	Impr (%)	Tc (°C)	Impr (%)	Tm (°C)	X_c (%)	Impr (%)
PP unfilled	168.6	40.41		108.2		167.7	39.26	
PP/5wt%M-5	169.2	61.49	52.17	122.9	13.59	169.1	60.14	53.18
PP/10wt% M-5	169.4	58.24	44.15	123.6	14.23	169.2	53.11	35.28
PP/15wt% M-5	169.6	57.36	41.97	124.1	14.70	169.8	49.73	26.68
PP/20wt% M-5	169.9	56.28	39.30	124.9	15.43	169.7	49.05	24.96

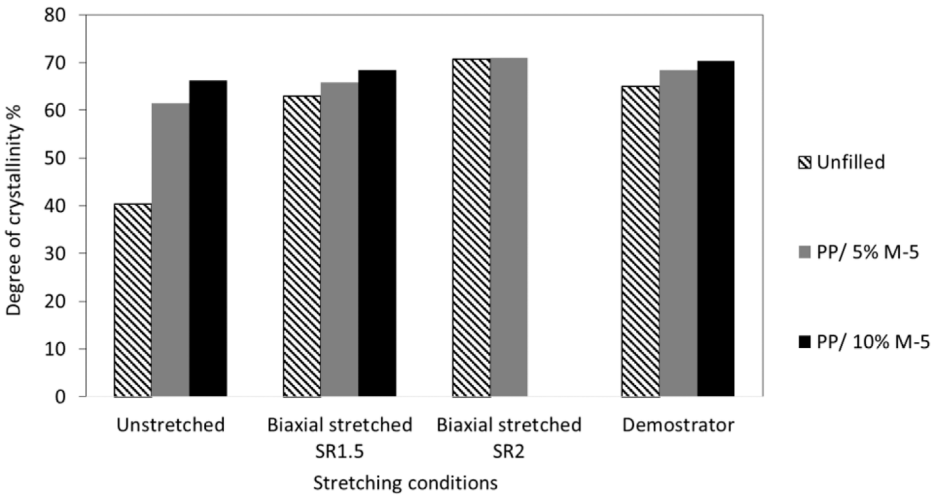

FIGURE 1 | Effect of GNP content and the biaxial stretching deformation on Xc% of unfilled PP, PP/GNP composites and the demonstrator parts.

etched for 60 s at an etching power of 100 w using a reactive ion etching system (STS Cluster C005) and then gold sputtered prior to imaging. These samples were examined using a JEOL 6500F Field Emission Scanning Electron Microscopy (FE-SEM) with an operating voltage of 5 kV.

RESULTS AND DISCUSSIONS

Thermal Properties

The melting and crystallization behavior of unfilled PP and PP/GNP composites were obtained based on the DSC data. **Table 3** shows the effect of GNP addition on the thermal properties of unfilled PP. The addition of GNP had little effect on the melting temperature (T_m) of PP. An increase in $\%X_c$ with increasing GNP content has been noticed, suggesting a change in the crystal type and the perfection. The presence of GNP is known to accelerate the PP crystallization kinetics (Beuguel et al., 2018), where GNP may serve as a nucleation site and PP chains may grow epitaxial on GNP (Jun et al., 2018). Similar behavior has also been reported in other polymer composite systems such as PA6/GNP composite (Mayoral et al., 2015).

Xc% of the testing materials (first heating) after biaxial deformation are given in **Figure 1** and more detailed data can be found in **Supplementary Table S1**. The results reflected a strain induced increase in crystallization, and a γ-β phase transition during the stretching process. Biaxial stretching of unfilled PP resulted in an increase in the crystallization temperature (T_c) of up to ~12 °C, depending on the SR. Significant increases in $X_c\%$ resulted from biaxial stretching, from ~40% (unstretched) to ~63% (SR1.5) and ~70% (SR2). This may be because as the strain rate increases, polymer chains have less time to relax leading to higher levels of chains orientation/alignment and thus higher degrees of strain-induced crystallization (Mayoral et al., 2013). No significant differences in T_g or T_m have been observed when the unfilled PP was biaxially deformed. For the PP/GNP composites, T_c increased by up to ~17 °C depending on the SR. The extent of $X_c\%$ increases is smaller as compared to unfilled PP. Under the same SR, the $X_c\%$ was similar for the unfilled PP and PP/GNP composites. The demonstrator parts showed similar Xc% with that of the biaxially stretched (SR1.5) neat PP and composite samples.

Mechanical Properties

The tensile mechanical properties of unfilled PP, PP/5%M-5 and PP/10% M-5 before and after biaxial deformation were presented in **Figure 2**. The typical stress-strain curves can be found in **Supplementary Figure S1**. Both Young's modulus and yield strength increased with the addition of GNP and with

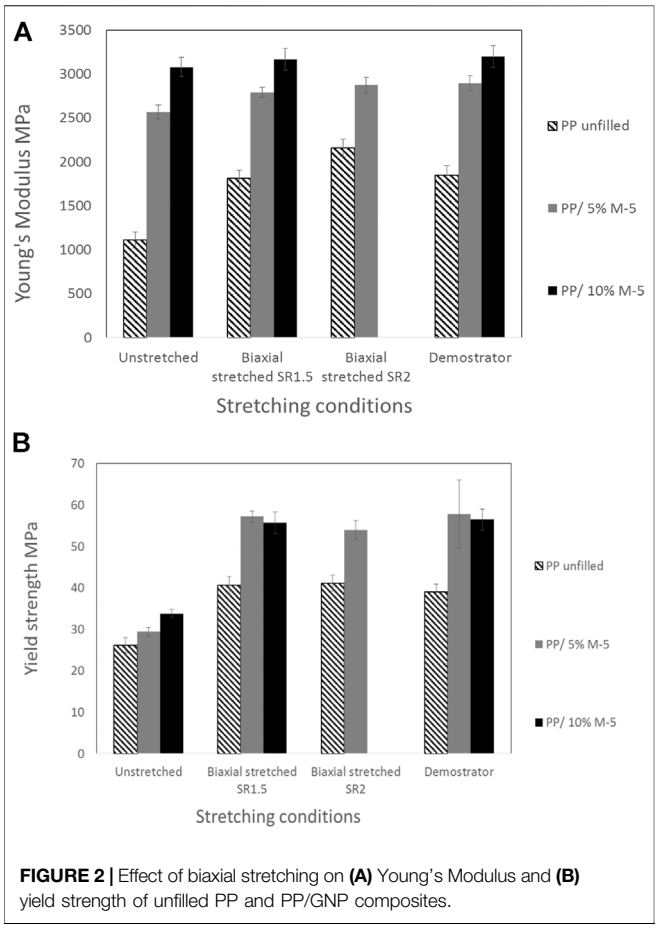

FIGURE 2 | Effect of biaxial stretching on **(A)** Young's Modulus and **(B)** yield strength of unfilled PP and PP/GNP composites.

increasing SR. The increase in Young's modulus due to stretching was most significant for unfilled PP, with SR giving ~2 fold increase in the Young's modulus. Such significant increase in stiffness may be attributed to the strong alignment of the crystalline region within the PP, producing more oriented chains in the stretching direction (Díez et al., 2005). This is also consistent with the crystallinity data shown in **Figure 1**, where biaxially stretched unfilled PP have greatly enhanced Xc%. In contrast, the effect of stretching on Young's moduli of PP/5% M-5 and PP/10% M-5 was less distinctive, as the presence of GNP has already led to significantly enhanced the composite crystallinity, and the Xc% change in these samples are less sensitive to stretching.

Figure 2B shows that biaxial stretching also resulted in increased yield strength for both unfilled PP and PP/GNP composites. The result is similar to the simulation results reported for biaxially stretched PP, where a higher yield stress observed as draw ratios increase was attributed to the increased crystalline structure orientation (Kershah et al., 2020). Enhanced yield strengths for PP/GNP composites may be due to the presence of GNP could have restricted the molecular chain mobility during the deformation process. In addition, the resulting yield strengths seen for unfilled PP and PP/5%M-5 are similar at SR1.5 and SR2. The mechanical properties measurements obtained for the demonstrator parts are in line with the results of the SR1.5 PP/GNP composites.

Electrical Properties

Figure 3 shows that the in-plane electrical resistivity of PP decreases 10^6 fold with addition of 10% GNP. This is due to the formation of the electrical percolation network, where the percolation threshold for PP/GNP system is reported to be ~5–10wt% (He et al., 2017; He et al., 2017). The electrical resistivity of PP/5%M-5 and PP/10% M-5 both slightly increased with increasing SR. This finding is consistent with (Du et al., 2011) and may be attributed to the distance between the GNPs being higher than the critical maximum distance for electron hopping after biaxial deformation. Note no resistivity data was collected for PP/10% M-5 at SR = 2 due to the failure of the sample (rupture) during testing. It is worth mentioning that in a study conducted by You et al. (2017), enhanced electrical conductivity has been achieved by bi-axially stretching PP/Polymethylmethacrylate (PMMA)/GNP nanocomposites. In this case, GNP were firstly blended with PMMA and then mixed into PP matrix and PMMA bridged the GNP to the non-polar PP matrix, hence facilitating the homogeneous dispersion and the orientation of the chemically converted GNP during the stretching process. Shen et al. (2012) on the other hand, reported that the change of electrical conductivity in stretched PP/CNT composite film followed two stages. The electrical resistivity first increased up to $10^{11}\,\Omega\,cm$ (up to SR = 2.5), and further stretching the film (SR = 3.5) led to reduction of resistivity by eight orders of magnitude. Their results suggested an electrical percolation network rebuilding process following the breaking of the CNT conducting network.

After biaxially stretching, PP/GNP composites samples (SR1.5) were annealed at 150°C (below the T_m of PP). The volume resistivity decreased (conductivity increased) and returned to approximately the same value measured prior to stretching. The finding is in line with (Xiang et al., 2018) where post-deformation annealing is believed to allow polymer chain relaxation. As a consequence, increased contacts between the conductive filler materials can be achieved to re-establish the electrical percolation network. The electrical conductivity of the demonstrator parts, before or after annealing, showed consistent results to those obtained for biaxially stretched samples (SR1.5).

Microstructural Analysis (SEM)

Figure 4 shows the typical SEM images of unstretched PP/GNP 5% M-5 composite and the demonstrator part with the same composition produced from the vacuum thermoforming process. A homogeneous dispersion of GNP in the PP matrix can be observed on both sets of micrographs. The biaxial stretching effect caused by the thermoforming process is clearly visible in the demonstrator parts as the GNP are more dispersed and oriented along the diagonal direction (45° direction denoted by black arrows) as a result of stretching. This result is in line with previously reported bi-axially stretched polymer nanocomposites, where nanofillers such as CNT and nanoclay appear oriented in the stretching plane after biaxial stretching (Abu-Zurayk et al., 2010; Xiang et al., 2015).

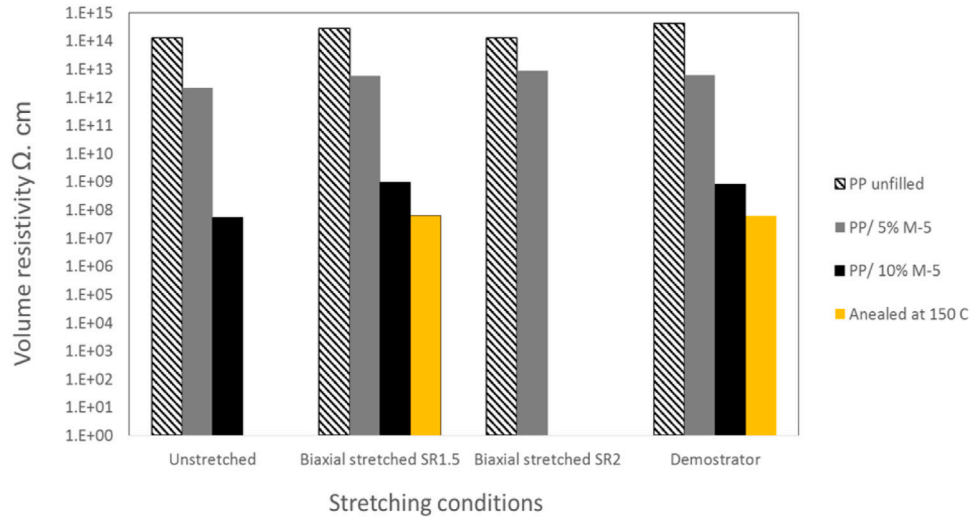

FIGURE 3 | Volume resistivity of unfilled PP, PP/GNP composites and their demonstrator parts.

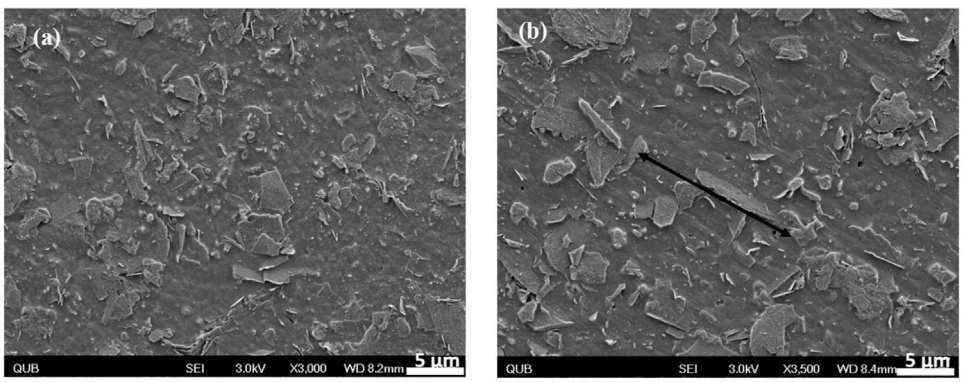

FIGURE 4 | SEM images of plasma etched **(A)** unstretched PP/GNP 5% M-5 and **(B)** the demonstrator part.

CONCLUSIONS

The effects of graphene nanoplatelet (GNP) addition and biaxial stretching on melt processed polypropylene (PP) and PP/GNP composites were investigated. Composite materials showed generally improved mechanical properties (Young's modulus and yield strength) as a result of GNP addition and biaxial stretching. The increased mechanical properties can be attributed to the increased polymer crystallinity and the greater restriction on molecular mobility. Thermal analysis of the stretched samples revealed a strain induced increase in crystallization. The volume resistivity of composites increased after biaxial stretching and with increasing SR, which is consistent with the disruption of GNP network pathways and increasing distance between GNP. However, the conductivity of stretched composites remained higher than unfilled PP, and annealing of the stretched specimens resulted in nearly full recovery of the conductivity prior to stretching. Further evaluation on the vacuum forming processed demonstrator parts showed similar thermal/mechanical and electrical properties comparable to those of the biaxially stretched (SR 1.5) samples. This confirms the biaxial stretching technique is capable of informing the structure and properties of the composites undergoing secondary processing such as vacuum forming.

This work provides the necessary platform for informed exploitation of polymer-graphene nanocomposites into processed articles, which will enable compounders, processors and designers of nanocomposite products to optimize the microstructure and properties of these materials to suit differing application requirements. The materials and processing techniques developed and utilized in this study have a wide range of potential applications such as low cost, light weight, electromagnetic insulating shielding and anti-static packaging, etc. Future work may be expanded to further explore the effect of biaxial stretching on wide range of polymer nanocomposite systems containing advanced functional

nanomaterials, such as CNT, graphene oxide, boron nitride nanosheets, tungsten disulphide (WS_2), molybdenum disulfide (MoS_2), etc.

DATA AVAILABILITY STATEMENT

The raw data supporting the conclusions of this article will be made available by the authors, without undue reservation.

AUTHOR CONTRIBUTIONS

BMa conducted the experiments. GM contributed to the bi-axial stretching experiment, PM contributed to the vacuum thermal forming experiments, GG contributed to the melt processing of polymer composites, BMi and PD contributed to the material characterization, AH and DS funding administration. All authors contributed to the results discussion/analysis, writing and revision of the manuscript.

FUNDING

Authors acknowledge QNRF NPRP award (NPRP5-039-2-014) (NRF) Qatar, Engineering and Physical Science Research Council (EP/M020851/1) for funding the research.

ACKNOWLEDGMENTS

The authors wish to thank the QNRF for research funding through NPRP award (NPRP5-039-2-014) (NRF) Qatar.The authors would also like to acknowledge the Engineering and Physical Science Research Council (EP/M020851/1) for funding support.

SUPPLEMENTARY MATERIAL

The Supplementary Material for this article can be found online at: https://www.frontiersin.org/articles/10.3389/fmats.2021.687282/full#supplementary-material

REFERENCES

Abu-Zurayk, R., Harkin-Jones, E., McNally, T., Menary, G., Martin, P., Armstrong, C., et al. (2010). Structure–property Relationships in Biaxially Deformed Polypropylene Nanocomposites. *Composites Sci. Techn.* 70 (9), 1353–1359. doi:10.1016/j.compscitech.2010.04.011

Beuguel, Q., Boyer, S. A. E., Settipani, D., Monge, G., Haudin, J-M., Vergnes, B., et al. (2018). Crystallization Behavior of Polypropylene/graphene Nanoplatelets Composites. *Polym. Crystallization* 1 (3), e10024. doi:10.1002/pcr2.10024

Díez, F. J., Alvariño, C., López, J., Ramírez, C., Abad, M. J., Cano, J., et al. (2005). Influence of the Stretching in the Crystallinity of Biaxially Oriented Polypropylene (BOPP) Films. *J. Therm. Anal. Calorim.* 81 (1), 21–25. doi:10.1007/s10973-005-0739-x

Du, J., Zhao, L., Zeng, Y., Zhang, L., Li, F., Liu, P., et al. (2011). Comparison of Electrical Properties between Multi-Walled Carbon Nanotube and Graphene Nanosheet/high Density Polyethylene Composites with a Segregated Network Structure. *Carbon* 49 (4), 1094–1100. doi:10.1016/j.carbon.2010.11.013

Feng, C., and Jiang, L. (2014). Micromechanics Modeling of Bi-Axial Stretching Effects on the Electrical Conductivity of CNT-Polymer Composites. *Int. J. Appl. Mech.* 07 (01), 1550005. doi:10.1142/S1758825115400050

He, M., Zhu, C., Xu, H., Sun, D., Chen, C., Feng, G., et al. (2020). Conducting Polyetheretherketone Nanocomposites with an Electrophoretically Deposited Bioactive Coating for Bone Tissue Regeneration and Multimodal Therapeutic Applications. *ACS Appl. Mater. Inter.* 12 (51), 56924–56934. doi:10.1021/acsami.0c20145

He, S., Zhang, J., Xiao, X., Hong, X., and Lai, Y. (2017a). Investigation of the Conductive Network Formation of Polypropylene/graphene Nanoplatelets Composites for Different Platelet Sizes. *J. Mater. Sci.* 52 (22), 13103–13119. doi:10.1007/s10853-017-1413-y

He, S., Zhang, J., Xiao, X., Lai, Y., Chen, A., and Zhang, Z. (2017b). Study on the Morphology Development and Dispersion Mechanism of Polypropylene/graphene Nanoplatelets Composites for Different Shear Field. *Composites Sci. Techn.* 153, 209–221. doi:10.1016/j.compscitech.2017.10.024

Jiang, Y., Yang, Y., Zheng, X., Yi, Y., Chen, X., Li, Y., et al. (2020). Multifunctional Load-Bearing Hybrid Hydrogel with Combined Drug Release and Photothermal Conversion Functions. *NPG Asia Mater.* 12 (1), 18. doi:10.1038/s41427-020-0199-6

Jun, Y-S., Um, J. G., Jiang, G., Lui, G., and Yu, A. (2018b). Ultra-large Sized Graphene Nano-Platelets (GnPs) Incorporated Polypropylene (PP)/GnPs Composites Engineered by Melt Compounding and its thermal, Mechanical, and Electrical Properties. *Composites B: Eng.* 133, 218–225. doi:10.1016/j.compositesb.2017.09.028

Jun, Y. S., Um, J. G., Jiang, G., and Yu, A. (2018a). A Study on the Effects of Graphene Nano-Platelets (GnPs) Sheet Sizes from a Few to Hundred Microns on the thermal, Mechanical, and Electrical Properties of Polypropylene (PP)/GnPs Composites. *Express Polym. Lett.* 12 (10), 885–897. doi:10.3144/expresspolymlett.2018.76

Kaszonyiová, M., Rybnikar, F., Kubišová, M., and Maňas, D. (2018). Effect of Beta Irradiation on the Structural Changes of Isotactic Polypropylene. *Materiali in tehnologije* 52 (1), 15–18. doi:10.17222/mit.2017.089

Kershah, T., Anderson, P. D., and van Breemen, L. C. A. (2020). Uniaxial and Biaxial Response of Anisotropic Polypropylene. *Macromolecular Theor. Simulations* 29 (4), 2000018. doi:10.1002/mats.202000018

King, J. A., Via, M. D., Morrison, F. A., Wiese, K. R., Beach, E. A., Cieslinski, M. J., et al. (2011). Characterization of Exfoliated Graphite Nanoplatelets/polycarbonate Composites: Electrical and thermal Conductivity, and Tensile, Flexural, and Rheological Properties. *J. Compos. Mater.* 46 (9), 1029–1039. doi:10.1177/0021998311414073

King, J. A., Tucker, K. W., Vogt, B. D., Weber, E. H., and Quan, C. (1999). Electrically and Thermally Conductive Nylon 6,6. *Polym. Composites* 20 (5), 643–654. doi:10.1002/pc.10387

Liang, J. Z., and Du, Q. (2018). Melt Flow and Flexural Properties of Polypropylene Composites Reinforced with Graphene Nano-Platelets. *Int. Polym. Process.* 33 (1), 35–41. doi:10.3139/217.3335

Maddah, H. A. (2016). Polypropylene as a Promising Plastic: A Review. *Am. J. Polym. Sci.* 6 (1), 1–11. doi:10.5923/j.ajps.20160601.0110.1155/2016/3478709

Martin, P. J., Tan, C. W., Tshai, K. Y., McCool, R., Menary, G., Armstrong, C. G., et al. (2005). Biaxial Characterisation of Materials for Thermoforming and Blow Moulding. *Plastics, Rubber and Composites* 34 (5-6), 276–282. doi:10.1179/174328905X64803

Mayoral, B., Garrett, G., and McNally, T. (2014). Effect of Screw Configuration Profiles on the Dispersion of MWCNTs in a Poly (Propylene) Matrix. *Macromolecular Mater. Eng.* 299, 748–756. doi:10.1002/mame.201300172

Mayoral, B., Harkin-Jones, E., Khanam, P. N., AlMaadeed, M. A., Ouederni, M., Hamilton, A. R., et al. (2015). Melt Processing and Characterisation of Polyamide 6/graphene Nanoplatelet Composites. *RSC Adv.* 5 (65), 52395–52409. doi:10.1039/C5RA08509H

Mayoral, B., Hornsby, P. R., McNally, T., Schiller, T., Jack, K., and Martin, D. J. (2013). Quasi-Solid State Uniaxial & Biaxial Deformation of PET/MWCNT Composites: Structural Evolution, Electrical and Mechanical Properties. *RSC Adv.* 3, 5162–5183. doi:10.1039/c3ra22597f

Nidamanuri, N., Li, Y., Li, Q., and Dong, M. (2020). Graphene and Graphene Oxide-Based Membranes for Gas Separation. *Engineered Sci.* 9, 3–16. doi:10.30919/es8d128906

Noorunnisa Khanam, P., AlMaadeed, M. A., Ouederni, M., Harkin-Jones, E., Mayoral, B., Hamilton, A., et al. (2016b). Melt Processing and Properties of Linear Low Density Polyethylene-Graphene Nanoplatelet Composites. *Vacuum* 130, 63–71. doi:10.1016/j.vacuum.2016.04.022

Noorunnisa Khanam, P., AlMaadeed, M. A., Ouederni, M., Mayoral, B., Hamilton, A., and Sun, D. (2016a). Effect of Two Types of Graphene Nanoplatelets on the Physico–Mechanical Properties of Linear Low–Density Polyethylene Composites. *Adv. Manufacturing: Polym. Composites Sci.* 2 (2), 67–73. doi:10.1080/20550340.2016.1235768

Shen, J., Champagne, M. F., Yang, Z., Yu, Q., Gendron, R., and Guo, S. (2012). The Development of a Conductive Carbon Nanotube (CNT) Network in CNT/polypropylene Composite Films during Biaxial Stretching. *Composites A: Appl. Sci. Manufacturing* 43 (9), 1448–1453. doi:10.1016/j.compositesa.2012.04.003

Singh, M. V. (2021). Conversions of Waste Tube-Tyres (WTT) and Waste Polypropylene (WPP) into Diesel Fuel through Catalytic Pyrolysis Using Base SrCO3. *Engineered Sci.* 13, 87–97. doi:10.30919/es8d1158

Tsai, P. (2020). Performance of Masks and Discussion of the Inactivation of SARS-CoV-2. *Engineered Sci.* 10, 1–7. doi:10.30919/es8d1110

Valentini, L., Biagiotti, J., Kenny, J. M., and López Manchado, M. A. (2003). Physical and Mechanical Behavior of Single-Walled Carbon Nanotube/polypropylene/ethylene–Propylene–Diene Rubber Nanocomposites. *J. Appl. Polym. Sci.* 89 (10), 2657–2663. doi:10.1002/app.12319

Xiang, D., Harkin-Jones, E., and Linton, D. (2015). Characterization and Structure–Property Relationship of Melt-Mixed High Density Polyethylene/multi-Walled Carbon Nanotube Composites under Extensional Deformation. *RSC Adv.* 5 (59), 47555–47568. doi:10.1039/C5RA06075C

Xiang, D., Wang, L., Zhang, Q., Chen, B., Li, Y., and Harkin-Jones, E. (2018). Comparative Study on the Deformation Behavior, Structural Evolution, and Properties of Biaxially Stretched High-Density Polyethylene/carbon Nanofiller (Carbon Nanotubes, Graphene Nanoplatelets, and Carbon Black) Composites. *Polym. Composites* 39 (S2), E909–E923. doi:10.1002/pc.24328

Xu, P., Qu, M., Ning, Y., Jia, T., Zhang, Y., Wang, S., et al. (2019). High Performance and Low Floating Fiber Glass Fiber-Reinforced Polypropylene Composites Realized by a Facile Coating Method. *Adv. Composites Hybrid Mater.* 2 (2), 234–241. doi:10.1007/s42114-019-00080-0

Yan, X., Liu, J., Khan, M. A., Sheriff, S., Vupputuri, S., Das, R., et al. (2020). Efficient Solvent-Free Microwave Irradiation Synthesis of Highly Conductive Polypropylene Nanocomposites with Lowly Loaded Carbon Nanotubes. *ES Mater. Manufacturing* 9, 21–33. doi:10.30919/esmm5f716

You, F., Li, X., Zhang, L., Wang, D., Shi, C-Y., and Dang, Z-M. (2017). Polypropylene/poly(methyl Methacrylate)/graphene Composites with High Electrical Resistivity Anisotropy *via* Sequential Biaxial Stretching. *RSC Adv.* 7 (10), 6170–6178. doi:10.1039/C6RA28486H

Yuan, D., Pedrazzoli, D., Pircheraghi, G., and Manas-Zloczower, I. (2017). Melt Compounding of Thermoplastic Polyurethanes Incorporating 1D and 2D Carbon Nanofillers. *Polymer-Plastics Techn. Eng.* 56 (7), 732–743. doi:10.1080/03602559.2016.1233265

Zhang, H-B., Zheng, W-G., Yan, Q., Yang, Y., Wang, J-W., Lu, Z-H., et al. (2010). Electrically Conductive Polyethylene Terephthalate/graphene Nanocomposites Prepared by Melt Compounding. *Polymer* 51 (5), 1191–1196. doi:10.1016/j.polymer.2010.01.027

Zhang, R-C., Huang, Z., Huang, Z., Zhong, M., Zang, D., Lu, A., et al. (2020). Uniaxially Stretched Polyethylene/boron Nitride Nanocomposite Films with Metal-like thermal Conductivity. *Composites Sci. Techn.* 196, 108154. doi:10.1016/j.compscitech.2020.108154

Zhao, S., Niu, M., Peng, P., Cheng, Y., and Zhao, Y. (2020). Edge Oleylaminated Graphene as Ultra-Stable Lubricant Additive for Friction and Wear Reduction. *Engineered Sci.* 9, 77–83. doi:10.30919/es8d807

Zhao, Y., Niu, M., Yang, F., Jia, Y., and Cheng, Y. (2019). Ultrafast Electro-Thermal Responsive Heating Film Fabricated from Graphene Modified Conductive Materials. *Engineered Sci.* 8, 33–38. doi:10.30919/es8d501

Zhou, Y., Wang, P., Ruan, G., Xu, P., and Ding, Y. (2021). Synergistic Effect of P[MPEGMA-IL] Modified Graphene on Morphology and Dielectric Properties of PLA/PCL Blends. *ES Mater. Manufacturing* 11, 20–29. doi:10.30919/esmm5f928

Zhu, S., Zhang, L., Sun, d., He, M., Tan, P., and Jiang, N. (2021). Graphene Reinforced Polyether Ether Ketone Nanocomposites for Bone Repair Applications. *Polymer Testing*, 107276. doi:10.1016/j.polymertesting.2021.107276

Conflict of Interest: Author MO was employed by the company Qatar Petrochemical Company.

The remaining authors declare that the research was conducted in the absence of any commercial or financial relationships that could be construed as a potential conflict of interest.

frontiers in Materials

ORIGINAL RESEARCH
published: 09 August 2021
doi: 10.3389/fmats.2021.725242

Synthesis of Modified Polycarboxylate and Its Application in Ultra-High Performance Concrete

*Shuncheng Xiang, Yansheng Tan and Yingli Gao**

School of Traffic and Transportation Engineering, Changsha University of Science and Technology, Changsha, China

Modified polyurethane prepolymer was prepared using the segmental synthesis method. Then, pectiniform polycarboxylate was synthesized at normal temperature in the complex initiation system of H_2O_2, APS, sodium bisulfite, Vc, and Rongalit according to the free radical polymerization reaction mechanism, using TPEG, AA, and PEG as raw materials and TGA as the chain transfer agent. Compared with commercial Sika polycarboxylate, its flowability, strength, drying shrinkage, and auto-shrinkage were studied. The experimental results show that the synthesized polycarboxylate could be better dispersed. Adding silica fume can enhance the compressive strength of ultra-high performance concrete (UHPC), while slag may decline its strength. By incorporating slag and silica fume, the drying shrinkage of UHPC was reduced, but its auto-shrinkage was increased.

Keywords: polycarboxylate, synthesis at indoor temperature, UHPC, application, interaction

OPEN ACCESS

Edited by:
Dong Xiang,
Southwest Petroleum University, China

Reviewed by:
Sicong Hu,
Nanchang University, China
Hongxia Gao,
Hunan University, China
Jiake Zhang,
Tongji University, China

****Correspondence:***
Yingli Gao
yingligao@126.com

Specialty section:
This article was submitted to Polymeric and Composite Materials, a section of the journal Frontiers in Materials

Received: *15 June 2021*
Accepted: *30 June 2021*
Published: *09 August 2021*

Citation:
Xiang S, Tan Y and Gao Y (2021) Synthesis of Modified Polycarboxylate and Its Application in Ultra-High Performance Concrete. Front. Mater. 8:725242. doi: 10.3389/fmats.2021.725242

INTRODUCTION

Multifunctional polycarboxylate has been developed rapidly over the decades. Polycarboxylate has functions such as slump protection, coagulation control, and shrinkage reduction. By adding polycarboxylate, the force between Portland cement particles and the physicochemical properties of their solid–liquid interface are changed, thus affecting the flowability of cement paste (Andersen et al., 1987; LI et al., 2005). However, at present, the synthesis of polycarboxylate is usually carried out by heating, with synthesis temperature between 60 and 90°C. However, preparation of polycarboxylate at indoor temperature has become a development trend of superplasticizer industry (Shang et al., 2009).

With the birth of polycarboxylate, preparing concrete mixtures with low water-to-binder ratio and high flowability becomes possible. Designing appropriate polycarboxylate can not only reduce the water demand of ultra-high performance concrete (UHPC) but also promote condensation hardening and strength development (Shi, 2009; Shi and He, 2010). According to the super-superposition effect of component properties, using two or more mineral admixtures to the compound can not only achieve the complementary advantages and further improve the comprehensive performance but also give full play to the excellent performance of composite mineral admixtures in view of the problem that the quality of mineral admixtures fluctuates greatly in China and affects quality control in the concrete production process (AITCIN, 2003).

In this paper, polyurethane-modified polycarboxylate was prepared at indoor temperature by controlling the molar ratio of acrylic acid to macromonomer. And its application in ultra-high performance concrete was studied by comparing with Sika high-performance polycarboxylate, which would be very valuable for practical engineering applications.

TABLE 1 | Chemical constitution of PI 42.5 Portland cement, slag, fly ash, and silica fume w/%.

Material	Chemical constitution w/%				
	SiO_2	Al_2O_3	Fe_2O_3	CaO	MgO
Cement	25.26	6.38	4.05	64.67	2.68
Slag	33	13.91	0.82	39.11	10.04
Silica fume	90.82	1.03	1.50	0.45	0.83

EXPERIMENT

Raw Materials

PI 42.5 cement, mineral powder, and silica fume were adopted as raw materials, as shown in **Table 1**. The average particle size of PI 42.5 cement, mineral powder, and silica fume is 36.96, 20.30, and 0.22 μm, respectively. The molecular structure of commercial Sika high-performance polycarboxylate is shown in **Figure 1**.

Isophorone diisocyanate, hydroxyl-terminated silicone, polyether glycol, N-methylpyrrolidone, 1,4-butanediol, dimethylolpropionic acid, and prenyl alcohol polyoxyethylene ether (TPEG) were used for synthesis; the pure acrylic acid (AA), thioglycolic acid, p-toluenesulfonic acid, polyethylene glycol-200 (PEG-200), ascorbic acid (Vc), hydrogen peroxide, dibutyltin dilaurate, ammonium persulfate, and deionized water were analyzed.

Synthesis of Side Chain

During the synthesis, alcohol and amine compounds and multi-functional groups were introduced into the main chain of polycarboxylate molecules, so as to bring about more short branches, promote the alternating distribution of long polyether branches and short branches of chain extenders of alcohol and amine compounds, and increase the dispersibility and adaptability of the superplasticizer.

22.2 g isophorone diisocyanate was placed in a three-necked flask, polyethylene glycol 1000 containing dibutyltin dilaurate (N-methylpyrrolidone solution with 0.2 g dibutyltin dilaurate), and dimethylolpropionic acid in 25 g polyethylene glycol 1000 (3.35 g dimethylolpropionic acid dissolved in 5 ml N-methylpyrrolidone) was added dropwise in turn with a dropping funnel, and then 50 g water was added. The mixture was heated to 70°C and kept warm. Then, the mixed solution of hydroxyl-terminated polysiloxane and 1,4-butanediol (9 g of hydroxyl-terminated polysiloxane mixed with 3 g of 1,4-butanediol), 2.5 g of ethylenediamine, and 1.5 g of sodium dodecylbenzenesulfonate were added dropwise while stirring before feeding. When the free-NCO content in the mixed solution was detected to be 16%, heating was stopped to obtain the polyurethane prepolymer. The principle of side chain reaction was shown in **Figure 2**.

Preparation of Polycarboxylate (M-PCE)

To ensure the equal molar concentration of double bonds in the system, the concentration of free radicals and molecular weight regulators was controlled, and the molar ratio of acrylic acid to TPEG was adjusted. TPEG (120 g), purified water (80 ml), and PEG-200 (10 g) were put into a 250 ml four-necked flask. After fully stirring the mixed solution, 0.1 g dibutyltin dilaurate, 1.2 g of p-toluenesulfonic acid, and 30% hydrogen peroxide were added. A and B solutions were prepared for later use.

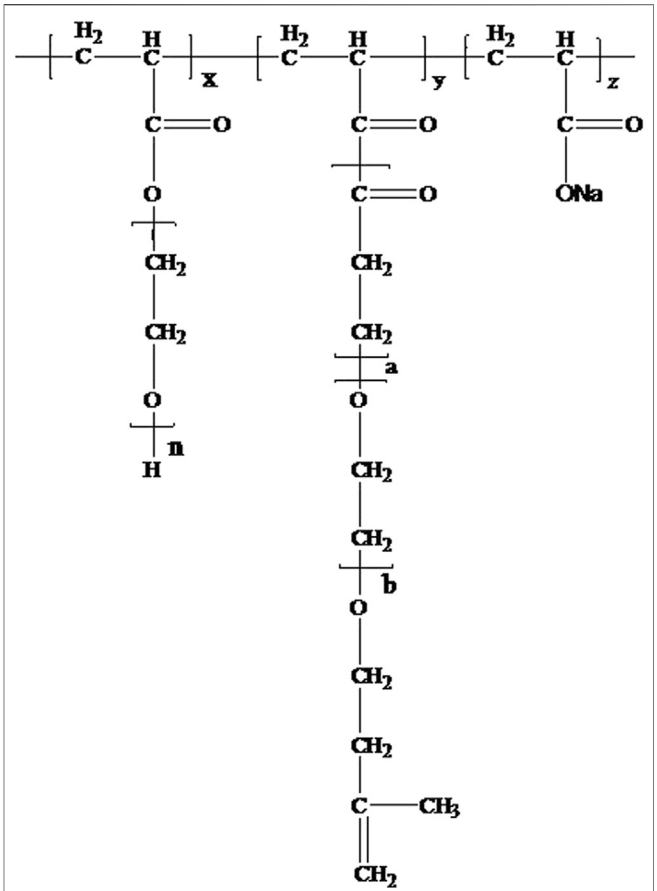

FIGURE 1 | Chemical structure of commercial Sika polycarboxylate.

Component A (acrylic acid + sodium bisulfite, Vc, or sodium formaldehyde sulfoxylate).

Component B (thioglycolic acid + ammonium persulfate).

A peristaltic pump was used to drip components A and B into the beaker at the rate of 2 ml/min, which lasted for 2.5 h. After that, the mixed solution was kept warm for a period of time, and the pH value was adjusted to 6–7 with NaOH to obtain mother liquor of polycarboxylate (M-PCE). The structure of synthesized M-PCE was shown in **Figure 3**.

Mortar Water-Reduction Rate Test

In view of GB/T8077-2012 *Test Method for Homogeneity of Concrete Admixtures*, the water reduction rate of polycarboxylate mortar is tested using the following formula:

$$\text{Mortar water reduction rate} = \frac{M_0 - M_1}{M_0} \times 100\%. \quad (1)$$

Here, M_0 is the water consumption of benchmark mortar flowability (mm) and M_1 is the water consumption when the flowability of mortar with admixture reaches 180±5 mm.

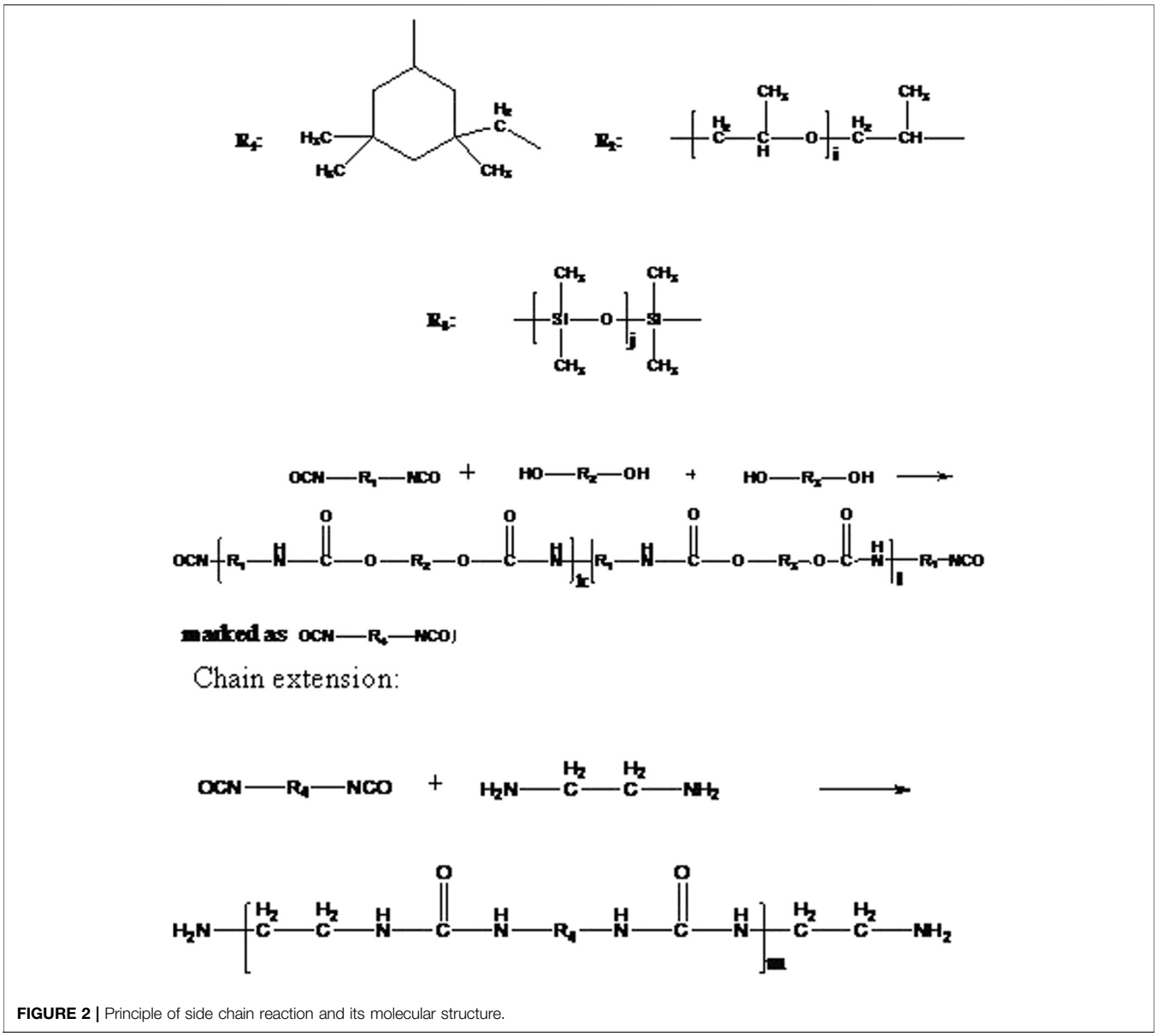

FIGURE 2 | Principle of side chain reaction and its molecular structure.

TABLE 2 | Binder constitution of UHPC.

No.	Portland cement (%)	Silica fume (%)	Slag (%)
N1	100	0	0
N2	85	15	0
N3	59.9	15	25.1
N4	72.2	11.1	16.7
N5	70	30	0
N6	58.3	16.7	25
N7	40	20	40

Mix Proportion of UHPC

The content of polycarboxylate is 2% (mass ratio) of cementitious components, the water-to-binder ratio of ultra-high performance concrete is 0.18, and the sand-to-binder ratio is 1.0. **Table 2** shows the mixture ratios.

Flowability

According to the standard GB/T2419-2005 "Method for Measuring Fluidity of Cement Mortar," fine sand below 2.36 mm was selected, the mass of cementitious material was 200 g, the sand-to-cement ratio was 1:1, the water-to-binder ratio was 0.18, and the polycarboxylate mother liquor content was 2%, then, the flowability of mortar was tested.

Strength

In the free shrinkage test, reference cement and standard sand were used, with the ratio of sand to cement of 1:1. The flowability of

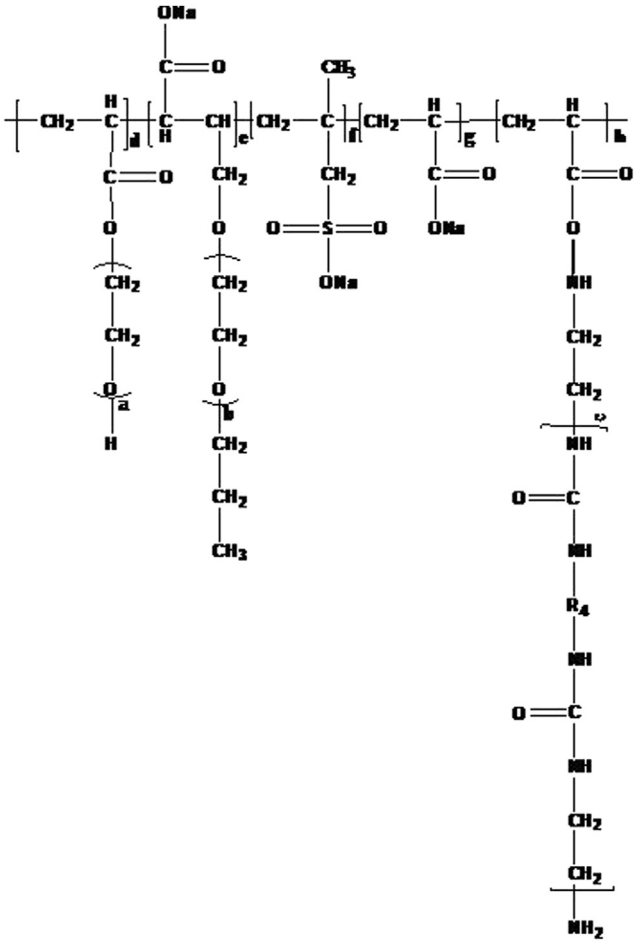

FIGURE 3 | Structure of synthesized modified polycarboxylate (M-PCE).

cement mortar was higher than 140 mm, and a set of 40 × 40 × 160 mm specimens was reported. The test molds were triple molds and were filled and maintained for 24 h. The temperature of the curing box was controlled to be 20°C ± 1°C, and the relative humidity was equal to or higher than 90%. Then, the mold was transferred to the steam curing room. The temperature in the drying room was 20 ± 3°C. Then, the strength at the 1st, the 3rd, the 7th, the 14th, and the 28th day was tested.

Drying Shrinkage

In view of JC/T603-2004 "Test Method for Drying Shrinkage of Cement Mortar," a group of 25 × 25 × 280 mm specimens should be formed in the drying shrinkage test of cement mortar, and the specimens should be demolded after being cured for 24 ± 1 h from the time of adding water. Then, the length of the test at the 1st day, 3rd day, 7th day, 14th day, 21st day, 28th day, 56th day, and 90th day was measured. The result was calculated according to the following formula, accurate to 0.001%:

$$S_n = \frac{(L_0 - L_{28}) \times 100}{280}, \quad (2)$$

where Sn is the drying shrinkage rate of the cement mortar specimen at the nth day (%); L_0 is the initial measurement reading (mm); L_{28} is the measured reading at the 28th day (mm); and 280 is the effective length of the specimen (mm).

Auto-Shrinkage

The auto-shrinkage of mortar in self-compacting cement mortar was measured with the combination of a bellow and a non-contact probe. The bellow has an inner diameter of 20 mm and a length of 340 ± 5 mm. The cement mortar flowability was higher than 140 mm, and the auto-shrinkage of cement mortar was continuously measured for 72 h.

RESULTS AND DISCUSSION

Water Reduction Rate of Mortar

The water consumption of benchmark mortar without superplasticizer was 93.7 g, which was 186 and 175 mm with an average of about 180 mm after rest. The experimental results are shown in **Table 3**.

The water reduction rate of mortar of M-PCE was similar to that of Sika. In terms of the molecular structure, the dispersing group of Sika was mainly a long-chain alkyl macromonomer. However, the dispersing ability of M-PCE was enhanced by the strong chemical bond of silicone groups in M-PCE and silicate phase (Jones et al., 1995). Due to its chemical structure, M-PCE has longer side chains than PCE, indicating good steric hindrance (Levi et al., 2002). Therefore, the dispersibility of M-PCE in cement is also excellent, which is consistent with the results of Kong et al. (Thompson et al., 1997) Silicone chains provide spatial repulsion between cement particles in some way, exerting dispersing effect on cement slurry. The anchoring ability of silicone groups has been confirmed by the enhanced adsorption behavior of silane-modified polycarboxylate in cement slurry (Kagi and Ren, 1995).

Flowability

The flowability of UHPC under the cement mortar–silica fume–mineral powder gelatinization system is shown in **Table 4**.

According to **Table 4**, the flowability of M-PCE was better than that of Sika under the same conditions, indicating that

TABLE 3 | Water reduction rate of polycarboxylate in mortar.

Polycarboxylate	Cement mortar (g)	Standard sand (g)	Water consumption M_1 (g)	Flowability	Water reduction rate (%)
M-PCE	150	450	51.8	180 mm, 183 mm	44.7
Sika	150	450	52.3	180 mm, 185 mm	44.2

TABLE 4 | Initial flowability of UHPC (mm).

Polycarboxylate	Number						
	N1	N2	N3	N4	N5	N6	N7
M-PCE	165	119	192	160	172	183	232
Sika	163	156	106	146	151	178	102

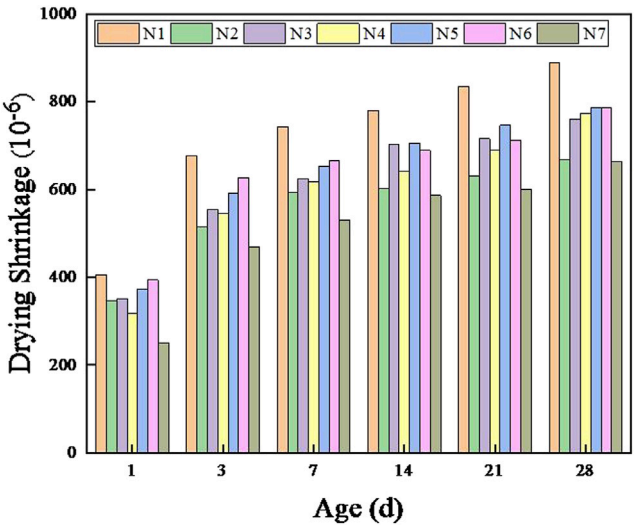

FIGURE 4 | Effect of M-PCE on drying shrinkage of UHPC.

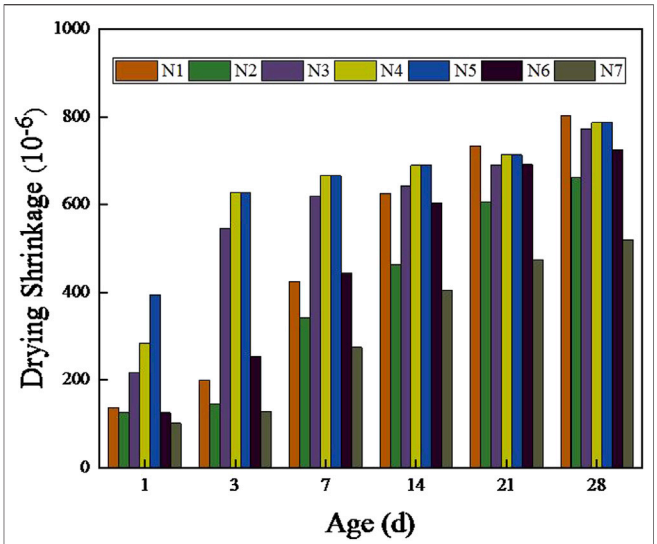

FIGURE 5 | Effect of Sika on drying shrinkage of UHPC.

M-PCE had better dispersion than Sika. In addition, the flowability of ultra-high performance concrete increased from 119 to 172 mm as silica fume content increased from 0 to 30%. However, when the amount of silica fume was too large, the flowability of concrete decreased. A large amount of superplasticizer will be adsorbed on the surface of silica fume with small particle size (Ganesh and Surya, 1995; Khatri et al., 1995). Under the action of superplasticizer, silica fume, as ultra-fine particles, disperses cement particles and releases more free water (Duval and Kadri, 1998). For ordinary concrete, the dosage of silica fume is lower than 10%. For high-strength concrete, the dosage of silica fume should be increased to 10% (Khayat et al., 1993). UHPC silica fume consumption is usually lower than 15% (Mazloom et al., 2004). For UHPC studied in this paper, if the amount of silica fume is over 30%, it will make concrete extremely viscous, reducing the flowability of concrete.

The specific surface area of mineral powder is larger than that of cement. Therefore, mineral powder significantly affects the flowability of UHPC. When the amount of mineral powder exceeds 40%, the flowability of UHPC is less than 140 mm.

Strength

Under the cement mortar–silica fume–mineral powder gelatinization system, M-PCE and Sika polycarboxylate were, respectively, used to prepare UHPC.

TABLE 5 | Compressive strength of UHPC (M-PCE).

Number	Compressive strength (MPa)			
	3d	7d	14d	28d
N1	73.4	81.6	92.9	97.4
N2	76.3	84.9	96.9	115.5
N3	71.0	83.7	90.4	100.9
N4	74.5	80.4	99.7	116.3
N5	72.7	81.0	93.2	101.4
N6	75.5	81.4	88.9	99.5
N7	63.6	72.9	89.4	103.6

As can be seen from **Table 4**, UHPC prepared with the two different superplasticizers had little difference in compressive strength. **Table 5** shows that, with the increase of silica fume dosage, the early compressive strength of UHPC increased. After the amount of silica fume exceeds 25%, the increment of strength slows down. When the amount of silica fume increased from 0 to 15%, the 28-day strength of concrete rose from 92.5 to 117.4 MPa. Therefore, silica fume could improve the compressive strength of ultra-high strength concrete. It is worth noting that, at the dosage of silica fume lower than 15%, the 28-day compressive strength of UHPC increased with the dosage of silica fume. **Table 6** also shows the same trend. In addition, we found that the addition of mineral powder would reduce the 3-day compressive strength of UHPC. Especially when the content of mineral powder was more than 25%, the early strength of concrete decreased from 71.0 to 63.6 MPa. At the 28th day, when the dosage of mineral powder increased from 10 to 20%, the compressive strength of UHPC reached the maximum value, and the strength reached 103.6 MPa. It is not difficult to see whether adding mineral powder alone would significantly improve the compressive strength of UHPC. However, when mixed with silica fume, slag would enhance the

TABLE 6 | Compressive strength of UHPC (M-PCE).

Number	Compressive strength (MPa)			
	3d	7d	14d	28d
N1	71.6	76.9	87.3	92.5
N2	74.5	82.8	96.8	117.4
N3	70.0	79.3	86.6	94.6
N4	66.7	80.0	93.5	109.4
N5	71.2	83.8	90.6	97.4
N6	70.9	82.7	98.3	108.5
N7	64.7	73.6	86.2	93.3

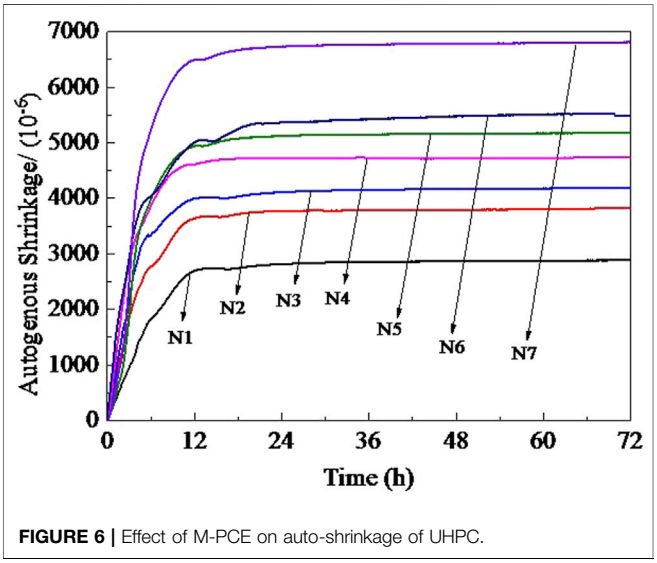

FIGURE 6 | Effect of M-PCE on auto-shrinkage of UHPC.

compressive strength of UHPC. According to previous studies, to improve the strength of concrete, the best constitution of cementitious materials is mainly associated with the calcium-to-silicon ratio (Erdem and Kırca, 2008; Elahi et al., 2010). When the calcium-to-silicon ratio is 1.30, the strength of UHPC is greater than that of silica fume (Taylor, 1997).

Drying Shrinkage

Under the cement mortar–silica fume–mineral powder gelatinization system, M-PCE and Sika polycarboxylate, respectively, were adopted to prepare UHPC. The drying shrinkage changes of UHPC are shown in **Figures 4**, **5**.

As shown in **Figures 4**, **5**, UHPC prepared with M-PCE had slightly higher drying shrinkage as compared with UHPC prepared with Sika. Sika as a compound product has stronger capacity of reducing the surface tension of pore solution, so UHPC prepared with Sika will have a smaller drying shrinkage value.

Figures 4, **5** show that the drying shrinkage value of UHPC was the smallest when the dose of mineral powder was about 50%. In addition, the drying shrinkage of UHPC increased with the addition of silica fume (N2 and N5 curves) because silica fume has high activity and can react with the hydration product $Ca(OH)_2$ to form CSH gel (Yazıcı, 2007). Theoretically, there is a positive correlation between the degree of pozzolanic reaction

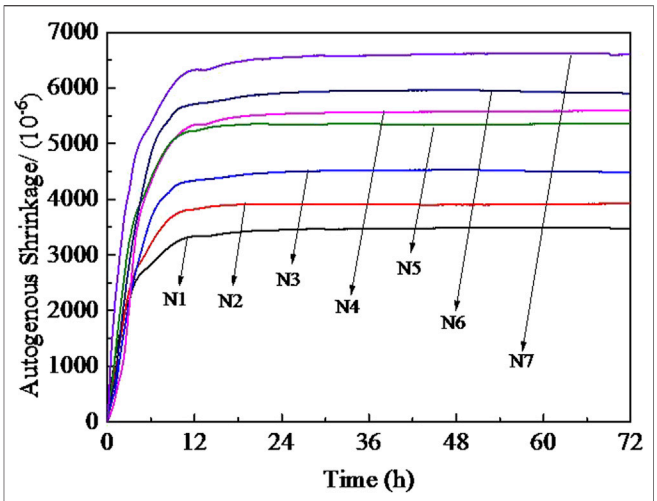

FIGURE 7 | Effect of Sika on auto-shrinkage of UHPC.

and the dose of silica fume. As a consequence, the dose of silica fume will increase the shrinkage value of UHPC (Zhang et al., 2003; Hong and Glasser, 2004).

Auto-Shrinkage

M-PCE and Sika polycarboxylates were, respectively, used to prepare UHPC. The auto-shrinkage changes of UHPC are shown in **Figures 6**, **7**.

According to **Figures 6**, **7**, under the same conditions, the influence of M-PCE on the auto-shrinkage of UHPC was similar to that of Sika. The auto-shrinkage of UHPC prepared with M-PCE or Sika is relatively smaller than that of UHPC prepared with pure Portland cement.

In addition, it was observed that the dosage of silica fume decreased the auto-shrinkage of UHPC (as shown in **Figures 6**, **7**). In **Figure 6**, the content of silica fume increases from 15 to 30% and the auto-shrinkage ranges from 3,800 to 5,400. In contrast, in **Figure 7**, this value ranges from 3,700 to 5,500, which is consistent with reference (Duan et al., 2020), mainly due to the fact that the silica fume has large fineness, exerting special filling on the pore structure of cement-based materials. With the increasing dosage of silica fume, the capillary diameter will be reduced, causing greater capillary pressure and greater auto-shrinkage of UHPC (Rong et al., 2014).

In **Figure 6**, the content of mineral powder increases from 25 to 50% and its auto-shrinkage ranges from 4,200 to 6,800. In **Figure 7**, the auto-shrinkage ranges from 4,400 to 6,600. From the point of view of mineral powder, the auto-shrinkage of UHPC is also greatly affected by single addition. The pozzolanic activity and hydration degree of mineral powder were higher than those of Portland cement, leading to accelerated speed of water consumption and faster internal drying process (He et al., 2019).

CONCLUSION

In this study, polyurethane-modified polycarboxylate was synthesized at indoor temperature and its applications in

UHPC, including water reduction rate of mortar, flowability, strength, drying shrinkage, and autogenous shrinkage, were investigated. The following conclusions were obtained based on the above experimental results and discussion:

(1) Because of the better compatibility with Portland cement of polyorganosiloxane in its molecular structure, M-PCE had better flowability and better dispersibility than the Sika superplasticizer.
(2) As far as compressive strength is concerned, UHPC prepared with M-PCE and Sika shows similar compressive strength. With the silica fume content ranging from 0 to 15%, the compressive strength of concrete rose from 92.5 to 117.4 MPa (28 days). Addition of mineral powder would reduce the compressive strength of UHPC (3 days). Especially when the content of mineral powder was more than 25%, the early compressive strength of concrete would decrease from 71.0 to 63.6 MPa, indicating that the compressive strength of UHPC was enhanced by adding silica fume but negatively affected by mineral powder.
(3) There is a negative relation between the dosage of mineral powder and silica fume and the drying shrinkage of UHPC. The larger the dosage of mineral powder is, the more obvious the decrease of drying shrinkage of UHPC is. However, the dosage of either mineral powder or silica fume may enhance its auto-shrinkage. The greater the dosage of mineral powder is, the greater the auto-shrinkage of UHPC is.

DATA AVAILABILITY STATEMENT

The original contributions presented in the study are included in the article/Supplementary Material, and further inquiries can be directed to the corresponding author.

AUTHOR CONTRIBUTIONS

SX conceptualized the study, was responsible for the methodology, investigated the data, performed data curation and formal analysis, and wrote the original draft. YG was involved in project administration, funding acquisition, and supervision. YT revised the manuscript.

ACKNOWLEDGMENTS

The authors gratefully acknowledge the financial support from National Natural Science Foundation of China and Civil Aviation Administration of China (U1833127), National Key R&D Program of China (Grant Number: 2018YFB1600100), National Natural Science Foundation of China (General Program: 51978080), Natural Science Foundation of Hunan Province(2021JJ40602) and Scientific Research Project of Hunan Provincial Department of Education(20B014).

REFERENCES

Aitcin, P. C. (2003). The Durability Characteristics of High Performance Con- crete: Review [J]. *Cem Concr Compos.* 25, 409–420. doi:10.1016/S0958-9465(02)00081-1

Andersen, P. J., Roy, D. M., Gaidis, J. M., and Grace & Co.fnm, W. R. (1987). The Effects of Adsorption of Superplasticizers on the Surface of Cement. *Cement Concrete Res.* 17 (5), 805–813. doi:10.1016/0008-8846(87)90043-3

Duan, K., Gao, Y., Yao, H., Zeng, W., Xu, Y., Zhou, W., et al. (2020). Comparison of Performances of Early Aged Pre-vibrated Cement-Stabilized Macadam Formed by Different Compactions. *Construction Building Mater.* 239, 117682. doi:10.1016/j.conbuildmat.2019.117682

Duval, R., and Kadri, E. H. (1998). Influence of Silica Fume on the Workability and the Compressive Strength of High-Performance Concretes. *Cement Concrete Res.* 28 (4), 533–547. doi:10.1016/s0008-8846(98)00010-6

Elahi, A., Basheer, P. A. M., Nanukuttan, S. V., and Khan, Q. U. Z. (2010). Mechanical and Durability Properties of High Performance Concretes Containing Supplementary Cementitious Materials. *Construction Building Mater.* 24, 292–299. doi:10.1016/j.conbuildmat.2009.08.045

Erdem, T. K., and Kırca, Ö. (2008). Use of Binary and Ternary Blends in High Strength concrete. *Construction Building Mater.* 22, 1477–1483. doi:10.1016/j.conbuildmat.2007.03.026

Ganesh, B. K., and Surya, P. P. V. (1995). Efficiency of Silica Fume in concrete. *Cement Concrete Res.* 25 (6), 1273–1283. doi:10.1016/0008-8846(95)00120-2

He, B., Gao, Y., Qu, L., Duan, K., Zhou, W., and Pei, G. (2019). Characteristics Analysis of Self-Luminescent Cement-Based Composite Materials with Self-Cleaning Effect. *J. Clean. Prod.* 225, 1169–1183. doi:10.1016/j.jclepro.2019.03.291

Hong, S.-Y., and Glasser, F. P. (2004). Phase Relations in the CaO-SiO2-H2o System to 200 °C at Saturated Steam Pressure. *Cement Concrete Res.* 34 (9), 1529–1534. doi:10.1016/j.cemconres.2003.08.009

Jones, M., Dhir, R., and Gill, J. (1995). Concrete Surface Treatment: Effect of Exposure Temperature on Chloride Diffusion Resistance. *Cement Concrete Res.* 25 (1), 197–208. doi:10.1016/0008-8846(94)00127-k

Kagi, D. A., and Ren, K. B. (1995). Reduction of Water Absorption in Silicate Treated concrete by post-treatment with Cationic Surfactants. *Building Environ.* 30 (2), 237–243. doi:10.1016/0360-1323(94)00047-v

Khatri, R. P., Sirivivatnanon, V., and Gross, W. (1995). Effect of Different Supplementary Cementitious Materials on Mechanical Properties of High Performance concrete. *Cement Concrete Res.* 25 (1), 209–220. doi:10.1016/0008-8846(94)00128-l

Khayat, K. H., and Aitcin, P. C. (1993). "Silica Fume: a Unique Supplementary Cementitious Material," in *Mineral Admixtures in Cement and concrete*. Editor S. N. Ghosh (New Delhi, India: ABI Books Private Limited), 227–265.

Levi, M., Ferro, C., Regazzoli, D., Dotelli, G., and Lo presti, A. (2002). Comparative Evaluation Method of Polymer Surface Treatments Applied on High Performance concrete. *J. Mater. Sci.* 37 (22), 4881–4888. doi:10.1023/a:1020810113110

Li, C. Z., Feng, N. Q., Li, Y. D., and Chen, R. J. (2005). Effects of Polyethlene Oxide Chains on the Performance of Polycarboxylate-type Water-Reducers. *Cement Concrete Res.* 35 (5), 867–873. doi:10.1016/j.cemconres.2004.04.031

Mazloom, M., Ramezanianpour, A. A., and Brooks, J. J. (2004). Effect of Silica Fume on Mechanical Properties of High-Strength concrete. *Cement and Concrete Composites* 26 (4), 347–357. doi:10.1016/s0958-9465(03)00017-9

Rong, Z. D., Sun, W., Xiao, H. J., and Wang, W. (2014). Effect of Silica Fume and Fly Ash on Hydration and Microstructure Evolution of Cement Based Composites at Low Water-Binder Ratios. *Construction Building Mater.* 51, 446–450. doi:10.1016/j.conbuildmat.2013.11.023

Shang, Y., Miao, C. W., Liu, J. P., and Ran, Q. P. (2009). *New Build Mater. (In Chinese)* 12 (4), 12–14.

Shi, C. J., and He, F. Q. (2010). "Properties and Microstructure of CO_2 Cured concrete Blocks," in Proceedings of the 2nd International Conference on Waste Engineering and Management, Shanghai, China, October 13-15,2010, 96–107.

Shi, C. J. (2009). "Recent Development of PC Superplasticizers [C]," in Proceedings of the 2nd International Symposium on Mix Design, Performance and Use of SCC, Beijing, June 5-7, 2009, 16–25.

Taylor, H. F. W. (1997). *Cement Chemistry*. London, England: Thomas Telford Services Ltd. doi:10.1680/cc.25929

Thompson, J. L., Silsbee, M. R., Gill, P. M., and Scheetz, B. E. (1997). Characterization of Silicate Sealers on concrete. *Cement concrete Res.* 27 (10), 1561–1567. doi:10.1016/s0008-8846(97)00167-1

Yazıcı, H. (2007). The Effect of Curing Conditions on Compressive Strength of Ultra High Performance concrete with High Volume mineral Admixtures. *Building Environ.* 42, 2083–2089. doi:10.1016/j.buildenv.2006.03.013

Zhang, M. H., Tam, C. T., and Leow, M. P. (2003). Effect of Water-To-Cementitious Materials Ratio and Silica Fume on the Autogenous Shrinkage of concrete. *Cement Concrete Res.* 33 (10), 1687–1694. doi:10.1016/s0008-8846(03)00149-2

Conflict of Interest: The authors declare that the research was conducted in the absence of any commercial or financial relationships that could be construed as a potential conflict of interest.

Publisher's Note: All claims expressed in this article are solely those of the authors and do not necessarily represent those of their affiliated organizations, or those of the publisher, the editors and the reviewers. Any product that may be evaluated in this article, or claim that may be made by its manufacturer, is not guaranteed or endorsed by the publisher.

frontiers in Materials

MINI REVIEW
published: 12 August 2021
doi: 10.3389/fmats.2021.725420

Conductive Polymer Composites Based Flexible Strain Sensors by 3D Printing: A Mini-Review

Libing Liu[1], Dong Xiang[1], Yuanpeng Wu[1], Zuoxin Zhou[2]*, Hui Li[1], Chunxia Zhao[1] and Yuntao Li[1]*

[1]School of New Energy and Materials, Southwest Petroleum University, Chengdu, China, [2]Center for Additive Manufacturing, Faculty of Engineering, University of Nottingham, Nottingham, United Kingdom

With the development of wearable electronic devices, conductive polymer composites (CPCs) based flexible strain sensors are gaining tremendous popularity. In recent years, the applications of additive manufacturing (AM) technology (also known as 3D printing) in fabricating CPCs based flexible strain sensors have attracted the attention of researchers due to their advantages of mold-free structure, low cost, short time, and high accuracy. AM technology, based on material extrusion, photocuring, and laser sintering, produces complex and high-precision CPCs based wearable sensors through layer-by-layer stacking of printing material. Some high-performance CPCs based strain sensors are developed by employing different 3D printing technologies and printing materials. In this mini-review, we summarize and discuss the performance and applications of 3D printed CPCs based strain sensors in recent years. Finally, the current challenges and prospects of 3D printed strain sensors are also discussed to provide an insight into the future of strain sensors using 3D printing technology.

Keywords: 3D printing, nanocomposites, strain sensor, nanofillers, performance

OPEN ACCESS

Edited by:
Andrea Dorigato, University of Trento, Italy

Reviewed by:
Yucai Shen, Nanjing Tech University, China
Andreas Schiffer, Khalifa University, United Arab Emirates

****Correspondence:***
Dong Xiang
dxiang01@hotmail.com
Zuoxin Zhou
alfredzhou61@hotmail.com

Specialty section:
This article was submitted to Polymeric and Composite Materials, a section of the journal Frontiers in Materials

Received: *15 June 2021*
Accepted: *03 August 2021*
Published: *12 August 2021*

Citation:
Liu L, Xiang D, Wu Y, Zhou Z, Li H, Zhao C and Li Y (2021) Conductive Polymer Composites Based Flexible Strain Sensors by 3D Printing: A Mini-Review. Front. Mater. 8:725420. doi: 10.3389/fmats.2021.725420

INTRODUCTION

In recent years, CPCs have been widely used in industrial and academic fields because of their flexibility, controllable conductive properties, easy processing, and low-cost synthesis (Wu et al., 2016; Wang T. et al., 2018; Li et al., 2018). Nanofillers are introduced to the insulating polymer matrix to improve their functional characteristics (Wang et al., 2018b). Due to the superior properties of functionalized CPCs, they are used to make strain sensors which are playing their role in medical diagnosis, soft robotics, health monitoring, human-computer interaction, and many other applications (Wang et al., 2018c; Wang et al., 2019; Zhang et al., 2019). Several methods for fabricating the strain sensors have been developed, such as hot pressing, casting, and extrusion. However, the processing technologies of these methods are complicated and not applicable to complex structures. For example, customized molds are needed to fabricate CPCs based strain sensors by hot pressing method (Huang et al., 2021). The development and production of mold limit the economic benefits during their industrial-scale production.

Since the last decade, AM technology, also known as 3D printing Zhang J. et al. (2020), is used by researchers for the fabrication of CPCs based strain sensors (Zhang et al., 2016; Gnanasekaran et al., 2017; Dawoud et al., 2018). Traditional fabrication methods used for preparing the molds of complex 3D objects are highly inefficient and time consuming. Compared with the conventional fabrication methods, 3D printing technology has the advantages of high resolution, high accuracy, low cost, fast

TABLE 1 | The principle and characteristics of 3D printing.

Process	Materials	Principle	Advantages	Disadvantages
FFF	Thermoplastics	Fusion-driven restacking	Fast printing low cost High strength	Pretreatment Weak interaction Rough surface
DIW	Thermoplastics Elastomers Hydrogels	Ink extrusion	Material diversity Low cost	Nozzle clogging Post-processing
DLP	Photosensitive resin	*In situ* photocuring	High resolution Intricate fabrication	Weak strength High cost
SLS	Thermoplastics	Laser sintering	Material diversity High efficiency High material utilization	Rough surface Powder pollution High cost

TABLE 2 | 3D-printed strain sensors.

Methods	Printed materials[a]	Printed parts	Maximum strain	Gauge factors (GF)	Ref
FFF	Modified CNT/TPU	Entire sensor	250%	117213	Xiang et al. (2019)
FFF	CNT/TPU	Entire sensor	100%	8.6–176	Christ et al. (2017)
FFF	CNT/GNP/TPU	Entire sensor	250%	136327.4	Xiang et al. (2020a)
FFF	Graphene/TPU	Entire sensor	200%	15.2–155.7	Gul et al. (2019)
FFF	Modified CNT/TPU	Entire sensor	30%	3–130.9	Xiang et al. (2020c)
FFF	AgNPs/CNT/TPU	Entire sensor	250%	43260	Xiang et al. (2020b)
DIW	PDMS	Substrate	30%	4.3	Abshirini et al. (2018)
DIW	EGO/PDMS	Entire sensor	40%	20.3	Shi et al. (2019)
DIW	Graphene/PDMS	Sensing layer	350%	18.5–88443	Ma et al. (2019)
DIW	Nanoclay/CB/TPU	Entire sensor	80%	0.39–4.7	Wei et al. (2019a)
DIW	Ag precursor	Sensing layer	50%	—	Song et al. (2017)
DIW	Ag-TPU	Entire sensor	>1600%	—	Sun et al. (2019)
DLP	CNT/EA	Entire sensor	60%	1.587–8.939	Xiao et al. (2020)
DLP	c-CNTs/ACMO	Entire sensor	100%	2	Guo et al. (2020)
DLP	ACMO/HUA	Substrate	150 kPa	0.005–0.111kPa^{-1}	Peng et al. (2020b)
SLS	Graphene/TPU	Entire sensor	15%	668.3	Mei et al. (2020)

[a]*ABS, acrylonitrile butadiene styrene; ACMO, N-acryloyl morpholine; Ag, silver; AgNPs, silver nanoparticles; CB, carbon black; CNT, carbon nanotube; CNTs, carboxyl carbon nanotubes; c-HUA, hydrolyzable crosslinking agent; EA, elastomer; EGO, electrochemically derived graphene oxide; GNP, graphene nanoplatelet; PDMS, poly (dimethylsiloxane); TPU, thermoplastic polyurethane.*

fabrication, and customized for mass production without the need for mold (Abshirini et al., 2019; Dul et al., 2020; Song et al., 2020). Furthermore, due to the micro-orientation in Fused Filament Fabrication (FFF) and Direct Ink Writing (DIW) 3D Printing, the nanofillers are uniformly dispersed in the polymer matrix, leading to the enhanced performance of obtained strain sensor (Guo et al., 2021). Therefore, 3D printing through layer-by-layer manufacturing has shown promising potential to produce flexible strain sensors with complex structures. Their application areas include wearable electronic devices, medical diagnostics, soft robots, and strain direction recognition (Wang et al., 2020; Dan et al., 2021; Gao et al., 2021). Although 3D printing has been widely used in the development of complex structures, it is still a novel method to fabricate strain sensors with complex structures and multiple functions.

At present, there are some reports on the fabrication of CPCs based strain sensors with high performance by 3D printing. Considering the wide application potential of 3D printing in CPCs based strain sensors, it is necessary to review this topic. In this mini-review, 3D printing technologies based on material extrusion, photocuring, and laser sintering, involving Fused Filament Fabrication (FFF), Direct Ink Writing (DIW), Digital Light Processing (DLP), and Selective Laser Sintering (SLS) are discussed. Moreover, high-performance CPCs based strain sensors fabricated by these 3D printing technologies are reviewed. Further, the printing principle, material selection, research progress, recent applications, and prospects of CPCs based 3D printed strain sensors are also discussed.

FABRICATION OF CPCS BASED FLEXIBLE STRAIN SENSORS BY 3D PRINTING

3D printed CPCs based flexible strain sensors involve four different fabrication approaches including FFF, DIW, DLP, and SLS. The summary of materials, printing principles,

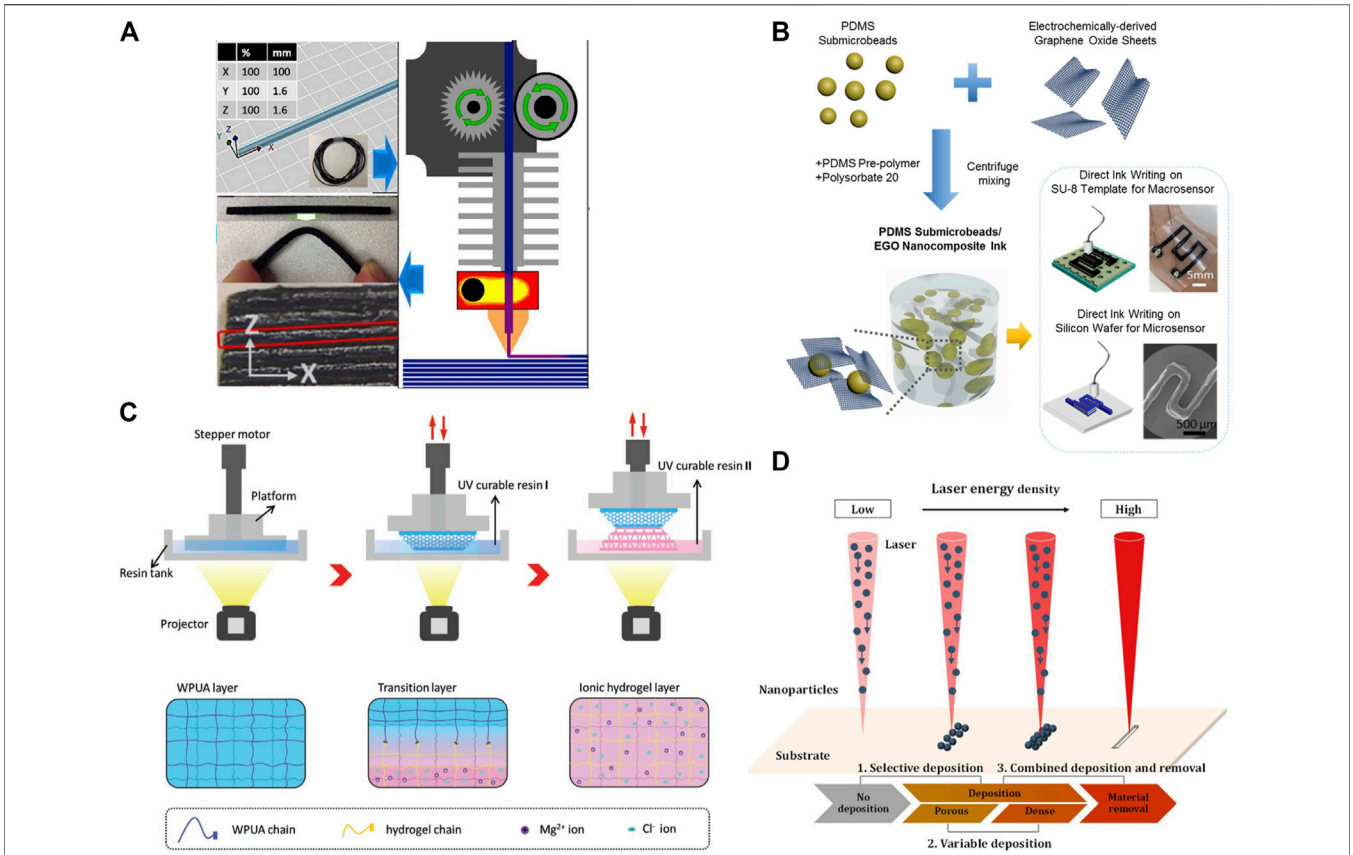

FIGURE 1 | The process for preparing strain sensor using **(A)** FFF (Christ et al., 2017), **(B)** DIW (Shi et al., 2019), **(C)** DLP (Yin et al., 2019), and **(D)** SLS (Song et al., 2020).

advantages, and disadvantages of these technologies is enlisted in **Table 1**; **Table 2** summarizes the representative researches of strain sensors fabricated by 3D printing in recent years.

Electrical properties of elastic polymer material improve with the introduction of conductive nanofillers. Furthermore, due to the increase of the interface density of nanofillers Arif et al. (2020) and the interaction between nanofillers and polymer matrix (Xiang et al., 2019), the interface between them is well combined, which facilitates a effective stress transfer under strain. Therefore, the mechanical properties of the composites, including strength, Young's modulus and toughness, are enhanced. (Pan et al., 2020). In addition, the sensing properties such as strain detection range, sensitivity, linearity, response time, resistance responsiveness, stability, and durability under different conditions are equally significant for CPCs based strain sensors. Material type, agglomeration and dispersion of nanofillers, macroscopic and microscopic structure of strain sensors, and different 3D printing parameters (Davoodi et al., 2020; Xu et al., 2020) determine the percolated network structure of the strain sensor, affecting the sensing properties of strain sensor. For example, when the percolation networks are in high density, numerous nanofillers contact with each other. The contact resistance is dominant and a robust percolation network is built. With the decrease of percolation networks density, more nanofillers are separated from each other, and contact resistance is gradually transformed into tunneling resistance. It makes the contact nodes between nanofillers easier to be disconnected, resulting in a higher sensitivity of composite. When the percolation networks are at low density, most of nanofillers could be in the state of tunneling effect. Here the tunneling resistance is dominant, leading to a fragile percolation network, which makes the sensitivity of composite increase sharply (Hu et al., 2012).

Flexible Strain Sensors Fabricated by FFF

Figure 1A illustrates the process for preparing strain sensor using FFF (Christ et al., 2017). The matrix material usually determines the stretchability of the fabricated strain sensor (Waheed et al., 2019; Alam et al., 2020; Arif et al., 2020), and TPU is undoubtedly a promising candidate for fabricating FFF based strain sensors because of its high strength, good elasticity and environmental resistance (Georgopoulou et al., 2020a). However, the lower dispersion of conductive nanofillers in these strain sensors leads to poor sensing performance.

The performance of 3D printed strain sensors could be enhanced through a synergistic effect between the nanofillers and increasing interaction between nanofillers and matrix to improve the dispersion of nanofiller in matrix (Georgopoulou

and Clemens, 2020b). Xiang et al. (2020b) used FFF to prepare AGNP/CNT/TPU strain sensors with a synergistic effect, where AGNPs interact with CNTs. Micro-orientation (Guo et al., 2021) due to CNTs rearrangement during printing and synergistic effect between AGNPs and CNTs results in a wide strain detection range (0–250%), high sensitivity (GF = 43,260 at 250% strain), linearity (R^2 = 0.97 within 50% strain) and fast response (~57 ms). Synergies between other nanofillers, such as CNTs and GNPs have also been reported to achieve high performance (Xiang et al., 2020a). 1-pyrene carboxylic acid (PCA) was used to modify the TPU/CNT composite, and the dispersion of CNTs in composites was improved by applying the non-covalent interactions between PCA, TPU, and CNTs (Xiang et al., 2019). A 3D-printed piezoresistive strain sensor with a complex structure was also fabricated by non-covalent modification (Xiang et al., 2020c).

Compared with the conventional methods, FFF has the advantages of rapid synthesis (Christ et al., 2017), improved material utilization (Gnanasekaran et al., 2017), simple post-processing, no harmful by-products to the environment (Xiang et al., 2020b), and custom-made mass production without the need of molds (Dul et al., 2020). However, FFF also has some disadvantages: before printing, the prepared composite needs to undergo preprocessing, including granulation of composite and filament extrusion (Xiang et al., 2019). In addition, the printed components have a rough surface and limited physical interaction between adjacent filaments that reduce the structural strength along the deposition direction (Waheed et al., 2019).

Flexible Strain Sensors Fabricated by DIW

Ink extrusion is an effective method to print high-performance strain sensors. Inks have unique rheological properties, including viscoelasticity, shear-thinning, and yield stress, which contribute to the implementation of the DIW process. Usually, DIW is used to print the core components of the sensor or the template to prepare the sensor Wang Z. et al. (2018) and to meet the versatility of test environments. The stretchability of CPCs based strain sensors varies dramatically with the types of polymer materials (Sun et al., 2019; Wei P. et al., 2019). Particularly, PDMS elastomers are widely used in DIW printed flexible strain sensors because of their high stretchability, physiological inertia, controllable viscosity, and room temperature curing ability (Abshirini et al., 2019). **Figure 1B** illustrates the process of preparing the EGO/PDMS strain sensor by DIW (Shi et al., 2019). However, strain sensors fabricated by DIW using PDMS elastomers have lower sensitivity.

The sensitivity of the strain sensors is improved in two ways. The first is to optimize different printing parameters such as printing times (Song et al., 2017), which affects the degree of conductive network constructed in strain sensors, thus affecting the sensitivity. The other is the construction of a different microstructure. The conductive network of strain sensors, with different microstructures, changes under strain and controls the sensitivity of sensors. For example, a self-compensating two-order strain sensor was fabricated by Ma et al. (2019) through DIW and coating that revealed high GF (from 18.5 to 88 443) in a strain range of 0–350%. These results demonstrated that graphene coated on the surface of the sensor provides an additional conductive path, which self-compensates the loss of conductivity under high strain. Moreover, due to the slip-off and disconnection (Zhang X. et al., 2020) of internal graphene sheets, reduced graphene layers improve the sensitivity under small strain.

In addition, the performance of the flexible strain sensor improves by introducing non-conductive fillers to the CPCs. The immiscible second phase fluid was introduced to Ag/PDMS and Ag/TPU inks to fabricate the strain sensor by DIW (Sun et al., 2019). Due to the capillary action and the connection between the Ag sheets and the immiscible second phase fluid, the strain sensor achieves ultra-stretchability (>1,600%). Moreover, the shear flow generated in DIW rearranges and redistributes the conductive nanofillers (Huang et al., 2018), which results in the better orientation and uniform dispersion of the conductive nanofillers in strain sensors.

Unlike FFF technology, which applies only to thermoplastics, DIW is not limited to specific materials and is suitable for a variety of materials such as metal-based materials (Kim et al., 2019), carbon-based materials (Abshirini et al., 2018), and conductive polymer composites (Shi et al., 2019). However, DIW printing technology also has certain limitations; for different inks with different components, the print pattern requires post-processing such as soaking, sintering, heating, and curing (Khosravani and Reinicke, 2020). In addition, the processing resolution of the DIW printed strain sensors is less than that of FFF.

Flexible Strain Sensors Fabricated by DLP

Photocurable 3D printing is an emerging 3D printing method for wearable electronic devices. In this technique, ultraviolet light illuminates the mixture of photoinitiators, monomers, and prepolymers, initiating layer-by-layer curing according to the software-designed structure.

Photosensitive resins typically include acrylics, polyesters, and polyurethane acrylate containing composite precursors. Amon these, acrylic-based composites demonstrate fragile mechanical strength (Liu et al., 2021). To solve this problem, researchers used reactive diluents of acrylic-based composites to improve the mechanical strength as well as the transparency of composites (Peng et al., 2020a). Some studies report significant improvement in the mechanical stability of DLP-based strain sensors through the interlayer chemical bond formation between two materials, and the preparation process is shown in **Figure 1C** (Yin et al., 2019). The sensor exhibits excellent structural stability and sensing performance (10,000 loading/unloading cycles) due to the chemical bonds between hydrogel and WPUA. On one hand, the mechanical properties of photosensitive resins could improve by adding nanofillers (Mu et al., 2017; Cortes et al., 2020). On the other hand, the addition of nanofillers may absorb ultraviolet light, leading to the decline of the mechanical properties of the photosensitive resin.

In many studies, the strain detection range of DLP-based strain sensors is low (less than 30%) Cortes et al. (2020) and difficult to meet the practical application requirements. To solve this problem, Xiao et al. (2020) fabricated a flexible strain sensor

based on CNTs/epoxy aliphatic acrylate (EAA)/aliphatic urethane diacrylate (AUD) composites and achieved a maximum strain detection range of 60%. Guo et al. (2020) introduced carboxyl CNTs to ACMO resin, which fully mitigated the over-curing of ACMO resin, thus, achieved a 100% strain detection range. Peng et al. (2020b) prepared a strain sensor with high stretchability (~510%) by DLP printing sacrificial mold method.

These strain sensors have low sensitivity that does not respond to subtle strains. Peng et al. (2018) used DLP to customize the microstructure (pyramid, semisphere, and semicylinder) template and to prepare the strain sensor with high sensitivity (maximum GF of $-3.6\ kPa^{-1}$). At present, the research on strain sensors with a high strain detection range and high sensitivity is still scarce, and most of the designed sensors only achieve sensitivity or detection range. For DLP-based strain sensors, more research needs be done in the future to achieve high performance.

Compared with FFF and DIW based 3D printing, DLP overcomes the pre-processing and post-printing processing and has higher efficiency. Besides, the sample printed by DLP has a high resolution, indicating its higher precision (Liu et al., 2021). However, DLP is limited to the printed materials, only applicable to photosensitive resins, and has a high printing cost, thus limiting the development of DLP technology. In addition, to decrease the resin viscosity and the ultraviolet absorption of nanofillers is challenging for the fabrication of photosensitive composite resins.

Flexible Strain Sensors Fabricated by SLS

Many flexible SLS-based strain sensors have been studied in recent years (Maier et al., 2013). The performance of the strain sensor can be improved by optimizing the printing parameters of SLS and constructing a special conductive network structure. The printing parameters are adjusted to make the conductive network structure in strain sensor more completed, as shown as **Figure 1D**; (Song et al., 2020). Zhuang et al. (2020) prepared CNT/TPU sensors with a wide range (17–240 kPa) and high sensitivity (0.12–0.549 $kPa^{-}1$) through SLS and improved the pressure detection range (3–240 kPa) and sensitivity ($1.357\ kPa^{-1}$ for 3–70 kPa, $0.0328\ kPa^{-1}$ for 70–240 kPa) by adjusting the SLS laser power, layer thickness, and scan spacing. (Zhuang et al., 2021). A segregated structure was constructed by SLS to make the nanofillers selectively distributed on the matrix surface. (Wei S. et al., 2019; Ronca et al., 2019). The segregated structure enables the sensor to achieve a low percolation threshold (0.05 wt%) (Gan et al., 2019). In addition, the synergistic effect improves the sensing performance of SLS-based strain sensors (Rollo et al., 2020).

Comparing the 3D printing methods discussed above, SLS has the highest production efficiency, and the material utilization rate is about 100%. However, powder pollution in the printing process, high operating costs, high equipment cost, and rough product surface are few problems associated with SLS. In addition, the printed product is deformed due to the long storage time and internal stress.

APPLICATION

3D printed high-performance strain sensors are applied in many fields such as medical diagnosis and health monitoring (Khosravani and Reinicke, 2020; Liu et al., 2021). For monitoring human movements, 3D printed strain sensors have a wide range of applications (Le et al., 2017), such as finger bending, wrist bending, elbow bending, walking, and running (Christ et al., 2018). In health care systems, 3D printed strain sensors monitor patients' respiratory and pulse rates, speech recognition, gestures, and blinking (Kim et al., 2017). Another potential application of 3D printed sensors is load recognition, including load distribution of heavy objects and light objects (Zhang et al., 2019). Besides, the high sensitivity strain sensors are also used to detect subtle acoustic vibration signals (Song et al., 2017). When the sensors are stimulated by external forces or sound waves, vibrations increase the sensing resistance patterns, and convert mechanical energy into electrical signals. In addition, DLP-based 3D printing combined with the self-pinning carbon nanotubes and assisted by out-of-plane capillary forces, the prepared strain sensor detects out-of-plane forces (Liu et al., 2018). In general, the 3D printed strain sensors have a wide range of applications in production, life, and scientific research (Bekas et al., 2019).

DISCUSSION

Among different methods for preparing the CPCs based strain sensors, extrusion, photocurable, and laser sintering 3D printing are rapid, precise, customized, and economical, compared to traditional methods. But these methods have certain drawbacks. FFF printing requires pretreatment of the composite material and filament manufacturing. During the FFF printing nozzle blockage and roughness of the surfaces of the finished product are other challenges. Due to the different compositions of the printing ink in the DIW process, the nozzle gets blocked. Moreover, the resolution of DIW is relatively low. DLP has a high manufacturing cost and is limited to photosensitive resins only. In addition, powder pollution in the printing process, high operating costs, high equipment cost, and rough product surface are few problems associated with SLS. Given the above shortcomings, combined with the challenges associated with industrial production, it is necessary to explore new 3D printing methods with high precision, high efficiency, and high applicability.

The development of wearable electronics is rapid, resulting in more electronic product waste and non-decomposable materials, which increase the pressure on the environment. Therefore, the development of recyclable, biodegradable, and biocompatible materials as 3D printing materials is the trend of 3D printed CPCs based strain sensors.

At present, most of the 3D printed CPCs based strain sensors have a single function. With the increasing demand for flexible strain sensors and their wide applicability, the realization of their multi-functional use is also a trend for the future development of 3D printed CPCs based strain sensors.

CONCLUSION

As a preparation method for flexible strain sensors, 3D printing technology is economical, rapid, highly precise, and has been widely used in industrial and academic fields. In this mini-review, we summarize the printing principle, material selection, advantages and challenges of 3D printing. Based on the research progress, the methods, involving synergistic effect, non-covalent modification, printing parameters, the construction of microstructure, are summarized to improve the strain detection range and sensitivity of 3D-printed strain sensors. Furthermore, 3D-printed strain sensors are used in human motion detection, health care systems, direction recognition and other fields. The challenges and future prospects are put forward. There are still some challenges to be solved to achieve commercialization, the development of 3D printing technology will continue to support the preparation of flexible strain sensors, which will make 3D printing an indispensable technology in the field of wearable electronic devices.

AUTHOR CONTRIBUTION

LL contributed to the compilation of data and the writing of the Manuscript. DX and ZZ contributed to the review, revision and editing of the Manuscript. YW, YL, HL, and CZ contributed to the review, revision of the Manuscript. All authors read and agree to the final text.

ACKNOWLEDGMENTS

The authors thank University of Nottingham for the support of this work. This work was also supported within the framework of the National Key Research and Development Program (2019YFE0120300), the Sichuan Science and Technology Program (2021YFH0031), the International Cooperation Project of Chengdu (2019-GH02-00054-HZ) and the Scientific Research Starting Project of SWPU (2019QHZ011).

REFERENCES

Abshirini, M., Charara, M., Liu, Y., Saha, M., and Altan, M. C. (2018). 3d printing of highly stretchable strain sensors based on carbon nanotube nanocomposites. *Adv. Eng. Mater.* 20, 1800425. doi:10.1002/adem.201800425

Abshirini, M., Charara, M., Marashizadeh, P., Saha, M. C., Altan, M. C., and Liu, Y. (2019). Functional nanocomposites for 3d printing of stretchable and wearable sensors. *Appl. Nanosci.* 9, 2071–2083. doi:10.1007/s13204-019-01032-2

Alam, F., Varadarajan, K. M., and Kumar, S. (2020). 3d printed polylactic acid nanocomposite scaffolds for tissue engineering applications. *Polym. Test.* 81, 106203. doi:10.1016/j.polymertesting.2019.106203

Arif, M. F., Alhashmi, H., Varadarajan, K. M., Koo, J. H., Hart, A. J., and Kumar, S. (2020). Multifunctional performance of carbon nanotubes and graphene nanoplatelets reinforced peek composites enabled via fff additive manufacturing. *Composites B: Eng.* 184, 107625. doi:10.1016/j.compositesb.2019.107625

Bekas, D. G., Hou, Y., Liu, Y., and Panesar, A. (2019). 3d printing to enable multifunctionality in polymer-based composites: A review. *Composites Part B: Eng.* 179, 107540. doi:10.1016/j.compositesb.2019.107540

Christ, J., Aliheidari, N., Pötschke, P., and Ameli, A. (2018). Bidirectional and stretchable piezoresistive sensors enabled by multimaterial 3d printing of carbon nanotube/thermoplastic polyurethane nanocomposites. *Polymers* 11, 11. doi:10.3390/polym11010011

Christ, J. F., Aliheidari, N., Ameli, A., and Pötschke, P. (2017). 3d printed highly elastic strain sensors of multiwalled carbon nanotube/thermoplastic polyurethane nanocomposites. *Mater. Des.* 131, 394–401. doi:10.1016/j.matdes.2017.06.011

Cortés, A., Sánchez-Romate, X. F., Jiménez-Suárez, A., Campo, M., Ureña, A., and Prolongo, S. G. (2020). Mechanical and strain-sensing capabilities of carbon nanotube reinforced composites by digital light processing 3d printing technology. *Polymers* 12, 975. doi:10.3390/polym12040975

Dan, L., Cheng, Q., Narain, R., Krause, B., Pötschke, P., and Elias, A. (2021). Three-dimensional printed and biocompatible conductive composites comprised of polyhydroxybutyrate and multiwalled carbon nanotubes. *Ind. Eng. Chem. Res.* 60, 885–897. doi:10.1021/acs.iecr.0c04753

Davoodi, E., Montazerian, H., Haghniaz, R., Rashidi, A., Ahadian, S., Sheikhi, A., et al. (2020). 3d-printed ultra-robust surface-doped porous silicone sensors for wearable biomonitoring. *ACS Nano* 14, 1520–1532. doi:10.1021/acsnano.9b06283

Dawoud, M., Taha, I., and Ebeid, S. J. (2018). Strain sensing behaviour of 3d printed carbon black filled abs. *J. Manufacturing Process.* 35, 337–342. doi:10.1016/j.jmapro.2018.08.012

Dul, S., Pegoretti, A., and Fambri, L. (2020). Fused filament fabrication of piezoresistive carbon nanotubes nanocomposites for strain monitoring. *Front. Mater.* 7. doi:10.3389/fmats.2020.00012

Gan, X., Wang, J., Wang, Z., Zheng, Z., Lavorgna, M., Ronca, A., et al. (2019). Simultaneous realization of conductive segregation network microstructure and minimal surface porous macrostructure by sls 3d printing. *Mater. Des.* 178, 107874. doi:10.1016/j.matdes.2019.107874

Gao, X., Qi, S., Kuang, X., Su, Y., Li, J., and Wang, D. (2021). Fused filament fabrication of polymer materials: A review of interlayer bond. *Additive Manufacturing* 37, 101658. doi:10.1016/j.addma.2020.101658

Georgopoulou, A., and Clemens, F. (2020b). Piezoresistive elastomer-based composite strain sensors and their applications. *ACS Appl. Electron. Mater.* 2, 1826–1842. doi:10.1021/acsaelm.0c00278

Georgopoulou, A., Sebastian, T., and Clemens, F. (2020a). Thermoplastic elastomer composite filaments for strain sensing applications extruded with a fused deposition modelling 3d printer. *Flex. Print. Electron.* 5, 035002. doi:10.1088/2058-8585/ab9a22

Gnanasekaran, K., Heijmans, T., van Bennekom, S., Woldhuis, H., Wijnia, S., de With, G., et al. (2017). 3d printing of cnt- and graphene-based conductive polymer nanocomposites by fused deposition modeling. *Appl. Mater. Today* 9, 21–28. doi:10.1016/j.apmt.2017.04.003

Gul, J. Z., Sajid, M., and Choi, K. H. (2019). Retracted Article: 3D printed highly flexible strain sensor based on TPU-graphene composite for feedback from high speed robotic applications. *J. Mater. Chem. C* 7, 4692–4701. doi:10.1039/c8tc03423k

Guo, B., Ji, X., Chen, X., Li, G., Lu, Y., and Bai, J. (2020). A highly stretchable and intrinsically self-healing strain sensor produced by 3d printing. *Virtual Phys. Prototyping* 15, 520–531. doi:10.1080/17452759.2020.1823570

Guo, H., Zhao, H., Niu, H., Ren, Y., Fang, H., Fang, X., et al. (2021). Highly thermally conductive 3d printed graphene filled polymer composites for scalable thermal management applications. *ACS Nano* 15, 6917–6928. doi:10.1021/acsnano.0c10768

Hu, B., Hu, N., Li, Y., Akagi, K., Yuan, W., Watanabe, T., et al. (2012). Multi-scale numerical simulations on piezoresistivity of CNT/polymer nanocomposites. *Nanoscale Res. Lett.* 7, 402. doi:10.1186/1556-276X-7-402

Huang, P., Xia, Z., and Cui, S. (2018). 3d printing of carbon fiber-filled conductive silicon rubber. *Mater. Des.* 142, 11–21. doi:10.1016/j.matdes.2017.12.051

Huang, Q., Tang, Z., Wang, D., Wu, S., and Guo, B. (2021). Engineering segregated structures in a cross-linked elastomeric network enabled by dynamic cross-link reshuffling. *ACS Macro Lett.* 10, 231–236. doi:10.1021/acsmacrolett.0c00852

Khosravani, M. R., and Reinicke, T. (2020). 3d-printed sensors: Current progress and future challenges. *Sensors Actuators A: Phys.* 305, 111916. doi:10.1016/j.sna.2020.111916

Kim, J. Y., Ji, S., Jung, S., Ryu, B.-H., Kim, H.-S., Lee, S. S., et al. (2017). 3d printable composite dough for stretchable, ultrasensitive and body-patchable strain sensors. *Nanoscale* 9, 11035–11046. doi:10.1039/c7nr01865g

Kim, S., Oh, J., Jeong, D., and Bae, J. (2019). Direct wiring of eutectic gallium-indium to a metal electrode for soft sensor systems. *ACS Appl. Mater. Inter.* 11, 20557–20565. doi:10.1021/acsami.9b05363

Le, M. Q., Ganet, F., Audigier, D., Capsal, J.-F., and Cottinet, P.-J. (2017). Printing of microstructure strain sensor for structural health monitoring. *Appl. Phys. A.* 123. doi:10.1007/s00339-017-0970-x

Li, Y., Zhou, B., Zheng, G., Liu, X., Li, T., Yan, C., et al. (2018). Continuously prepared highly conductive and stretchable swnt/mwnt synergistically composited electrospun thermoplastic polyurethane yarns for wearable sensing. *J. Mater. Chem. C* 6, 2258–2269. doi:10.1039/c7tc04959e

Liu, H., Zhang, H., Han, W., Lin, H., Li, R., Zhu, J., et al. (2021). 3d printed flexible strain sensors: From printing to devices and signals. *Adv. Mater.* 33, 2004782. doi:10.1002/adma.202004782

Liu, Z., Qi, D., Leow, W. R., Yu, J., Xiloyannnis, M., Cappello, L., et al. (2018). 3d-structured stretchable strain sensors for out-of-plane force detection. *Adv. Mater.* 30, 1707285. doi:10.1002/adma.201707285

Ma, J., Wang, P., Chen, H., Bao, S., Chen, W., and Lu, H. (2019). Highly sensitive and large-range strain sensor with a self-compensated two-order structure for human motion detection. *ACS Appl. Mater. Inter.* 11, 8527–8536. doi:10.1021/acsami.8b20902

Maier, R. R. J., MacPherson, W. N., Barton, J. S., Carne, M., Swan, M., Sharma, J. N., et al. (2013). Embedded fiber optic sensors within additive layer manufactured components. *IEEE Sensors J.* 13, 969–979. doi:10.1109/jsen.2012.2226574

Mei, S., Zhang, X., Ding, B., Wang, J., Yang, P., She, H., et al. (2020). 3D-Printed thermoplastic polyurethane/graphene composite with porous segregated structure: Toward ultralow percolation threshold and great strain sensitivity. *J. Appl. Polym. Sci.* 138, 50168. doi:10.1002/app.50168

Mu, Q., Wang, L., Dunn, C. K., Kuang, X., Duan, F., Zhang, Z., et al. (2017). Digital light processing 3d printing of conductive complex structures. *Additive Manufacturing* 18, 74–83. doi:10.1016/j.addma.2017.08.011

Pan, L., Wang, F., Cheng, Y., Leow, W. R., Zhang, Y.-W., Wang, M., et al. (2020). A supertough electro-tendon based on spider silk composites. *Nat. Commun.* 11, 1332. doi:10.1038/s41467-020-14988-5

Peng, S., Blanloeuil, P., Wu, S., and Wang, C. H. (2018). Rational design of ultrasensitive pressure sensors by tailoring microscopic features. *Adv. Mater. Inter.* 5, 1800403. doi:10.1002/admi.201800403

Peng, S., Li, Y., Wu, L., Zhong, J., Weng, Z., Zheng, L., et al. (2020a). 3d printing mechanically robust and transparent polyurethane elastomers for stretchable electronic sensors. *ACS Appl. Mater. Inter.* 12, 6479–6488. doi:10.1021/acsami.9b20631

Peng, S., Wang, Z., Lin, J., Miao, J. T., Zheng, L., Yang, Z., et al. (2020b). Tailored and Highly Stretchable Sensor Prepared by Crosslinking an Enhanced 3D Printed UV-Curable Sacrificial Mold. *Adv. Funct. Mater.* 31, 2008729. doi:10.1002/adfm.202008729

Rollo, G., Ronca, A., Cerruti, P., Gan, X. P., Fei, G., Xia, H., et al. (2020). On the synergistic effect of multi-walled carbon nanotubes and graphene nanoplatelets to enhance the functional properties of sls 3d-printed elastomeric structures. *Polymers* 12, 1841. doi:10.3390/polym12081841

Ronca, A., Rollo, G., Cerruti, P., Fei, G., Gan, X., Buonocore, G., et al. (2019). Selective laser sintering fabricated thermoplastic polyurethane/graphene cellular structures with tailorable properties and high strain sensitivity. *Appl. Sci.* 9, 864. doi:10.3390/app9050864

Shi, G., Lowe, S. E., Teo, A. J. T., Dinh, T. K., Tan, S. H., Qin, J., et al. (2019). A versatile pdms submicrobead/graphene oxide nanocomposite ink for the direct ink writing of wearable micron-scale tactile sensors. *Appl. Mater. Today* 16, 482–492. doi:10.1016/j.apmt.2019.06.016

Song, J.-H., Kim, H.-J., Kim, M.-S., Min, S.-H., Wang, Y., and Ahn, S.-H. (2020). Direct printing of performance tunable strain sensor via nanoparticle laser patterning process. *Virtual Phys. Prototyping* 15, 265–277. doi:10.1080/17452759.2020.1733431

Song, J. H., Kim, Y.-T., Cho, S., Song, W.-J., Moon, S., Park, C.-G., et al. (2017). Surface-embedded stretchable electrodes by direct printing and their uses to fabricate ultrathin vibration sensors and circuits for 3d structures. *Adv. Mater.* 29, 1702625. doi:10.1002/adma.201702625

Sun, H., Han, Z., and Willenbacher, N. (2019). Ultrastretchable conductive elastomers with a low percolation threshold for printed soft electronics. *ACS Appl. Mater. Inter.* 11, 38092–38102. doi:10.1021/acsami.9b11071

Waheed, S., Cabot, J. M., Smejkal, P., Farajikhah, S., Sayyar, S., Innis, P. C., et al. (2019). Three-dimensional printing of abrasive, hard, and thermally conductive synthetic microdiamond-polymer composite using low-cost fused deposition modeling printer. *ACS Appl. Mater. Inter.* 11, 4353–4363. doi:10.1021/acsami.8b18232

Wang, L., Chen, Y., Lin, L., Wang, H., Huang, X., Xue, H., et al. (2019). Highly stretchable, anti-corrosive and wearable strain sensors based on the pdms/cnts decorated elastomer nanofiber composite. *Chem. Eng. J.* 362, 89–98. doi:10.1016/j.cej.2019.01.014

Wang, T., Zhang, Y., Liu, Q., Cheng, W., Wang, X., Pan, L., et al. (2018a). A self-healable, highly stretchable, and solution processable conductive polymer composite for ultrasensitive strain and pressure sensing. *Adv. Funct. Mater.* 28, 1705551. doi:10.1002/adfm.201705551

Wang, Y., Hao, J., Huang, Z., Zheng, G., Dai, K., Liu, C., et al. (2018b). Flexible electrically resistive-type strain sensors based on reduced graphene oxide-decorated electrospun polymer fibrous mats for human motion monitoring. *Carbon* 126, 360–371. doi:10.1016/j.carbon.2017.10.034

Wang, Y., Jia, Y., Zhou, Y., Wang, Y., Zheng, G., Dai, K., et al. (2018c). Ultra-stretchable, sensitive and durable strain sensors based on polydopamine encapsulated carbon nanotubes/elastic bands. *J. Mater. Chem. C* 6, 8160–8170. doi:10.1039/c8tc02702a

Wang, Z., Liu, X., Shen, X., Han, N. M., Wu, Y., Zheng, Q., et al. (2018d). An Ultralight Graphene Honeycomb Sandwich for Stretchable Light-Emitting Displays. *Adv. Funct. Mater.* 28, 1707043. doi:10.1002/adfm.201707043

Wang, Z., Ren, J., Liu, R., Sun, X., Huang, D., Xu, W., et al. (2020). Three dimensional core-shell structured liquid metal/elastomer composite via coaxial direct ink writing for electromagnetic interference shielding. *Composites A: Appl. Sci. Manufacturing* 136, 105957. doi:10.1016/j.compositesa.2020.105957

Wei, P., Leng, H., Chen, Q., Advincula, R. C., and Pentzer, E. B. (2019a). Reprocessable 3d-printed conductive elastomeric composite foams for strain and gas sensing. *ACS Appl. Polym. Mater.* 1, 885–892. doi:10.1021/acsapm.9b00118

Wei, S., Zhang, L., Li, C., Tao, S., Ding, B., Zhu, H., et al. (2019b). Preparation of soft somatosensory-detecting materials via selective laser sintering. *J. Mater. Chem. C* 7, 6786–6794. doi:10.1039/c9tc01331h

Wu, X., Han, Y., Zhang, X., Zhou, Z., and Lu, C. (2016). Large-area compliant, low-cost, and versatile pressure-sensing platform based on microcrack-designed carbon black@polyurethane sponge for human-machine interfacing. *Adv. Funct. Mater.* 26, 6246–6256. doi:10.1002/adfm.201601995

Xiang, D., Zhang, X., Han, Z., Zhang, Z., Zhou, Z., Harkin-Jones, E., et al. (2020a). 3d printed high-performance flexible strain sensors based on carbon nanotube and graphene nanoplatelet filled polymer composites. *J. Mater. Sci.* 55, 15769–15786. doi:10.1007/s10853-020-05137-w

Xiang, D., Zhang, X., Harkin-Jones, E., Zhu, W., Zhou, Z., Shen, Y., et al. (2020b). Synergistic effects of hybrid conductive nanofillers on the performance of 3d printed highly elastic strain sensors. *Composites Part A: Appl. Sci. Manufacturing* 129, 105730. doi:10.1016/j.compositesa.2019.105730

Xiang, D., Zhang, X., Li, Y., Harkin-Jones, E., Zheng, Y., Wang, L., et al. (2019). Enhanced performance of 3d printed highly elastic strain sensors of carbon nanotube/thermoplastic polyurethane nanocomposites via non-covalent interactions. *Composites Part B: Eng.* 176, 107250. doi:10.1016/j.compositesb.2019.107250

Xiang, D., Zhang, Z., Han, Z., Zhang, X., Zhou, Z., Zhang, J., et al. (2020c). Effects of non-covalent interactions on the properties of 3d printed flexible piezoresistive strain sensors of conductive polymer composites. *Compos. Inter.* 28, 577–591. doi:10.1080/09276440.2020.1794479

Xiao, T., Qian, C., Yin, R., Wang, K., Gao, Y., and Xuan, F. (2020). 3D Printing of Flexible Strain Sensor Array Based on UV-Curable Multiwalled Carbon Nanotube/Elastomer Composite. *Adv. Mater. Technol.* 6, 2000745. doi:10.1002/admt.202000745

Xu, Y.-T., Wang, Y., Zhou, C.-G., Sun, W.-J., Dai, K., Tang, J.-H., et al. (2020). An electrically conductive polymer composite with a co-continuous segregated structure for enhanced mechanical performance. *J. Mater. Chem. C* 8, 11546–11554. doi:10.1039/d0tc02265a

Yin, X. Y., Zhang, Y., Xiao, J., Moorlag, C., and Yang, J. (2019). Monolithic Dual-Material 3D Printing of Ionic Skins with Long-Term Performance Stability. *Adv. Funct. Mater.* 29, 1904716. doi:10.1002/adfm.201904716

Zhang, D., Chi, B., Li, B., Gao, Z., Du, Y., Guo, J., et al. (2016). Fabrication of highly conductive graphene flexible circuits by 3d printing. *Synth. Met.* 217, 79–86. doi:10.1016/j.synthmet.2016.03.014

Zhang, J., Ye, S., Liu, H., Chen, X., Chen, X., Li, B., et al. (2020a). 3d printed piezoelectric bnnts nanocomposites with tunable interface and microarchitectures for self-powered conformal sensors. *Nano Energy* 77, 105300. doi:10.1016/j.nanoen.2020.105300

Zhang, S., Liu, H., Yang, S., Shi, X., Zhang, D., Shan, C., et al. (2019). Ultrasensitive and highly compressible piezoresistive sensor based on polyurethane sponge coated with a cracked cellulose nanofibril/silver nanowire layer. *ACS Appl. Mater. Inter.* 11, 10922–10932. doi:10.1021/acsami.9b00900

Zhang, X., Xiang, D., Zhu, W., Zheng, Y., Harkin-Jones, E., Wang, P., et al. (2020b). Flexible and high-performance piezoresistive strain sensors based on carbon nanoparticles@polyurethane sponges. *Composites Sci. Tech.* 200, 108437. doi:10.1016/j.compscitech.2020.108437

Zhuang, Y., Guo, Y., Li, J., Jiang, K., Yu, Y., Zhang, H., et al. (2020). Preparation and laser sintering of a thermoplastic polyurethane carbon nanotube composite-based pressure sensor. *RSC Adv.* 10, 23644–23652. doi:10.1039/d0ra04479b

Zhuang, Y., Guo, Y., Li, J., Yu, Y., Jiang, K., Zhang, H., et al. (2021). Study on the forming and sensing properties of laser-sintered tpu/cnt composites for plantar pressure sensors. *Int. J. Adv. Manuf Technol.* 112, 2211–2222. doi:10.1007/s00170-020-06560-8

Conflict of Interest: The authors declare that the research was conducted in the absence of any commercial or financial relationships that could be construed as a potential conflict of interest.

Publisher's Note: All claims expressed in this article are solely those of the authors and do not necessarily represent those of their affiliated organizations, or those of the publisher, the editors and the reviewers. Any product that may be evaluated in this article, or claim that may be made by its manufacturer, is not guaranteed or endorsed by the publisher.

frontiers in Materials

ORIGINAL RESEARCH
published: 19 August 2021
doi: 10.3389/fmats.2021.725328

Synthesis of Comb-Polyurethane-Modified Polycarboxylate at Indoor Temperature and Its Interaction With Portland Cement

*Shuncheng Xiang, Yansheng Tan and Yingli Gao**

School of Traffic and Transportation Engineering, Changsha University of Science and Technology, Changsha, China

According to the principle of radical polymerization reaction, different polycarboxylates with comb structures were synthesized. With the other two commercial polycarboxylates (C-PCE-1 and C-PCE-2), the effects of all the polycarboxylates on adsorption, hydration, zeta potential, liquid surface tension, and flowability in Portland cement were determined. Compared to O-PCE and C-PCEs, the adsorption value of M-PCE increased by 14.1% and the adsorption rate increased by 24% maximum. O-PCE, C-PCE-1, and C-PCE-2 have a delayed effect on the hydration of the cementitious materials, but M-PCE does not. Due to higher adsorption amount, M-PCE with siloxane groups has an excellent comprehensive performance of zeta potential, liquid surface tension, and flowability in cementitious materials.

Keywords: polyurethane-modified, polycarboxylate, radical polymerization, indoor temperature, interaction

OPEN ACCESS

Edited by:
Eileen Harkin-Jones, Ulster University, United Kingdom

Reviewed by:
Zhihua Ou, Hunan University of Technology, China
Fu Bo, North Minzu University, China

****Correspondence:***
Yingli Gao
yingligao@126.com

Specialty section:
This article was submitted to Polymeric and Composite Materials, a section of the journal Frontiers in Materials

Received: *15 June 2021*
Accepted: *23 July 2021*
Published: *19 August 2021*

Citation:
Xiang S, Tan Y and Gao Y (2021) Synthesis of Comb-Polyurethane-Modified Polycarboxylate at Indoor Temperature and Its Interaction With Portland Cement. Front. Mater. 8:725328. doi: 10.3389/fmats.2021.725328

INTRODUCTION

Polycarboxylate superplasticizer (PCE) has been extensively used in concrete technology since the 1980s (Plank and Bian, 2010). The side chain of PEO is suspended between the Portland cement particles to exert its steric hindrance effect, thereby dispersing Portland cement (Li et al., 2005; Wang, 2009). Compared with other plasticizers, PCE has advantages in water reduction, slump retention, and compatibility. During the synthesis of polycarboxylates, the active groups can react with the -COOH groups on the main and side chains of the polycarboxylate, and -C=C- double bond can be connected to the main chain.

Many scholars are devoted to improving the structure and performance of PCE. Yu et al. (2016) conducted synthesis using butenyl alkylene polyoxyethylene-polyoxypropylene ether (BAPP) as the macromonomer and 2,2′-azoisobutyronitrile as the initiator for 48 h at 70°Cin N_2 atmosphere, which greatly accelerated cement hydration of polycarboxylate. In Liu's research (Liu et al., 2014), at 130–150°C, polycarboxylate (amide-type PCE) of five amide structures was produced by the amidation reaction between polyacrylic acid (PAA) and amino-terminated methoxy polyethylene glycol (amino-PEG). It was found that the amide-type PCE significantly facilitated the formation of strong hydrogen bonds between amide and polyether chains. Plank et al. (Plank et al., 2016) used acrylic acid and isoprenoxy polyethylene glycol (IPEG) to synthesize polycarboxylates at 60°C and used ^{13}C NMR spectroscopy in characterization, finding that optimal PCE dispersion effect was obtained when the molecular weight (Mw) was about 40,000 in narrow distribution. Lange and Plank (2016) used acrylic acid and

TABLE 1 | Chemical composition of PI 42.5 Portland cement w/%.

Material	Chemical composition w/%										
	SiO_2	Al_2O_3	Fe_2O_3	CaO	MgO	SO_3	TiO_2	K_2O	Na_2O	Total	Loss
Cement	21.18	4.73	3.41	62.49	2.53	2.83	—	—	0.56	97.73	1.76

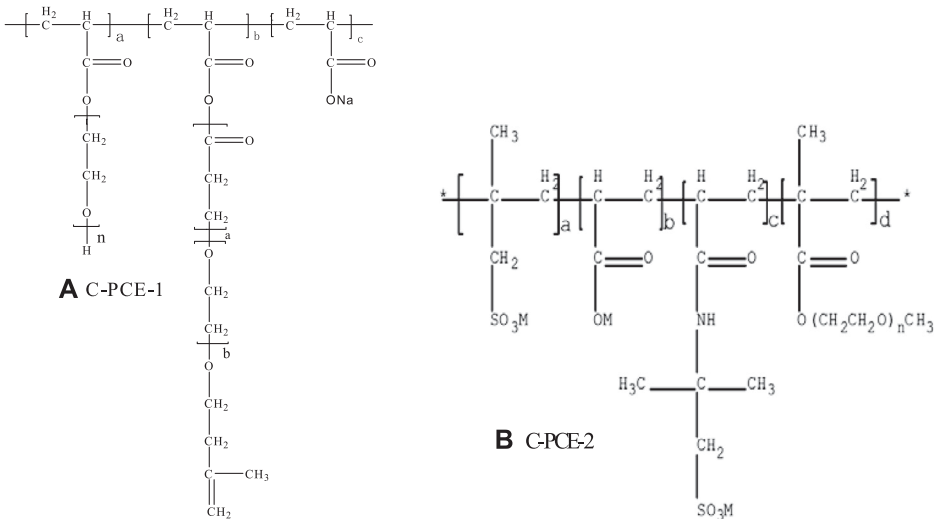

FIGURE 1 | Chemical structure of commercial polycarboxylate (C-PCE-1 and C-PCE-2).

ω-methoxy polyethylene glycol methacrylate to synthesize non-adsorbent polycarboxylate within 4 h at 80°C. Research results showed that such non-adsorbent polycarboxylate can also significantly improve the Portland cement flowability at a low water–binder ratio.

In addition to polycarboxylate synthesis by heating, in terms of synthesis at indoor temperature, Jiang et al. (2013) used the redox method to synthesize PCE at indoor temperature (20–40°C). When the dosage was 0.2%, the initial flowability could reach 295 mm. Yang et al. (Yang et al., 2011) used free radical copolymerization of dendritic activated macromers and acrylic acid to synthesize PCE at indoor temperature. However, due to the indoor temperature changes and restrictions in synthesis conditions, the synthesized PCE exhibited unstable performance. Therefore, they believed that PCE synthesized at indoor temperature is still inferior to PCE synthesized at high temperature.

In this study, organosiloxane modified polyurethane with appropriate molecular weight was used as the side chain to be connected with the polycarboxylate acid backbone, while other functional groups such as carboxyl, hydroxyl, and polyoxyethylene group were introduced into the molecular structure of polycarboxylate. The best indoor temperature synthesis process of polycarboxylate was obtained through orthogonal design. Also, this article studied their interaction with Portland cement and the law of influence, which lays a theoretical basis for the structure design, synthesis, and selection of water reducers.

EXPERIMENT

Raw Materials

P·I 42.5 cement, with an average particle size of 36.96 μm, is shown in **Table 1**. Common commercially available polycarboxylates, C-PCE-1 and C-PCE-2, are shown in **Figure 1**.

The used synthetic raw materials include isophorone diisocyanate, hydroxy-terminated siloxane, polyether glycol, N-methylpyrrolidone, 1,4-butanediol, dimethylolpropionic acid, P·I 42.5 cement, isopentenyl polyether (TPEG) with molecular weight 2,400; analytically pure acrylic acid (AA), mercaptoacetic acid, p-toluene sulfonic acid, hydroquinone, benzoyl peroxide, polyethylene glycol-200 (PEG-200), hydrogen peroxide, ascorbic acid (Vc), ammonium persulfate, dibutyltin dilaurate, and deionized water. All chemicals are of analytical purity.

Synthesis of Side Chain

In the synthesis of the side chain, alcohol and amine compounds containing hydroxyl or amino groups were introduced in the main chain of polycarboxylate molecules, which increased the number of short branches, promoted alternate distribution of polyether long branches, and branched short chains of the chain extender of alcohol and amine compounds, thereby increasing dispersibility and adaptability of the water reducer. The specific operations are as follows.

Place 22.2 g of isophorone diisocyanate in a three-necked flask, and use a dropping funnel to dropwise add polyethylene glycol

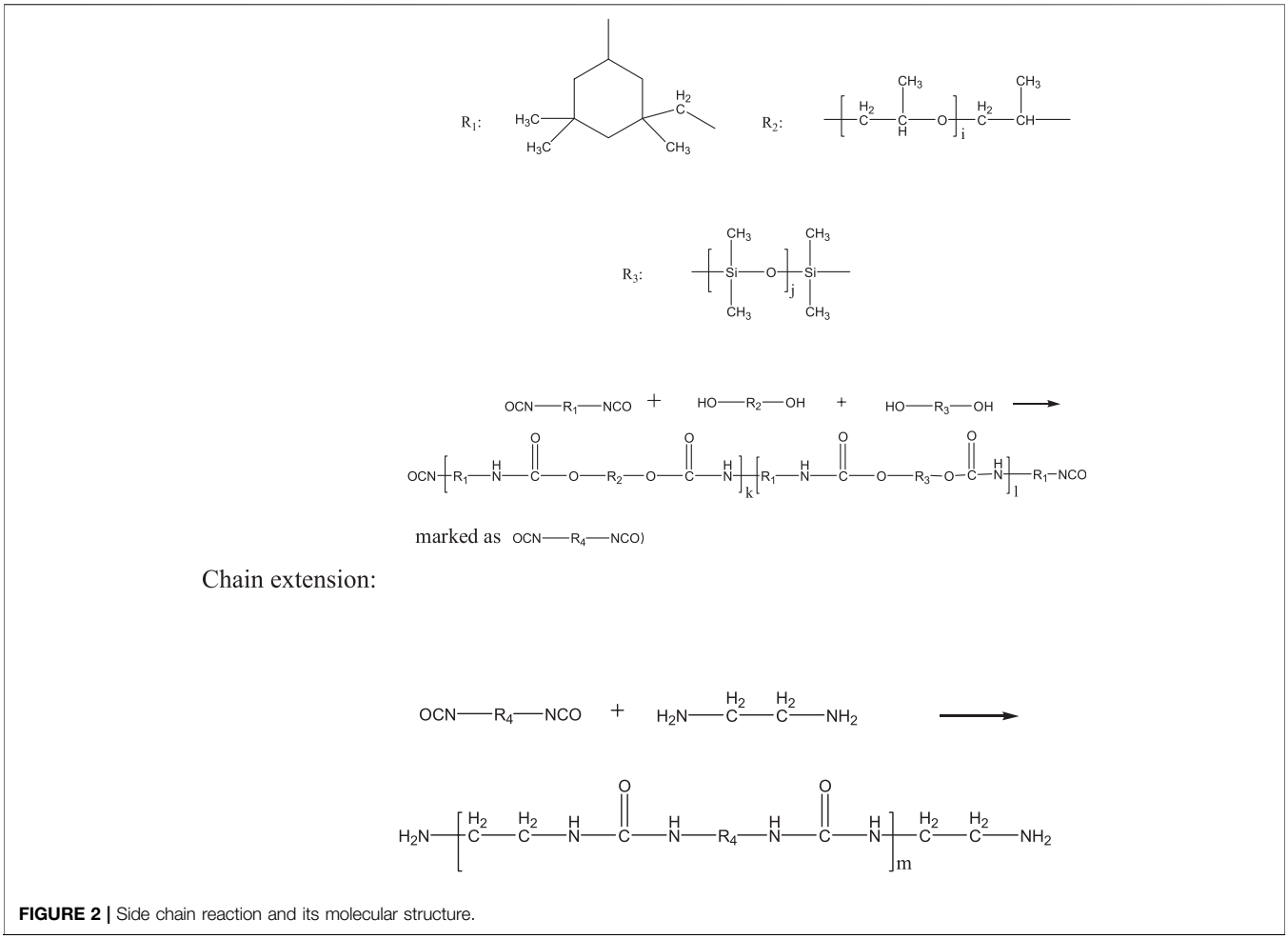

FIGURE 2 | Side chain reaction and its molecular structure.

1,000 containing dibutyltin dilaurate (25 g polyethylene glycol 1,000 contained 0.2 g dilaurate and N-methylpyrrolidone solution of dimethylolpropionic acid; 3.35 g dimethylolpropionic acid was dissolved in 5 ml N-methylpyrrolidone). Then, add 50 g water, heat to 70°C, and keep warm, and after that dropwise add a mixed solution of hydroxyl-terminated polysiloxane and 1,4-butanediol (9 g hydroxyl-terminated polysiloxane mixed with 3 g 1,4-butanediol), 2.5 g ethylenediamine, and 1.5 g sodium dodecylbenzene sulfonate. Stir after the addition was complete, and when the mass percentage of free -NCO in the mixed solution was detected to be 16%, stop heating to obtain a polyurethane prepolymer. The principle of side chain reaction was shown in **Figure 2**.

Preparation of Polycarboxylate

The designed polycarboxylate molecular structure is shown in **Figure 3**. To ensure equal molar concentration of double bonds in the system, the molar ratio of acrylic acid to TPEG was adjusted. TPEG 120g, purified water 80ml, and PEG -200 10 g were stirred well in a 250 ml four-necked flask. Then, 0.1 g dibutyltin dilaurate, 1.2 g p-toluenesulfonic acid, and 30% hydrogen peroxide were added to prepare A and B two-component solutions for later use.

Group A: 10.8 g AA, 0.384 g thioglycolic acid, and 25 g deionized water.

Group B: 3.4 g Vc, 0.3 g ammonium persulfate, and 25 g deionized water.

Components A and B were added into the beaker at a rate of 2 ml/min using a peristaltic pump, and the process lasted for about 2.5 h. After keeping it for a period of time, adjust the PH value to 6-7 with NaOH to obtain the polycarboxylate mother liquor M-PCE. The radical polymerization reactions and chemical structure of M-PCE are shown in **Figure 3**.

In addition, for comparison experiments, the above step 1.3 can be performed separately to synthesize a common unmodified polycarboxylate (O-PCE), as shown in **Figure 4**. Moreover, in order to control the chain reaction and carry out future research, the concentration of free radicals and the molar ratio of AA and TPEG needed to be adjusted. Please find the orthogonal experiment study in Section 2.1 for details.

Determination of the Adsorption Amount of Polycarboxylate

The adsorption equilibrium was obtained using a constant temperature shaker before performing suction filtration. The

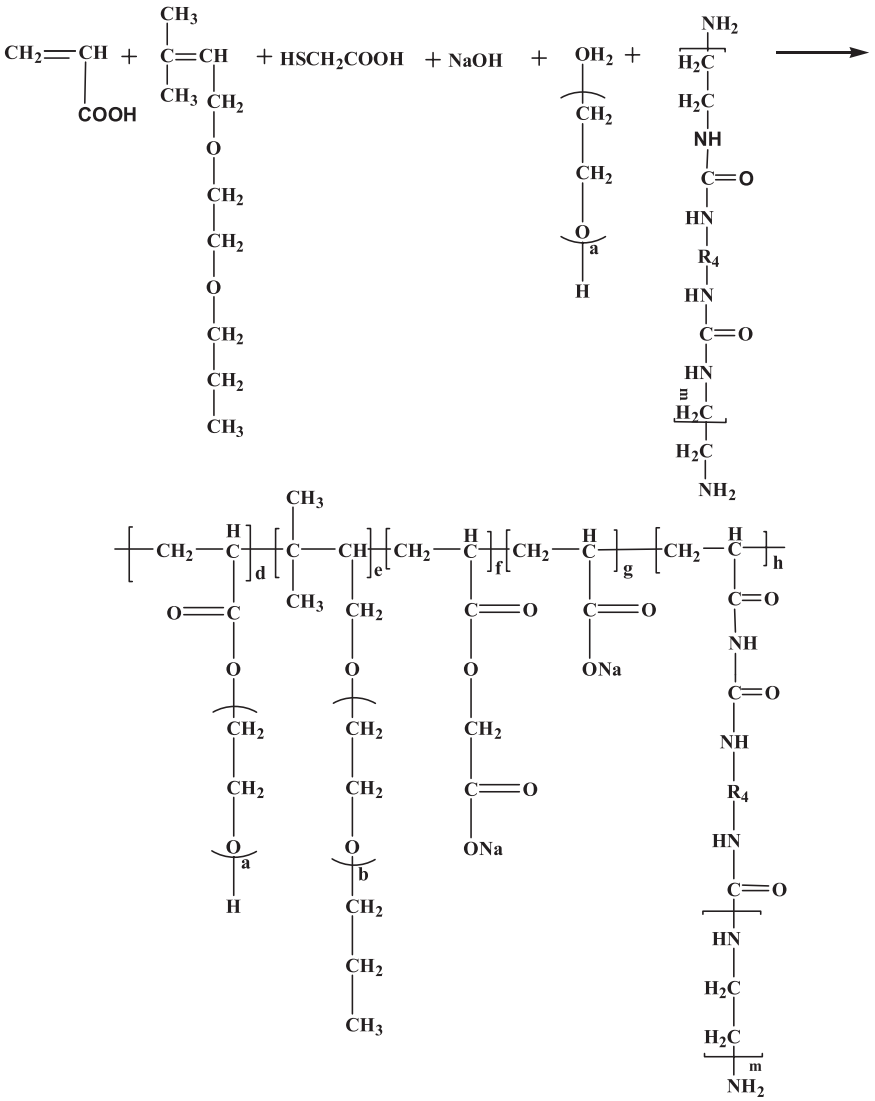

FIGURE 3 | Radical polymerization reactions and chemical structure of (M-PCE).

resulting filtrate was centrifuged, and the supernatant was taken out and centrifuged twice. The residual concentration of polycarboxylate in the clear liquid was measured. Then, calculate the amount of polycarboxylate adsorbed to the surface of cement particles using the following formula:

$$Q_e = \frac{(C_0 - C_e)V}{M}, \tag{1.1}$$

where Q_e is the adsorption capacity, unit mg·g^{-1}; C_0 is the concentration of polycarboxylate solution before adsorption, unit mg·g^{-1}; C_e is the equilibrium concentration of polycarboxylate after adsorption, unit mg·g^{-1}; V is the solution volume, unit l; and M is the cement mass, unit g.

The water reducer solution was prepared according to the designed water–binder ratio and water reducer dosage, mixed with the cementitious material, stirred magnetically for 10 min, oscillated on an oscillator to separate the gelled slurry with a centrifuge for 10 min. The supernatant after separation was taken out and then filtered by suction through a 0.45 μm nylon microporous membrane. The filtrate was transferred to a volumetric flask and diluted 100 times with deionized water. The diluted solution was tested by the Liquid TOC to detect the carbon content, calculate the concentration of PCE water reducer in the solution, and then infer the adsorption. The polycarboxylate PC dosage was 0.2%, the water–cement ratio was 0.4, and the cement dosage was 50 g.

Hydration Heat

The hydration heat release rate and heat release of the cementitious material paste were quantitatively analyzed using an eight-channel isothermal microcalorimeter. Put 4 g cementitious material in a beaker to test hydration heat of

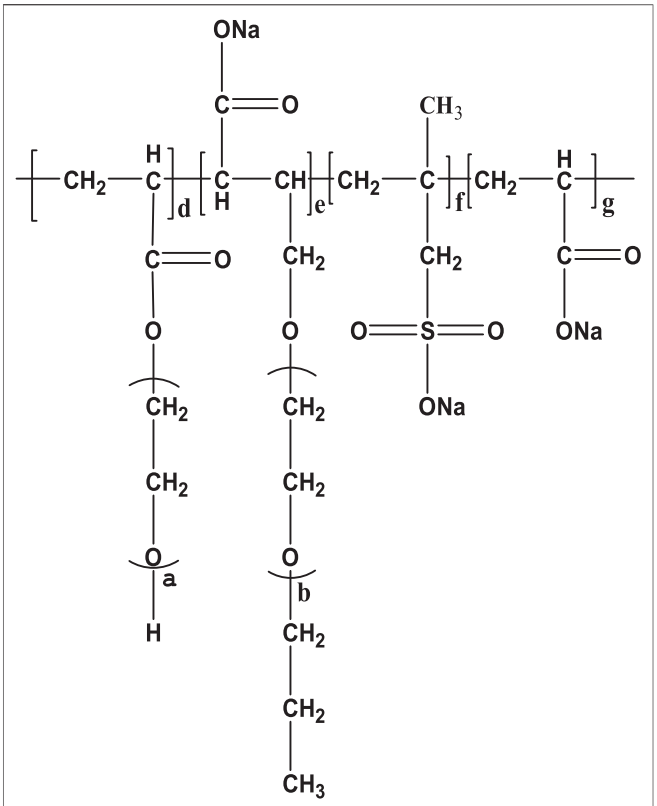

FIGURE 4 | Structure of synthesized ordinary polycarboxylate (O-PCE).

Portland cement sample at the 72nd hour under polycarboxylate solid content of 0.2%, with water–binder ratio of 0.4. The ambient temperature was controlled at 20 ± 1°C.

Zeta Potential

Put 50 g cementitious material in a beaker, and mix the polycarboxylate (the solid content was 0, 0.1, 0.2, 0.3, 0.4, and 0.5% of the mass of the cementitious material) with certain water in the beaker, with water–binder ratio of 0.4. By stirring at a low rate for 2 min and then at a high rate for 1 min, the Zeta potential of cement paste under different water–binder ratios and polycarboxylate contents was tested.

Surface Tension

1) The surface tension test of the synthesized polycarboxylate was carried out under different concentrations using the A-60 automatic surface tension meter manufactured by Kino Industries Co., Ltd. of the United States.
2) Liquid phase surface tension test on Portland cement paste: put 50 g Portland cement in a beaker, fix the water–binder ratio to 0.4, and mix polycarboxylate (the solid content was 0, 0.1, 0.2, 0.3, 0.4, and 0.5% of the mass of the cementitious material) with 20 g water, stir at a low rate for 2 min and then a high rate for 1 min. Afterward, the cement paste was centrifuged to collect the supernatant and test the liquid phase surface tension.

Flowability

According to GB/T8077-2000 "Test Method for the Homogeneity of Concrete Admixtures," the initial flowability, 1 and 2 h cement paste flowability was tested by the hollow cylindrical mold test. Flowability of four kinds of polycarboxylates was tested under Portland cement mass of 300 g, water–cement ratio of 0.29, and polycarboxylate solid content of 0.15%.

RESULTS AND DISCUSSION

Orthogonal Experiment

By investigating the law of synthesis of polycarboxylates at indoor temperature, referring to relevant literature and experimental experience, a four-factor and three-level orthogonal experiment L_9 (3^4) was performed for the synthesis of polycarboxylates at indoor temperature. When using the orthogonal table to arrange the experiment, we can select representative experimental conditions from the multiple experimental conditions and infer better production conditions through a small number of experiments. At the same time, it is possible to make further statistical analysis to get more accurate results. Based on single factor experiments, n (TGA), n (H_2O_2), n (AA): n (TPEG), n (H_2O_2): n (APS): n (Vc) are considered as the four primary factors that affect the dispersion performance of ether polycarboxylates. Therefore, a four-factor and three-level orthogonal experiment was designed, as shown in **Table 2**. The effect of the polycarboxylate synthesized by the above factors on the adsorption of Portland cement was studied, with results shown in **Table 3**.

To comprehensively evaluate the effect of various factors on the saturated adsorption Q_{em} and surface tension, the composite indicators were obtained after comprehensive processing of the two indicators and listed in the table. The specific method is to firstly set the maximum value of saturated adsorption Q_{em} and surface tension to 100 and the minimum value to 0 so that the other measured values of the two indicators are converted into a percentage system. Considering that the cement paste flowability and macromonomer conversion rate have the same proportion, the composite indicator was calculated by the weighted average of 50% proportion each. In the table, K1–K3 is the mean value of the composite indicators at each level, and R is the range. According to analysis of the above results, it is the best synthesis process and the order of influence decreases sequentially, A1>D2>C2>B3, namely, n (TGA) = 0.01, n (H_2O_2):n (APS):n (Vc) = 15:1:1, n (AA): n (TPEG) = 2:1, and n (H_2O_2) = 0.05 mol.

Polycarboxylate was prepared under 40°C for 4 h. The dispersibility was marked as M-PCE, as shown in **Table 4**.

Adsorption of Polycarboxylate to Portland Cement

At 20°C, test the adsorption values of different polycarboxylates against Portland cement, as shown in **Figure 5**.

From **Figure 5**, it can be seen that, as the PCE dosage increases, the microscopic flocculation structure of the cementitious system changes. After the addition of PCE

TABLE 2 | Factors and levels of factorial design.

Level	Factor			
	A: n (TGA)/mol	B: n (H_2O_2)/mol	C: n (AA): n (TPEG)	D:n (H_2O_2):n (APS):n (Vc)
1	0.01	0.03	1:1	10:1:1
2	0.015	0.04	2:1	15:1:1
3	0.02	0.05	3:1	20:1:1

TABLE 3 | Results of factorial design.

Test no.	n (TGA)/mol	n (H_2O_2)/mol	n (AA): n (TPEG)	n (H_2O_2):n (APS): n (Vc)	Adsorption Q_{em} ($mg·g^{-1}$)	Surface tension (40%wt)/ ($nN·m^{-1}$)	Composite indicator
1	1	1	1	1	1.00 (52.6)	52.7 (59.5)	56.1
2	1	2	2	2	1.19 (100)	58.6 (100)	100
3	1	3	3	3	1.15 (89.5)	45.9 (12.6)	51.1
4	2	1	2	3	1.06 (68.4)	47.6 (24.3)	46.4
5	2	2	3	1	1.11 (78.9)	44.1 (0)	39.5
6	2	3	1	2	1.11 (78.9)	57.9 (95.4)	87.2
7	3	1	3	2	0.82 (10.5)	47.4 (22.9)	16.7
8	3	2	1	3	0.76 (0)	47.8 (25.7)	12.9
9	3	3	2	1	0.88 (27.9)	50.2 (42.2)	36.2
K1	69.07	39.73	52.07	43.93			
K2	57.7	50.8	60.87	67.97			
K3	21.93	58.17	35.77	36.8			
R	47.14	18.44	25.1	31.17			

TABLE 4 | Basic performance of M-PCE.

Sample	Dosage (%)	Saturated adsorption Q_e	Surface tension ($nN·m^{-1}$)	Flowability (mm)		
				Initial	1 h	2 h
M-PCE	0.15	1.34 ($mg·g^{-1}$)	40.31	340	320	305

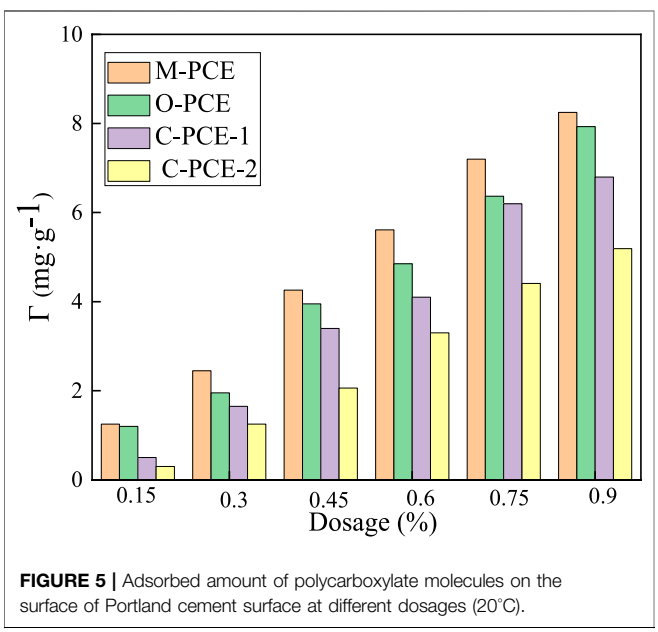

FIGURE 5 | Adsorbed amount of polycarboxylate molecules on the surface of Portland cement surface at different dosages (20°C).

molecule, due to its high negative charge, it will be quickly adsorbed to the surface of the gel particles and early hydration products and generate electrostatic repulsion. On the one hand, the gel particles are wrapped, which delays hydration, and on the other hand, the gel particles wrapped by the hydration product are released, so that the flocculation structure of the gel particles disintegrates. When a sufficient amount of polycarboxylate was added, the flocculation structure in the cementitious system was completely disintegrated, and the gel particles were well dispersed. The results in Figure 6 show, with the extension of reaction time, the adsorption capacity of the two polycarboxylates will gradually increase and approach a saturation value. Self-made polycarboxylates have greater adsorption than C-PCE-1 and C-PCE-2. After the addition of polycarboxylate PCE molecule, due to its high negative charge, it will be quickly adsorbed to the surface of the gel particles and early hydration products and generate electrostatic repulsion. On the one hand, the gel particles are wrapped by a water reducer, which delays hydration, and on the other hand, the gel particles wrapped by the hydration product are released, so that the flocculation structure of the gel particles disintegrates. Therefore, as the reaction time

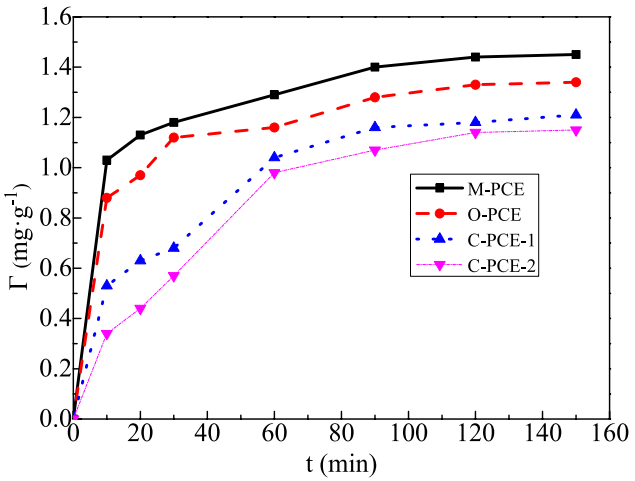

FIGURE 6 | Adsorption amount of polycarboxylate molecules on the surface of Portland cement at 20°C (0.2% dosage).

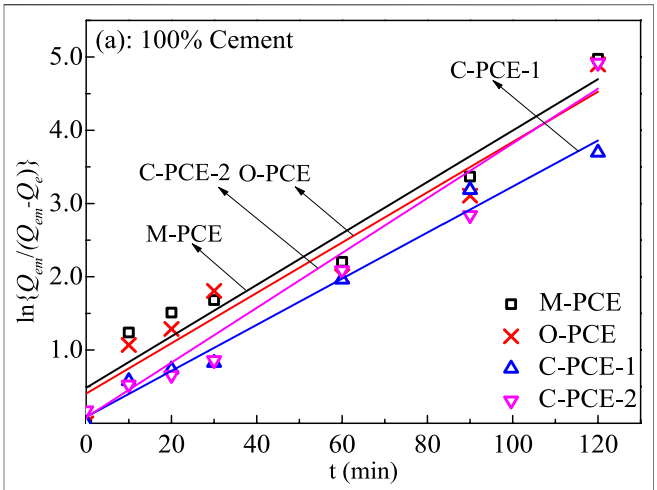

FIGURE 8 | Lagergren fitted line of adsorption rate equation of polycarboxylate at cement particle surfaces (20°C).

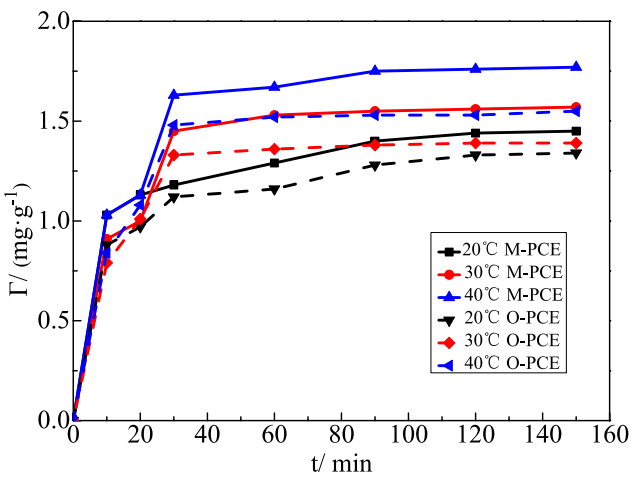

FIGURE 7 | Adsorbed amount of polycarboxylate molecules at different times and temperatures (0.2% dosage).

extended, more and more polycarboxylate would adsorb to the surface of the gel particles and its hydration products until the gel particles reached the highest degree of hydration (the highest degree of hydration within 2 h), with adsorption tending to be balanced.

In addition, an obvious common trend is that, within 10–20 min, the adsorption of the water reducer will increase sharply, which can basically reach about 2/3 or even 3/4 of the saturated adsorption. Subsequently, the adsorption will remain relatively stable or there will be a slight decrease. After 0.5 h, adsorption will continue to slowly increase until the saturated adsorption. Adsorption undergoes a rapid increase in the initial stage. With the addition of polycarboxylate, due to its high negative charge, it will be quickly adsorbed to the surface of gel particles and early hydration products and generate electrostatic repulsion. The subsequent relatively stable or small decline is possible because, with the hydration of the gel particles, the gel particles in the cementitious system will desorb from the water reducer molecules. At the same time, the newly added hydration products will create a shielding effect on the water reducer adsorption layer, resulting in a stable or slight decline in adsorption. In the subsequent stage with adsorption slowly increasing to the saturated adsorption, it is generally believed that, as the degree of hydration increases until full hydration, the hydration products continue to increase, making adsorption slowly increase until the saturated adsorption.

According to the graph obtained from the experiment, the Lagergren adsorption rate equation can be used to fit **Figure 6** and **Figure 7**:

$$Ln\frac{Q_{em}}{Q_{em}-Q_e} = -Ln(1-F) = Kt, \tag{2.1}$$

where t represents the adsorption time, min; Q_e is the adsorption at time t, mg·g^{-1}; Q_{em} is the saturated adsorption at adsorption equilibrium, mg·g^{-1}; $F = Q_e/Q_{em}$; and k represents the apparent adsorption rate constant of the first-order kinetic equation, min^{-1}. Use -Ln (1-F) to plot t for linear fitting. The results are shown in **Figures 8**, **9**. The adsorption rate k can be calculated according to the slope of the straight line, with the calculation results shown in **Tables 5**-**6**.

According to the Arrhenius equation, the apparent adsorption activation energy can be calculated:

$$k = k_0 \exp\left(\frac{-E_a}{RT}\right), \tag{2.2}$$

where k_0 represents the pre-exponential factor (frequency factor), min^{-1}; E_a represents the apparent activation energy, KJ·mol^{-1}; R is the molar gas constant, $R = 8.3145 \times 10^{-3}$ kJ·mol-1·K^{-1}; and T is

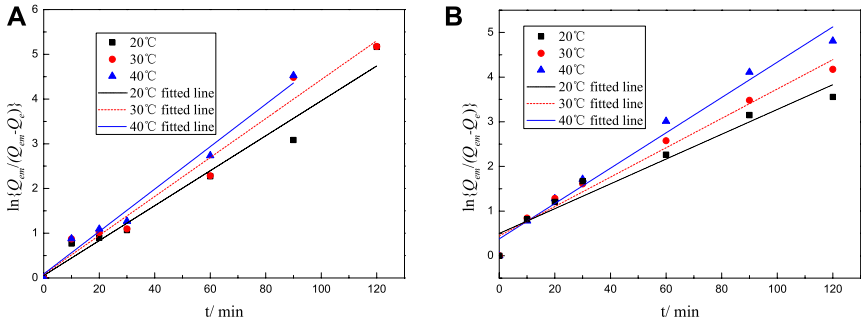

FIGURE 9 | Lagergren fitted line of adsorption rate equation of M-PCE at cement particle surfaces at different temperatures: **(A)** M-PCE and **(B)** O-PCE.

TABLE 5 | Fitted values of Lageren adsorption rate equation derived from polycarboxylate at 20°C.

Cementitious materials	M-PCE			O-PCE			C-PCE-1			C-PCE-2		
	Q_{em}/ mg·g^{-1}	k/ min^{-1}	r^2	Q_{em}/ mg·g^{-1}	k/ min^{-1}	r^2	Q_{em}/ mg·g^{-1}	k/min^{-1}	r^2	Q_{em}/ mg·g^{-1}	k/min^{-1}	r^2
Cement	1.45	0.0390	0.96379	1.34	0.0278	0.9387	1.21	0.03845	0.98202	1.15	0.03842	0.95792

TABLE 6 | Fitted values of Lageren adsorption rate equation derived from polycarboxylate at cement particles surfaces.

T/°C	M-PCE			O-PCE		
	Q_{em}/mg·g^{-1}	k/min^{-1}	r^2	Q_{em}/mg·g^{-1}	k/min^{-1}	r^2
20	1.45	0.0390	0.96379	1.34	0.0278	0.9387
30	1.57	0.0435	0.96710	1.38	0.0329	0.9688
40	1.77	0.0474	0.97755	1.55	0.0382	0.9765
E_a/KJ·mol^{-1}	5.3574			8.5094		
k_0/min^{-1}	2.7755			10.5838		

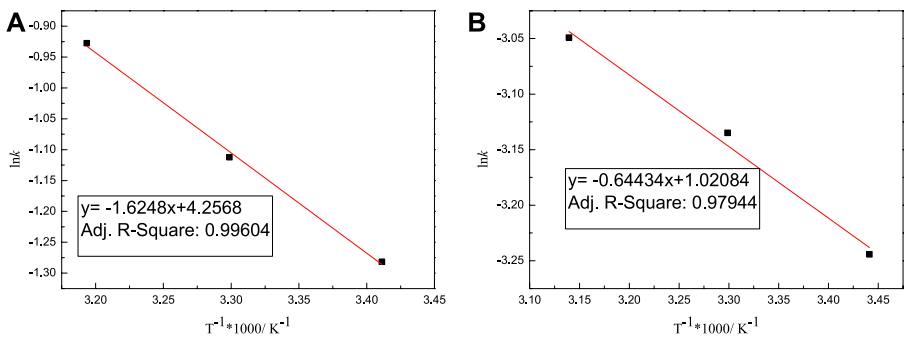

FIGURE10 | Determination result of activation energy of adsorption of PCE: **(A)** M-PCE and **(B)** O-PCE.

the adsorption temperature, *K*. Plot 1/T using Lnk, with the result shown in **Figure 10**. According to the intercept and slope of the straight line, k_0 and E_a can be calculated, with the calculation results shown in **Tables 5**-**6**.

It can be seen from **Tables 5**-**6** that the correlation coefficient of polycarboxylate on the Lagergren model is greater than 0.93, and the fitting effect is good, indicating that the isothermal adsorption of M-PCE, O-PCE, C-PCE-1, and C-PCE-1 follows the Lagergren model, which is consistent with the results of Hsu (1999) and Peng et al. (2005). The saturated adsorption (Q_{em}) and adsorption rate constant (k) of M-PCE increase from 1.45 mg g^{-1} and 0.0390 min^{-1} to 1.77 mg g^{-1} and 0.0474 min^{-1}, respectively. The saturated adsorption and adsorption rate constant of O-PCE polycarboxylate are only

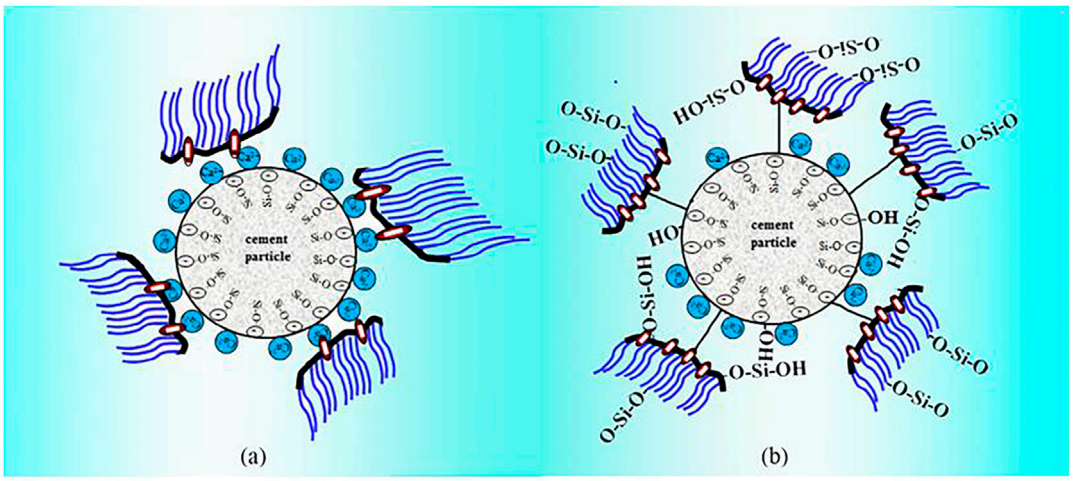

FIGURE 11 | The adsorption mechanisms of polycarboxylate: **(A)** O-PCE and C-PCEs and **(B)** M-PCE.

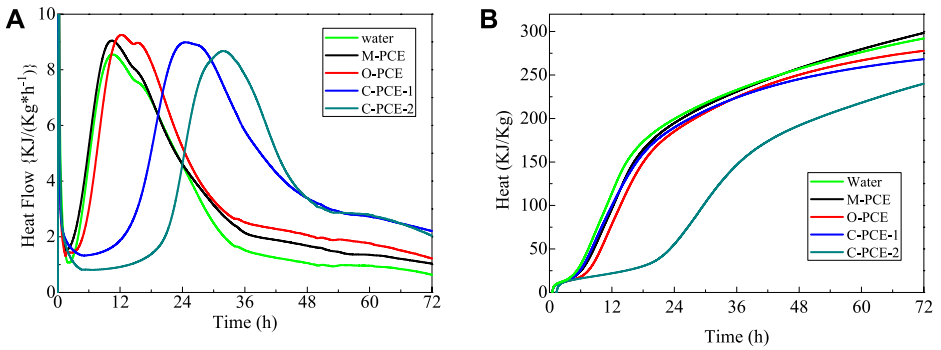

FIGURE 12 | Influence of polycarboxylate on the hydration of cement pastes: **(A)** heat evolution and **(B)** hydration heat.

1.55 mg g^{-1} and 0.0382 min^{-1} at 40°C, respectively. In addition, M-PCE has a low slope (k) and apparent activation energy (Ea). This suggests that M-PCE is more easily adsorbed by cement, and the saturated adsorption state can be reached more quickly, as shown in **Figure 11**. In this study, by replacing the carboxylic acid component with methylsiloxane, the adsorption rate of M-PCE on cement was enhanced. Yu et al. (2016) proved that silicate formed strong covalent bonds with inorganic chains of CSH and siloxane groups. Due to the increased electrostatic interaction between COO- and aluminate, the bigger function of methylsiloxane led to bigger adsorption (Plank et al., 2008). However, the adsorption of electropositive aluminates by ordinary polycarboxylates (O-PCE, C-PCEs) was based on electrostatic interaction with carboxylate groups, so the adsorption effect was weakened.

Hydration Heat

Unlike O-PCE and C-PCEs, M-PCE may produce different hydration effects on Portland cement due to the incorporation of organosiloxane groups. **Figure 12** shows the effect of different polycarboxylate dosage on the hydration heat of Portland cement paste under water–binder ratio of 0.4.

The main hydration equations in cementitious materials are as follows:

$$C_3A + 3CSH_2 + 26H \rightarrow C_6AS_3H_{32}, \quad (3.1)$$

$$2C_3A + C_6AS_3H_{32} + 4H \rightarrow 3C_4ASH_{12}, \quad (3.2)$$

$$C_3S + (3 - x + n)H_2O \rightarrow C_xS - Hn + (3 - x)CH. \quad (3.3)$$

The hydrolysis reaction of organosiloxane is as follows:

$$R'Si(OR)_{3-n} + H_2O \rightleftarrows R'Si(OR)_{3-n}(OH)_n + ROH, \quad (3.4)$$

$$R'Si(OR)_{3-n}(OH)_n + R'Si(OR)_{3-n}(OH)_n \rightleftarrows Si - O - Si + H_2O, \quad (3.5)$$

$$R'Si(OR)_3 + R'Si(OR)_{3-n}(OH)_n \rightleftarrows Si - O - Si + H_2O. \quad (3.6)$$

As can be seen from **Figure 12**, incorporation of O-PCE or C-PCEs delayed the hydration of Portland cement. For this reason, the M-PCE molecules adsorbed restrict the diffusion of water and ions in cement mineral and pore solution interface, and the chelation formed inhibited the nucleation and precipitation of

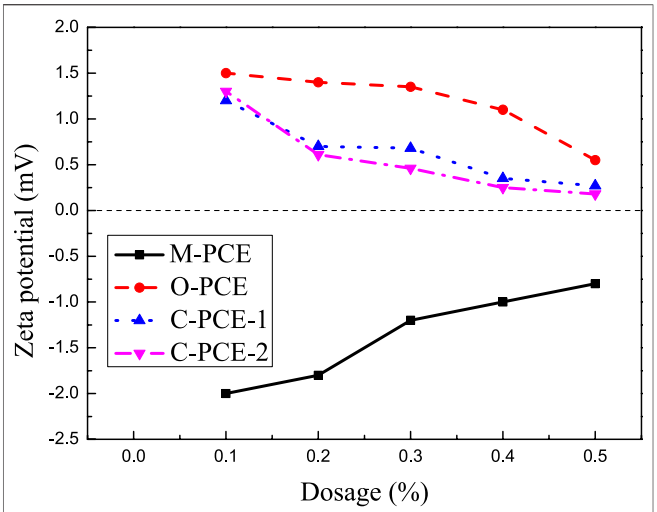

FIGURE 13 | Zeta potential of polycarboxylate.

hydrate products (Kong et al., 2016). Differently, M-PCE does not delay the hydration of Portland cement, which is mainly due to the fact that the high content of carboxylate groups in PCE brought about more adsorption sites, making cement particles better wrapped and dispersed in the solution. However, polyacrylic acid (PAA) homopolymers formed under excess AA monomers can also be adsorbed on the cement surface, thereby reducing the hydration rate (Zhou et al., 2017). In addition, in Kong's research (Švegl et al., 2008), polycarboxylates were prepared by grafting tetraethoxysilane into the main chain. Reports have confirmed that polyurethane side chain can be completely hydrolyzed, and the hydrolysates of methanol and ethanol in M-PCE insignificantly decline the main hydration peak, without delay (Scrivener and Nonat, 2011). Therefore, it can be inferred that M-PCE does not delay cement hydration as a result of silane molecules.

After adding C-PCE-1, C-PCE-2, and O-PCE, the heat release rate and total heat release of cement hydration exhibited better mitigation and reduction effects. Due to the incorporation of polycarboxylate, in the initial cement hydration stage, on the one hand, the adsorption of water reducer acted on the surface of cement particles; on the other hand, in the alkaline medium of cement hydration, the active group in the molecular chain of water reducer (such as -COO-, $-SO_3^-$) acted with hydration-generated ions (such as Ca^{2+}) to form unstable complexes, which delayed cement hydration and inhibited the precipitation and growth of minerals in the initial phase (Kong et al., 2016). Moreover, the effect strengthened with the increase of dosage; that is, the dissolution peak decreased. Due to adsorption, complexation, and retardation effects of the polycarboxylate side chain on Portland cement, hydration of hydrated minerals was inhibited, and more time was needed to break the hydration energy barrier (Wang and Wang, 2003; Ylmén et al., 2009). Therefore, the longer induction period of hydration was manifested as the delay and weakening of the second exothermic peak. Similarly, with the increase of polycarboxylate dosage, the retardation effect became more obvious, which was manifested as a shift of the second exothermic peak to the right (Ylmén et al., 2010).

Zeta Potential

The effect of polycarboxylate on the Zeta potential of Portland cement under different dosages is shown in **Figure 13**.

As seen from the above figure, it can be known that, as the polycarboxylate dosage increases, the absolute value of zeta potential in the cement paste exhibits a downward trend. Zeta potential has a close relation with the electrostatic repulsion between molecules. The Debye–Hückel formula is shown as follows:

$$\frac{1}{F_{ES}} = \frac{-1}{2\pi\varepsilon\varepsilon_0\overline{a}\psi^2} \times K^{-1} \times \left[e^{k(h-2l)} + 1\right]. \quad (4)$$

where F_{ES} is the electrostatic repulsion; ε is the relative permittivity of water; ε_o is the vacuum permittivity; $\overline{a}$ is the average radius of the particles; ψ is the electrokinetic potential; K is the Debye–Hückel parameter; h is the particle-to-particle distance; and l is the adsorption layer thickness.

The adsorption of polycarboxylate to the Portland cement surface conforms to the Langmuir adsorption equation (LI et al., 2014). It can be seen from **formula (4)** that, as the polycarboxylate increases, the thickness l of the adsorption layer between two particles remains unchanged. As the distance h gets smaller, the electrostatic repulsion gets smaller (Wang, 2009), the system stability becomes worse, and the zeta potential value decreases. In addition, the zeta potential values of O-PCE, C-PCE-1, and C-PCE-2 are positive, but the value of M-PCE is negative. The main mineral components of cement are C2S, C3S, C3A, and C4AF. The hydration products of C2S and C3S are negatively charged, while those of C3A and C4AF are positively charged. Since aluminate has stronger solubility than silicate, the hydration product is positively charged, and the measured zeta potential is positive (Schmid and Plank, 2021). Although some negatively charged polycarboxylates were added, Zeta potential showed a decreasing trend, but its content remained small, with low water–cement ratio, which, however, did not affect the hydration products of aluminate. Therefore, the zeta potentials of these three polycarboxylates were positive. For M-PCE, the side chain was partially replaced by siloxane with a high negative charge, so M-PCE reduced Zeta potential to a bigger negative value, which is attributed to the higher polymer adsorption, as discussed in **Figure 7**. When cement particles contacted water, positive ions such as K^+ and Na^+ were dissolved in the interstitial solution, while SiO_3^{3-} and AlO_3^{3-} skeletons were maintained. Such a phenomenon led to a latent cement surface. Therefore, the inner layer is composed of positive ions and the outer layer is composed of negative ions (Zhang and Kong, 2015). The electronegative groups in the main chain will be adsorbed on the electropositive outer layer through electrostatic adhesion. Therefore, the Zeta potential of the cement paste also changed from positive value to negative value. The higher adsorption of anionic polymers against solid particles leads to a decreased Zeta potential and a greater electrostatic barrier effect,

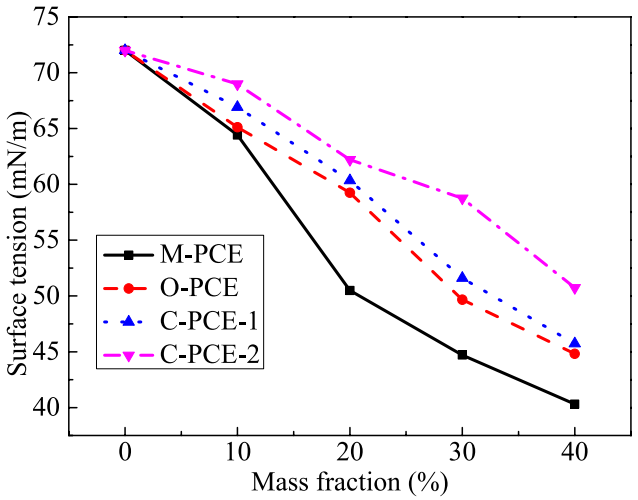

FIGURE 14 | The surface tension of polycarboxylates at different mass fractions.

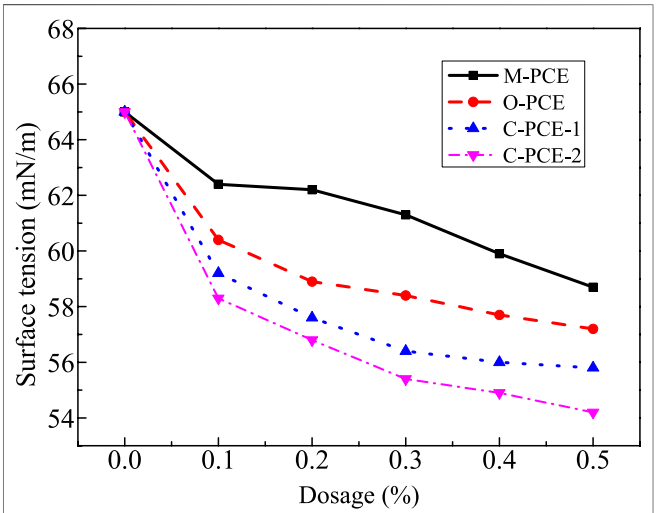

FIGURE 15 | Liquid surface tensions of polycarboxylate in cement pastes at varied dosages.

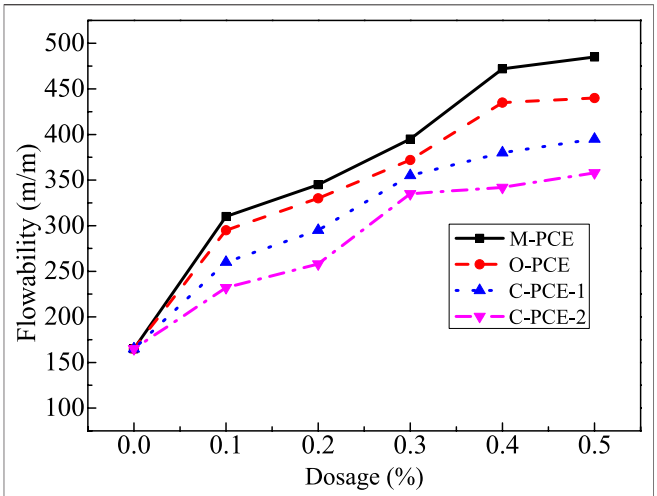

FIGURE 16 | Flowability of polycarboxylate.

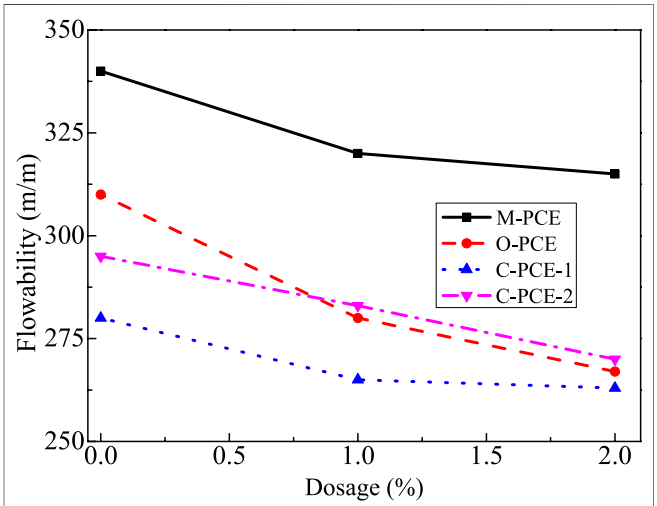

FIGURE 17 | Flowability retention of polycarboxylate (0.15% dosage).

while greater electrostatic barrier effect contributes to higher dispersibility (Plank and Hirsch, 2007).

Surface Tension

This study investigates the surface tension of polycarboxylates with different mass fractions and the effect of different polycarboxylate dosages on the liquid phase surface tension of Portland cement, with results shown in **Figures 14**, **15**.

It can be seen from **Figures 14**, **15** that, as the polycarboxylate mass fraction increases, the solution surface tension displays a continuous downward trend. It is because, under higher mass fraction, there are more hydrophobic groups in the solution, leading to declined surface tension. In addition, we found that M-PCE had the biggest decline in surface tension. From the point of view of liquid phase surface tension of Portland cement, the largest drop was observed after incorporation of M-PCE, with a decrease of 20.4%. For this reason, as the polycarboxylate dosage increases, polycarboxylate molecules cannot be adsorbed and maintained in the liquid phase, so there are more and more hydrophobic groups on the skeleton, such as long-chain alkyl groups, which are directionally aligned on the aqueous solution surface, leading to reduced surface tension of the liquid. M-PCE has the largest decrease in liquid surface tension because the organosiloxane group on the polyurethane side chain in its molecular structure has very strong hydrophobicity (Fan et al., 2012), resulting in its greater surface tension compared to other PCEs as its dosage in the cement increases.

Flowability

This study investigated the cement paste flowability of polycarboxylates under different dosages as well as flowability

retention under dosage of 0.15%, with results shown in **Figures 16**, **17**.

As shown in **Figures 16**, **17**, when the polycarboxylate content increases, the initial flowability of the cement paste increases sharply. As the M-PCE amount increases from 0 to 0.5%, the maximum increase in cement is about 193%. The enhanced dispersibility of M-PCE is due to the chemical bonds being induced by the siloxane groups in the M-PCE and silicate phase promoting the dispersibility of M-PCE (Yan et al., 2017). In addition, due to its chemical structure, M-PCE has longer side chains than PCE (Borget et al., 2005), so M-PCE has better dispersibility in cement, which is consistent with the results of Kong et al. (2015). Regarding the reason for the excellent dispersing ability, the siloxane groups in the polyurethane side chains produced by the hydrolysis of the alkoxy groups in the silane molecules act as anchoring groups, which facilitates the adsorption of silane molecules to cement particles. Moreover, the siloxane chain provides spatial repulsion between the cement particles, which enhances the dispersion effect. The anchoring effect of siloxane groups on cement or hydration products has been confirmed by the enhanced adsorption of silane-modified polycarboxylate superplasticizer in cement paste (Švegl et al., 2008). In addition, it was also found that although M-PCE had the biggest initial flowability, the four polycarboxylates exhibited good flowability retention.

CONCLUSION

The following conclusions could be drawn based on the above experimental results and discussions:

1) Appropriately increasing the molar ratio of acrylic acid to TPEG under the same circumstances will help improve polycarboxylate dispersion performance. The best indoor temperature synthesis process is as follows: n (TGA) = 0.01, n (H_2O_2): n (APS): n (Vc) = 15:1:1, n (AA): n (TPEG) = 2:1, and n (H_2O_2) = 0.05 mol.
2) Since the siloxane groups in Portland cement and polycarboxylate molecules form covalent bonds, M-PCE has higher adsorption than O-PCE and C-PCE, resulting in a higher adsorbability. In addition, compared with O-PCE and C-PCEs, the adsorption amount of M-PCE was increased by 14.1%, and the maximum adsorption rate was increased by 24%.
3) Under the same dosage, the incorporation of M-PCE had a promoting effect on the hydration of Portland cement. Due to the shielding effect of the long-chain alkyl group, O-PCE, C-PCE-1, and C -PCE-2 showed a certain hydration delay effect.
4) The Zeta potential value of M-PCE was negative, but its absolute value was higher than the Zeta potential of the other three polycarboxylates under the same circumstances, indicating that the Portland cement paste was more stable after incorporation of M-PCE.
5) As the PCE dosage increased, the liquid phase surface tension of Portland cement continually decreased, where M-PCE exhibited the smallest change. In terms of cement paste flowability and its retention, M-PCE showed the strongest dispersibility, which was also because the formation of hydrogen bonds in organosiloxane of M-PCE and Portland cement promoted the dispersibility of M-PCE.

DATA AVAILABILITY STATEMENT

The original contributions presented in the study are included in the article/Supplementary Material; further inquiries can be directed to the corresponding author.

AUTHOR CONTRIBUTIONS

SX conceptualized the study, was responsible for methodology, investigated the data, performed data curation and formal analysis, and wrote the original draft. YG was involved in project administration, funding acquisition, and supervision. YT revised the manuscript.

FUNDING

The authors gratefully acknowledge the financial support from National Natural Science Foundation of China (General Program:51978080), National Natural Science Foundation of China and Civil Aviation Administration of China (U1833127), Natural Science Foundation of Hunan Province (2021JJ40602) and Scientific Research Project of Hunan Provincial Department of Education(20B014).

REFERENCES

Borget, P., Galmiche, L., Le Meins, J.-F., and Lafuma, F. (2005). Microstructural Characterisation and Behaviour in Different Salt Solutions of Sodium Polymethacrylate-G-PEO Comb Copolymers. *Colloids Surf. A: Physicochemical Eng. Aspects* 260, 173–182. doi:10.1016/j.colsurfa.2005.03.008

Fan, W., Stoffelbach, F., Rieger, J., Regnaud, L., Vichot, A., Bresson, B., et al. (2012). A New Class of Organosilane-Modified Polycarboxylate Superplasticizers with Low Sulfate Sensitivity. *Cement Concrete Res.* 42 (1), 166–172. doi:10.1016/j.cemconres.2011.09.006

Hsu, K. C. (1999). Effect of Addition Time of a Superplasticizer on Cement Adsorption and on Concrete Workability. *Cem. Concr. Compos.* 21 (5-6), 425–430. doi:10.1016/s0958-9465(99)00030-x

Jiang, Z., Fang, Y., Guo, X., Lin, T., Guan, M., and You, R. (2013). Preparation of an Extra High-Concentration Polycarboxylate Superplasticizer. *New Build. Mater.* 3, 29–31.

Kong, F.-R., Pan, L.-S., Wang, C.-M., Zhang, D.-L., and Xu, N. (2016). Effects of Polycarboxylate Superplasticizers with Different Molecular Structure on the Hydration Behavior of Cement Paste. *Construction Building Mater.* 105, 545–553. doi:10.1016/j.conbuildmat.2015.12.178

Kong, X.-M., Liu, H., Lu, Z.-B., and Wang, D.-M. (2015). The Influence of Silanes on Hydration and Strength Development of Cementitious Systems. *Cement Concrete Res.* 67, 168–178. doi:10.1016/j.cemconres.2014.10.008

Lange, A., and Plank, J. (2016). Contribution of Non-adsorbing Polymers to Cement Dispersion. *Cement Concrete Res.* 79, 131–136. doi:10.1016/j.cemconres.2015.09.003

Li, C.-Z., Feng, N.-Q., Li, Y.-D., and Chen, R.-J. (2005). Effects of Polyethlene Oxide Chains on the Performance of Polycarboxylate-Type Water-Reducers. *Cement Concrete Res.* 35 (5), 867–873. doi:10.1016/j.cemconres.2004.04.031

Li, Y., Yang, C., Zhang, Y., Zheng, J., Guo, H., and Lu, M. (2014). Study on Dispersion, Adsorption and Flow Retaining Behaviors of Cement Mortars with TPEG-Type Polyether Kind Polycarboxylate Superplasticizers. *Construction Building Mater.* 64, 324–332. doi:10.1016/j.conbuildmat.2014.04.050

Liu, X., Wang, Z., Zhu, J., Zheng, Y., Cui, S., Lan, M., et al. (2014). Synthesis, Characterization and Performance of a Polycarboxylate Superplasticizer with Amide Structure. *Colloids Surf. A: Physicochemical Eng. Aspects* 448, 119–129. doi:10.1016/j.colsurfa.2014.02.022

Peng, J., Qu, J., Zhang, J., Chen, M., and Wan, T. (2005). Adsorption Characteristics of Water-Reducing Agents on gypsum Surface and its Effect on the Rheology of gypsum Plaster. *Cement Concrete Res.* 35 (3), 527–531. doi:10.1016/j.cemconres.2004.04.016

Plank, J., and Bian, H. (2010). Method to Assess the Quality of Casein Used as Superplasticizer in Self-Levelling Compounds. *Cement Concrete Res.* 40 (5), 710–715. doi:10.1016/j.cemconres.2010.01.005

Plank, J., and Hirsch, C. (2007). Impact of Zeta Potential of Early Cement Hydration Phases on Superplasticizer Adsorption. *Cement Concrete Res.* 37 (4), 537–542. doi:10.1016/j.cemconres.2007.01.007

Plank, J., Li, H., Ilg, M., Pickelmann, J., Eisenreich, W., Yao, Y., et al. (2016). A Microstructural Analysis of Isoprenol Ether-Based Polycarboxylates and the Impact of Structural Motifs on the Dispersing Effectiveness. *Cement Concrete Res.* 84, 20–29. doi:10.1016/j.cemconres.2016.02.010

Plank, J., Pöllmann, K., Zouaoui, N., Andres, P. R., and Schaefer, C. (2008). Synthesis and Performance of Methacrylic Ester Based Polycarboxylate Superplasticizers Possessing Hydroxy Terminated Poly(ethylene Glycol) Side Chains. *Cement Concrete Res.* 38 (10), 1210–1216. doi:10.1016/j.cemconres.2008.01.007

Schmid, M., and Plank, J. (2021). Interaction of Individual Meta Clays with Polycarboxylate (PCE) Superplasticizers in Cement Investigated via Dispersion, Zeta Potential and Sorption Measurements. *Appl. Clay Sci.* 207, 106092. doi:10.1016/j.clay.2021.106092

Scrivener, K. L., and Nonat, A. (2011). Hydration of Cementitious Materials, Present and Future. *Cement Concrete Res.* 41, 651–665. doi:10.1016/j.cemconres.2011.03.026

Švegl, F., Šuput-Strupi, J., Škrlep, L., and Kalcher, K. (2008). The Influence of Aminosilanes on Macroscopic Properties of Cement Paste. *Cem. Concr. Res.* 38, 945–954. doi:10.1016/j.cemconres.2008.02.006

Wang, B., and Wang, L. (2003). Effects of Super Retarder on the Hydration of Portland Cement. *J. Building Mater.* 6 (1), 90–94. doi:10.3969/j.issn.1007-9629.2003.01.018

Wang, Z. M. (2009). "Polycarboxylate Superplasticizer-Preparation ● Performance and Application (In Chinese)," in *Preparation of High Performance Polycarboxylate* (Beijing: China Architecture & Building Press), 123–137.

Yan, He., Zhang, X., and Hooton, R. D. (2017). Effects of Organosilane-Modified Polycarboxylate Superplasticizer on the Flowability and Hydration Properties of Cement Paste[J]. *Constr. Build. Mater.* 132, 112–123. doi:10.1016/j.conbuildmat.2016.11.122

Yang, Y., Ran, Q. P., Liu, J. P., Zhang, Z. Y., and Miao, C. W. (2011). Synthesis of Comb-Branched Polycarboxylate Superplasticizers. *New Build. Mater.* 7, 54–57. doi:10.3969/j.issn.1001-702X.2011.07.017

Ylmén, R., Jäglid, U., Steenari, B.-M., and Panas, I. (2009). Early Hydration and Setting of Portland Cement Monitored by IR, SEM and Vicat Techniques. *Cement Concrete Res.* 39 (5), 433–439. doi:10.1016/j.cemconres.2009.01.017

Ylmén, R., Wadsö, L., and Panas, I. (2010). Insights into Early Hydration of Portland limestone Cement from Infrared Spectroscopy and Isothermal Calorimetry. *Cement Concrete Res.* 40 (10), 1541–1546. doi:10.1016/j.cemconres.2010.06.008

Yu, B., Zeng, Z., Ren, Q., Chen, Y., Liang, M., and Zou, H. (2016). Study on the Performance of Polycarboxylate-Based Superplasticizers Synthesized by Reversible Addition-Fragmentation Chain Transfer (RAFT) Polymerization. *J. Mol. Struct.* 1120, 171–179. doi:10.1016/j.molstruc.2016.05.035

Zhang, Y., and Kong, X. (2015). Correlations of the Dispersing Capability of NSF and PCE Types of Superplasticizer and Their Impacts on Cement Hydration with the Adsorption in Fresh Cement Pastes. *Cement Concrete Res.* 69, 1–9. doi:10.1016/j.cemconres.2014.11.009

Zhou, X., Fang, C., Lei, W., Su, J., Li, L., and Li, Y. (2017). Thermal and Crystalline Properties of Waterborne Polyurethane by *In Situ* Water Reaction Process and the Potential Application as Biomaterial. *Prog. Org. Coat.* 104, 1–10. doi:10.1016/j.porgcoat.2016.12.001

Conflict of Interest: The authors declare that the research was conducted in the absence of any commercial or financial relationships that could be construed as a potential conflict of interest.

Publisher's Note: All claims expressed in this article are solely those of the authors and do not necessarily represent those of their affiliated organizations, or those of the publisher, the editors, and the reviewers. Any product that may be evaluated in this article, or claim that may be made by its manufacturer, is not guaranteed or endorsed by the publisher.

frontiers in Materials

MINI REVIEW
published: 13 September 2021
doi: 10.3389/fmats.2021.725422

Biaxial Stretching of Polymer Nanocomposites: A Mini-Review

Xiaoyu Chen[1], Dong Xiang[1], Zuoxin Zhou[2]*, Yuanpeng Wu[1], Hui Li[1], Chunxia Zhao[1] and Yuntao Li[1]*

[1]School of New Energy and Materials, Southwest Petroleum University, Chengdu, China, [2]Centre for Additive Manufacturing, Faculty of Engineering, University of Nottingham, Nottingham, United Kingdom

Polymer nanocomposites with excellent physical and chemical properties and multifunctional performance have been widely used in various fields. Biaxial stretching is not only an advanced film manufacturing process, but also a deformation mode in other processing methods such as blow film extrusion and thermoforming. In recent research, high-performance polymer nanocomposites have been fabricated *via* sequential and simultaneous biaxial stretching. This fabrication method enhances the mechanical properties, optical performance, and thermal properties of polymer nanocomposites by changing the structure or orientation of materials during the process of stretching. Therefore, it is particularly suitable for use in optimizing material performance and preparing thin films with excellent properties in the packaging industry. With the emergence of new materials and technologies, polymer nanocomposites prepared by biaxial stretching have demonstrated multifunctional properties and their range of applications has further expanded. In this mini-review, the effect of biaxial stretching on the structure and properties of nanocomposites based on various nanofillers is discussed and applications are summarized. In addition, the challenges and future prospects of this technology are analyzed. The presented work will be beneficial for improving preparation processes and improving future research for the production of high-performance polymer nanocomposites.

Keywords: biaxial stretching, polymer, nanocomposites, nanofillers, orientation

OPEN ACCESS

Edited by:
Andreas J. Brunner, Retired, Zürich, Switzerland

Reviewed by:
Jianfeng Wang, Zhengzhou University, China
Pei Huang, Chongqing University, China
Souvik Chakraborty, Clausthal University of Technology, Germany

****Correspondence:***
Dong Xiang
dxiang01@hotmail.com
Zuoxin Zhou
alfredzhou61@hotmail.com

Specialty section:
This article was submitted to Polymeric and Composite Materials, a section of the journal Frontiers in Materials

Received: *15 June 2021*
Accepted: *01 September 2021*
Published: *13 September 2021*

Citation:
Chen X, Xiang D, Zhou Z, Wu Y, Li H, Zhao C and Li Y (2021) Biaxial Stretching of Polymer Nanocomposites: A Mini-Review. Front. Mater. 8:725422. doi: 10.3389/fmats.2021.725422

INTRODUCTION

Over the years, polymer composites reinforced with nanofillers have attracted significant attention. These materials are widely applied in medical equipment, electronics, and aerospace applications, and are used in wearable electronic devices, electromagnetic interference shielding, and for antistatic protection (Oladele et al., 2020; Guo et al., 2021). Nanofillers can provide polymers with new functionalities such as high electrical conductivity, dielectric properties, and a unique response to stimulation by light, thermal, pH, or magnetic fields. There may be slippage between surfaces of individual nanofillers in the absence of adhesive and polymers can be used as an adhesive to fix the nanofiller directional position and transfer the load between nanofillers efficiently (Christian et al., 2019). However, polymer nanocomposites produced by traditional synthesis methods such as solution processing, extrusion, or calendaring are always randomly oriented, which limits their properties. Improving the dispersion of nanofillers in polymer matrices and enhancing interface adhesion between the nanofiller and matrix are crucial strategies for the preparation of high-performance polymer nanocomposites (Lavagna et al., 2020; Min et al., 2020).

It is known that the improvement of polymeric mechanical properties *via* chain orientation is a simple and efficient strategy. Methods for achieving this include biaxial stretching, blow molding, extrusion, and melt spinning. Compared to conventional methods, the biaxial stretching process results in a high degree of orientation and regular alignment of chains by intermolecular friction (Li et al., 2020). The structure, orientation degree, and surface morphology of polymers can be changed by adjusting the stretching ratio (SR) of biaxial stretching to enhance strength and tensile modulus in the oriented direction (Soon et al., 2012; Mayoral et al., 2021). Molecular alignment of amorphous polymer chains in the oriented direction and strain-induced crystallization are also influenced by biaxial tension (Delpouve et al., 2012; Ouchiar et al., 2016; Van Berkel et al., 2018). Generally, the degree of molecular orientation, amount of strain-induced crystallization, and extent of amorphous chain confinement all affect the barrier performance and thermomechanical properties of polymer nanocomposites (Delpouve et al., 2012; Mayoral et al., 2021). Another benefit of biaxial stretching is the ability to disperse nanofillers in the polymer matrix without using compatibilizers (Xiang et al., 2015). Therefore, biaxial stretching is particularly suitable for use in optimizing polymer material performance and preparing thin films with excellent properties in the packaging industry.

Biaxial tension is not only an advanced composite manufacturing process, but also a deformation mode in other processing methods, such as blow film extrusion (Espinosa et al., 2016) and thermoforming (Mayoral et al., 2021). Moreover, the use of biaxial stretching in changing the structure, dispersion, and orientation of neat polymer materials to enhance performance has been widely studied for polymers including biaxially oriented polypropylene (Xing et al., 2019), biaxially oriented polyethylene (Chen et al., 2020), and biaxially oriented polyethylene terephthalate (Onyishi and Oluah, 2020). However, there is significantly less research on the performance and applications of biaxially oriented polymer nanocomposites.

This mini-review summarizes the effect of biaxial stretching on the structure and properties of polymer nanocomposites. The application of biaxially stretched polymer nanocomposites in the packaging industry is outlined and reported data of polymer nanocomposites in field applications are described and discussed. Moreover, the advances and challenges of producing polymer nanocomposites *via* biaxial stretching method are outlined.

BIAXIAL STRETCHING OF POLYMER NANOCOMPOSITES

With unique optical, electrical, thermal, and mechanical properties, nanomaterials have been reported as reinforcing materials for the fabrication of multifunctional nanocomposites combined with the process of biaxial stretching.

Polymer/Clay Nanocomposites

Polymer/clay nanocomposites, also known as polymer/layered silicate nanocomposites, have excellent electrical conductivity, magnetic properties, and thermal insulation properties. Moreover, the addition of clay can reduce gas permeability and flammability as well as improve mechanical properties (Singha and Hedenqvist, 2020; Kovačević et al., 2021). The Toyota Company produced a nylon 6/clay nanocomposite, finding a significant enhancement in modulus and strength with the addition of clay (Kojima et al., 1993). The most commonly used clays include saponite, montmorillonite (Liu et al., 2018), and hectorite. **Figure 1A** shows a schematic of biaxial stretching modes including simultaneous and sequential biaxial stretching. Taking clay/polymer nanocomposites as an example, **Figures 1B–F** illustrate the effect of biaxial stretching on the morphology and properties of clay/polymer nanocomposites.

The properties of polymer/clay nanocomposites mainly depend on the degree of exfoliation, content, and orientation of the clay (Chowreddy et al., 2019; Maria et al., 2011). From **Figures 1B,C**, it can be seen that for the biaxial stretching process of clay-filled nanocomposites, the initial biaxial tension causes the delamination of clay tactoids. Subsequent stretching reduces stack thickness, indicating that a higher degree of exfoliation occurred as SR increasing, and uniformly dispersed clay nanoparticles have an oriented arrangement in the direction of stretching. A 44% improvement in yield stress for 5 wt% clay-filled PP compared with pure PP at the same SR has been demonstrated (Abu-Zurayk et al., 2009). Furthermore, orientation distribution also becomes narrower with increasing SR (Abu-Zurayk et al., 2010). The presence of clay agglomeration can decrease the tensile properties of nanocomposites, which are more affected by the orientation of clay tactoids than the dispersion degree (Wang et al., 2007). **Figure 1D** shows that the addition of clay and biaxial tension does not enhance the tensile modulus of the composites until SR = 2.5 due to the presence of large tactoids under low strain tension, which has no effect on the tensile properties of the PP/clay nanocomposites. With an increase in SR above 2.5, the clay nanoparticle degree of orientation and degree of exfoliation increase, improving the tensile properties of the composites.

Soon et al. (2012) studied the morphology, mechanical properties, and barrier properties of biaxially stretched polyethylene terephthalate (PET)/mica nanocomposites, finding that the tensile process promoted the orientation and exfoliation of mica. The mechanical properties of the nanocomposites increased with an increase in SR. Furthermore, barrier properties improved with the addition of mica and the effect of drawing. Wu et al. (2015) also compared the tensile properties, optical performances, gas barrier properties, water vapor barrier properties, and cold crystallization behavior of biaxially stretched PET/clay, Poly (ethylene glycol-co-1,3/1,4-cyclohexanedimethanol terephthalate) (PETG)/clay, and PET/PETG/clay nanocomposite films. A significant enhancement in tensile, optical, and gas barrier properties was achieved due to the improved dispersion and orientation degree of clay platelets during the biaxial stretching process. Biaxial stretching improved the oxygen transmission rate performance of the PET/clay, PETG/clay, and PET/PETG/clay nanocomposite films by approximately 18, 45, and 34%, respectively, shown in

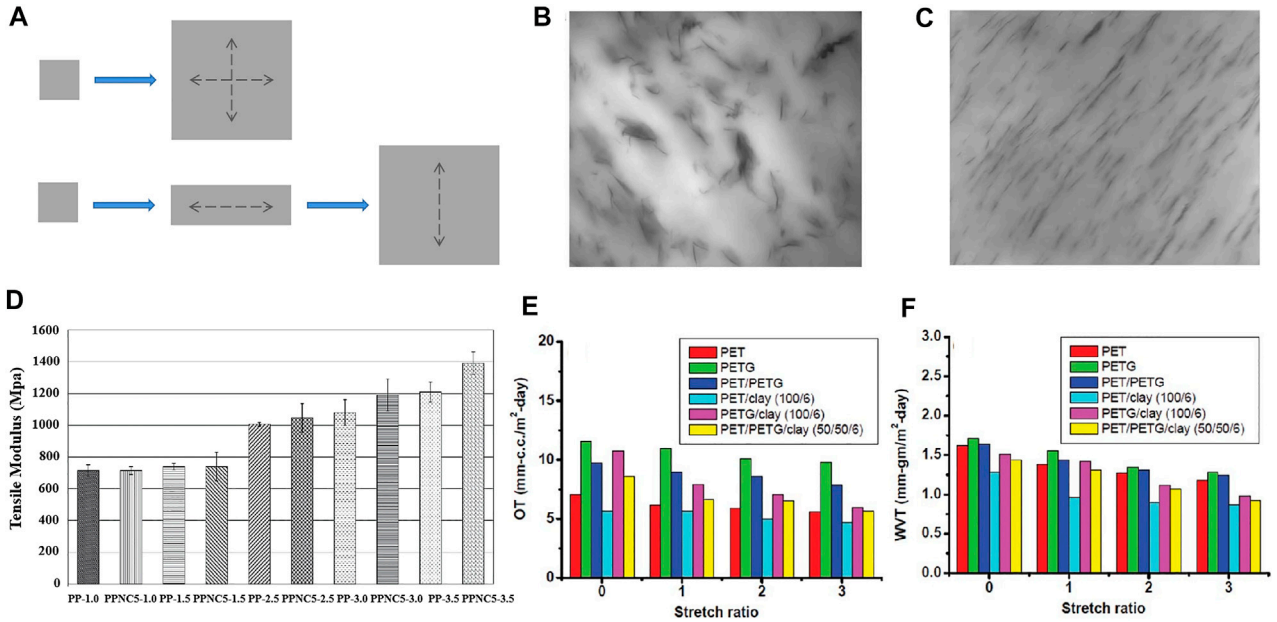

FIGURE 1 | (A) Schematic of biaxial stretching modes (SR = 3). TEM images: **(B)** unstretched sheet, **(C)** stretched sheet (SR = 3), magnification = 28,500, scale bar = 500 nm. **(D)** Tensile modulus of PP/clay nanocomposites (Abu-Zurayk et al., 2009). Effect of SR on **(E)** oxygen transmission rate and **(F)** water vapor transmission rate of biaxially stretched PET/clay, PETG/clay, and PET/PETG/clay nanocomposites (Wu et al., 2015).

Figure 1E. The water vapor transmission rate performance of PET/clay, PETG/clay, and PET/PETG/clay was improved by 32, 35, and 35%, respectively, shown in **Figure 1F**. Moreover, the biaxial tension process triggered a strain-induced crystallization in the amorphous PETG matrix and PET/PETG composite.

Polymer/Carbon Nanocomposites

With extraordinary electrical, mechanical, and thermal properties, carbon nanotubes (CNTs) have been widely studied since their first discovery (Iijima, 1991). CNTs are an ideal functional and reinforcing material, with ultra-strong mechanical properties that significantly improve the strength and toughness of polymer nanocomposites. The unique photoelectric properties of CNTs can also endow polymer nanocomposites with new photoelectric functionalities. The development of carbon nanotube networks in CNT/PP nanocomposites demonstrated a unique process of destruction and rebuilding of a conductive network during simultaneous biaxial stretching (Shen et al., 2012a; Shen et al., 2012b). Xiang et al. (2018) prepared multiwalled carbon nanotube/high-density polyethylene (MWCNT/HDPE) nanocomposites, showing that the processability and deformation stability of HDPE was significantly enhanced with the addition of carbon nanofillers (4 wt%) upon biaxial stretching (**Table 1**). At an SR of 3, the resistivity of a biaxially stretched MWCNT/HDPE nanocomposite increased by ~10^8 compared with an unstretched sample, indicating that biaxial deformation resulted in the damage of conductive pathways in the composite material while interlacing or entanglement of the 1D MWCNTs was beneficial for rebuilding conductive network.

Furthermore, uniaxially, sequential (seq-) biaxially, and simultaneous (sim-) biaxially stretched neat HDPE and MWCNT/HDPE nanocomposites were conducted to study the processability of HDPE with the addition of 4 wt% MWCNTs and the effect of tension on the final structure and properties of nanocomposites, as shown in **Table 1**. It showed that sequential biaxial stretching improved the tensile properties of nanocomposites effectively, due to more agglomerate disentanglement during stretching. A similar phenomenon had been reported for PP/CNT composite by Shen et al. (2012a). While the tensile properties of simultaneous biaxially stretched nanocomposites can be improved *via* reducing the strain rate, due to more disentanglement of the MWCNTs at a lower strain rate, therefore the resistivity of simultaneous biaxially stretched composites stretched at a lower strain rate increased by 10^{11} Ω cm (Xiang et al., 2015).

Graphene nanoplatelets (GNPs) are another exceptional two-dimensional carbon nanofiller. GNPs consist of single-atom thickness sp^2 hybrid carbon sheets and have excellent mechanical and electrical properties (Pei et al., 2021; Wang and Shi, 2015; Yang B. et al., 2020). A biaxially stretched GNP/HDPE nanocomposite exhibited a 63% enhancement to Young's modulus, with the oxygen permeability coefficient reduced to only 4.1 × 10^{-16} cm^3 cm/cm^2 s Pa at SR = 3, as shown in **Table 1**. Liu et al. (2020) prepared a polydimethylsiloxane (PDMS)/GNP composite film near the threshold concentration, finding that biaxial stretching effectively enhanced the sensitivity of the PDMS/GNP composite film by an order of magnitude compared with traditional uniaxial stretching. Traditionally prepared

TABLE 1 | Effect of carbon nanofillers on the mechanical, electrical, and barrier properties of uniaxially, seq-biaxially, and sim-biaxially stretched polymeric nanocomposites.

Sample	Filler content (wt%)	Stretching mode	SR	Electrical resistivity (Ω·cm)	ΔE (%)	Δs_b (%)	Δe_b (%)	Change in oxygen permeability (%)	Ref
PP/CNT	5	Seq-biaxial stretching	1.0 × 1.0	~10^4	—	—	—	—	Shen et al. (2012a)
			2.2 × 2.2	~10^{10}					
			3.5 × 3.5	~10^3					
		Sim-biaxial Stretching	2.2 × 2.2	~10^{11}					
			3.5 × 3.5	~10^5					
PP/CNT	5	Uni-stretching	1.8 × 1.0	~10^{12}	—	—	—	—	Shen et al. (2012b)
			2.2 × 1.0	~10^{12}					
			4.3 × 1.0	~10^{12}					
		Sim-biaxial Stretching	1.8 × 1.8	~10^8					
			2.2 × 2.2	~10^{11}					
			4.3 × 4.3	~10^4					
HDPE/ MWCNT	4	Sim-biaxial Stretching	1.0 × 1.0	~10^1	+111.6	−40.5	−94.8	−5	Xiang et al. (2018)
			2.0 × 2.0	~10^5	+15.4	−3.4	−52.6	—	
			2.5 × 2.5	~10^4	+17.6	−33.2	−27.0	—	
			3.0 × 3.0	~10^{10}	+40.0	+75.5	−71.6	−10	
HDPE/GNP	4	Sim-biaxial Stretching	1.0 × 1.0	~10^{14}	+125.5	−15.4	−98.6	−64	
			2.0 × 2.0	~10^{15}	+46.0	+49.2	−54.3	—	
			2.5 × 2.5	~10^{15}	+45.6	−16.6	−12.4	—	
			3.0 × 3.0	~10^{15}	+63.1	+139.5	−65.6	−100	
HDPE/CB	4	Sim-biaxial Stretching	1.0 × 1.0	~10^3	+29.7	−40.1	−97.0	−5	
			2.0 × 2.0	~10^{12}	+6.9	+68.7	−3.2	—	
			2.5 × 2.5	~10^{13}	+11.4	+24.9	+20.3	—	
			3.0 × 3.0	~10^{13}	+15.4	+204.4	−53.6	−10	
HDPE/ MWCNT	4	Uni-stretching	1.0 × 1.0	~10^1	—	—	—	—	Xiang et al. (2015)
			3.0 × 1.0	~10^8	+136	+154	−87		
		Seq-biaxial stretching	3.0 × 3.0	~10^{13}	+63	+97	−57		
		Sim-biaxial stretching	3.0 × 3.0	~10^{10}	+40	+76	−72		

Changes in values are defined by comparing with neat polymer at corresponding SRs. + and - represent an increase or decrease relative to neat polymer, respectively.
Note: ΔE, $\Delta\sigma_b$ and $\Delta\varepsilon_b$ represent the changes in Young's modulus, stress at break, and strain at break, respectively.

GNP/polymer nanocomposites often have poor dispersion, while the shear force during biaxial stretching is beneficial to improve the dispersion of nanofillers in polymer matrices (Shen et al., 2011).

As an amorphous carbon nanoparticle, carbon black (CB) has the characteristics of disordered graphite-like structure, small particle size, good conductivity, and strong ultraviolet absorption. CB/polymer nanocomposites with good mechanical, thermal, electrical, and chemical properties (Kausar, 2017; Azizi et al., 2019), are widely used in solar cells (Yue et al., 2016), supercapacitors (Xing et al., 2015), sensors (Yang H. et al., 2020), and electromagnetic shielding (Zhang et al., 2021). The morphology and dispersion state of CB particles are important factors affecting the properties of polymer composites. During biaxial tension, clustered CB can disperse more evenly in a polymer matrix. Compared with biaxially stretched pure HDPE, the stress at break (σ_b) of a biaxially stretched CB/HDPE nanocomposite at the same SR increased by 204% due to the intensive breakup of CB clusters (**Table 1**).

In conclusion, material processability, electrical properties, and barrier properties are affected by different carbon nanofillers, and biaxial tension affects the structure and properties of polymer/carbon nanocomposites. Moreover, there is also some research investigating the synergetic effect of hybrid carbon nanofillers to further improve the mechanical, tensile, barrier, and electrical properties of polymer nanocomposites with lower cost (Xiang et al., 2017; Xiang et al., 2020).

Polymer/Oxide Nanocomposites

The introduction of oxide nanoparticles to a polymer matrix for the enhancement of physical and mechanical properties has been widely studied. Uniformly dispersed nanoparticles can improve Young's modulus, tensile strength, conductivity, and thermal capacity as well as significantly decrease polymer combustibility (Benabid et al., 2019; Deepalekshmi et al., 2019). However, these nanofillers may also result in increasing rigidity, leading to fractures or cracks and causing the degradation of the composite material's properties (Tang et al., 2020; Goncharova Daria et al., 2021).

A study investigating the effect of biaxial orientation on the mechanical performances of PP/ZnO nanocomposites found that the addition of ZnO nanoparticles increased the polymer's yield point, but biaxial orientation at a higher degree of deformation allowed the plasticity of the polymer nanocomposites to be maintained if a high content of ZnO nanoparticles were incorporated into the polymer matrix (Kechek'yan et al.,

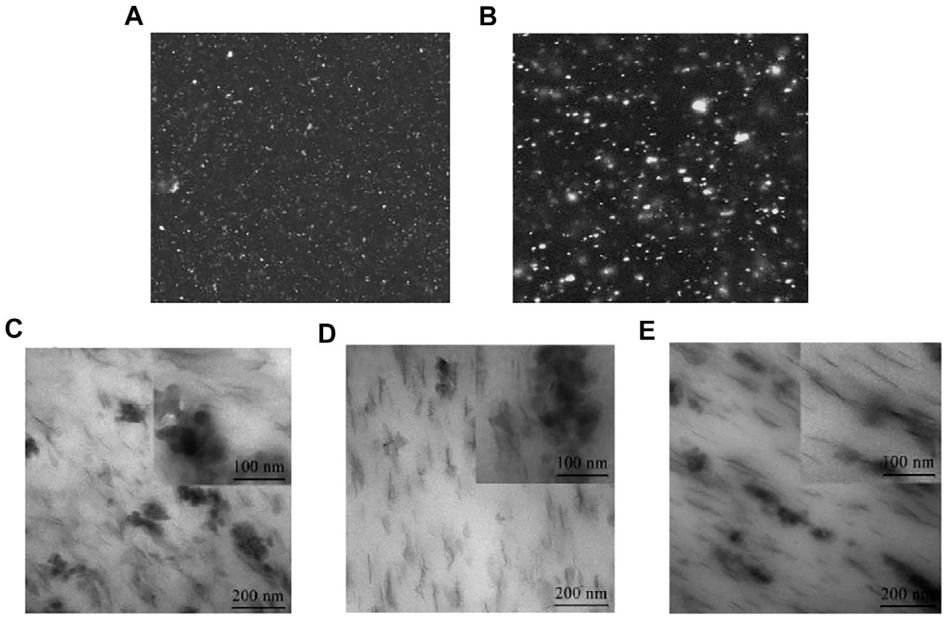

FIGURE 2 | SEM images **(A)** Surface of ZnO-BOPP nanocomposite with spherical ZnO. **(B)** Cross-section of ZnO-BOPP nanocomposite (Lepot et al., 2011). TEM images of the **(C)** unstretched (1.0 × 1.0), **(D)** uniaxially stretched (3.0 × 1.0), and **(E)** biaxially stretched (3.0 × 2.0) PA6-66-MMT-NS films (Liu et al., 2019).

TABLE 2 | The relative crystallinity (X_c), tensile strength, and thermal shrinkage of uniaxially and biaxially stretched PA6-66-MMT-nanosilica composites.

Stretching mode	SR	X_c (%)	Tensile strength (MPa)	Thermal shrinkage (%)	Ref
Uniaxial stretching	1.0 × 1.0	18.71	73.1	~0.6	Liu et al. (2019)
	1.5 × 1.0	18.81	~85.0	~2.1	
	2.0 × 1.0	20.34	~115.0	~3.1	
	3.0 × 1.0	20.51	~155.0	~5.0	
	4.0 × 1.0	22.07	245.1	~6.1	
Biaxial stretching	1.5 × 1.5	19.55	~85.0	~2.6	
	2.0 × 2.0	20.60	~80.0	~7.3	
	3.0 × 3.0	21.18	~125.0	~11.0	

2018). Lepot et al. (2011) investigated the effect of introducing 0, 2, 5, and 7.5 wt% ZnO nanoparticles on the processing and properties of biaxially oriented polypropylene (BOPP)-ZnO nanocomposites, finding that the addition of ZnO nanoparticles improved mechanical and oxygen barrier properties of BOPP-ZnO nanocomposites. **Figures 2A,B** showed that the BOPP-ZnO films with 5 wt% ZnO had a good dispersion.

Uniaxially and biaxially stretched PA6-66-MMT-nanosilica composite films were prepared through a cast film process, finding that tension led to an oriented conformation of the MMT and nanosilica, as shown in **Figures 2C,E**.

From **Table 2**, for the uniaxially stretched films, the tensile strength in the stretching direction gradually increased with increasing SR, and the biaxially stretched nanocomposite films showed more balanced mechanical properties and thermal shrinkage along the machine direction and transverse direction compared with the uniaxially stretched composite (Liu et al., 2019).

In conclusion, reinforced polymer/oxide materials combined with biaxial stretching can effectively enhance nanocomposite properties.

APPLICATIONS

The application classification of biaxially stretched nanocomposites is shown in **Figure 3**. The development of new polymer films for packaging and agricultural applications has recently attracted significant attention (Liu et al., 2014; Lai et al., 2020; Zhou et al., 2020). Studies have shown that the barrier properties and mechanical properties of polymer nanocomposites are enhanced after being biaxially stretched into films. Due to this, biaxially stretched polymer nanocomposites are widely used in the packaging industry (Shen et al., 2011; Youm et al., 2020; Li et al., 2021). Biodegradable polymers such as poly (butylene adipate-co-terephthalate) (PBAT) have the advantage of low

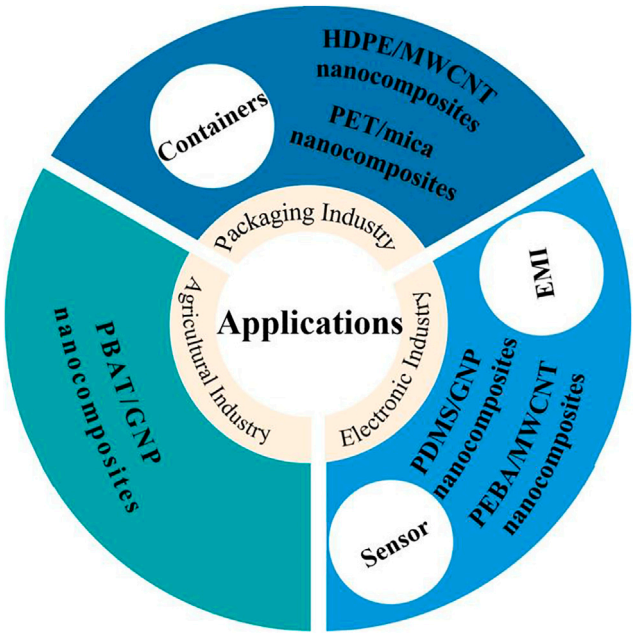

FIGURE 3 | Applications of biaxially stretched nanocomposites.

environmental impact, but poor oxygen permeation and water vapor barrier properties limit their practical application (Falcão et al., 2017; Roy and Rhim, 2020). Well-dispersed and oriented nanofillers, such as GNPs and organically modified montmorillonite (OMMT), can efficiently improve the barrier properties of nanocomposites *via* biaxial stretching, revealing a promising solution (Xiang et al., 2017; Li et al., 2018). By way of example, Li et al. (2018) prepared a series of 0–13 wt% PBAT/OMMT nanocomposite films *via* film blowing and biaxial stretching, finding that the addition of 13 wt% OMMT significantly reduced water vapor permeation values and two technologies enhanced in-plane polymer chain alignment, which aligns OMMT particles. Furthermore, OMMT layers were better oriented parallel to film surfaces with biaxial orientation, indicating that biaxial stretching had the ability to improve the water vapor barrier properties more effectively. Also, research into PBAT/GNP nanocomposite films prepared by biaxially stretched orientation and rod scraping demonstrate that these films possess good barrier properties, UV-blocking properties, and aging performance (Li et al., 2021). These studies demonstrate the potential for the use of biaxially oriented and biodegradable nanocomposites in sustainably developed packaging and the agricultural industry. Moreover, biaxially stretched nanocomposites reinforced by nanometer-scale materials have the advantage of high transparency compared with the use of other fillers. Compared with traditional packaging materials, food and beverage packaging products produced with PET-mica nanocomposites are lighter. In addition, mica loadings (1, 2, and 5 wt%) have been shown to improve the mechanical properties of PET at high temperatures, which can be applied for hot filling of containers (Soon et al., 2012).

Some research into the application of biaxially stretched polymer nanocomposites in sensors and electromagnetic interference (EMI) shielding has also been published. For instance, a sensor prepared near the threshold concentration (0.98 wt%) based on GNP/PDMS composite was reported for monitoring human motion. Biaxial stretching was shown to efficiently improve the sensitivity (gauge factor (GF) = 687.43) of the GNP/PDMS composite compared with uniaxially stretched sample (GF = 68.81). Furthermore, the biaxially stretched sensor showed excellent signal responses to various bending degrees of knee joint (Liu et al., 2020). The application of nanocomposite films assisted by biaxial stretching in EMI shielding has been studied recently. Wang et al. (2021) prepared nanocellular MWCNT/poly (ether-block-amide) (PEBA) nanocomposite films for high-performance EMI shielding applications with the assistance of biaxial stretching, finding that MWCNTs and biaxial stretching caused a greatly refined cellular structure. The cellular structure became more obviously refined with the increasing SR, leading to enhanced EMI shielding performance (shielding effectiveness up to 41 dB) and electrical conductivity. In addition, the conductive and flexible MWCNT/PEBA nanocomposite film with excellent absorption-dominated EMI shielding performance has potential in other applications such as lightning strike protection in aerospace due to the similar requirement on electrical conductivity.

DISCUSSION

According to literature, the orientation and structural changes of polymeric nanocomposites caused by the biaxial stretching process are clearly beneficial for enhancing material properties. Biaxial stretching can also be used to enhance the performance of more materials and their composites. Although sequential biaxial stretching and simultaneous biaxial stretching have been used to fabricate various polymer nanocomposites, there is still potential for optimization. To design multifunctional polymer nanocomposites, biaxial stretching and structure design can be combined.

Overall, the field of biaxially oriented polymer matrix nanocomposites is still in its infancy. The future development direction of biaxially oriented polymer nanocomposites should focus on optimizing the preparation process, reducing production costs, and improving the compatibility between nanofillers and polymer matrices. Furthermore, the potential application of biaxially oriented polymer nanocomposites in many fields has not been widely studied. Polymer nanocomposites prepared by biaxial stretching have significant potential practical value and broad development prospects.

CONCLUSION

In this mini-review, the effect of biaxial stretching on the properties of polymer composites with different nanofillers has been summarized. A suitable stretching ratio and careful choice of nanofiller can provide polymer nanocomposite materials with a unique structure and surface morphology as well as a high orientation degree to enhance mechanical, electrical, and

barrier properties. As multifunctional high-performance materials, biaxially stretched polymer nanocomposites have a significant potential for application in the fields of packaging, strain sensors, and capacitors.

AUTHOR CONTRIBUTIONS

XC as the main writer of the mini-review, completed the collection and analysis of relevant literature and the writing of the first draft of the paper; YW, HL, CZ, and YL participate in the analysis and collation of literature; DX and ZZ are the designers and directors of the mini-review, guiding the mini-review writing. All authors read and agree to the final mini-review.

FUNDING

This work was also supported within the framework of the National Key Research and Development Program (2019YFE0120300), the Sichuan Science and Technology Program (2021YFH0031), the International Cooperation Project of Chengdu (2019-GH02-00054-HZ) and the Scientific Research Starting Project of SWPU (2019QHZ011).

ACKNOWLEDGMENTS

The authors thank University of Nottingham for the support of this work.

REFERENCES

Abu-Zurayk, R., Harkin-Jones, E., Mcnally, T., Menary, G., Martin, P., and Armstrong, C. (2009). Biaxial Deformation Behavior and Mechanical Properties of a Polypropylene/clay Nanocomposite. *Composites Sci. Tech.* 69, 1644–1652. doi:10.1016/j.compscitech.2009.03.014

Abu-Zurayk, R., Harkin-Jones, E., Mcnally, T., Menary, G., Martin, P., Armstrong, C., et al. (2010). Structure-property Relationships in Biaxially Deformed Polypropylene Nanocomposites. *Composites Sci. Tech.* 70, 1353–1359. doi:10.1016/j.compscitech.2010.04.011

Azizi, S., David, E., Fréchette, M. F., Nguyen-Tri, P., and Ouellet-Plamondon, C. M. (2019). Electrical and thermal Phenomena in Low-Density Polyethylene/carbon Black Composites Near the Percolation Threshold. *J. Appl. Polym. Sci.* 136, 47043. doi:10.1002/app.47043

Benabid, F., Kharchi, N., Zouai, F., Mourad, A.-H. I., and Benachour, D. (2019). Impact of Co-mixing Technique and Surface Modification of ZnO Nanoparticles Using Stearic Acid on Their Dispersion into HDPE to Produce HDPE/ZnO Nanocomposites. *Polym. Polym. Composites* 27, 389–399. doi:10.1177/0967391119847353

Chen, Q., Wang, Z., Zhang, S., Cao, Y., and Chen, J. (2020). Structure Evolution and Deformation Behavior of Polyethylene Film during Biaxial Stretching. *ACS omega* 5, 655–666. doi:10.1021/acsomega.9b03250

Chowreddy, R. R., Nord-Varhaug, K., and Rapp, F. (2019). Recycled Poly(Ethylene Terephthalate)/Clay Nanocomposites: Rheology, Thermal and Mechanical Properties. *J.Polym. Environ.* 27, 37–49. doi:10.1007/s10924-018-1320-6

Delpouve, N., Stoclet, G., Saiter, A., Dargent, E., and Marais, S. (2012). Water Barrier Properties in Biaxially Drawn Poly(lactic Acid) Films. *J. Phys. Chem. B.* 116, 4615–4625. doi:10.1021/jp211670g

Espinosa, K. R., Castillo, L. A., and Barbosa, S. E. (2016). Blown Nanocomposite Films from Polypropylene and Talc. Influence of Talc Nanoparticles on Biaxial Properties. *Mater. Des.* 111, 25–35. doi:10.1016/j.matdes.2016.08.045

Falcão, G. A. M., Vitorino, M. B. C., Almeida, T. G., Bardi, M. A. G., Carvalho, L. H., and Canedo, E. L. (2017). PBAT/organoclay Composite Films: Preparation and Properties. *Polym. Bull.* 74, 4423–4436. doi:10.1007/s00289-017-1966-6

Goncharova, D. A., Bolbasov, E. N., Nemoykina, A. L., Aljulaih, A. A., Tverdokhlebova, T. S., Kulinich, S. A., et al. (2021). Structure and Properties of Biodegradable PLLA/ZnO Composite Membrane Produced via Electrospinning. *Materials* 14, 2–13. doi:10.3390/MA14010002

Guo, Z., Poot, A. A., and Grijpma, D. W. (2021). Advanced Polymer-Based Composites and Structures for Biomedical Applications. *Eur. Polym. J.* 149, 110388. doi:10.1016/J.EURPOLYMJ.2021.110388

Harito, C., Bavykin, D. V., Yuliarto, B., Dipojono, H. K., and Walsh, F. C. (2019). Polymer Nanocomposites Having a High Filler Content: Synthesis, Structures, Properties, and Applications. *Nanoscale* 11, 4653–4682. doi:10.1039/C9NR00117D

Iijima, S. (1991). Helical Microtubules of Graphitic Carbon. *Nature* 354, 56–58. doi:10.1038/354056a0

Kausar, A. (2017). Contemporary Applications of Carbon Black-Filled Polymer Composites: An Overview of Essential Aspects. *J. Plast. Film Sheeting* 34, 256–299. doi:10.1177/8756087917725773

Kechek'yan, P. A., Bazhenov, S. L., and Kechek'yan, A. S. (2018). The Influence of Biaxial Orientation on the Mechanical Properties of Polyethylene Filled with ZnO Nanoparticles. *Polym. Sci. Ser. A.* 60, 373–380. doi:10.1134/S0965545X18030057

Kojima, Y., Usuki, A., and Kawasumi, M. (1993). Synthesis and Mechanical Properties of Nylon6-Clay Hybrid. *J. Mater. Life Soc.* 11, 1179–1185. doi:10.1557/JMR.1993.1185

Kovačević, Z., Flinčec Grgac, S., and Bischof, S. (2021). Progress in Biodegradable Flame Retardant Nano-Biocomposites. *Polymers* 13, 741. doi:10.3390/POLYM13050741

Lai, L., Li, J., Liu, P., Wu, L., Severtson, S. J., and Wang, W.-J. (2020). Mechanically Reinforced Biodegradable Poly(butylene Adipate-Co-Terephthalate) with Interactive Nanoinclusions. *Polymer* 197, 122518. doi:10.1016/j.polymer.2020.122518

Lavagna, L., Marchisio, S., Merlo, A., Nisticò, R., and Pavese, M. (2020). Polyvinyl Butyral-based Composites with Carbon Nanotubes: Efficient Dispersion as a Key to High Mechanical Properties. *Polym. Composites* 41, 3627–3637. doi:10.1002/pc.25661

Lee, M. G., Lee, S., Cho, J., Bae, S., and Jho, J. Y. (2020). Effect of the Fluorination of Graphene Nanoflake on the Dispersion and Mechanical Properties of Polypropylene Nanocomposites. *Nanomaterials* 10, 1171. doi:10.3390/nano10061171

Lepot, N., Van Bael, M. K., Van den Rul, H., D'Haen, J., Peeters, R., Franco, D., et al. (2011). Influence of Incorporation of ZnO Nanoparticles and Biaxial Orientation on Mechanical and Oxygen Barrier Properties of Polypropylene Films for Food Packaging Applications. *J. Appl. Polym. Sci.* 120, 1616–1623. doi:10.1002/app.33277

Li, J., Chen, Q., Zhang, Q., Fan, T., Gong, L., Ye, W., et al. (2020). Improving Mechanical Properties and Biocompatibilities by Highly Oriented Long Chain Branching Poly(lactic Acid) with Bionic Surface Structures. *ACS Appl. Mater. Inter.* 12, 14365–14375. doi:10.1021/acsami.9b20264

Li, J., Lai, L., Wu, L., Severtson, S. J., and Wang, W.-J. (2018). Enhancement of Water Vapor Barrier Properties of Biodegradable Poly(butylene Adipate-Co-Terephthalate) Films with Highly Oriented Organomontmorillonite. *ACS Sust. Chem. Eng.* 6, 6654–6662. doi:10.1021/acssuschemeng.8b00430

Li, J., Wang, S., Lai, L., Liu, P., Wu, H., Xu, J., et al. (2021). Synergistic Enhancement of Gas Barrier and Aging Resistance for Biodegradable Films with Aligned Graphene Nanosheets. *Carbon* 172, 31–40. doi:10.1016/J.CARBON.2020.09.071

Liu, A., Ni, Z., Chen, J., and Huang, Y. (2020). Highly Sensitive Graphene/Polydimethylsiloxane Composite Films Near the Threshold Concentration with Biaxial Stretching. *Polymers* 12, 71. doi:10.3390/polym12010071

Liu, E. K., He, W. Q., and Yan, C. R. (2014). ''White Revolution' to 'white Pollution'-Agricultural Plastic Film Mulch in China. *Environ. Res. Lett.* 9, 091001. doi:10.1088/1748-9326/9/9/091001

Liu, X., Liu, Y., Yang, J., Wang, W., Lai, D., Mao, L., et al. (2019). Effects of the Biaxial Orientation on the Mechanical and Optical Properties and Shrinkage of Polyamide 6-66-Montmorillonite-Nanosilica Nanocomposite Films. *J. Appl. Polym. Sci.* 136, 47504. doi:10.1002/app.47504

Liu, X., Liu, Y., Yang, J., Yi, Z., Mao, L., Zheng, W., et al. (2018). A Comparative Study of the Structure and Mechanical Properties of Uniaxially and Biaxially

Stretched PA6-66/Montmorillonite Films. *Nanosci Nanotechnol Lett.* 10, 167–176. doi:10.1166/nnl.2018.2618

Mayoral, B., Menary, G., Martin, P., Garrett, G., Millar, B., Douglas, P., et al. (2021). Characterizing Biaxially Stretched Polypropylene/Graphene Nanoplatelet Composites. *Front. Mater.* 8. doi:10.3389/fmats.2021.687282

Oladele, I. O., Omotosho, T. F., Adediran, A. A., and Morales-Cepeda, A. (2020). Polymer-Based Composites: An Indispensable Material for Present and Future Applications. *Int. J. Polym. Sci.* 2020, 1–12. doi:10.1155/2020/8834518

Onyishi, H. O., and Oluah, C. K. (2020). Effect of Stretch Ratio on the Induced Crystallinity and Mechanical Properties of Biaxially Stretched PET. *Phase Transitions* 93, 924–934. doi:10.1080/01411594.2020.1813291

Ouchiar, S., Stoclet, G., Cabaret, C., Addad, A., and Gloaguen, V. (2016). Effect of Biaxial Stretching on Thermomechanical Properties of Polylactide Based Nanocomposites. *Polymer* 99, 358–367. doi:10.1016/j.polymer.2016.07.020

Pei, H., Yang, L., Xiong, Y., Chen, Y., Shi, S., and Jing, J. (2021). Fabrication, Characterisation and Properties of Polyvinyl Alcohol/graphene Nanocomposite for Fused Filament Fabrication Processing. *Plastics, Rubber and Composites* 50, 263–275. doi:10.1080/14658011.2020.1868668

Ponnamma, D., Cabibihan, J.-J., Rajan, M., Pethaiah, S. S., Deshmukh, K., Gogoi, J. P., et al. (2019). Synthesis, Optimization and Applications of ZnO/polymer Nanocomposites. *Mater. Sci. Eng. C.* 98, 1210–1240. doi:10.1016/j.msec.2019.01.081

Romero-Guzmán, M. E., Flores, O., Flores, A., Romo-Uribe, A., Campillo, B. B., Araceli, B., et al. (2011). Cold-drawn Induced Microstructure in PVC-Bentonite Nanocomposites. *Polym. Adv. Technol.* 22, 836–846. doi:10.1002/pat.1586

Roy, S., and Rhim, J.-W. (2020). Curcumin Incorporated Poly(Butylene Adipate-Co-Terephthalate) Film with Improved Water Vapor Barrier and Antioxidant Properties. *Materials* 13, 4369. doi:10.3390/ma13194369

Shen, J., Champagne, M. F., Gendron, R., and Guo, S. (2012b). The Development of Conductive Carbon Nanotube Network in Polypropylene-Based Composites during Simultaneous Biaxial Stretching. *Eur. Polym. J.* 48, 930–939. doi:10.1016/j.eurpolymj.2012.03.005

Shen, J., Champagne, M. F., Yang, Z., Yu, Q., Gendron, R., and Guo, S. (2012a). The Development of a Conductive Carbon Nanotube (CNT) Network in CNT/polypropylene Composite Films during Biaxial Stretching. *Composites A: Appl. Sci. Manufacturing* 43, 1448–1453. doi:10.1016/j.compositesa.2012.04.003

Shen, Y., Harkin-Jones, E., Hornsby, P., Mcnally, T., and Abu-Zurayk, R. (2011). The Effect of Temperature and Strain Rate on the Deformation Behaviour, Structure Development and Properties of Biaxially Stretched PET-clay Nanocomposites. *Composites Sci. Tech.* 71, 758–764. doi:10.1016/j.compscitech.2011.01.024

Singha, S., and Hedenqvist, M. S. (2020). A Review on Barrier Properties of Poly(Lactic Acid)/Clay Nanocomposites. *Polymers* 12, 1095. doi:10.3390/polym12051095

Soon, K., Harkin-Jones, E., Rajeev, R. S., Menary, G., Martin, P. J., and Armstrong, C. G. (2012). Morphology, Barrier, and Mechanical Properties of Biaxially Deformed Poly(ethylene Terephthalate)-Mica Nanocomposites. *Polym. Eng. Sci.* 52, 532–548. doi:10.1002/pen.22114

Tang, Z., Fan, F., Chu, Z., Fan, C., Qin, Y., Bikiaris, D., et al. (2020). Barrier Properties and Characterizations of Poly(lactic Acid)/ZnO Nanocomposites. *Molecules* 25, 1310. doi:10.3390/molecules25061310

Van Berkel, J. G., Guigo, N., SbirrazzuoliKolstad, N., and Nathanael, S. (2018). Biaxial Orientation of Poly(ethylene 2,5-furandicarboxylate): An Explorative Study. *Macromol. Mater. Eng.* 303, 1700507. doi:10.1002/mame.201700507

Wang, G., Zhao, J., Ge, C., Zhao, G., and Park, C. B. (2021). Nanocellular Poly(ether-Block-Amide)/MWCNT Nanocomposite Films Fabricated by Stretching-Assisted Microcellular Foaming for High-Performance EMI Shielding Applications. *J. Mater. Chem. C.* 9, 1245–1258. doi:10.1039/d0tc04099a

Wang, K., Liang, S., Zhao, P., Qu, C., Tan, H., Du, R., et al. (2007). Correlation of Rheology-Orientation-Tensile Property in Isotactic Polypropylene/organoclay Nanocomposites. *Acta Materialia* 55, 3143–3154. doi:10.1016/j.actamat.2007.01.020

Wang, X., and Shi, G. (2015). Flexible Graphene Devices Related to Energy Conversion and Storage. *Energy Environ. Sci.* 8, 790–823. doi:10.1039/c4ee03685a

Wu, J.-H., Yen, M.-S., Kuo, M. C., Tsai, Y., and Leu, M.-T. (2014). Poly(ethylene Terephthalate)/poly(ethylene Glycol-Co-1,3/1,4-Cyclohexanedimethanol Terephthalate)/clay Nanocomposites: Mechanical Properties, Optical Transparency, and Barrier Properties. *J. Appl. Polym. Sci.* 131, a–n. doi:10.1002/app.39869

Xiang, D., Harkin-Jones, E., and Linton, D. (2015). Characterization and Structure-Property Relationship of Melt-Mixed High Density Polyethylene/multi-Walled Carbon Nanotube Composites under Extensional Deformation. *RSC Adv.* 5, 47555–47568. doi:10.1039/c5ra06075c

Xiang, D., Wang, L., Tang, Y., Harkin-Jones, E., Zhao, C., and Li, Y. (2017). Processing-property Relationships of Biaxially Stretched Binary Carbon Nanofiller Reinforced High Density Polyethylene Nanocomposites. *Mater. Lett.* 209, 551–554. doi:10.1016/j.matlet.2017.08.104

Xiang, D., Wang, L., Zhang, Q., Chen, B., Li, Y., and Harkin-Jones, E. (2018). Comparative Study on the Deformation Behavior, Structural Evolution, and Properties of Biaxially Stretched High-Density Polyethylene/carbon Nanofiller (Carbon Nanotubes, Graphene Nanoplatelets, and Carbon Black) Composites. *Polym. Compos.* 39, E909–E923. doi:10.1002/pc.24328

Xiang, D., Zhang, X., Han, Z., Zhang, Z., Zhou, Z., Harkin-Jones, E., et al. (2020). 3D Printed High-Performance Flexible Strain Sensors Based on Carbon Nanotube and Graphene Nanoplatelet Filled Polymer Composites. *J. Mater. Sci.* 55, 15769–15786. doi:10.1007/s10853-020-05137-w

Xing, B., Cao, J., Wang, Y., Yi, G., Zhang, C., Chen, L., et al. (2015). Preparation of lignite-based Activated Carbon with High Specific Capacitance for Electrochemical Capacitors. *Funct. Mater. Lett.* 08, 1550031. doi:10.1142/S1793604715500319

Xing, Z., Lu, W., Cheng, L., Zhang, C., Xiao, Y., Shi, X., et al. (2019). Influences of Bi-axial Orientation on the Crystallization and DC Breakdown Properties of Polypropylene Films. *Proc. 21st Int. Symp. High Voltage Eng.* 599, 91–98. doi:10.1007/978-3-030-31680-8_10

Yang, B., Pan, Y., Yu, Y., Wu, J., Xia, R., Wang, S., et al. (2020a). Filler Network Structure in Graphene Nanoplatelet (GNP)-filled Polymethyl Methacrylate (PMMA) Composites: From Thermorheology to Electrically and Thermally Conductive Properties. *Polym. Test.* 89, 106575. doi:10.1016/j.polymertesting.2020.106575

Yang, H., Gong, L. H., Zheng, Z., and Yao, X. F. (2020b). Highly Stretchable and Sensitive Conductive Rubber Composites with Tunable Piezoresistivity for Motion Detection and Flexible Electrodes. *Carbon* 158, 893–903. doi:10.1016/j.carbon.2019.11.079

Youm, J. S., Park, J.-J., and Kim, J. C. (2020). Effect of Electron Beam Irradiation on Gas-Barrier Property of Biaxially Drawn Nylon/Montmorillonite Nanocomposite Films. *Macromol. Res.* 28, 925–931. doi:10.1007/s13233-020-8119-8

Yue, G., Li, F., Yang, G., and Zhang, W. (2016). Efficient Nickel Sulfide and Graphene Counter Electrodes Decorated with Silver Nanoparticles and Application in Dye-Sensitized Solar Cells. *Nanoscale Res. Lett.* 11, 239. doi:10.1186/s11671-016-1456-z

Zhang, W., Wei, L., Ma, Z., Fan, Q., and Ma, J. (2021). Advances in Waterborne Polymer/carbon Material Composites for Electromagnetic Interference Shielding. *Carbon* 177, 412–426. doi:10.1016/J.CARBON.2021.02.093

Zhou, J., Zheng, Y., Shan, G., Bao, Y., Wang, W.-J., and Pan, P. (2020). Stretch-induced Crystalline Structural Evolution and Cavitation of Poly(butylene Adipate-Ran-Butylene Terephthalate)/poly(lactic Acid) Immiscible Blends. *Polymer* 188, 122121. doi:10.1016/j.polymer.2019.122121

Conflict of Interest: The authors declare that the research was conducted in the absence of any commercial or financial relationships that could be construed as a potential conflict of interest.

Publisher's Note: All claims expressed in this article are solely those of the authors and do not necessarily represent those of their affiliated organizations, or those of the publisher, the editors and the reviewers. Any product that may be evaluated in this article, or claim that may be made by its manufacturer, is not guaranteed or endorsed by the publisher.

frontiers in Materials

ORIGINAL RESEARCH
published: 15 September 2021
doi: 10.3389/fmats.2021.724958

Melt-Blended Multifunctional PEEK/Expanded Graphite Composites

Mozaffar Mokhtari[1]*, *Edward Archer*[1], *Noel Bloomfield*[2], *Eileen Harkin-Jones*[1] and *Alistair Mcilhagger*[1]

[1]School of Engineering, Ulster University, Newtownabbey, United Kingdom, [2]Denroy Plastics, Bangor, United Kingdom

In this work, antistatic, high-performance composites of poly (ether ether ketone) (PEEK) and concentrations of 0.5–7 vol% expanded graphite (EG) were fabricated via twin-screw extrusion and injection moulding at mould temperatures of 200°C. The morphological, electrical, rheological, thermal, mechanical, and wear properties of the composites were investigated. Scanning electron microscope (SEM) images indicate that distribution and dispersion of EG platelets in the PEEK matrix are enhanced at higher EG loadings. The electrical conductivity of the composites with 5 vol% of EG exhibits a sharp rise in the electrical conductivity range of antistatic materials because of the formation of conductive paths. The formation of a three-dimensional EG network led to a rapid increase in the storage modulus of the melt of the 2 vol% of EG-loaded composite at a frequency of 0.1 rad/s and temperature of 370°C. The neat PEEK and composites containing 0.5–5 vol % EG indicated a cold-crystallisation peak in the first heating scan of a non-isothermal differential scan calorimetry (DSC) test and their crystallinity degrees changed slightly. However, after removing their thermal and stress histories, the EG platelets promoted nucleation and increased the PEEK crystallinity remarkably, indicating that annealing of the PEEK composites can improve their mechanical performance. The neat PEEK exhibits the standard tensile and flexural stress-strain behaviour of thermoplastics, and the composites exhibit elastic behaviour initially followed by a weak plastic deformation before fracture. The addition of 5 vol% of EG to PEEK increased the tensile and flexural modulus from 3.84 and 3.55 GPa to 4.15 and 4.40 GPa, decreased the strength from 96.73 and 156.41 MPa to 62 and 118.19 MPa, and the elongation at break from 27.09 and 12.9% to 4 and 4.6%, respectively. The wear resistance of the composite containing 3 vol% EG was enhanced by 37% compared with the neat PEEK.

Keywords: high-temperature composite, cost-effective, expanded graphite, antistatic, wear resistance, cold-crystallization

OPEN ACCESS

Edited by:
Jiabin Shen,
Sichuan University, China

Reviewed by:
Ming Wang,
Southwest University, China
Shengtai Zhou,
Sichuan University, China

***Correspondence:**
Mozaffar Mokhtari
m.mokhtari@ulster.ac.uk
mozaffar.mokhtari@gmail.com

Specialty section:
This article was submitted to Polymeric and Composite Materials, a section of the journal Frontiers in Materials

Received: *14 June 2021*
Accepted: *12 August 2021*
Published: *15 September 2021*

Citation:
Mokhtari M, Archer E, Bloomfield N, Harkin-Jones E and Mcilhagger A (2021) Melt-Blended Multifunctional PEEK/Expanded Graphite Composites. Front. Mater. 8:724958. doi: 10.3389/fmats.2021.724958

INTRODUCTION

Poly (ether ether ketone) (PEEK) has a variety of promising properties such as high chemical resistance, outstanding mechanical properties, and good thermal and dimensional stabilities due to its aromatic and semicrystalline backbone. These properties and the easier processing of PEEK as compared with metals, biocompatibility, and transparency to radiation have increased interest in its usage in industries such as biomedical, aerospace, and automotive. Also, the improvement of the electrical conductivity and wear resistance of PEEK has extended its applications noticeably (Pei et al., 2019; Puértolas et al., 2019; Zhang et al., 2019; Schroeder et al., 2020). For example,

electrically conductive PEEK materials have been utilised to manufacture reflectors for parabolic space antenna in satellites, cryogenic storage tanks in space launchers, electro-thermal de-icing materials in icebreaker vessels, antistatic catheters, disposable surgical instruments, and sterilisation trays (Flanagan et al., 2017; Kalra et al., 2019; Rival et al., 2019; Pan et al., 2020). Also, metals have been extensively replaced by high wear resistance PEEK materials in mechanical and biomaterial parts such as bearings, pumps, pistons, dental implants, trauma, knee, and spine (Kalin et al., 2015; Kurtz et al., 2019). Therefore, the simultaneous improvement of the wear resistance and electrical conductivity of PEEK by the incorporation of a cost-effective filler using melt mixing is very desirable for industrial applications.

Nano-fillers such as carbon nanotubes (CNTs) and nano-clay have been effective in the enhancement of polymer properties due to their high aspect ratio. However, CNTs are still quite expensive, and cost-effective nano-clays are not electrically conductive (Sarathi et al., 2007; Arjmand et al., 2012). Graphite on the other hand combines the lower price and the layered structure of clays with the superior thermal and electrical properties of CNTs (Kim et al., 2007). However, the aspect ratio of graphite is not as high as nano-clay, and graphite intercalation compounds (GICs) have been developed to exfoliate graphite and increase its aspect ratio (Noel and Santhanam 1998). Expanded graphite (EG) is the most beneficial exfoliated graphite which is obtained by a sudden evaporation of an intercalate in an expansion process. After the expansion, EG forms a porous network structure with a high surface area with graphite nanosheets with thicknesses less than 100 nm (Li and Chen, 2007; Zhao et al., 2007; Dhakate et al., 2008; Dong et al., 2019). In addition, –OH, –COOH functional groups resulting from the expansion on the surfaces of EG galleries can enhance the adsorption of polymer molecules to EG (Cao et al., 1996; Goyal et al., 2010).

The low concentration of quasi-free π-electrons in graphite (about 5×10^{-5} electrons per atom) is a cause of weak metallic bond forces between graphene layers at the same order of the van der Waals bonds (RozpAlocha et al., 2007). The weak metallic interlayer bond of graphite leads to a self-lubricating behaviour and high electrical conductivity in the c-axis direction that can improve simultaneously the wear resistance and the electrical conductivity of polymers (Fukushima et al., 2010).

Zheng et al. reported that through-thickness and in-plane volume electrical conductivities of poly (styrene-co-acrylonitrile) increased to 83.3 and 117.6 S cm^{-1} with the incorporation of 15 wt% of EG, respectively, using in situ polymerisation and hot compression (Zheng et al., 2004). Kim et al. and Chen e al. showed that the electrical conductivity of PS/EG composites increased sharply at about 10 and 3 wt% loading of EG to 1.3 $\times 10^{-1}$ and 10^{-1} S cm^{-1} *via in situ* polymerisation, respectively (Chen et al., 2001; Kim et al., 2007). Zheng et al. indicated that the loading of 1 wt% of EG to poly (methyl methacrylate) using stirring and ultrasonication increased its electrical conductivity to 10^{-4} S cm^{-1} (Zheng et al., 2004). Song et al. reported that the electrical conductivity of an aromatic polysulphide increased to 24.3 S cm^{-1} by the incorporation of 10 wt% EG with an expansion ratio of 200 *via* stirring (Song et al., 2006). Weng et al. and Du et al. showed that the induction of 0.75 wt% foliated graphite (prepared by the fragmentation of EG using ultrasonic irradiation) and 5 wt% EG to nylon 6 and poly (4,4′-oxybis (benzene)disulfide) by *in situ* polymerisation increased their electrical conductivities to about 2×10^{-8} and 10^{-3} S cm^{-1}, respectively (Du et al., 2004; Weng et al., 2004). One study has been identified for electrically conductive PEEK/EG nanocomposites, and this used solution processing to manufacture the composite. This achieved a promising electrical percolation threshold of about 10^{-1} S cm^{-1} at 1.5 wt % EG loading and conductivities of 3.24 S cm^{-1} and 12.3 S cm^{-1} for 5 and 10 wt% EG-loaded composites, respectively (Goyal et al., 2013).

Jia et al. reported that the wear resistance of polyimide increased 200 times by the incorporation of 15 wt% EG via hot compression moulding (Jia et al., 2015). Aderikha et al. manufactured PTFE/EG composites via sintering and showed that the filling of PTFE with EG allowed a reduction in its wear rate up to a factor of ≈700 to 6×10^{-7} mm^3 Nm^{-1} depending on the friction conditions (Aderikha et al., 2017). Also, Yang et al. reported that the wear resistance of PTFE/nano-EG composite containing 15 wt% EG manufactured via electrical sintering increased 31.6 times (Yang et al., 2010).

As discussed above, EG is a cost-effective carbon filler with outstanding electrical and antifriction properties which has been incorporated into various thermoplastics and shown to improve their electrical conductivity and wear resistance. Hence, the coordinated enhancement of the electrical conductivity and wear resistance of PEEK by including cost-effective EG with outstanding electrical and antifriction properties using melt mixing can be very beneficial. However, to the best of our knowledge, EG has not been combined with PEEK to enhance its mechanical and wear properties *via* melt processing. Thus, the purpose of this study is to fill that gap by reporting on the ability of EG to improve the mechanical and wear performance of melt-processed PEEK.

In this study, PEEK/EG composites were manufactured via twin-screw extrusion, and specimens were injection-moulded at a mould temperature of 200°C for subsequent characterisation. The EG dispersion state was examined via SEM and melt rheology. Crystallinity and melting behaviour, tensile and flexural properties, and wear resistance of the samples were characterised *via* DSC, a tensile testing, and microscale abrasion testing, respectively.

EXPERIMENTAL

Materials

The polymer (PEEK 2000P) was purchased from Evonik (Marl, Germany) in fine powder form with a melt volume flow rate (380°C/5 kg) of 70 cm^3/10 min and a density of 1.3 g cm^{-3}. The expanded graphite (GFG200) used in this work was kindly provided by SGL Carbon (Wiesbaden, Germany) in platelet form. It has a mean diameter of 200 μm and a density of 2.28 g cm^{-3}.

Preparation of Composites

PEEK and EG powders were put in an oven at 170°C for 12 h before use to remove absorbed moisture. After drying, the polymer and 0.5, 1, 2, 3, 5, and 7% volume fractions of EG powders were physically mixed. The melt compounding of the mixtures was accomplished in a co-rotating twin-screw extruder (Rheomex PTW16/40 OS) with a diameter of 16 mm and L/D = 40 operating at a barrel to die temperature range from 365 to 385°C and screw speed of 45 rpm. As explained in previous work, reverse and kneading mixing elements were utilised in an in-house screw configuration to improve the distribution and dispersion of the EG platelets in the PEEK (Mokhtari et al., 2021).

For testing and characterisation, dumbbells were moulded via an injection moulder (SmartPower 35/130 UNILOG B8). Before injection, the pellets were placed in the oven at 100°C for 12 h. The mould temperature, cooling time, heating zone temperatures, and injection and holding pressures of the injection moulder were 200°C, 60 s, 320/380/385/390°C, 2000, and 1,200 bar, respectively.

Material Characterisation

Scanning Electron Microscope

The surface morphology of cryogenic-fractured samples was analysed using a Hitachi SU5000 SEM. The sample surfaces were coated with a 5–10 nm Au/Pd layer to minimise the charging effect.

Differential Scan Calorimetry

Non-isothermal DSC experiments were carried out in a TA Q100 differential scanning calorimeter. Samples of 8 mg which were cut from the injection-moulded dumbbells were sealed in standard aluminium hermetic pans to investigate the effects of the EG content and cooling process on the crystallisation behaviour of the PEEK. The samples were heated to 390°C, held isothermally for 15 min, cooled to 40°C, and reheated to 390°C. All the steps were at a constant rate of 10°C/min. Crystallisation temperature (T_c) was determined as the maximum of the cooling scan peak. The temperature and enthalpy of cold crystallisation (T_{cc} and ΔH_{cc}) were obtained from the maximum and area under the exothermic peak around the glass transition region of the first heating cycle. Also, the melting enthalpies and temperatures of the PEEK crystals were obtained from the minimum and area under the endothermic peaks of the first and second heating scans, respectively. The crystallinity degrees of the first and second heating scans were calculated by **Eq. 1** and **Eq. 2**, respectively. Here, ΔH_{mfh} and ΔH_{msh} are the melting enthalpies of the composites in the first and second heating scans, respectively, ΔH_f is the melting enthalpy of the ideal PEEK crystal (130 J/g), and w_p is the weight fraction of the polymer (Blundell and Osborn 1983).

$$X_{cfh} = \Delta H_{mfh} - \Delta H_{cc} \Big/ \left(\Delta H_f \times w_p\right), \tag{1}$$

$$X_{csh} = \Delta H_{msh} \Big/ \left(\Delta H_f \times w_p\right). \tag{2}$$

Rheology

Linear viscoelastic properties of the composite melts were analysed using an AR2000 rotational rheometer with 25-mm steel parallel plates at a gap setting of 1 mm and 370°C. Frequency of the oscillation test was changed between 0.06 and 600 rad s^{-1} and a strain amplitude of 6.25×10^{-3} within the linear viscoelastic region was chosen for it.

Electrical Conductivity Measurements

DC volume conductivity measurements were performed at 18°C and a humidity of 75% using an electrometer/high resistance meter (Keithley 6517B) and an interactive digital source meter (Keithley 2450) for low and moderately conductive composites, respectively. Samples of 18 × 18 × 1.5 mm^3 were placed between two electrodes, and a potential difference was applied between them. Both surfaces of the samples were coated with a conductive silver paste to reduce the contact resistance between the samples and electrodes. From resistance (R) which was obtained directly from the measurements and geometry of the samples, the volume resistivity (ρ) was calculated using **Equation (3)**:

$$\rho = R\, A/t, \tag{3}$$

where t and A are the thickness and the cross-sectional area of the sample. The electrical conductivity is the reciprocal of the volume resistivity.

Tensile and Bending Tests

Tensile and bending tests were performed at 18°C and humidity of 75% on an electromechanical Instron 5500R universal Testing System (UTS) at a constant crosshead speed of 2 mm min^{-1}. Dumbbells with overall length, overall width, gauge length, and thickness of 170, 10, 8, and 4 mm, respectively, and rectangular samples with length, width, and thickness of 8, 10, and 4 mm, respectively, were employed for the tensile and bending tests. An extensometer was utilised during the tensile test to measure the displacements of each specimen accurately. The presented data were obtained from the average of 5 measurements.

Micro-Abrasion Test

A TE-66 microscale abrasion tester (Phoenix Tribology Ltd., United Kingdom) was utilised to perform microscale abrasion tests on 4 N normal load against a stainless-steel ball with 25.4 mm diameter rotating for 22,500 revolutions, corresponding to a sliding distance of 1795.4 m (ASTM 52100). After the tests, the samples were removed from the equipment, and the diameter of the resulting abrasion scars was estimated via optical microscopy. By assuming that the geometry of the crater is like the spherical geometry of the ball, the volume of a spherical wear scar can be calculated by **Equation (4)**:

$$V \approx \frac{\pi b^4}{64R} \qquad b \ll R, \tag{4}$$

where b and R are the crater diameter and the ball radius, respectively. The volumetric wear rate is the ratio of the volume wear to the sliding distance (Stack and Mathew 2003; Souza et al., 2016).

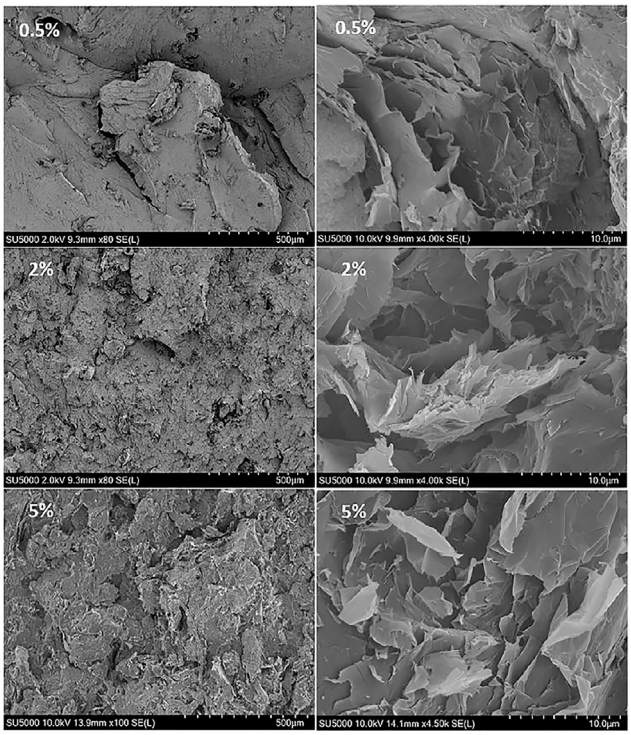

FIGURE 1 | SEM images of the neat PEEK and the composites containing 0.5, 2 and 5 vol% EG.

RESULTS AND DISCUSSION

Morphology Analysis

SEM analysis was performed to examine the morphology of the EG platelets of the injected PEEK/EG composites. **Figure 1** shows the SEM images of the neat PEEK and the composites containing 0.5, 2, and 5 vol% of EG. SEM images show that at lower EG loadings, EG platelets agglomerated and did not distribute well in the PEEK matrix, while with an increase in the EG loading, they were almost uniformly distributed and formed a continuous three-dimensional network. This can be ascribed to the higher shear stress in the processing of the high EG content composites that led to the penetration of the PEEK melt into the pores of the EG honeycomb-like structure and the creation of good mechanical interlockings between the EG galleries and the matrix (Zheng et al., 2004; Li and Chen, 2007). Also, the penetration of the melt into the EG pores caused an increase in the distance between the EG galleries preventing collapse and maintaining their network structure which are strongly effective in the formation of an electrically conductive three-dimensional network (Goyal 2013).

Rheology Analysis

A frequency sweep test in the range of 0.01–100 HZ was carried out to study the linear viscoelastic properties of the composite melts which was utilised to investigate the state of the EG platelet dispersion and structural change in the composites. **Figures 2A,B** show the variation of the storage modulus of the composites as a function of angular frequency and the EG volume fraction at a fixed frequency of 0.1 rad s^{-1}, respectively. There are no particle contacts and sufficient space for the EG platelets to slip over each other, and their self-lubricant effect led to slipping and orientation of the polymer chains in the composites containing 0.5 and 1 vol% EG that caused to an unexpected decrease in their storage modulus compared with the neat PEEK at low and intermediate frequencies (Kim and Macosko 2009). However, the storage modulus of the 2 vol% of EG-loaded composite increased sharply and indicated a reduction in the dependence on angular frequency compared with the neat PEEK. This behaviour indicates the attainment of the rheological percolation threshold (φ_{per}) where a transition from liquid-like to pseudo-solid-like behaviour occurs due to a confinement of polymer chain motions. The hindrance of the polymer chain motions is caused by direct elastic filler–filler interactions, the immobilisation of the polymer segments near the particles at the interphase regions, and the formation of the PEEK-EG network (Liebscher et al., 2020).

To gain a more detailed insight into the rheological percolation threshold, the relationship between storage modulus and filler volume fraction (φ) ($\varphi > \varphi_{per}$) can be expressed with a power law relationship (Bangarusampath et al., 2009; Zhang et al., 2012):

$$G'\alpha\left(\varphi - \varphi_{per}\right)^{t} \tag{5}$$

where t is the critical exponent. As shown in the inset in **Figure 2B**, the composite modulus agreed well with the power law for the fixed frequency of 0.1 rad s^{-1}, and the onset of percolation was determined as 0.02 volume fraction.

Figure 3A shows the variation of the complex viscosity as a function of angular frequency. At low and intermediate frequencies, fully relaxed neat PEEK chains and the composites containing 0.5 and 1 vol% EG exhibited a typical Newtonian viscosity plateau. With the addition of 2 vol% EG, the low frequency complex viscosity increases noticeably due to the restriction of the long-chain PEEK relaxations in the composites by the EG platelets. Hence, the Newtonian plateau vanishes progressively, and a significant shear-thinning behaviour is observed (Wagener and Reisinger 2003).

Also, a pseudo-solid-like network of an anisometric filler in a polymer matrix indicates an apparent yield stress which is obvious by plotting complex viscosity versus the complex modulus. In **Figure 3B**, an apparent yield stress in composites containing EG of more than 2 vol% observed that the complex viscosity increased rapidly as the complex modulus decreased (Cassagnau 2008; Abbasi et al., 2009).

Crystallisation Behaviour

The dynamic crystallisation behaviour of semicrystalline thermoplastic composites is of great interest since most processing methods happen under these conditions, and the crystal perfection and crystallinity degree of these materials depend on thermal history imparted during processing (Wu et al., 2007; Zhao et al., 2011). **Figure 4** and **Table 1** show the

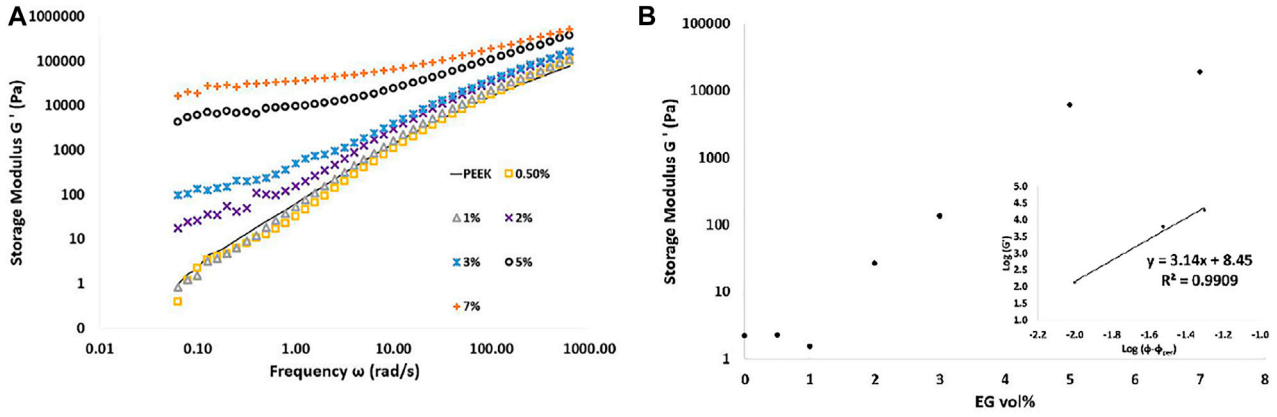

FIGURE 2 | Storage modulus **(A)** of the PEEK/EG composite melts versus angular frequency for different EG loadings and **(B)** storage modulus as a function of the EG volume fraction at a fixed frequency of 0.1 rad s^{-1} at 370°C. Inset: log–log plot of the storage modulus versus the reduced volume fraction.

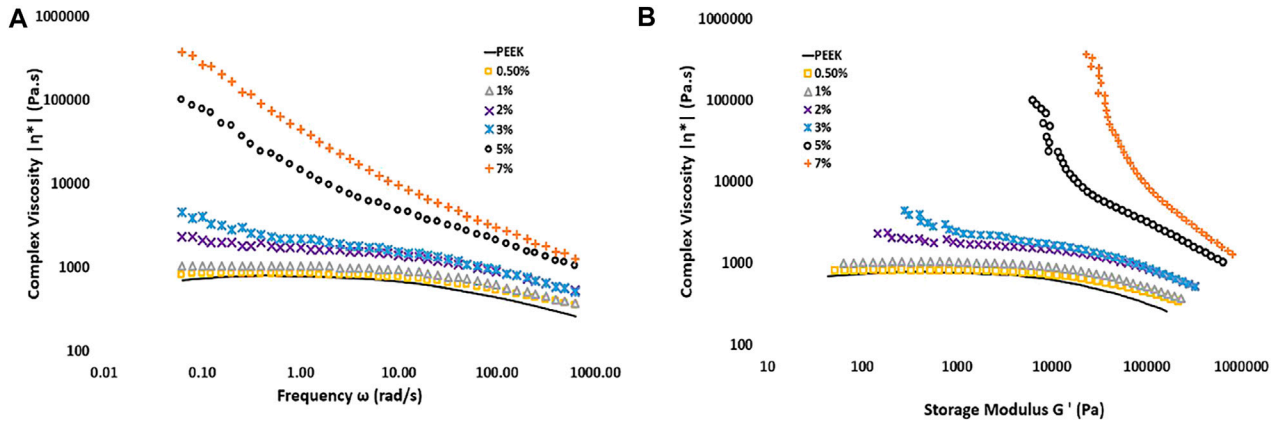

FIGURE 3 | Complex viscosity of the PEEK/EG composite melts **(A)** versus angular frequency **(B)** versus storage modulus for different EG loadings at 370°C.

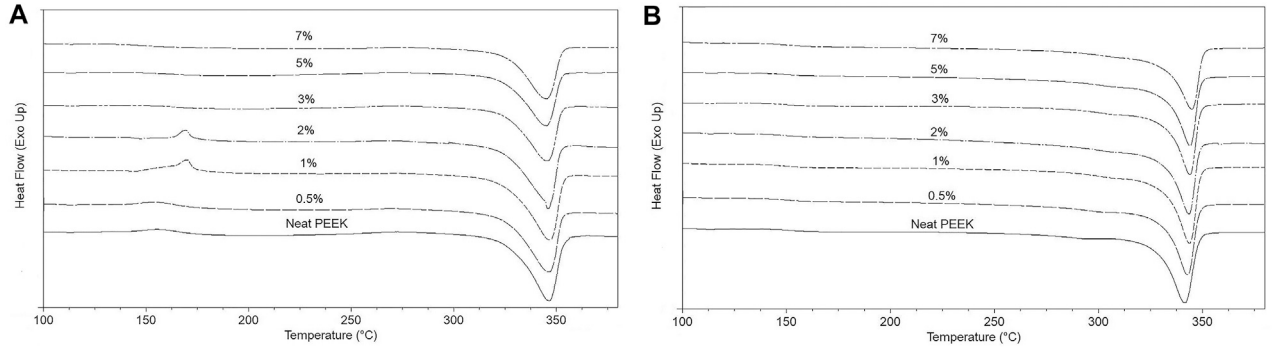

FIGURE 4 | DSC results of the neat PEEK and the composite samples at 10°C/min **(A)** the first heating scan **(B)** the second heating scan.

results of non-isothermal DSC tests that were carried out at 10°C/min to evaluate the influence of the EG content and processing conditions on the crystallisation and melting behaviour of the PEEK matrix.

Post or cold crystallisation is due to a physical aging process which typically happens in semicrystalline thermoplastics around the glass transition region due to a thermodynamically unstable state caused by cooling conditions during processing. In cold

TABLE 1 | Non-isothermal crystallisation parameters of PEEK/EG composites obtained from the DSC measurements.

EG content (vol%)	T_{mfh} (°C)	ΔH_{mfh} (J g^{-1})	T_{cc} (°C)	ΔH_{cc} (J g^{-1})	X_{cfh} (%)	T_{msh} (°C)	ΔH_{msh} (J g^{-1})	X_{csh} (%)	T_c (°C)
0	347	37.2	154.3	2.78	26.5	341.9	46.3	40	291.8
0.5	346.4	35.9	156.5	2.72	25.8	342.8	48.2	38.7	298.1
1	346.9	41.7	169.9	6.43	27.6	343.7	57.7	45.12	303.2
2	346.2	33.8	169.3	2.26	25.5	343.7	53.6	43.4	303.6
3	345.8	34.3	157.2	1.4	26.6	343.8	50.8	40.9	303.6
5	345.9	31.6	151.5	0.7	26.9	343.6	52.5	44.1	303.2
7	344.7	36	----	0	32.1	344.5	44.18	38.5	303.4

T_{mfh}, ΔH_{mfh}, T_{cc}, ΔH_{cc}, X_{cfh}: melt temperature, melting enthalpy, cold-crystallisation enthalpy, cold-crystallisation temperature, and crystallisation degree obtained from the first heating scan; T_{msh}, ΔH_{msh}, X_{csh}: melt temperature, melting enthalpy, and crystallisation degree obtained from the second heating scan.

TABLE 2 | Tensile properties of the composites: E_T = Young's modulus, σ_T = tensile strength, and ε_T = elongation at break.

EG (vol%)	E_T (GPa)	σ_T (MPa)	ε_T (%)
0	3.84 ± 0.11	96.73 ± 1.96	27.09 ± 2.88
0.5	4.09 ± 0.12	87.70 ± 1.21	10.37 ± 1.6
1	4.14 ± 0.27	83.17 ± 2.64	7.36 ± 1.7
2	4.16 ± 0.21	78.21 ± 1.21	5.88 ± 0.7
3	4.00 ± 0.08	70.29 ± 0.63	5.03 ± 0.44
5	4.15 ± 0.05	62.01 ± 3.21	4.00 ± 0.23
7	4.57 ± 0.10	56.49 ± 0.43	2.72 ± 0.08

crystallisation, changes in the physical structure of chains occur at either transition zones between the existing crystals and the amorphous regions or the imperfect existing crystalline structures which lead to an increase in the crystallinity degree and lamella thickness as well as to the perfection of the existing crystal structure (Wang et al., 2003; Antoniadis et al., 2009). The appearance of the cold-crystallisation peak in the first heating scan and a noticeable difference between the values of the melting enthalpies and crystallisation degrees of the samples in the first and second heating scans (except sample containing 7 vol% EG) verified that the cooling process in the mould of the injection moulder did not provide enough time for the PEEK chains to form a thermodynamically stable crystalline structure. The neat PEEK and the composites containing 0.5 vol% EG showed a broad cold-crystallisation peak which overlapped with the glass transition region. However, with an increase in the EG content to 1 and 2 vol%, the peak was sharper and happened at a higher temperature. EG platelets can affect crystallisation behaviour of the PEEK matrix through a nucleation effect and by altering the mobility of the PEEK chain segments via a confinement effect (Zhang et al., 2008; Rong et al., 2010). At the loadings of 1 and 2 vol% EG, the nucleation effect was dominant with EG platelets providing heterogeneous nucleation sites with lower energy for the PEEK chains to crystalise faster compared to the neat PEEK and the 0.5 vol% EG-loaded composites. However, the PEEK chains were not able to crystalise perfectly and became thermodynamically unstable due to the fast cooling in the mould. After a reheating to around T_g in the first heating scan of the DSC test, the frozen imperfect crystals could rearrange to a thermodynamically stable state, release heat, and equilibrating to a lower free energy. Hence, visible and sharp cold-crystallisation peaks appeared.

At the higher EG loadings, the PEEK chains could not crystalise as much as the chains of the samples with lower EG loadings (samples 1 and 2%) due to the dominance of the chain mobility confinement effect. Hence, during the reheating to around Tg in the first heating scan of the DSC test, fewer frozen imperfect crystals were available for rearrangement compared to the samples with lower EG loadings. Therefore, the cold-crystallisation degree decreased, and its peak moved to lower temperatures and disappeared in the sample containing 7 vol% EG.

Based on the first heating scan results, the crystallinity degree of the composite containing 7 vol% EG increased remarkably compared with the neat PEEK while the crystallinity degree of other composites changed slightly. The 7 vol% of EG-loaded composite did not show the cold-crystallisation peak in the first heating scan which means the cooling rate in the mould was slow enough for the PEEK chains to form thermodynamically stable crystals that did not rearrange in the first heating cycle. Also, the crystallinity degrees and melt temperatures of this composite in the first and second heating scans were similar. The estimated crystallinity degree from the second heating scan was related to the crystals that were formed in the cooling scan after removing the thermal and stress histories of the PEEK chains in an isothermal step at 390°C. By comparison of the crystallinity degrees of all samples in the first and heating scans, the PEEK chains crystalised more perfectly to a thermodynamically stable state in the cooling scan of the DSC test compared with the cooling process in the mould since they did not have a cold-crystallisation peak in the second heating cycle. Hence, it can be concluded that the formed crystalline structure of the injection moulded 7 vol% of EG composite was perfect enough, and its crystallinity degree increased compared with the neat PEEK due to heterogeneous crystallisation.

The significantly higher crystallinity degree of the samples in the second heating scan than the first one indicates that annealing can have a strong effect on the reduction of defects in the crystals of processed PEEK and can lead to an enhancement of their mechanical performance.

Based on a comparison between the melt temperatures of the samples (apart from the sample 7%) in the first and second

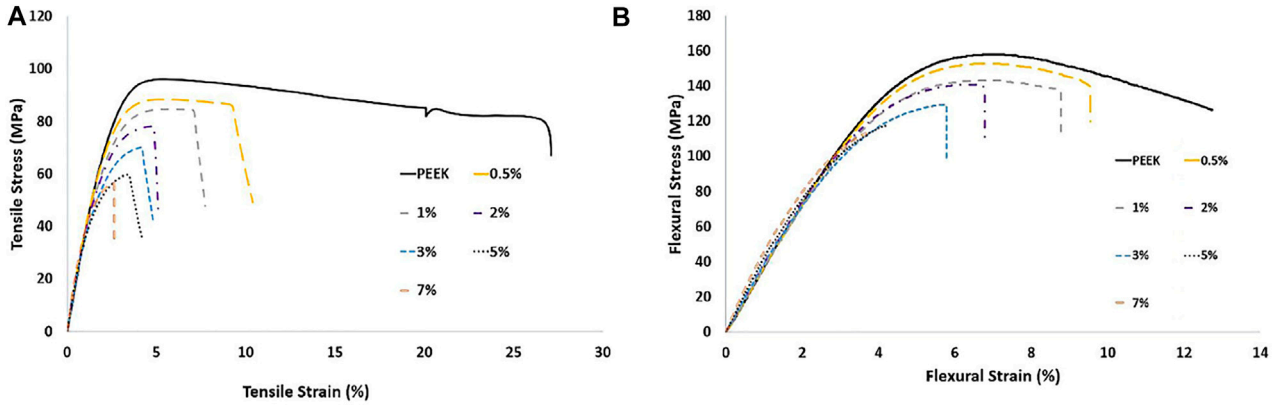

FIGURE 5 | (A) stress-strain curves from uniaxial tensile tests and **(B)** stress-displacement curves from 3-point bending tests of the neat PEEK and the PEEK/EG composites.

TABLE 3 | Flexural properties of the composites: E_b = flexural modulus, σ_b = flexural strength, and ε_b = fracture strain.

EG (vol%)	E_b (GPa)	σ_b (MPa)	ε_b (%)
0	3.55 ± 0.10	156.41 ± 3.05	12.90 ± 0.22
0.5	3.65 ± 0.11	152.69 ± 2.17	9.73 ± 1.77
1	3.71 ± 0.06	146.44 ± 2.45	8.90 ± 0.26
2	3.96 ± 0.05	141.50 ± 1.98	6.40 ± 0.55
3	3.97 ± 0.07	130.20 ± 1.72	5.60 ± 0.33
5	4.40 ± 0.05	118.19 ± 1.26	4.60 ± 0.18
7	4.92 ± 0.04	111.92 ± 0.87	3.78 ± 0.14

heating scans of the DSC test in **Table 2** and **Figures 4A,B**, crystals formed in the cooling process in the mould melted at a higher melt temperature and showed a broader endothermic melting peak as compared with the crystals formed in the cooling scan. This can be ascribed to the crystal perfection in the recrystallisation during the first heating scan that can increase the thickness of lamellae and the existence of a broad distribution of lamellae sizes due to the imperfect crystallisation in the cooling process in the mould. Also, it is worth noting that the composites in the first heating scan have slightly lower melt temperatures than the neat PEEK while the composites in the second heating scan have slightly higher melt temperature than the neat PEEK thus showing the strong effect of the cooling rate on the crystal structures.

As presented in **Table 1**, the crystallisation temperature of the composites increased remarkably due to the nucleation effect of the EG platelets. It is clear from the results of the second heating scans that the composites have slightly higher melt temperatures due to higher values of T_c that led to fewer defects in the PEEK crystals, and the crystallinity degrees of the composites were higher than the neat PEEK due to heterogeneous crystallisation. Also, the crystallinity degree increased up to the rheological percolation threshold and then dropped due to the formation of a filler network at percolation which reduced chain mobility. Beyond the rheological percolation threshold, the value of crystallinity of the composite containing 5 vol% EG increased due to nucleation promotion (Alvaredo et al., 2019).

Mechanical Properties

Figure 5 shows the room temperature tensile and flexural stress-strain curves for the neat PEEK and the PEEK/EG composites, and **Table 2** and **Table 3** present the influence of EG loading on the average tensile and flexural properties of the samples. In the tensile stress-strain curve, the neat PEEK presented a yield stress of 96.73 ± 1.96 MPa after an elastic region with a Young's modulus of 3.84 ± 0.11 GPa, a neck-formed region, neck propagation at a constant stress without strain hardening, and a final break at an elongation of 27.09 ± 2.88%. While the composites exhibited a linear elastic behaviour, which was followed by plastic deformation before fracture, the kink at about 20.6% tensile strain in the neat PEEK is the point where the extensometer was detached from the specimen. Also, the flexural stress-strain diagram of the neat PEEK shows an initial elastic region with flexural modulus of 3.55 ± 0.1 GPa which is followed by an ultimate strength of 156.41 ± 3.05 MPa and finally fractured at a strain of 12.90 ± 0.22%. As expected, stress-strain diagrams of the composites indicate a positive link between EG volume fraction and tensile and flexural moduli. The incorporation of 7 vol% EG into the PEEK increased the tensile and flexural moduli to 4.57 ± 0.10 and 4.92 ± 0.04 GPa which correspond to increases of 19 and 39% in stiffness, respectively.

According to the DSC results of the first heating cycle, crystallinity degree which directly affects the modulus of semicrystalline polymers did not change significantly as compared with the value of neat PEEK crystallinity apart from the sample containing 7 vol% EG (Díez-Pascual et al., 2019). Hence, the observed enhancements in the modulus of the composites with respect to the neat PEEK can be related to higher intrinsic modulus of the EG and its high aspect ratio which provided large interfaces with the matrix (Sever et al., 2013; Puértolas et al., 2019). However, the introduction of EG into the PEEK led to decreases in tensile and flexural strengths and fracture strains of the composites. The lower strength of the composites could be attributed to weak interfacial bonding at the interfaces of the EG galleries and the matrix and agglomerations

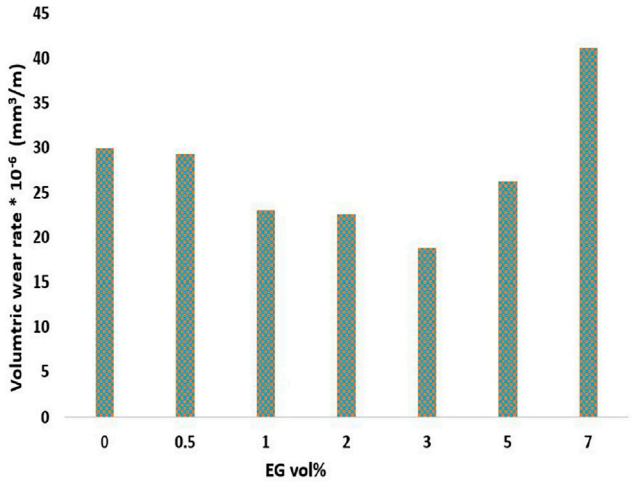

FIGURE 6 | Volumetric wear rate of the neat PEEK and the PEEK/EG composites.

of the EG platelets which caused a weak load transfer between the EG platelets and the PEEK matrix (Fukushima et al., 2010; Song, Xiao, and Meng 2006; Zhao et al., 2007). Also, the incorporation of the EG platelets into the PEEK remarkably hindered the motions of polymer chains such that the imposed external mechanical energy could not be dissipated effectively and led to the lower strength and significantly smaller fracture strains of the composites (Hatui et al., 2014).

Wear Properties

Figure 6 presents the variation of the volumetric wear rate of the neat PEEK and the composites. It can be seen from **Figure 6** that the wear rate of the neat PEEK decreased from 30 to 18.87 mm^3 m^{-1} by the incorporation of the 3 vol% EG which corresponds to 37% improvement in the wear resistance. After reaching the critical volume fraction of 3 vol%, further increase in the EG content resulted in a higher wear rate.

With the gradual increase of the EG content, the contact zone between the composites and steel ball counterpart covered not only the PEEK matrix but also the EG platelets. Before reaching the critical volume fraction, the PEEK matrix contributed more than the EG galleries to decreasing the wear rate of the composites. The PEEK matrix with its outstanding mechanical properties and high strength and ductility in the interfacial regions provided local support for the EG galleries and absorbed the shear energy of the steel ball counterpart. This reduced the probability of the fracture of large EG particles from the composite's surfaces. Hence, they could enhance and decrease the anti-friction character and the wear rate of the composite, respectively, by peeling off in tiny particles and forming a lubricant film on the composite's surface. After a loading of EG platelets more than the critical volume fraction, EG platelets contribute more than the PEEK matrix to the wear resistance of the composite. Hence, the poor shear strength of the EG platelets and the reduction of the strength and ductility of the matrix at the interfacial regions which deformed through elongation rather than breakage aggravate the wear performance of the composites (Zhao et al., 2007; Puértolas et al., 2019). However, if the volume fraction of the EG is less than the critical volume fraction, there are not enough EG galleries to decrease the friction between the matrix and the steel ball counterpart and form a lubricant film. Therefore, the wear resistance would be also low (Hu et al., 2005).

Moreover, as shown in **Figure 7** the worn surfaces of the neat PEEK and the composites containing 3 and 7 vol% of EG which indicated the best and worse wear resistance were analysed via SEM to provide more information about the wear mechanism of the PEEK/EG composites. As shown in **Figures 7A,D**, the neat PEEK deformed and evident abrasive furrows on its worn surface formed due to the friction between the matrix and the steel ball counterpart. However, as shown in **Figures 7B,C**, the obvious furrows disappear in the worn surfaces of the composites, and they became smoother and flatter with an increase in the EG content. This can be ascribed to the fact that the graphite particles were peeled off and formed a lubricant film, reducing the direct contact between the matrix and counterpart and transferring the friction force to the graphite sheets (Wang et al., 2012). **Figure 7E** shows that the ductility and strength of the matrix at the interfacial regions of the 3 vol% of EG-loaded composite are high enough to provide local support for the EG galleries such that tiny EG particles are peeled off to form the lubricant film, and a small number of micro-cracks are formed on the composite surface (Jia et al., 2015; Sun et al., 2021). While, as shown in **Figures 7C,F**, more micro-cracks and the EG galleries are observed on the surface of the composite containing 7 vol% EG, this can be attributed to the fact that the EG galleries were directly chipped off the composite surface due to their poor shear strength and inadequate adhesion strength between the EG galleries and the matrix producing more aggravated wear of the composite as compared with the neat PEEK (Chang et al., 2006; Huang et al., 2008).

Electrical Properties

An efficient way to prevent a build-up of electrostatic charge in high-temperature electrically conductive thermoplastic composite is the incorporation of thermally conductive carbon fillers (Díez-Pascual et al., 2010; Moniruzzaman and Winey 2006). In this work, EG platelets were incorporated into PEEK to increase its electrically conductivity. **Figure 8** presents the effect of the EG content on the room temperature DC electrical conductivity values of the PEEK/EG composites. At low EG contents (≤3 vol%), the electrical conductivity values of the composites increased only slightly due to a large distance between the particles. However, the electrical conductivity value of the 5 vol% of EG-loaded composite increases suddenly to 3.2×10^{-5} S m^{-1} which is higher than the required electrical conductivity for antistatic applications (10^{-6} S m^{-1}). This is due to the formation of electrically conductive paths caused by either direct particle-particle interactions or interfacial regions between particles with a distance shorter than the tunnelling distance (10 nm) in agreement with the SEM observations (Debelak and Lafdi 2007). No remarkable change was noticed with increasing the

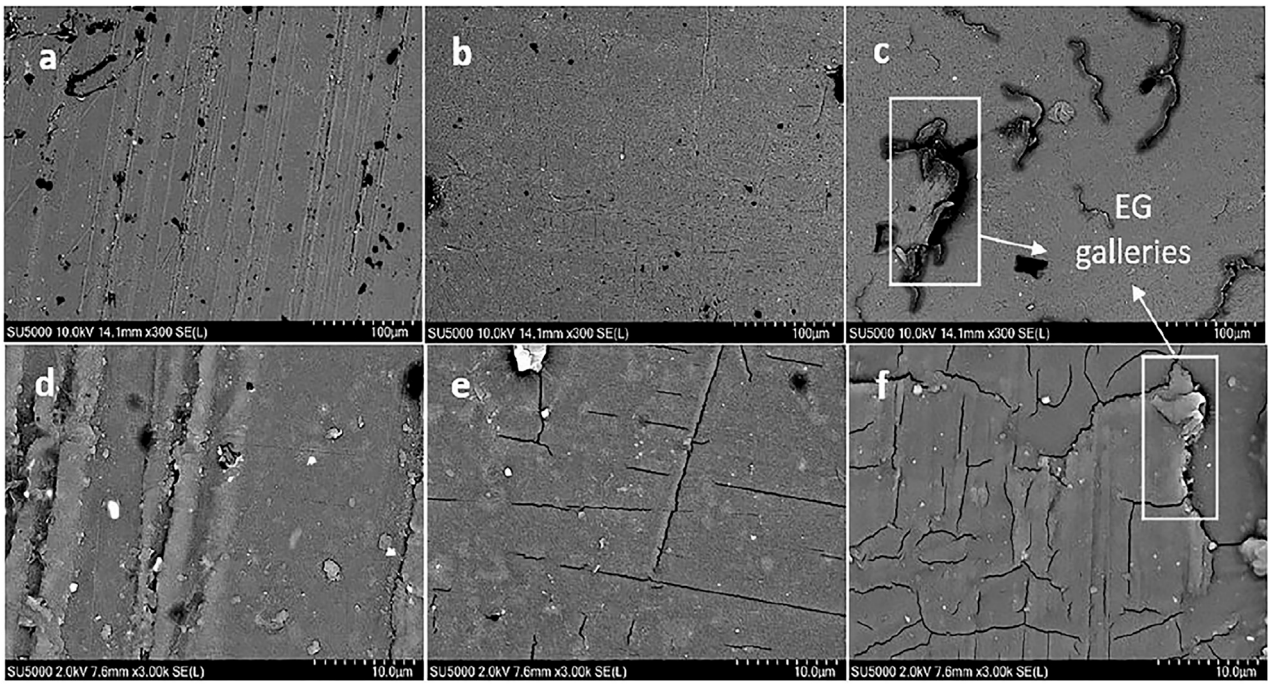

FIGURE 7 | Low and high magnification SEM images of the worn surfaces of the neat PEEK **(A,D)** and the PEEK/EG composites containing 3 **(B,E)** and 7 **(C,F)** vol % EG.

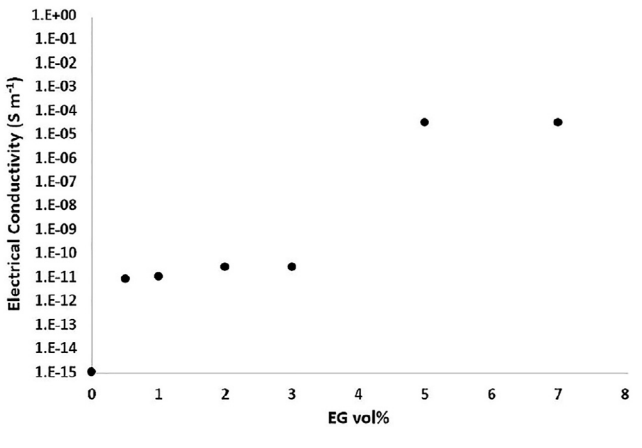

FIGURE 8 | DC volume electrical conductivity of the PEEK/EG composites at room temperature.

EG loading, which suggests the EG content is beyond the electrical percolation threshold. The electrical percolation threshold is significantly bigger than the rheological one. The difference can be ascribed to a shorter required filler-filler distance for electron tunnelling as the predominant mechanism of electrical conductivity as compared with that required for confinement of polymer chain motions at the rheological percolation threshold (Abbasi et al., 2009). Also, the electrical conductivity measurements were done on a room-temperature solid sample, whereas the rheological threshold was measured at temperatures above T_m so there is likely to be much more particleparticle contacts in the rheological measurement.

CONCLUDING REMARKS

PEEK/EG composites were prepared via twin-screw extrusion and subsequent injection moulding. The rheological and electrical percolation thresholds occurred at EG loadings of 2 and 5 vol%, respectively. Annealing of the PEEK composites can improve their mechanical performance. The incorporation of EG into PEEK increased its tensile and flexural modulus and decreased its tensile and flexural strengths and fracture stains. The composite containing 3 vol% of EG exhibited the maximum wear resistance. The electrical conductivity value at the electrical percolation threshold was in the required range of electrical conductivity for ESD materials.

DATA AVAILABILITY STATEMENT

The raw data supporting the conclusion of this article are available from the corresponding author upon reasonable request.

AUTHOR CONTRIBUTIONS

MM: conceptualisation, data curation, formal analysis, investigation, methodology, project administration,

visualisation, writing—original draft, writing—review and editing. EA: conceptualisation, formal analysis, supervision, resources, project administration, writing—review, and editing. NB: conceptualisation, supervision, resources, writing—review and editing. EH-J: conceptualisation, formal analysis, supervision, resources, writing—review and editing. AM: conceptualisation, formal analysis, project administration, supervision, funding acquisition, resources, writing—review and editing.

FUNDING

The North West Centre for Advanced Manufacturing (NW CAM) project is supported by the European Union's INTERREG VA Programme, managed by the Special EU Programmes Body (SEUPB). The views and opinions in this document do not necessarily reflect those of the European Commission or the Special EU Programmes Body (SEUPB). If you would like further information about NW CAM please contact the lead partner, Catalyst, for details.

REFERENCES

Abbasi, S., Carreau, P. J., Derdouri, A., and Moan, M. (2009). Rheological Properties and Percolation in Suspensions of Multiwalled Carbon Nanotubes in Polycarbonate. *Rheol. Acta* 48, 943–959. doi:10.1007/s00397-009-0375-7

Aderikha, V. N., Krasnov, A. P., Naumkin, A. V., and Shapovalov, V. A. (2017). Effects of Ultrasound Treatment of Expanded Graphite (EG) on the Sliding Friction, Wear Resistance, and Related Properties of PTFE-Based Composites Containing EG. *Wear* 386-387, 63–71. doi:10.1016/j.wear.2017.04.022

Alvaredo, Á., Martín, M., Castell, P., Guzmán de Villoria, R., and Fernández-Blázquez, J. (2019). Non-Isothermal Crystallization Behavior of PEEK/Graphene Nanoplatelets Composites from Melt and Glass States. *Polymers* 11, 124. doi:10.3390/polym11010124

Antoniadis, G., Paraskevopoulos, K. M., Bikiaris, D., and Chrissafis, K. (2009). Kinetics Study of Cold-Crystallization of Poly(ethylene Terephthalate) Nanocomposites with Multi-Walled Carbon Nanotubes. *Thermochim. Acta* 493, 68–75. doi:10.1016/j.tca.2009.04.005

Arjmand, M., Apperley, T., Okoniewski, M., and Sundararaj, U. (2012). Comparative Study of Electromagnetic Interference Shielding Properties of Injection Molded versus Compression Molded Multi-Walled Carbon Nanotube/polystyrene Composites. *Carbon* 50, 5126–5134. doi:10.1016/j.carbon.2012.06.053

Bangarusampath, D. S., Ruckdäschel, H., Altstädt, V., Sandler, J. K. W., Garray, D., and Shaffer, M. S. P. (2009). Rheological and Electrical Percolation in Melt-Processed Poly(ether Ether Ketone)/multi-wall Carbon Nanotube Composites. *Chem. Phys. Lett.* 482, 105–109. doi:10.1016/j.cplett.2009.09.064

Blundell, D. J., and Osborn, B. N. (1983). The Morphology of Poly(aryl-Ether-Ether-Ketone). *Polymer* 24, 953–958. doi:10.1016/0032-3861(83)90144-1

Cao, N., Shen, W., Wen, S., and Liu, Y. (1996). Surface Properties of Expanded Graphite. *Chemistry-Peking*, 37–40.

Cassagnau, P. (2008). Melt Rheology of Organoclay and Fumed Silica Nanocomposites. *Polymer* 49, 2183–2196. doi:10.1016/j.polymer.2007.12.035

Chang, L., and Zhang, Z. (2006). Tribological Properties of Epoxy Nanocomposites. *Wear* 260, 869–878. doi:10.1016/j.wear.2005.04.002

Chen, G.-H., Wu, D.-J., Weng, W.-G., He, B., and Yan, W.-l. (2001). Preparation of Polystyrene-Graphite Conducting Nanocomposites via Intercalation Polymerization. *Polym. Int.* 50, 980–985. doi:10.1002/pi.729

Debelak, B., and Lafdi, K. (2007). Use of Exfoliated Graphite Filler to Enhance Polymer Physical Properties. *Carbon* 45, 1727–1734. doi:10.1016/j.carbon.2007.05.010

Dhakate, S., Sharma, S., Borah, M., Mathur, R., and Dhami, T. (2008). Expanded Graphite-Based Electrically Conductive Composites as Bipolar Plate for PEM Fuel Cell. *Int. J. Hydrogen Energ.* 33, 7146–7152. doi:10.1016/j.ijhydene.2008.09.004

Díez-Pascual, A. M., Naffakh, M., González-Domínguez, J. M., Ansón, A., Martínez-Rubi, Y., Martínez, M. T., et al. (2010). High Performance PEEK/carbon Nanotube Composites Compatibilized with Polysulfones-II. Mechanical and Electrical Properties. *Carbon* 48, 3500–3511. doi:10.1016/j.carbon.2010.05.050

Dong, X., Xu, H., Chen, H., Wang, L., Wang, J., Fang, W., et al. (2019). Commercial Expanded Graphite as High-Performance Cathode for Low-Cost Aluminum-Ion Battery. *Carbon* 148, 134–140. doi:10.1016/j.carbon.2019.03.080

Du, X. S., Xiao, M., Meng, Y. Z., and Hay, A. S. (2004). Synthesis and Properties of Poly(4,4′-Oxybis(benzene)disulfide)/graphite Nanocomposites via *In Situ* Ring-Opening Polymerization of Macrocyclic Oligomers. *Polymer* 45, 6713–6718. doi:10.1016/j.polymer.2004.07.026

Flanagan, M., Grogan, D. M., Goggins, J., Appel, S., Doyle, K., Leen, S. B., et al. (2017). Permeability of Carbon Fibre PEEK Composites for Cryogenic Storage Tanks of Future Space Launchers. *Composites A: Appl. Sci. Manufacturing* 101, 173–184. doi:10.1016/j.compositesa.2017.06.013

Fukushima, K., Murariu, M., Camino, G., and Dubois, P. (2010). Effect of Expanded Graphite/layered-Silicate clay on thermal, Mechanical and Fire Retardant Properties of Poly(lactic Acid). *Polym. Degrad. Stab.* 95, 1063–1076. doi:10.1016/j.polymdegradstab.2010.02.029

Goyal, R. K. (2013). Cost-efficient High Performance Polyetheretherketone/expanded Graphite Nanocomposites with High Conductivity for EMI Shielding Application. *Mater. Chem. Phys.* 142, 195–198. doi:10.1016/j.matchemphys.2013.07.005

Goyal, R. K., Samant, S. D., Thakar, A. K., and Kadam, A. (2010). Electrical Properties of Polymer/expanded Graphite Nanocomposites with Low Percolation. *J. Phys. D: Appl. Phys.* 43, 365404. doi:10.1088/0022-3727/43/36/365404

Hatui, G., Bhattacharya, P., Sahoo, S., Dhibar, S., and Das, C. K. (2014). Combined Effect of Expanded Graphite and Multiwall Carbon Nanotubes on the Thermo Mechanical, Morphological as Well as Electrical Conductivity of *In Situ* Bulk Polymerized Polystyrene Composites. *Composites Part A: Appl. Sci. Manufacturing* 56, 181–191. doi:10.1016/j.compositesa.2013.10.007

Hu, J., Li, D. Y., and Llewellyn, R. (2005). Computational Investigation of Microstructural Effects on Abrasive Wear of Composite Materials. *Wear* 259, 6–17. doi:10.1016/j.wear.2005.02.017

Huang, L., Zhu, P., Chen, Z., Song, Y., Wang, X., and Huang, P. (2008). Tribological Performances of Graphite Modified Thermoplastic Polyimide. *Mater. Sci. Eng. Hangzhou* 26, 268–272.

Jia, Z., Hao, C., Yan, Y., and Yang, Y. (2015). Effects of Nanoscale Expanded Graphite on the Wear and Frictional Behaviors of Polyimide-Based Composites. *Wear* 338-339, 282–287. doi:10.1016/j.wear.2015.06.019

Kalin, M., Zalaznik, M., and Novak, S. (2015). Wear and Friction Behaviour of Poly-Ether-Ether-Ketone (PEEK) Filled with Graphene, WS 2 and CNT Nanoparticles. *Wear* 332-333, 855–862. doi:10.1016/j.wear.2014.12.036

Kalra, S., Munjal, B. S., Singh, V. R., Mahajan, M., and Bhattacharya, B. (2019). Investigations on the Suitability of PEEK Material under Space Environment Conditions and its Application in a Parabolic Space Antenna. *Adv. Space Res.* 63, 4039–4045. doi:10.1016/j.asr.2019.03.006

Kim, H., and Macosko, C. W. (2009). Processing-property Relationships of Polycarbonate/graphene Composites. *Polymer* 50, 3797–3809. doi:10.1016/j.polymer.2009.05.038

Kim, H., Thomas Hahn, H., Viculis, L. M., Gilje, S., and Kaner, R. B. (2007). Electrical Conductivity of Graphite/polystyrene Composites Made from Potassium Intercalated Graphite. *Carbon* 45, 1578–1582. doi:10.1016/j.carbon.2007.02.035

Kurtz, S. M. (2019). *PEEK Biomaterials Handbook*. Philadelphia: William Andrew, Applied Science Publisher

Li, Y.-C., and Chen, G.-H. (2007). HDPE/expanded Graphite Nanocomposites Prepared via Masterbatch Process. *Polym. Eng. Sci.* 47, 882–888. doi:10.1002/pen.20772

Liebscher, M., Domurath, J., Saphiannikova, M., Müller, M. T., Heinrich, G., and Pötschke, P. (2020). Dispersion of Graphite Nanoplates in Melt Mixed PC/SAN

Polymer Blends and its Influence on Rheological and Electrical Properties. *Polymer* 200, 122577. doi:10.1016/j.polymer.2020.122577

Mokhtari, M., Archer, E., Bloomfield, N., Harkin-Jones, E., and McIlhagger, A. (2021). High-performance and Cost-Effective Melt Blended Poly(ether Ether Ketone)/expanded Graphite Composites for Mass Production of Antistatic Materials. *Polym. Int.* 70, 1137–1145. doi:10.1002/pi.6226

Moniruzzaman, M., and Winey, K. I. (2006). Polymer Nanocomposites Containing Carbon Nanotubes. *Macromolecules* 39, 5194–5205. doi:10.1021/ma060733p

Noel, M., and Santhanam, R. (1998). Electrochemistry of Graphite Intercalation Compounds. *J. Power Sourc.* 72, 53–65. doi:10.1016/S0378-7753(97)02675-X

Pan, L., Liu, Z., kızıltaş, O., Zhong, L., Pang, X., Wang, F., et al. (2020). Carbon Fiber/poly Ether Ether Ketone Composites Modified with Graphene for Electro-thermal Deicing Applications. *Composites Sci. Techn.* 192, 108117. doi:10.1016/j.compscitech.2020.108117

Pei, X.-Q., Lin, L., Schlarb, A. K., and Bennewitz, R. (2019). Correlation of Friction and Wear across Length Scales for PEEK Sliding against Steel. *Tribology Int.* 136, 462–468. doi:10.1016/j.triboint.2019.04.001

Puértolas, J. A., Castro, M., Morris, J. A., Ríos, R., and Ansón-Casaos, A. (2019). Tribological and Mechanical Properties of Graphene Nanoplatelet/PEEK Composites. *Carbon* 141, 107–122. doi:10.1016/j.carbon.2018.09.036

Rival, G., Paulmier, T., and Dantras, E. (2019). Influence of Electronic Irradiations on the Chemical and Structural Properties of PEEK for Space Applications. *Polym. Degrad. Stab.* 168, 108943. doi:10.1016/j.polymdegradstab.2019.108943

Rong, C., Ma, G., Zhang, S., Song, L., Chen, Z., Wang, G., et al. (2010). Effect of Carbon Nanotubes on the Mechanical Properties and Crystallization Behavior of Poly(ether Ether Ketone). *Composites Sci. Techn.* 70, 380–386. doi:10.1016/j.compscitech.2009.11.024

Rozpłoch, F., Patyk, J., and Stankowski, J. (2007). Graphenes Bonding Forces in Graphite. *Acta Phys. Pol. A.* 112 (3), 557–562. doi:10.12693/APhysPolA.112.557

Sarathi, R., Sahu, R. K., and Rajeshkumar, P. (2007). Understanding the thermal, Mechanical and Electrical Properties of Epoxy Nanocomposites. *Mater. Sci. Eng. A* 445-446, 567–578. doi:10.1016/j.msea.2006.09.077

Schroeder, S., Braun, S., Mueller, U., Vogel, M., Sonntag, R., Jaeger, S., et al. (2020). Carbon-fibre-reinforced PEEK: An Alternative Material for Flexion Bushings of Rotating Hinged Knee Joints?. *J. Mech. Behav. Biomed. Mater.* 101, 103434. doi:10.1016/j.jmbbm.2019.103434

Sever, K., Tavman, İ. H., Seki, Y., Turgut, A., Omastova, M., and Ozdemir, I. (2013). Electrical and Mechanical Properties of Expanded Graphite/high Density Polyethylene Nanocomposites. *Composites B: Eng.* 53, 226–233. doi:10.1016/j.compositesb.2013.04.069

Song, L. N., Xiao, M., and Meng, Y. Z. (2006). Electrically Conductive Nanocomposites of Aromatic Polydisulfide/expanded Graphite. *Composites Sci. Techn.* 66, 2156–2162. doi:10.1016/j.compscitech.2005.12.013

Souza, J. C. M., Bentes, A. C., Reis, K., Gavinha, S., Buciumeanu, M., Henriques, B., et al. (2016). Abrasive and Sliding Wear of Resin Composites for Dental Restorations. *Tribology Int.* 102, 154–160. doi:10.1016/j.triboint.2016.05.035

Stack, M. M., and Mathew, M. (2003). Micro-abrasion Transitions of Metallic Materials. *Wear* 255, 14–22. doi:10.1016/S0043-1648(03)00204-7

Sun, Z., Zhao, Z.-K., Zhang, Y.-Y., Li, Y.-Q., Fu, Y.-Q., Sun, B.-G., et al. (2021). Mechanical, Tribological and thermal Properties of Injection Molded Short Carbon Fiber/expanded Graphite/polyetherimide Composites. *Composites Sci. Techn.* 201, 108498. doi:10.1016/j.compscitech.2020.108498

Wagener, R., and Reisinger, T. J. G. (2003). A Rheological Method to Compare the Degree of Exfoliation of Nanocomposites. *Polymer* 44, 7513–7518. doi:10.1016/j.polymer.2003.01.001

Wang, L., Zhang, L., and Tian, M. (2012). Effect of Expanded Graphite (EG) Dispersion on the Mechanical and Tribological Properties of Nitrile Rubber/EG Composites. *Wear* 276-277, 85–93. doi:10.1016/j.wear.2011.12.009

Wang, Y., Shen, C., and Chen, J. (2003). Nonisothermal Cold Crystallization Kinetics of Poly(ethylene Terephthalate)/Clay Nanocomposite. *Polym. J.* 35, 884–889. doi:10.1295/polymj.35.884

Weng, W., Chen, G., Wu, D., Chen, X., Lu, J., and Wang, P. (2004). Fabrication and Characterization of Nylon 6/foliated Graphite Electrically Conducting Nanocomposite. *J. Polym. Sci. B Polym. Phys.* 42, 2844–2856. doi:10.1002/polb.20140

Wu, D., Wu, L., Wu, L., Xu, B., Zhang, Y., and Zhang, M. (2007). Nonisothermal Cold Crystallization Behavior and Kinetics of Polylactide/clay Nanocomposites. *J. Polym. Sci. B Polym. Phys.* 45, 1100–1113. doi:10.1002/polb.21154

Yang, Y.-l., Jia, Z.-n., Chen, J.-j., and Fan, B.-l. (2010). Tribological Behaviors of PTFE-Based Composites Filled with Nanoscale Lamellar Structure Expanded Graphite. *J. Tribol.* 132 (3), 031301. doi:10.1115/1.4001546

Zhang, G., Schlarb, A. K., Tria, S., and Elkedim, O. (2008). Tensile and Tribological Behaviors of PEEK/nano-SiO2 Composites Compounded Using a ball Milling Technique. *Composites Sci. Techn.* 68, 3073–3080. doi:10.1016/j.compscitech.2008.06.027

Zhang, H.-B., Zheng, W.-G., Yan, Q., Jiang, Z.-G., and Yu, Z.-Z. (2012). The Effect of Surface Chemistry of Graphene on Rheological and Electrical Properties of Polymethylmethacrylate Composites. *Carbon* 50, 5117–5125. doi:10.1016/j.carbon.2012.06.052

Zhang, J., Tian, W., Chen, J., Yu, J., Zhang, J., and Chen, J. (2019). The Application of Polyetheretherketone (PEEK) Implants in Cranioplasty. *Brain Res. Bull.* 153, 143–149. doi:10.1016/j.brainresbull.2019.08.010

Zhao, Y. F., Xiao, M., Wang, S. J., Ge, X. C., and Meng, Y. Z. (2007). Preparation and Properties of Electrically Conductive PPS/expanded Graphite Nanocomposites. *Composites Sci. Techn.* 67, 2528–2534. doi:10.1016/j.compscitech.2006.12.009

Zhao, Y., Qiu, Z., Yan, S., and Yang, W. (2011). Crystallization Behavior of Biodegradable poly(L-Lactide)/multiwalled Carbon Nanotubes Nanocomposites from the Amorphous State. *Polym. Eng. Sci.* 51, 1564–1573. doi:10.1002/pen.21933

Zheng, G., Wu, J., Wang, W., and Pan, C. (2004). Characterizations of Expanded Graphite/polymer Composites Prepared by *In Situ* Polymerization. *Carbon* 42, 2839–2847. doi:10.1016/j.carbon.2004.06.029

Conflict of Interest: Author NB was employed by company Denroy Plastics, United Kingdom.

The remaining authors declare that the research was conducted in the absence of any commercial or financial relationships that could be construed as a potential conflict of interest.

Publisher's Note: All claims expressed in this article are solely those of the authors and do not necessarily represent those of their affiliated organizations, or those of the publisher, the editors and the reviewers. Any product that may be evaluated in this article, or claim that may be made by its manufacturer, is not guaranteed or endorsed by the publisher.

frontiers in Materials

ORIGINAL RESEARCH
published: 28 September 2021
doi: 10.3389/fmats.2021.737689

Simulated Effect of Carbon Black on High Speed Laser Transmission Welding of Polypropylene With Low Line Energy

M. Mahmood Ali[1,2], *Foram Dave*[1,2], *Richard Sherlock*[1,3], *Alistair Mcilhagger*[4] *and David Tormey*[1,2]*

[1]Department of Mechanical and Manufacturing Engineering, Institute of Technology Sligo, Sligo, Ireland, [2]Centre for Precision Engineering, Materials and Manufacturing Research, Institute of Technology Sligo, Sligo, Ireland, [3]Department of Life Sciences, School of Science, Institute of Technology Sligo, Sligo, Ireland, [4]School of Engineering, Ulster University, Newtownabbey, United Kingdom

OPEN ACCESS

Edited by:
Dong Xiang, Southwest Petroleum University, China

Reviewed by:
Tang Zhenhua, Chongqing University, China
Jingyao Sun, Beijing University of Chemical Technology, China

***Correspondence:**
David Tormey
Tormey.David@itsligo.ie

Specialty section:
This article was submitted to Polymeric and Composite Materials, a section of the journal Frontiers in Materials

Received: *07 July 2021*
Accepted: *13 September 2021*
Published: *28 September 2021*

Citation:
Ali MM, Dave F, Sherlock R, Mcilhagger A and Tormey D (2021) Simulated Effect of Carbon Black on High Speed Laser Transmission Welding of Polypropylene With Low Line Energy. Front. Mater. 8:737689. doi: 10.3389/fmats.2021.737689

Laser welding is an important manufacturing tool for a wide variety of polymer products including consumer goods, automotive components and medical devices. The laser process parameters and polymer properties have a significant impact on weld quality. Due to higher heat density generated by the laser transmission welding (LTW) technique, defining a set of suitable parameters for LTW of thermoplastics and composites can be challenging. In this work the effect of carbon black along other control parameters has been investigated for high speed welding using a laser source of 980 nm wavelength with low line energy. In this work, the finite element method (FEM)-based software COMSOL Multiphysics is used to create a 3D transient thermal model for LTW of isotactic polypropylene (iPP) and its composites with carbon black (CB) of concentrations ranging from 0.5 wt% to 1.5 wt%. The design of experiments based on Box-Behnken design (BBD) is used to organize the simulation experiments and mathematical models are developed based on multiple curvilinear regression analysis on the simulation findings. Independent control variables include the laser power, welding speed, beam diameter, and carbon black content in the absorbent polymer. The maximum weld temperature, weld width, and weld depth within the transmissive and absorptive layers are considered as dependent response variables. Furthermore, sensitivity analysis is carried out to investigate the impact of carbon black along with other independent variables on the responses. The welding feasibility check was performed on the basis of melt and degradation temperature of the materials, and weld depths of transmissive and absorptive layers. It has been observed that the composites containing 0.5 wt% and 1 wt% of CB can be welded successfully with neat iPP. However, due to a degradation temperature problem, composites having a larger proportion of CB (>1 wt%) appear to be more difficult to weld.

Keywords: carbon black, laser transmission welding, simulation, high speed laser processing, polypropylene composite, low line energy

INTRODUCTION

Laser processing technology has become well established, playing a crucial role in solving several challenging manufacturing issues for about 4 decades (Purtonen et al., 2014). Laser welding, for example, is one of the processes that has emerging as a result of its unique characteristics, such as thermal and power stability, immunity to external interference, and suitability for joining two surfaces of specific materials (De Pelsmaeker et al., 2018; Dave et al., 2021). There are several types of laser welding categorized on the basis of laser source (solid-state, gas, diode, fibre), temporal characteristics (continuous, pulsed); material geometry, (butt, corner, edge, lap, T-joint), laser-material interaction (direct, surface heating, through transmission), and mode of laser beam delivery (contour, simultaneous, quasi-simultaneous, masked) (Grewell et al., 2003; Grewell and Benatar, 2007; Troughton, 2008; Tres, 2017; Dave et al., 2021). Laser transmission welding (LTW) is an innovative technique due to its advantages as non-contamination, rapidity, a high spatial resolution, with no vibration from tool (Dave et al., 2021), (Borges, 2016), (Jones, 2013). LTW is the most common technique used for polymers in lap geometry using continuous laser diode by contour welding as shown in **Figure 1**.

The LTW in lap geometry involves two dissimilar materials: the top layer (transmissive layer) is transparent or semi-transparent which allows the laser beam propagation to the bottom layer (absorptive layer) which is absorptive in nature and the energy coming from the laser beam is absorbed and converted into heat. The process has a key advantage that the majority of the laser energy is delivered only at the interface where the weld is to be formed, although some energy can be lost due to absorption and/or light scattering in the transmissive layer. Due to close contact, the heat is propagated by conduction into both layers, leading to melting and bonding of the materials when the local temperature exceeds the melting temperature ($T > T_m$). However, local temperatures in excess of the degradation temperature of one or other of the constituent materials can result in contamination of the weld zone and poor joint characteristics.

The necessary optical properties of the absorptive polymer material typically arise from the inclusion of fillers such as carbon nanotubes, graphene nanoparticles, fibres and, most commonly, carbon black (CB) nanoparticles. These additives enhance the absorption coefficient (Chen et al., 2011; Rodríguez-Vidal et al., 2014; Wippo et al., 2014). CB is also used as a compounding component to increase the end product's strength. It is a type of spherical elemental carbon particle that has consolidated into colloidal size aggregates and can be considered as an intermediate matter that has a two-dimensional repeating pattern within each layer. Carbon black particles with primary particle sizes of 20 and 60 nm and concentrations by weight are blended into the base material during an extrusion process (Haberstroh and Lützeler, 2001).

For modelling or analysing the performance of manufacturing technology, numerical methods are widely used. Moreover, analytical and numerical techniques are widely used to simulate the laser transmission welding process. Many researchers have reported the work for achieving the best quality welds with the aid of simulations and furthermore optimization of the process (Potente et al., 1999) (Kumar et al., 2019) (Labeas et al., 2010; Acherjee et al., 2011; Wang et al., 2012; Nakhaei et al., 2013). Potente et al. (Potente et al., 1999) analysed the heating phase in laser transmission welding of polyamide (PA). In that work, the material properties are assumed to be constant and the effect of heat convection during the welding process was ignored. Also, a correction factor is added in order to allow for the different temperature profile in case of an absorbing part having a low absorption coefficient. For achieving the best quality weld, the modelling of optical laser transmission welding and analysis has been considered as shown in **Figure 2**.

The modelling of thermal profile for LTW of two thermoplastic parts of polypropylene (PP) has been carried out in this research. The transmissive layer of an isotactic polypropylene (iPP) is responsible for scattering and reflection losses whereas most of the transmissive power is absorbed at the

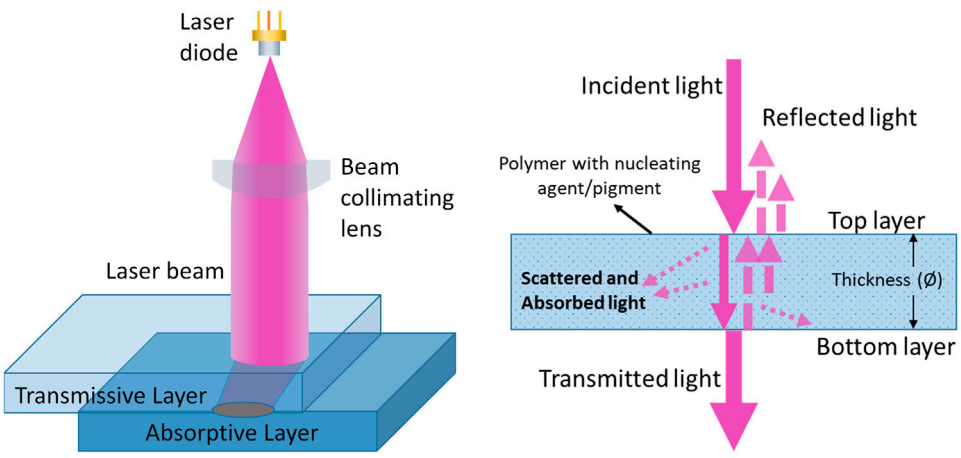

FIGURE 1 | Schematic of transmission laser welding of lap geometry of materials (left) and light transmission through transmissive layer with reflected, scattered and absorbed light phenomena (right).

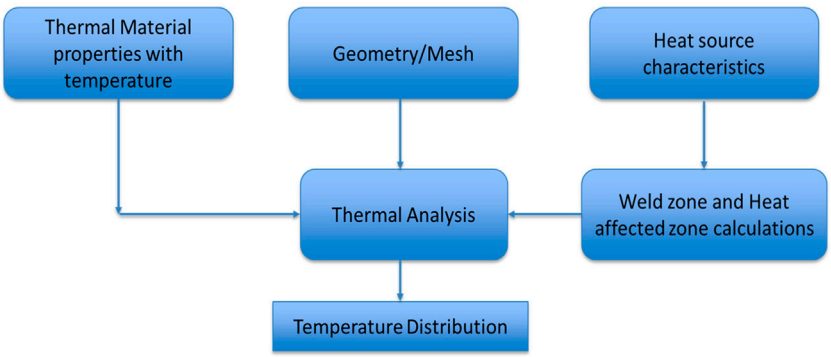

FIGURE 2 | Block diagram for modelling of optical laser transmission welding and analysis for achieving quality weld.

absorptive layer which contains wt% fraction of carbon black (CB) filler, responsible for absorption which is converted ultimately into heat source for welding. In this work, wt% of CB in PP is the key parameter for changing the absorption coefficient. Light scattering, reflection, and absorption occur in materials, and these events alter the energy and spatial distribution of the laser beam. The amount of energy transferred between the components to be connected determines the amount of melted volume. Furthermore, the clamping mechanism or breakdown of the cohesiveness between the filler and the matrix can induce deformations due to high thermal energy. To avoid poor joint quality, a process parameter optimization based on optical and thermal properties of materials is required (Labeas et al., 2010). Good temperature estimations can allow for a more accurate representation of how individual materials behave during laser welding, as well as identifying suitable process conditions. Acherjee et al. (Acherjee et al., 2012a), (Acherjee et al., 2012b) conducted a computational study of the influence of carbon black on the temperature field and weld profile during laser transmission welding of polymers using polycarbonate as the work material. That work was conducted for high line energy however, for low line energy with high speed laser, the effect of carbon black on the performance of laser transmission welding needs to be investigated. Therefore, the present work has investigated the influence of carbon black in detail.

Line energy in laser transmission welding is defined as the ratio of laser power to the scan speed (Kumar et al., 2019; Gupta et al., 2018). The line energy used in this study is in the range of 0.05–0.12 J/mm. This range has been found to be effective for high-speed welding in experimental trials carried out by the authors that will be reported separately. The line energies used here are substantially lower than in the reported research work of Acherjee et al., which are in the range of 0.4–1.2 J/mm (Acherjee et al., 2012a). In real-time laser welding process of polymer composites with given laser line energy, the microstructure changes are expected in the material as presented by Ghorbel et al. (Ghorbel et al., 2009). However this work involves the analysis of thermal profile of the lap joint area carried out with the aid of simulations utilising the heat transfer module of COMSOL Multiphysics software and it doesn't include the microstructure changing during welding process. The current work is based on industrial project where polypropylene (PP) is used as the base material and also polypropylene is widely used worldwide polymer for most of the applications in industries. PP is also preferred for various properties due to its semi-crystalline nature, such as mechanical thermal and chemical resistance etc. The modelling approach has been developed in such a way that in future, the suitability of laser welding of different polymer materials can also be tested using their thermal properties.

In this paper, the details of properties used for numerical modelling and investigations have been provided in **section 2**. In **section 3**, the optical modelling of the laser beam has been discussed. The light scattering decay and beam broadening effect due to scattering has been considered in the model of the laser beam. Moreover, it has been explained that how this beam is absorbed by the absorptive layer with the aid of the Beer-Lambert law. It is apparent that the volume term source and heat flux generated during laser welding are the effects of absorption. In **section 4**, the model of laser beam has been used to compute the temperature field evolution during LTW. In order to understand the importance of the optical properties of the material in the LTW, a parameter study is realized on the absorption coefficient of the absorptive part by taking into account the CB (wt%) in polymer matrix.

In **section 5**, the design of experiment has been presented in detail. Box-Behnken design has been used as it has fewer design points than central composite design (CCD) with the same number of factors, and so can be less expensive to perform. The process parameters are laser power (P), speed (S), diameter (D), CB in wt% whereas the responses are considered as weld width (WW), weld depth of absorptive layer (D_A), weld depth of transmissive layer (D_T) and maximum weld temperature (T_{max}).

Finally, in **section 6**, the results have been discussed and the values of process parameters have been investigated for defining feasible laser transmission welding parameters. Finally, conclusions and future work have been presented in **section 7**.

MATERIAL SELECTION AND GEOMETRY PROPERTIES

All materials in the FE model, namely PP and its composite PP/CB, are used in simulations as thermal-brick components with

TABLE 1 | Thermophysical and optical properties of the PP used in simulations.

Property	iPP	PP with 0.5 wt% CB	PP with 1.0 wt% CB	PP with 1.5 wt% CB
Density = ρ [kg/m3]		900		
Specific heat = c [J/(kg.K)]		$= \begin{cases} 1.92[1 + 3(T-25)10^{-3}] \text{ for } T \le T_m \\ 2.54[1 + 1.4(T-25)10^{-3}] \text{ for } T > T_m \end{cases}$ $T_m = (140 + 273)$ K		
Thermal conductivity = k [W/(m.K)]	0.210	0.235	0.260	0.285
Absorption coefficient = Ac (1/mm)	—	35	70	105

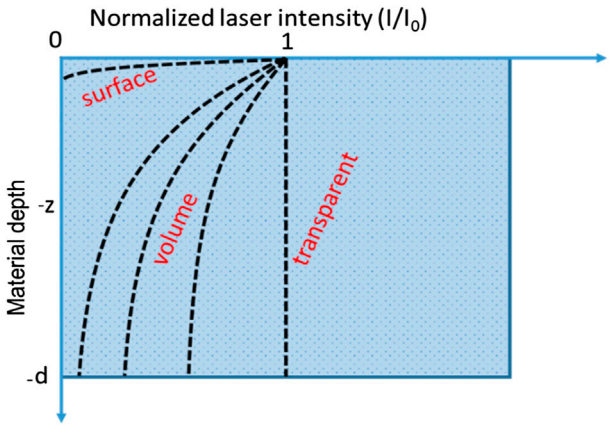

FIGURE 3 | Illustration of surface or volume absorption of laser beam by material.

only one temperature degree of freedom at constant pressure. **Table 1** shows the material parameters such as density (ρ), thermal conductivity (k), and specific heat (c), these values have been taken after consulting the literature (Petrović et al., 1993; Wang et al., 2014; Geiger et al., 2009). For the sake of simplicity, the changes in material characteristics, with the exception of specific heat, are assumed to be temperature independent during the LTW process. The lap joint geometry is used where only the overlapped area is considered for simulations to reduce the computation time. The thickness of each layer is L_z = 2 mm whereas the overlapped width is L_y = 5 mm and length along the contour is L_x = 10 mm.

MODELLING OF LASER BEAM

For most polymers in their natural state there is typically little or no absorption at the wavelengths emitted by the diode lasers commonly employed in welding machinery (wavelengths in the range 800–980 nm approx.). Hence the polymers are considered as transparent or sometimes semi-transparent due to the presence of low level absorption and/or light scattering.

As light passes through a medium, it is absorbed according to Lambert-Beer's law, $I(z) = I_0\, e^{-A_c z}$ where I_0 denotes the intensity of the light and A_c represents the absorption coefficient depends on the intrinsic properties of the material, operating wavelength, temperature and other parameters. Generally, A_c can cover values from zero (fully transparent) over a medium range (volume absorber) up to $10^4\,\text{cm}^{-1}$ (surface absorber) (Bonten and Tüchert, 2002; Bachmann and Russek, 2003). The concept of absorption in volume or surface is illustrated in the generalized diagram shown in **Figure 3**. In this study, the laser wavelength is fixed at 980 nm. The absorbed light in the material is converted to heat, leading to a temperature increase, which may cause melting or thermal degradation.

The laser beam power propagated through the transmissive layer can be modelled in terms of Gaussian beam as (AkuéAsséko et al., 2015)

$$P(x,y,z) = \frac{P_0(1-R_c)}{2\pi\sqrt{(\sigma_x^2(z)+\sigma_0^2)}\sqrt{(\sigma_y^2(z)+\sigma_0^2)}} e^{-\left(\frac{(x-x_0)^2}{2\left(\sigma_x^2(z)+\sigma_0^2\right)}+\frac{(y-y_0)^2}{2\left(\sigma_y^2(z)+\sigma_0^2\right)}\right)} e^{-D_s z} \tag{1}$$

where P_0 is the initial power of laser beam, R_c is the reflection coefficient. D_s is the scattering coefficient. σ_0 is the beam standard deviation in x and y-axis whereas σ_x and σ_y are the functions of z, refraction index of matrix, spherulites and nucleating agents/ pigments.

After considering the thickness of transmissive layer L_z, the equivalent volume heat source at absorber layer can be modelled as

$$Q(x,y,z) = \frac{P_0(1-R_C)A_c}{2\pi\sqrt{(\sigma_x^2(L_z)+\sigma_0^2)}\sqrt{(\sigma_y^2(L_z)+\sigma_0^2)}} e^{-\left(\frac{(x-x_0)^2}{2\left(\sigma_x^2(L_z)+\sigma_0^2\right)}+\frac{(y-y_0)^2}{2\left(\sigma_y^2(L_z)+\sigma_0^2\right)}\right)} e^{-D_s L_z} e^{-A_c z} \tag{2}$$

For moving laser source in LTW, scan speed is also included in the model, therefore in **(2)**,

$$x_0 = -(L_x + D) + S \times t$$

where D is the beam diameter in mm, S is the speed in mm/s and t is the time in s. The scattering effect in the transmissive layer is illustrated in **Figure 4**.

In present study, the following values are used: R_c = 0.04, $D = 4\sigma_0$, $\sigma_x(L_z) = \sigma_y(L_z) = cL_z$ where c is constant used for compensating the effect of broadening of beam due to scattering.

HEAT TRANSFER MODELLING OF HIGH SPEED LTW OF PP AND PP/CB WITH LOW LINE ENERGY

In real-time laser welding process of polymer composites, the microstructure changes are expected in the material as presented by Ghorbel et al. (Ghorbel et al., 2009). However in this work, the analysis of thermal profile of the lap joint area was carried out

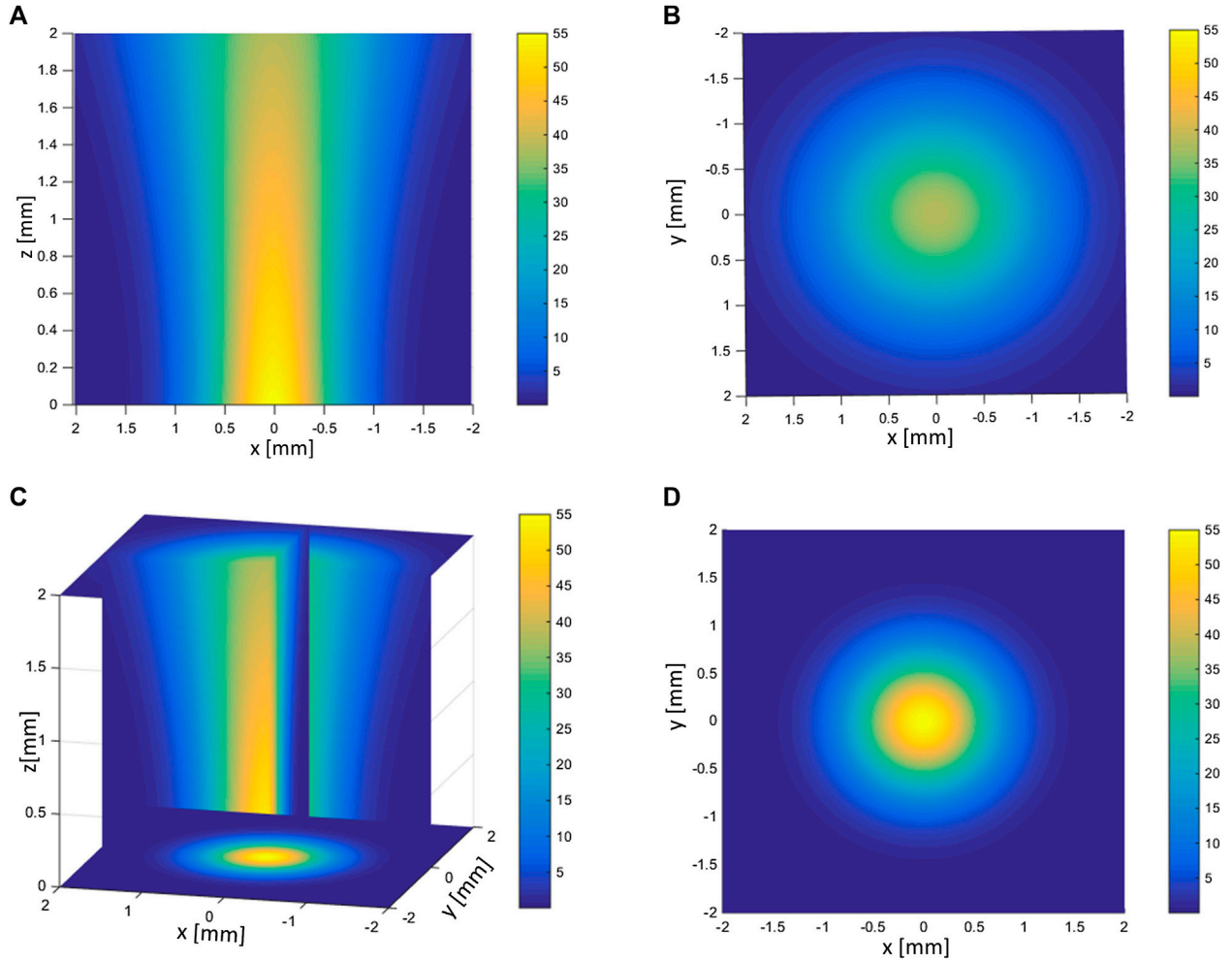

FIGURE 4 | Illustration of beam intensity decay and broadening due to scattering from semi-transparent polypropylene layer **(A)** cross-sectional view of input beam profile **(B)** cross-sectional view of transmitted beam including scattering effect, **(C)** 3D view and **(D)** 2D view on xz-plane.

with the aid of simulations utilising the heat transfer module of COMSOL Multiphysics software. In order to calculate the temperature field, the following assumptions have been made (Acherjee et al., 2010):

1 The contacting welding materials of the PP and its composite with CB were deemed to be in close proximity. During the LTW process, isotropic thermophysical behavior has been considered.
2 The heat conduction of the PP and its composite with CB, as well as free convection between the surfaces of the PP and its composite with CB, were considered. The heating effects of phase transitions were neglected.
3 The portion of the geometry where the temperature gets higher than the melting temperature (T_m), has been considered as the "weld zone."

The thermophysical and optical properties used in the simulation are provided in **Table 1**. The differential equation for the three-dimensional model was considered to model the heat transfer in the LTW process through COMSOL that defined the temperature distribution within the body, and it follows the energy conservation law.

The rate of internally generated heat within the body can be represented by heat equation to model heat transfer in solids as (Comsol, 2020)

$$\rho c \frac{\partial T}{\partial t} + \rho c \, \mathbf{u}. \nabla T + \nabla . \mathbf{q} = Q \tag{3}$$

where the following material properties, fields, and sources: ρ (SI unit: kg/m3) is the polymer density, c (SI unit: J/(kgK)) is the specific heat capacity at constant pressure, k (SI unit: W/(mK)) is the thermal conductivity of the polymer and u (SI unit: m/s) is the velocity field defined by the translational motion subnode when parts of the model are moving in the material frame and Q (SI unit: W/m^3) is the heat source. Moreover, the thermal conductivity k describes the relationship between the heat flux vector q and the temperature gradient ∇T in $q = -k\nabla T$, which is Fourier's law of heat conduction.

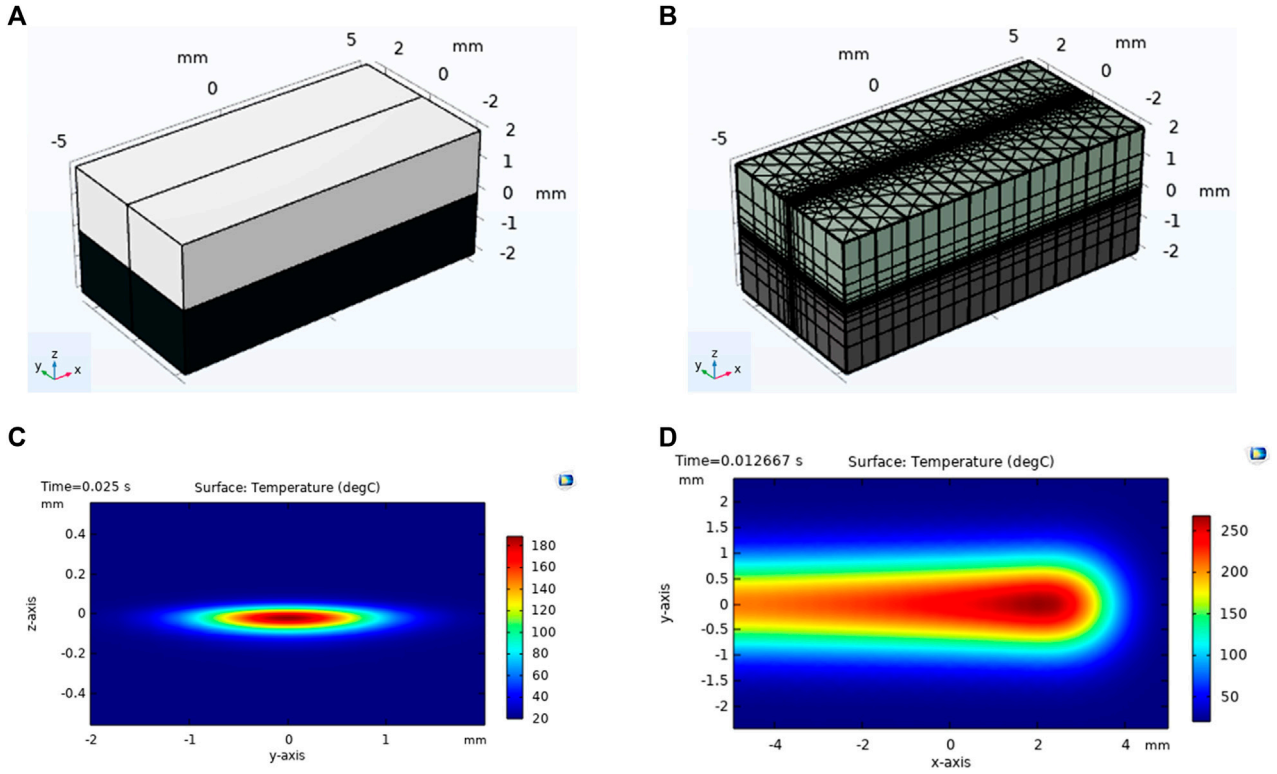

FIGURE 5 | (A) Schematics of the transmissive PP and absorptive PP with wt% CB with the lapped portion, **(B)** illustration of non-uniform mesh pattern used for the geometrical model, **(C)** thermal profile (temperature) of (0, y, z) plane during LTW at t = 0.025 s, (d) thermal profile (temperature) of (x, y, 0) plane during LTW at t = 0.0127 s simulated for the absorptive layer of 0.5 wt% CB/PP for p = 100 W, speed = 1,200 mm/s.

To consider the heat transfer from boundaries to the ambient, the net inward heat flux from surface-to-ambient radiation and due to convective heat transfer, can be written as (Comsol (2020); Heat Trans, 2020)

$$-\mathbf{n}.\mathbf{q} = h\left(T - T_{amb}\right) + \varepsilon\sigma\left(T^4 - T_{amb}^4\right) \tag{4}$$

where ε is the surface emissivity, σ is the Stefan-Boltzmann constant, and T_{amb} is the ambient temperature. The value of surface emissivity is set as 0.97 for polypropylene whereas the heat transfer coefficient (h) for the convective heat transfer part has been considered as 10 W/(m^2.K) (Wang et al., 2014). The degradation temperature was used as 500°C (Esmizadeh et al., 2020).

Only the lap joint area has been used for the simulation as shown in **Figure 5A**. To reduce, computational time, a non-uniform meshing was considered by keeping the mesh size to a minimum near to the weld contour and using a relatively larger mesh size approaching the external boundaries of the geometry, as shown in **Figure 5B**. By varying the power (P), speed (S) of laser beam with diameter of 2 mm, maximum weld temperature was calculated. In addition, criteria was also set so that values of P and S that generate temperatures less than the melting point (140°C) and greater than the degradation temperature (500 C) are not suitable as welding input parameters. The thermal profile simulated for the absorptive layer of 0.5 wt% CB/PP for p = 100 W, speed = 1,200 mm/s at (0, y, z) plane during LTW at t = 0.025 s is shown in **Figure 5C**. A thermal profile (temperature) of (x, y, 0) plane during LTW at t = 0.0127 s is shown in **Figure 5D**.

Figures 6A, B shows the changing temperature along the welding contour xz-plane at 0.0087 and 0.05 s, respectively. It can be seen that the temperature gets increased initially and the then slowly decreases and disperses. On the basis of the maximum width covered by the thermal plot above melting point of PP (140 C) the bond started to form at the weld interface when the temperature reached at 140 C and eventually the weld width and depth are calculated which is illustrated by **Figures 6C, D**. The temperature increased rapidly along the x direction at the time of laser interaction with material and dropped gradually after the laser passes away from that point which is shown in **Figure 6E**. The maximum temperature of the weld occurs in the absorptive layer instead of instead of interface, which shows that this is volume absorption and therefore the asymmetric thermal profile can be seen along y-axis transverse to the welding direction **Figure 6C**.

DESIGN OF EXPERIMENTS AND EMPIRICAL MODELING

Low energy levels can cause a weak, and low-strength joint, whereas excessive energy levels potentially lead to degradation and vaporization, which also can result in poor joint quality. in.

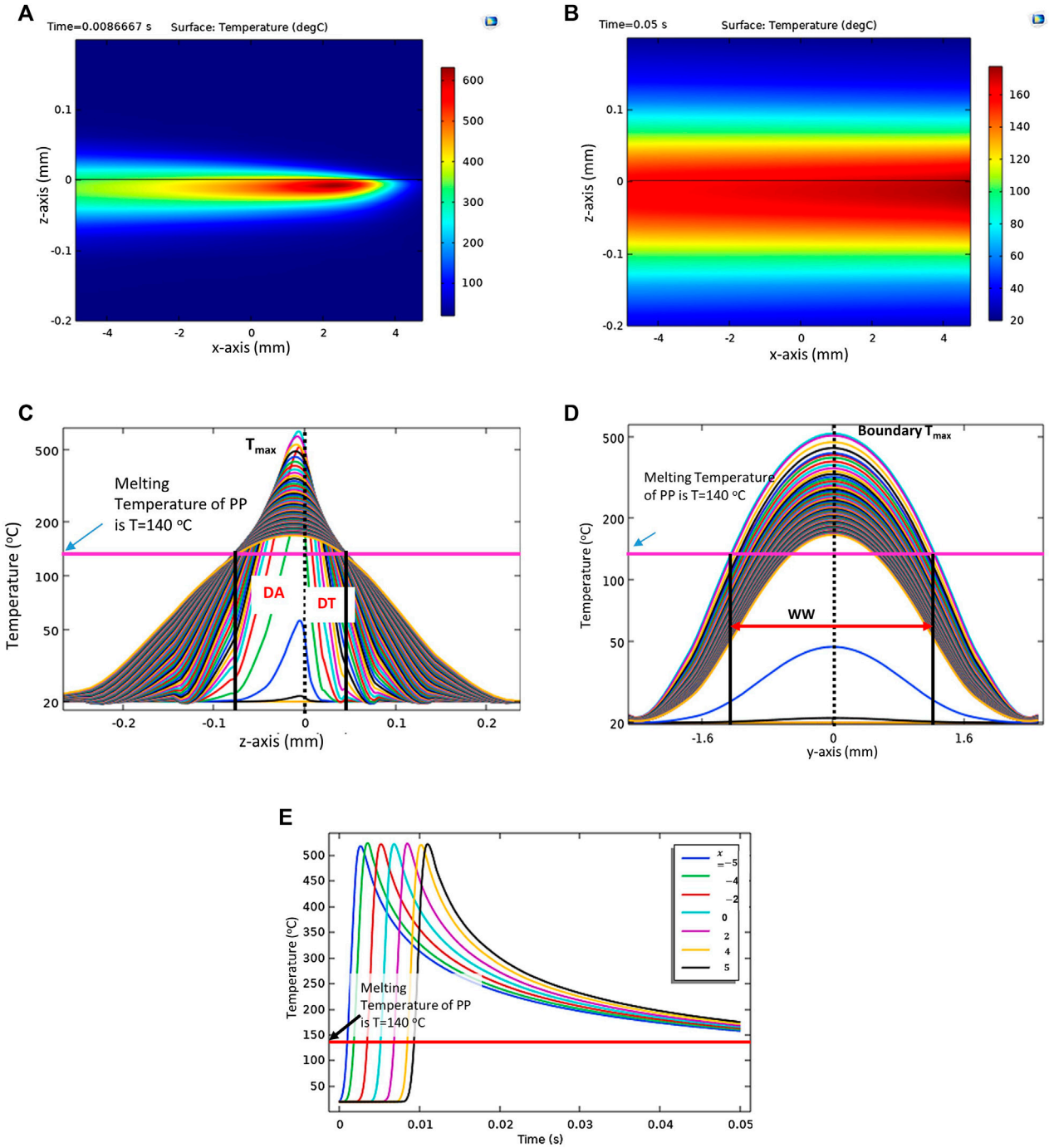

FIGURE 6 | Thermal profile (temperature) at (x, 0, z) plane during LTW at **(A)** t = 0.0087 s and **(B)** t = 0.05 s simulated for the absorptive layer of 1.0 wt% CB/PP for p = 120 W, speed = 1,200 mm/s with beam diameter 1.9 mm, **(C)** temperature curves evolution with time during LTW along z-axis at x = y = 0 used for the measurement of weld depth for transmissive layer (D_T) and absorptive layer (D_A), **(D)** temperature curves evolution with time during LTW along y-axis at x = z = 0 used for the measurement of weld width (WW) and **(E)** temperature versus time at x = −5, −4, −2, 0, 2, 4, and 5.

As a result, the energy provided to the surfaces for each process application must be optimized. This can be achieved either by performing an essential number of experiments, which increases the cost and the required development time of the desired product, or by a parametric investigation through numerical simulation. Therefore, a validated numerical simulation tool for the analysis and optimization of the LTW process parameters needs to be developed. The heat transfer module of COMSOL Multiphysics 5.6 software is utilized for numerical model simulations developed for this optimisation study.

A three-level-four-factor Box-Behnken design (BBD) was applied to determine the best combination of control variables for good quality weld. **Table 2** shows the ranges and levels of the selected process control parameters, as well as the units, levels, and notations studied in this study.

Empirical models are developed for simulation results in **Table 3** using multiple curvilinear regression analysis as presented by Kim et al. (Kim et al., 2003). A functional relationship between input and output variables is assumed as the following:

$$y_i = \beta_{0i}\,(P)^{\beta_{1i}}\,(S)^{\beta_{2i}}\,(D)^{\beta_{3i}}\,(C)^{\beta_{4i}}, \qquad 1 \le i \le 4 \tag{5}$$

where y_i is the output response i.e., $y_1 = WW$, $y_2 = D_T$, $y_3 = D_A$ and $y_4 = T_{max}$ and the β's are a set of unknown parameters, called regression coefficients. A regression equation of the following form is obtained by taking common logarithm of **(5)**,

$$\log y_i = \log \beta_{0i} + \beta_{1i} \log P + \beta_{2i} \log S + \beta_{3i} \log D + \beta_{4i} \log C \tag{6}$$

$$Y_i = b_{0i} + b_{1i}X_1 + b_{2i}X_2 + b_{3i}X_3 + b_{4i}X_4 \tag{7}$$

where

$$\beta_{ji} = \begin{cases} 10^{b_{ji}}, & j = 0 \\ b_{ji}, & 0 < j \le 4 \end{cases}$$

(6)can be treated as a first-order regression model as illustrated in **(7)**. After running the regression analysis on **(7)** in Microsoft Excel, the model equation for each response are obtained as in **(5)**.

The developed empirical models for maximum temperature (T_{max}) during LTW, weld width (WW), weld depth in transparent part (D_T), and weld depth in absorbing part (D_A), which can be used for prediction within same design space, is given as follows:

$$WW = 3.983092\,P^{0.4241}\,S^{-0.3369}\,D^{-0.2011}\,C^{0.2783} \tag{8}$$

$$D_T = 5.16259\,P^{1.4814}\,S^{-1.474}D^{-2.2485}C^{0.5105} \tag{9}$$

$$D_A = 1.139741\,P^{0.8466}\,(S)^{-0.8421}\,(D)^{-1.2744}\,(C)^{-0.1716} \tag{10}$$

$$T_{max} = 2212.976\,(P)^{0.847}\,(S)^{-0.62685}\,(D)^{-1.3693}\,(C)^{0.3943} \tag{11}$$

ANOVA results for $\log WW$, $\log D_T$, $\log D_A$, and $\log T_{max}$ are provided in **Table 4**. The correlation between the actual and anticipated values of T_{max} (°C), WW (mm), D_T (mm), and D_A (mm) is shown in **Figures 7A–D**. These figures show that the established models are appropriate, and the anticipated outcomes are consistent with the actual data.

TABLE 2 | Process Control parameters and their levels.

Parameter	Notation	Unit	Levels		
			−1	0	1
Power	*P*	W	80	100	120
Speed	*S*	mm/s	1,000	1,200	1,400
Beam Diameter	*D*	mm	1.9	2	2.1
Carbon black content	*C*	wt%	0.5	1	1.5

TABLE 3 | Box-Behnken experimental design and response values for weld width (WW), weld depths in transmissive layer (D_T) and absorptive layer (D_A), and maximum weld temperature (T_{max}).

Order no	Defining levels using BBD				Actual values				Response parameters			
	P	S	D	C	P	S	D	C	WW (mm)	D_T (mm)	D_A (mm)	T_{max} (°C)
1	−1	−1	0	0	80	1,000	2.0	1.0	2.20	0.0290	0.0570	467
2	−1	1	0	0	80	1,400	2.0	1.0	1.96	0.0170	0.0435	379
3	1	−1	0	0	120	1,000	2.0	1.0	2.56	0.0480	0.0800	660
4	1	1	0	0	120	1,400	2.0	1.0	2.34	0.0320	0.0610	534
5	0	0	−1	−1	100	1,200	1.9	0.5	1.88	0.0230	0.0710	400
6	0	0	−1	1	100	1,200	1.9	1.5	2.48	0.0370	0.0600	614
7	0	0	1	−1	100	1,200	2.1	0.5	1.80	0.0170	0.0630	350
8	0	0	1	1	100	1,200	2.1	1.5	2.46	0.0310	0.0520	533
9	−1	0	0	−1	80	1,200	2.0	0.5	1.58	0.0125	0.0560	309
10	−1	0	0	1	80	1,200	2.0	1.5	2.27	0.0250	0.0460	472
11	1	0	0	−1	120	1,200	2.0	0.5	2.04	0.0280	0.0780	435
12	1	0	0	1	120	1,200	2.0	1.5	2.60	0.0420	0.0660	669
13	0	−1	−1	0	100	1,000	1.9	1.0	2.43	0.0430	0.0735	605
14	0	−1	1	0	100	1,000	2.1	1.0	2.40	0.0350	0.0650	528
15	0	1	−1	0	100	1,400	1.9	1.0	2.20	0.0270	0.0555	491
16	0	1	1	0	100	1,400	2.1	1.0	2.14	0.0215	0.0485	429
17	−1	0	−1	0	80	1,200	1.9	1.0	2.10	0.0245	0.0520	448
18	−1	0	1	0	80	1,200	2.1	1.0	2.06	0.0195	0.0460	391
19	1	0	−1	0	120	1,200	1.9	1.0	2.44	0.0430	0.0735	632
20	1	0	1	0	120	1,200	2.1	1.0	2.42	0.0350	0.0650	550
21	0	−1	0	−1	100	1,000	2.0	0.5	2.00	0.0283	0.0783	423
22	0	−1	0	1	100	1,000	2.0	1.5	2.58	0.0420	0.0650	635
23	0	1	0	−1	100	1,400	2.0	0.5	1.69	0.0145	0.0590	337
24	0	1	0	1	100	1,400	2.0	1.5	2.36	0.0280	0.0480	521
25	0	0	0	0	100	1,200	2.0	1.0	2.28	0.0300	0.0590	504
26	0	0	0	0	100	1,200	2.0	1.0	2.28	0.0300	0.0590	504
27	0	0	0	0	100	1,200	2.0	1.0	2.28	0.0300	0.0590	504

TABLE 4 | ANOVA results for log*WW*, log D_T, log D_A and log T_{max}.

Source	log ***WW***		log D_T		log D_A		log T_{max}	
	F-value	***p*-value**	**F-value**	***p*-value**	**F-value**	***p*-value**	**F-value**	***p*-value**
Model	171.0085	<0.001	164.2804	<0.001	2,479.358	<0.001	902.7742	<0.001
log ***P***	—	<0.001	—	<0.001	—	<0.001	—	<0.001
log ***S***	—	<0.001	—	<0.001	—	<0.001	—	<0.001
log ***D***	—	0.1734	—	<0.001	—	<0.001	—	<0.001
log ***C***	—	<0.001	—	<0.001	—	<0.001	—	<0.001
R-sq	96.88%		96.76%		99.78%		99.39%	
R-sq (adj)	96.32%		96.17%		99.74%		99.28%	

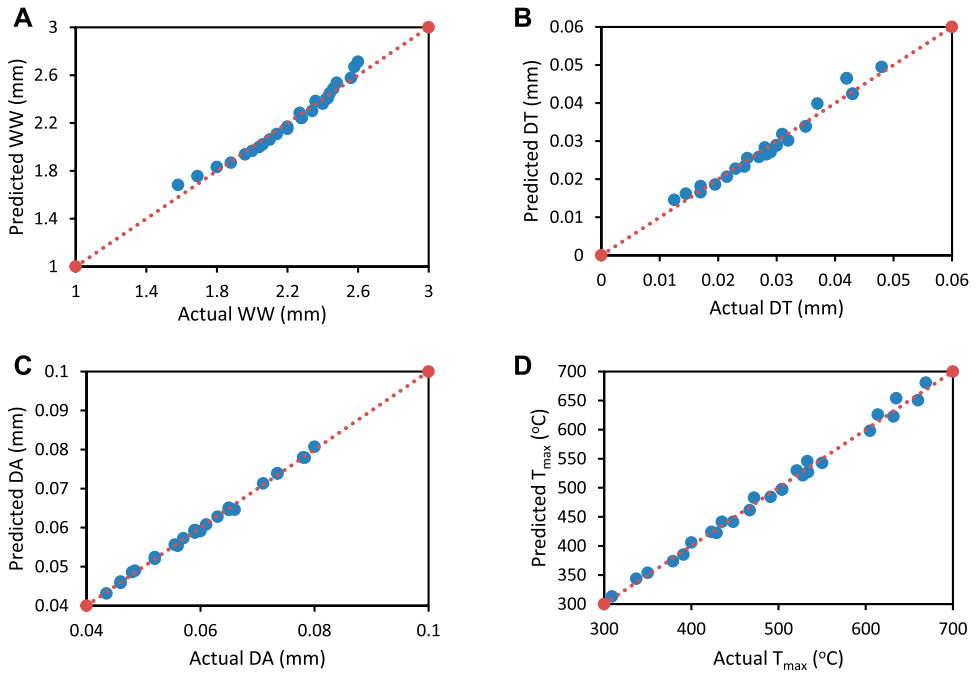

FIGURE 7 | Plot of actual vs predicted response of **(A)** WW (mm), **(B)** DT (mm), and **(C)** DA (mm) **(D)** T_{max} (°C), results.

Under a given set of assumptions, the sensitivity analysis approach is used to discover how changing values of an independent variable would influence a certain dependent variable. Sensitivity analysis provides information regarding the parameter that has to be measured the most precisely, as well as the impact of minor changes in that parameter on the overall design goals (KaraoğluSeçgin, 2008).

The partial derivative of a design objective function with respect to its variables is the sensitivity of that function with regard to control parameter in mathematics. **Eq. 8–11** are differentiated with respect to power for calculating the sensitivity of WW, D_T, D_A, and T_{max} with respect to power as

$$\partial WW/\partial P = 1.689338\, P^{-0.5759}\, S^{-0.3369}\, D^{-0.2011}\, C^{0.2783} \quad (12)$$

$$\partial D_T/\partial P = 7.647889\, P^{0.4814}\, S^{-1.474} D^{-2.2485} C^{0.5105} \quad (13)$$

$$\partial D_A/\partial P = 0.964898\, P^{-0.1534}\, (S)^{-0.8421}\, (D)^{-1.2744}\, (C)^{-0.1716} \quad (14)$$

$$\partial T_{max}/\partial P = 1874.389\, (P)^{-0.153}\, (S)^{-0.6269}\, (D)^{-1.3693}\, (C)^{0.3943} \quad (15)$$

Equations 8–11 are differentiated with respect to speed for calculating the sensitivity of WW, D_T, D_A, and T_{max}, with respect to speed.

$$\partial WW/\partial S = -1.34182\, P^{0.4241}\, S^{-1.3369}\, D^{-0.2011}\, C^{0.2783} \quad (16)$$

$$\partial D_T/\partial S = -7.60944\, P^{1.4814}\, S^{-2.474} D^{-2.2485} C^{0.5105} \quad (17)$$

$$\partial D_A/\partial S = -0.95979\, P^{0.8466}\, (S)^{-1.8421}\, (D)^{-1.2744}\, (C)^{-0.1716} \quad (18)$$

$$\partial T_{max}/\partial S = -1387.21\, (P)^{0.847}\, (S)^{-1.6269}\, (D)^{-1.3693}\, (C)^{0.3943} \quad (19)$$

Equations 8–11 are differentiated with respect to beam diameter for calculating the sensitivity of WW, D_T, D_A, and T_{max} with respect to diameter.

$$\partial WW/\partial D = -0.8009\, P^{0.4241}\, S^{-0.3369}\, D^{-1.2011}\, C^{0.2783} \quad (20)$$

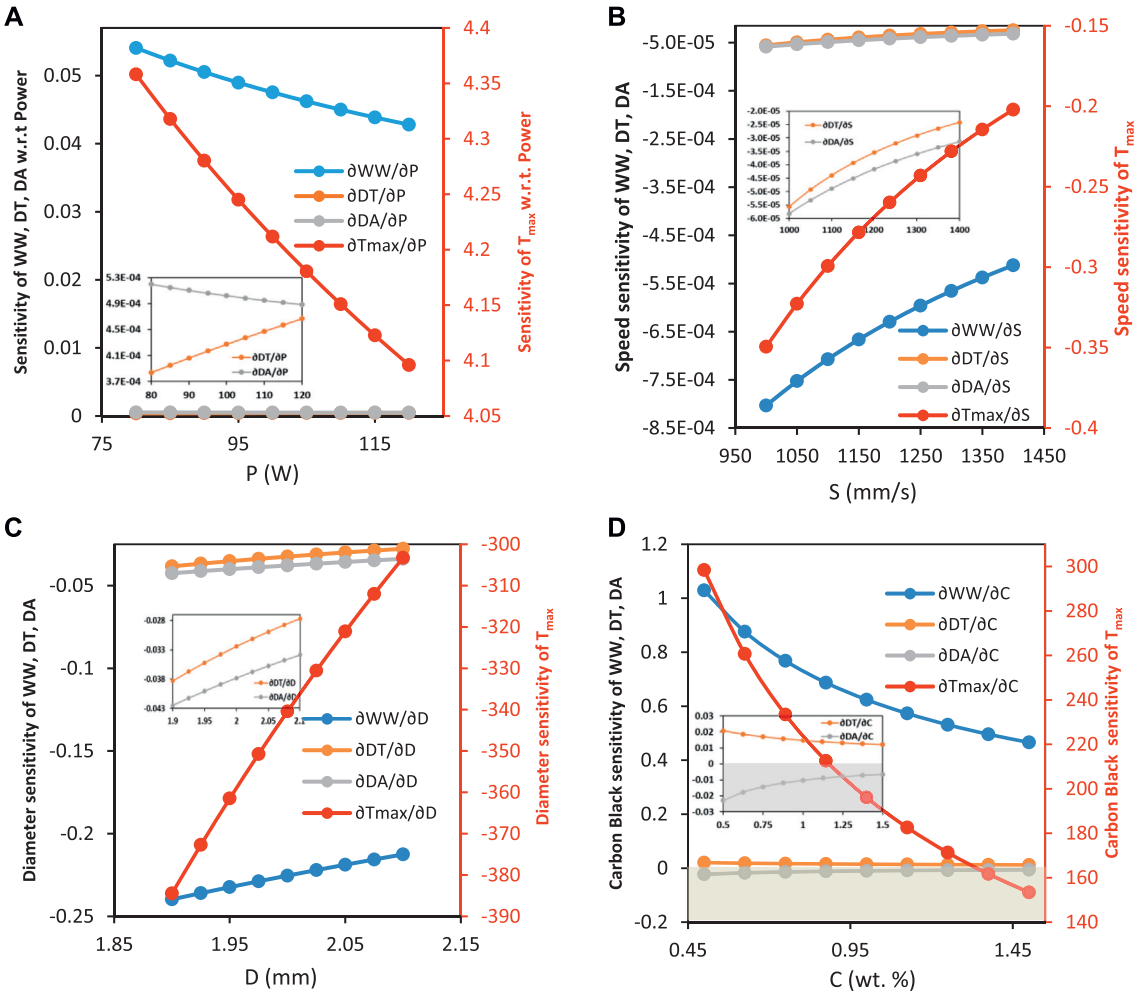

FIGURE 8 | Sensitivity analysis results for **(A)** power (constant parameters: welding speed = 1,200 mm/s, beam diameter = 2 mm, and carbon black content 1 wt% **(B)** speed (constant parameters: power = 100 W, beam diameter = 2 mm, and carbon black content 1 wt% **(C)** beam diameter (constant parameters: power = 100 W, welding speed = 1,200 mm/s, and carbon black content 1 wt% **(D)** carbon black (constant parameters: power = 100 W, welding speed = 1,200 mm/s, and beam diameter = 2 mm.

$$\partial D_T/\partial D = -11.6078\, P^{1.4814}\, S^{-1.474} D^{-3.2485} C^{0.5105} \quad (21)$$

$$\partial D_A/\partial D = -1.45253\, P^{0.8466}\, (S)^{-0.8421}\, (D)^{-2.2744}\, (C)^{-0.1716} \quad (22)$$

$$\partial T_{max}/\partial D = -3030.2\, (P)^{0.847}\, (S)^{-0.6269}\, (D)^{-2.3693}\, (C)^{0.3943} \quad (23)$$

RESULTS AND DISCUSSION

Sensitivity analysis is used to investigate the impact of process control variables on the outputs in the design space studied in this research. Positive sensitivities indicate that the output variable rises as the input variable rises, whereas negative sensitivities indicate that the output variable rises as the input variable falls (KaraoğluSeçgin, 2008). The sensitivity plots of all output responses with regard to each input control variable are shown in **Figure 8**. In addition, an inset picture is used for all subfigures of **Figure 8** to provide a clear visualisation of the sensitivity variation of D_T and D_A. **Figure 8 (a)** shows that all of the weld dimensions such as WW, D_T, and D_A exhibit a positive sensitivity with respect to power. This effect occurs because an increase in power causes an increase in heat input, resulting in more molten material and, as a result, larger weld dimensions. The sensitivity of WW with reference to power is also demonstrated to be greater than that of D_T and D_A. As can be seen, the WW and D_A are more sensitive in the lower power range, but the D_T is more sensitive in the higher power range. This means that increases in power cause minute changes in D_T and D_A but significant changes in WW. Also on the secondary vertical axis of **Figure 8A**, the sensitivity of T_{max} with respect to power is plotted which is positive. This implies a rise in the value of T_{max} as the laser power rises. This is because when the laser power increases, the heat input to the irradiation zone rises, leading in a greater T_{max}. Furthermore, T_{max} is likewise more sensitive in the lower power zone than in the higher power zone, as shown in the preceding figure. This implies that a small variation of power in lower region causes higher deviation in T_{max} than that in higher power region.

The sensitivity findings for outputs with reference to the laser scan speed are shown in **Figure 8B**. The figure shows that the

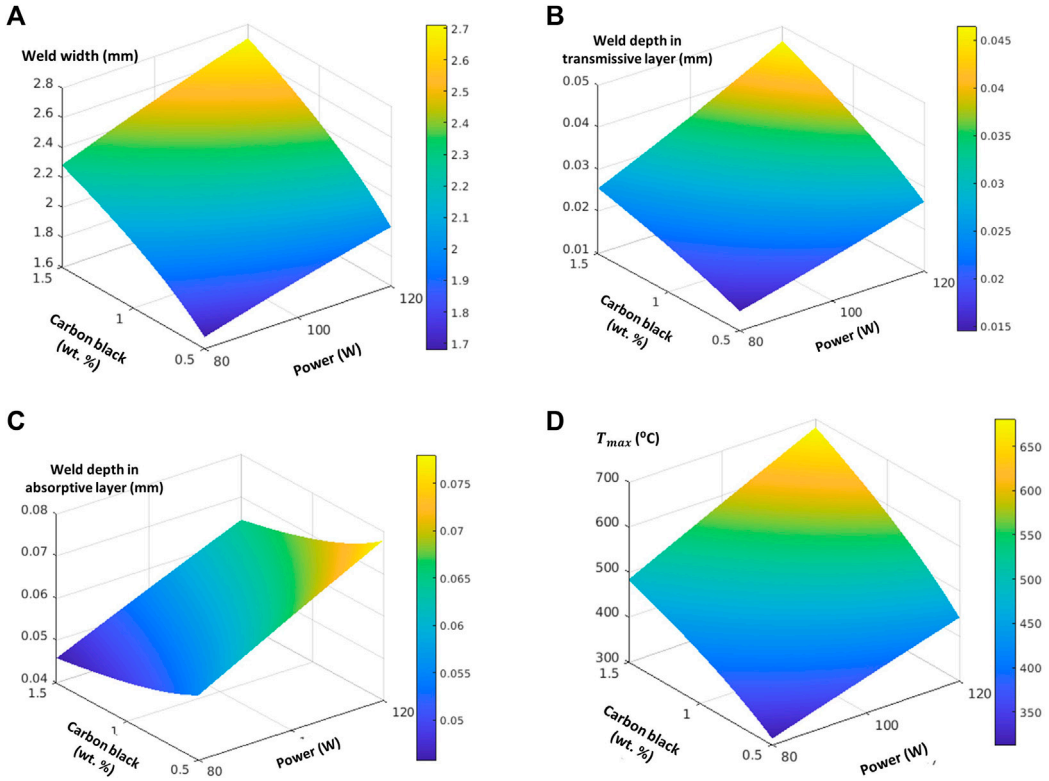

FIGURE 9 | (A) Simultaneous effect of laser power and carbon black content on the weld width (constant parameters: welding speed = 1,200 mm/s, and diameter = 2 mm), **(B)** Simultaneous effect of laser power and carbon black content on the weld depth of transmissive layer (constant parameters: welding speed = 1,200 mm/s, and diameter = 2 mm), **(C)** Simultaneous effect of laser power and carbon black content on the weld depth of absorptive layer (constant parameters: welding speed = 1,200 mm/s, and diameter = 2 mm) and **(D)** Simultaneous effect of laser power and carbon black content on maximum weld temperature of transmissive layer (constant parameters: welding speed = 1,200 mm/s, and diameter = 2 mm).

sensitivity of all weld diameters with regard to welding speed are negative. This is owing to the fact that when welding speed increases, the irradiation period decreases, resulting in a decrease in line energy. As a consequence of reduced provided heat, the volume of the molten material reduces, resulting in a narrow weld. The welding speed sensitivity of D_T and D_A is found to be greater than that of WW. This means that welding speed has a greater impact on the D_T and D_A than on the WW. Also, from secondary axis of **Figure 8B** T_{max}'s sensitivity towards laser scan speed is negative, indicating that as welding speed increases, T_{max} decreases. The desired temperature can be defined as a function of the laser power density and irradiation period, if other parameters are fixed. It is evident that by decreasing the welding speed lengthens the irradiation duration, resulting in a greater T_{max}. Also, from **Figure 8B**, it can be concluded that the T_{max} and all weld dimensions are likewise more sensitive at higher laser scan speed values than lower values of speed.

It can be seen from **Figure 8C** that the weld dimensions WW, D_T and D_A have negative sensitivities with respect to beam diameter, this trend is similar to their sensitivities with respect to speed. It is interesting to note that the sensitivity of WW for beam diameter is negative in this work whereas it is reported positive by Acherjee et al. (Acherjee et al., 2012a). The reasons that can be considered are power density, which gets decreased with the increase of beam diameter, coupled with low line energy resulting in the reduction of WW in the current study. On the other hand a smaller beam diameter results in more targeted power input, which increases power density and improves weld penetration (D_T and D_A). The sensitivity of beam diameter on T_{max} is also negative, as seen on the secondary axis of the plot. It demonstrates that the value of the T_{max} decreases as the beam diameter increases. This is because, expanding the beam diameter causes the laser energy to be distributed across a larger region. T_{max} and all weld dimensions are likewise more sensitive at higher laser scan speed values than lower values of speed.

The findings of the sensitivity analysis for carbon black concentration are shown in **Figure 8D**. The figure shows that the WW and D_T sensitivity to carbon black concentration are positive, whereas the sensitivity of D_A is negative. Increased carbon black concentration increases the absorption coefficient as discussed in section reduces optical penetration depth, resulting in the laser beam being absorbed at a lower depth in the absorbing material, increases the temperature at the interface which further results in a wider WW and deeper D_T but a lower D_A. The change of carbon black content affects the WW more strongly than D_T and D_A.

T_{max} increases with carbon black concentration in the absorbing polymer, as evidenced by positive sensitivity values in the secondary

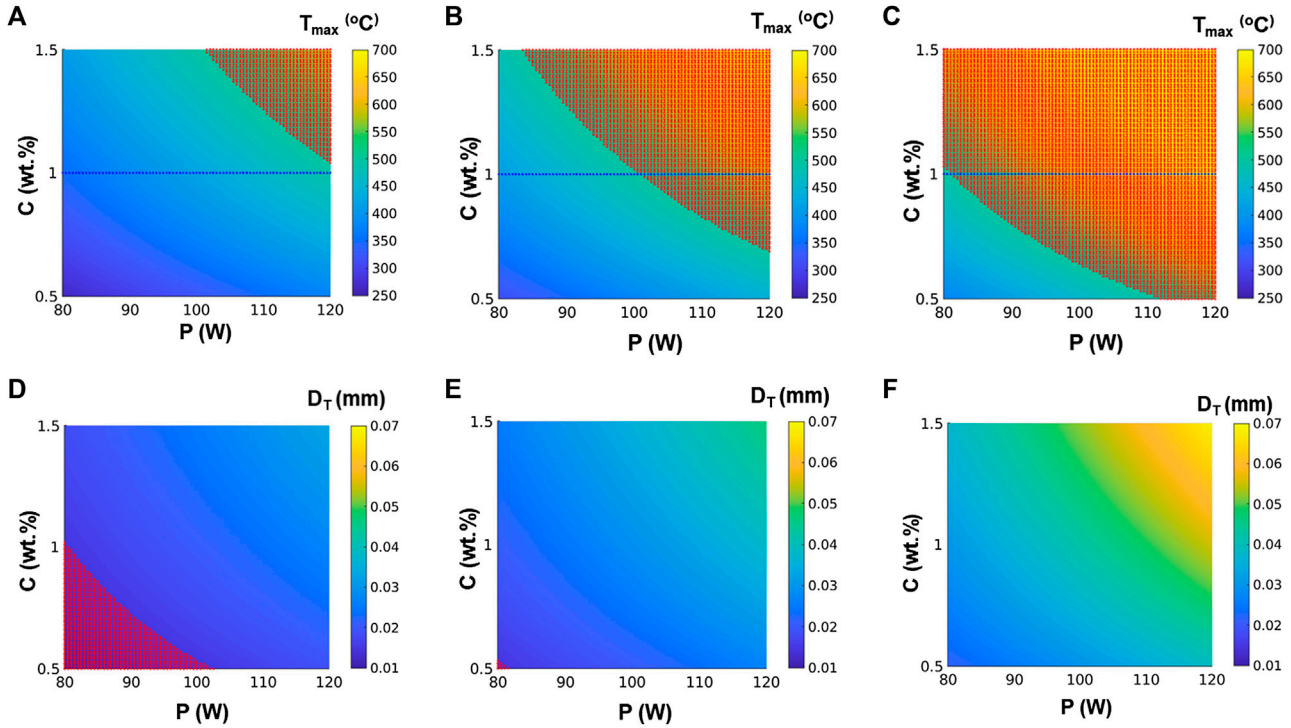

FIGURE 10 | Simultaneous effect of laser power and carbon black content on maximum weld temperature with constant parameters: **(A)** welding speed = 1,400 mm/s, and diameter = 2.1 mm, **(B)** welding speed = 1,200 mm/s, and diameter = 2 mm, **(C)** welding speed = 1,000 mm/s, and diameter = 1.9 mm, and their effect on the weld depth of transmissive layer with constant parameters: **(D)** welding speed = 1,400 mm/s, and diameter = 2.1 mm, **(E)** welding speed = 1,200 mm/s, and diameter = 2 mm, **(F)** welding speed = 1,000 mm/s, and diameter = 1.9 mm.

axis of the plot. Increased carbon black concentration raises the absorbent polymer's absorption coefficient, which improves laser absorption and results in a higher T_{max}. All of the output variables are likewise more sensitive at lower carbon black concentration levels than at higher ones. It can also be observed that the weld depth in absorptive and transmissive layer in this work is less than 0.1 mm whereas in the literature it's greater than 0.1 as reported in (Acherjee et al., 2012a). This is due to the high speed of laser and also due to larger absorption coefficient, the absorption is closer to surface absorption and it results in the reduction of weld depth. This shows that the laser transmission welding is strongly affected by optical properties of the absorptive layer and hence the carbon black is the control factor.

Figures 9A–D shows the simultaneous effect of laser power and carbon black content on output variables by keeping the other parameters constant.

The **Figure 10A–C** shows that increase in the carbon black concentration, raises the maximum weld temperature by keeping the other set of welding conditions constant. As a result, increasing the carbon black concentration of the absorbing polymer can partially compensate for a drop in laser power, an increase in welding speed, or an increase in beam diameter. It means that the amount of laser power required is highly dependent on the amount of carbon black in the absorbing portion. It's also evident that under given set control parameters, it's harder to weld polypropylene with higher CB wt% due to the rise in the maximum weld temperature from degradation temperature (500°C).

Also, a reduction in the carbon black concentration decreases the weld depth of the transmissive layer which eventually results in the decrease of weld strength as shown in **Figure 10D–F**. If D_T is less than 0.02 mm the region is shaded and regarded as not suitable for welding. It is clear from the figure that the suitable values of control parameters are i.e., p = 100 W, S = 1,200 mm/s, and D = 2 mm. It is mentioned that the threshold value of D_T has been chosen arbitrarily and in the future work, this value will be revisited on the basis of experimental investigations.

CONCLUSION

The effect of carbon black and other control parameters such as power, speed, and beam diameter on the responses such as maxim weld temperature, weld width and weld depths has been investigated. Finite element analysis and design of experiments approaches have been used for the simulation of the laser transmission contour welding process. To simulate the process and provide results, a three-dimensional COMSOL model for laser transmission welding of polypropylene with a moving laser beam was developed. To design the experimental matrix, the Box-Behnken design (BBD) method is used. Multiple curvilinear regression analysis is used to construct empirical models based on simulation findings. In

sensitivity analysis, the constructed empirical models are used to identify the relative effects of different inputs on the process outcomes. The findings of the sensitivity analysis revealed the important parameters that needed to be considered with the greatest precision. The sensitivity analysis leads to some unique findings.

1 Welding speed had a negative sensitivity effect on all of the responses studied, whereas laser power has a positive sensitivity effect.
2 The impact of power on WW in terms of sensitivity is positive and higher than that of D_T and D_A, whereas for welding speed all outputs the sensitivity is negative.
3 T_{max}, WW, D_T, and D_A all have negative sensitivity to beam diameter.
4 The WW is more affected by changes in carbon black concentration than DT and DA.
5 Sensitivities of T_{max}, WW and D_T carbon black content are positive, whereas, DA has negative sensitivity. It shows that T_{max} can increase higher than the degradation temperatures of polypropylene with the increased of carbon black concentration, which can result in decomposition rather than welding.
6 It is concluded that carbon black concentration in the polypropylene has strong influence on the achievement of quality weld. By increasing carbon black concentration, maximum weld temperature increases which may exceed from degradation temperature. Maximum achievable weld temperature can be reduced by increasing the speed which eventually results in decreasing the weld depth of transmissive layer resulting in limited weld strength. Therefore, it has been observed that the polypropylene containing higher than 1wt% carbon black is difficult to weld by high speed and low line energy lasers.
7 High speed of laser and larger absorption coefficient result in the absorption closer to surface which has consequences in the reduction of weld depth. This shows that the laser transmission welding is strongly affected by optical properties of the absorptive layer and hence the carbon black can be considered as an influencing factor.

This work will be used as a basis in future for further experimental investigations on LTW of polypropylene and its composites with carbon black.

DATA AVAILABILITY STATEMENT

The raw data supporting the conclusions of this article are available from the corresponding author, DT, upon reasonable request.

AUTHOR CONTRIBUTIONS

MA, DT, and RS: Conceptualisation MA: Simulations on LTW and Paper Writing, FD; materials'data and discussions on design of experiments and analysis, MA, FD, RS, AM and DT: writing–review and editing DT, and RS: research funding and supervision. All authors have read and agreed to the published version of the manuscript.

FUNDING

This research was funded by The North West Centre for Advanced Manufacturing (NWCAM) project is supported by the European Union's INTERREG VA Programme, managed by the Spe-cial EU Programmes Body (SEUPB).

ACKNOWLEDGMENTS

The views and opinions in this document do not necessarily reflect those of the European Commission or the Special EU Programmes Body (SEUPB). For further information about NWCAM please contact the lead partner, Catalyst Inc, for details.

REFERENCES

Acherjee, B., Kuar, A., Mitra, S., and Mitra, D. (2010). Finite Element Simulation of Laser Transmission Welding of Dissimilar Materials between Polyvinylidene Fluoride and Titanium. *Int. J. Eng. Sci. Tech.* 2 (4), 176–186. doi:10.4314/ijest.v2i4.59285

Acherjee, B., Kuar, A. S., Mitra, S., and Misra, D. (2012). Effect of Carbon Black on Temperature Field and weld Profile during Laser Transmission Welding of Polymers: A FEM Study. *Opt. Laser Tech.* 44 (3), 514–521. doi:10.1016/j.optlastec.2011.08.008

Acherjee, B., Kuar, A. S., Mitra, S., and Misra, D. (2012). Modeling of Laser Transmission Contour Welding Process Using FEA and DoE. *Opt. Laser Tech.* 44 (5), 1281–1289. doi:10.1016/j.optlastec.2011.12.049

Acherjee, B., Mondal, S., Tudu, B., and Misra, D. (2011). Application of Artificial Neural Network for Predicting weld Quality in Laser Transmission Welding of Thermoplastics. *Appl. Soft Comput.* 11 (2), 2548–2555. doi:10.1016/j.asoc.2010.10.005

Akué Asséko, A. C., Cosson, B., Deleglise, M., Schmidt, F., Le Maoult, Y., and Lafranche, E. (2015). Analytical and Numerical Modeling of Light Scattering in Composite Transmission Laser Welding Process. *Int. J. Mater. Form.* 8 (1), 127–135. doi:10.1007/s12289-013-1154-7

Bachmann, F. G., and Russek, U. A. (2003). Laser Welding of Polymers Using High-Power Diode Lasers. *Adv. Mater. Laser Microtechnologies* 5121, 385. doi:10.1117/12.515630

Bonten, C., and Tüchert, C. (2002). Welding of Plastics-Introduction into Heating by Radiation. *J. Reinforced Plastics Composites* 21 (8), 699–709. doi:10.1177/073168402128988436

Borges, M. (2016). Transmission Laser Welding of Large Plastic Components. *Ltj* 13 (5), 26–29. doi:10.1002/latj.201600035

Chen, M., Zak, G., and Bates, P. J. (2011). Effect of Carbon Black on Light Transmission in Laser Welding of Thermoplastics. *J. Mater. Process. Tech.* 211 (1), 43–47. doi:10.1016/j.jmatprotec.2010.08.017

Comsol (2020). Heat Transfer Module: User's Guide. *COMSOL Multiphysics* 5 (6), 1–822.

Dave, F., Ali, M. M., Sherlock, R., Kandasami, A., and Tormey, D. (2021). Laser Transmission Welding of Semi-crystalline Polymers and Their Composites: A Critical Review. *Polymers* 13 (5), 675–752. doi:10.3390/polym13050675

De Pelsmaeker, J., Graulus, G.-J., Van Vlierberghe, S., Thienpont, H., Van Hemelrijck, D., Dubruel, P., et al. (2018). Clear to clear Laser Welding for

Joining Thermoplastic Polymers: A Comparative Study Based on Physicochemical Characterization. *J. Mater. Process. Tech.* 255, 808–815. doi:10.1016/j.jmatprotec.2017.12.011

Esmizadeh, E., Tzoganakis, C., and Mekonnen, T. H. (2020). Degradation Behavior of Polypropylene during Reprocessing and its Biocomposites: Thermal and Oxidative Degradation Kinetics. *Polymers* 12 (8), 1627. doi:10.3390/POLYM12081627

Geiger, M., Frick, T., and Schmidt, M. (2009). Optical Properties of Plastics and Their Role for the Modelling of the Laser Transmission Welding Process. *Prod. Eng. Res. Devel.* 3 (1), 49–55. doi:10.1007/s11740-008-0141-1

Ghorbel, E., Casalino, G., and Abed, S. (2009). Laser Diode Transmission Welding of Polypropylene: Geometrical and Microstructure Characterisation of weld. *Mater. Des.* 30 (7), 2745–2751. doi:10.1016/j.matdes.2008.10.027

Grewell, D. A., Benatar, A., and Park, J. B. (2003). *Plastics and Composites Welding Handbook*, 25. Munich, Germany: Carl Hanser Verlag GmbH & Co, 407.

Grewell, D., and Benatar, A. (2007). Welding of Plastics: Fundamentals and New Developments. *Int. Polym. Process.* 22 (1), 43–60. doi:10.3139/217.0051

Gupta, S. K., Jaypuria, S., Pratihar, D. K., and Saha, P. (2018). *Numerical Simulations and Experimental Verification of Laser Welding of Nylon 6*. no. 2.

Haberstroh, E., and Lützeler, R. (2001). Influence of Carbon Black Pigmentation on the Laser Beam Welding of Plastics Micro Parts. *J. Polym. Eng.* 21 (2–3), 119–130. doi:10.1515/POLYENG.2001.21.2-3.119

Jones, I. (2013). "Laser Welding of Plastics," in *Handbook of Laser Welding Technologies* (Oxford: Woodhead Publishing Series in Electronic and Optical Materials), 280–301e. doi:10.1533/9780857098771.2.280

Kim, I. S., Son, K. J., Yang, Y. S., and Yaragada, P. K. D. V. (2003). Sensitivity Analysis for Process Parameters in GMA Welding Processes Using a Factorial Design Method. *Int. J. Machine Tools Manufacture* 43 (8), 763–769. doi:10.1016/S0890-6955(03)00054-3

Kumar, N., Sherlock, R., and Tormey, D. (2019). Prediction of weld Interface Depth and Width at Optimum Laser Welding Temperature for Polypropylene. *Proced. CIRP* 81, 1272–1277. doi:10.1016/j.procir.2019.03.306

Labeas, G. N., Moraitis, G. A., and Katsiropoulos, C. V. (2010). Optimization of Laser Transmission Welding Process for Thermoplastic Composite Parts Using Thermo-Mechanical Simulation. *J. Compos. Mater.* 44 (1), 113–130. doi:10.1177/0021998309345325

Nakhaei, M. R., Mostafa Arab, N. B., Naderi, G., and Hoseinpour Gollo, M. (2013). Experimental Study on Optimization of CO2 Laser Welding Parameters for Polypropylene-clay Nanocomposite Welds. *J. Mech. Sci. Technol.* 27 (3), 843–848. doi:10.1007/s12206-013-0109-8

Petrović, Z. S., Martinović, B., Divjaković, V., and Budinski–Simendić, J. (1993). Polypropylene-Carbon Black Interaction in Conductive Composites. *J. Appl. Polym. Sci.* 49 (9), 1659–1669. doi:10.1002/app.1993.070490919

Potente, H., Korte, J., and Becker, F. (1999). *Laser Transmission Welding of Thermoplastics: Analysis of the Heating Phase*, Vol. 18. Plastics Design Library.

Purtonen, T., Kalliosaari, A., and Salminen, A. (2014). Monitoring and Adaptive Control of Laser Processes. *Phys. Proced.* 56, 1218–1231. doi:10.1016/j.phpro.2014.08.038

Rodríguez-Vidal, E., Quintana, I., and Gadea, C. (2014). Laser Transmission Welding of ABS: Effect of CNTs Concentration and Process Parameters on Material Integrity and weld Formation. *Opt. Laser Tech.* 57, 194–201. doi:10.1016/j.optlastec.2013.10.020

Karaoğlu, S., and Seçgin, A. (2008). Sensitivity Analysis of Submerged Arc Welding Process Parameters. *J. Mater. Process. Tech.* 202 (1–3), 500–507. doi:10.1016/j.jmatprotec.2007.10.035

Tres, P. A. (2017). *Designing Plastic Parts for Assembly*. 8th ed. Munich, Germany: Carl Hanser Verlag GmbH & Co.

Troughton, M. (2008). *Handbook of Plastics Joining: A Practical Guide*. 2nd ed. New York, NY: William Andrew Inc.

Wang, X., Chen, H., and Liu, H. (2014). Investigation of the Relationships of Process Parameters, Molten Pool Geometry and Shear Strength in Laser Transmission Welding of Polyethylene Terephthalate and Polypropylene. *Mater. Des.* 55, 343–352. doi:10.1016/j.matdes.2013.09.052

Wang, X., Zhang, C., Li, P., Wang, K., Hu, Y., Zhang, P., et al. (2012). Modeling and Optimization of Joint Quality for Laser Transmission Joint of Thermoplastic Using an Artificial Neural Network and a Genetic Algorithm. *Opt. Lasers Eng.* 50 (11), 1522–1532. doi:10.1016/j.optlaseng.2012.06.008

Wippo, V., Jaeschke, P., Brueggmann, M., Suttmann, O., and Overmeyer, L. (2014). Advanced Laser Transmission Welding Strategies for Fibre Reinforced Thermoplastics. *Phys. Proced.* 56, 1191–1197. doi:10.1016/j.phpro.2014.08.034

Conflict of Interest: The authors declare that the research was conducted in the absence of any commercial or financial relationships that could be construed as a potential conflict of interest.

frontiers in Materials

ORIGINAL RESEARCH
published: 29 September 2021
doi: 10.3389/fmats.2021.745088

Additive Manufacturing and Injection Moulding of High-Performance IF-WS_2/PEEK Nanocomposites: A Comparative Study

Atefeh Golbang, Mozaffar Mokhtari, Eileen Harkin-Jones, Edward Archer and Alistair Mcilhagger*

Ulster University, Jordanstown, United Kingdom

OPEN ACCESS

Edited by:
Patricia Krawczak,
Institut Mines-Télécom, France

Reviewed by:
Roham Rafiee,
University of Tehran, Iran
Veronique Michaud,
École Polytechnique Fédérale de Lausanne, Switzerland

****Correspondence:***
Eileen Harkin-Jones
e.harkin-jones@ulster.ac.uk

Specialty section:
This article was submitted to Polymeric and Composite Materials, a section of the journal Frontiers in Materials

Received: *21 July 2021*
Accepted: *06 September 2021*
Published: *29 September 2021*

Citation:
Golbang A, Mokhtari M, Harkin-Jones E, Archer E and Mcilhagger A (2021) Additive Manufacturing and Injection Moulding of High-Performance IF-WS_2/PEEK Nanocomposites: A Comparative Study. Front. Mater. 8:745088. doi: 10.3389/fmats.2021.745088

In this study, PEEK nanocomposites with 0, 0.5, 1, and 2wt% IF-WS_2 were manufactured by injection moulding and Fused Deposition Modelling (FDM). To compare the impact of the two processing methods and the incorporated nanoparticles on the morphology, crystallization and final mechanical properties of the nanocomposites, SEM, DSC and tensile testing were performed. In general, a good distribution of nanoparticles was observed in PEEK, although larger agglomerates were visible at 2 wt% IF-WS_2. The crystallization degree of PEEK increased with increasing loading of IF-WS_2 nanoparticles up to 1wt% and then declined at 2 wt%, due to lower level of particle dispersion in this sample. The 3D printed samples showed slightly higher crystallinity at each IF-WS_2 loading in relation to the injection moulded samples and extruded filaments, because of multiple reheating effect from subsequent layer deposition during FDM, causing recrystallization. In general, incorporation of IF-WS_2 nanoparticles increased the mechanical properties of pure PEEK in both 3D printed and injection moulded samples. However, this increment was more noticeable in the 3D-printed nanocomposite samples, resulting in smaller gap between the mechanical properties of the 3D-printed samples and the injection moulded counterparts, in respect to pure PEEK, particularly at 1 wt% IF-WS_2. This effect is ascribed to the increased inter-layer bonding of PEEK in the presence of IF-WS_2 nanoparticles in FDM. In general, the lower mechanical properties of the 3D printed samples compared with the injection moulded ones are ascribed to poor interlayer bonding between the deposited layers and the presence of voids. However, addition of just 1 wt% of IF-WS2 nanoparticles into PEEK increased the tensile strength and Young's modulus of the FDM PEEK materials to similar levels to those achieved for unfilled injection moulded PEEK. Therefore, incorporation of IF-WS2 nanoparticles into PEEK is a useful strategy to improve the mechanical performance of FDM PEEK.

Keywords: high-performance nanocomposite, additive manufacturing, injection moulding, PEEK (poly ether ether ketone), inorganic fullerene tungsten sulphide (IF-WS2)

INTRODUCTION

Owing to their high thermal and chemical stability, exceptional strength-to-weight ratio, and recyclability, high performance thermoplastic polymers, such as Polysulfone (PSU), polyetherimide (PEI), and polyether ether ketone (PEEK) are becoming increasingly attractive in competition with metals and ceramics for load bearing applications under harsh operating conditions (Wiesli and Özcan, 2015; Al Christopher et al., 2021). Apart from the intrinsic properties of the polymer, the applied manufacturing method, processing conditions, and the material composition play a major role on the final quality and properties of high-performance thermoplastic parts (Golbang et al., 2017; Golbang et al., 2020; Liu and Kunc, 2020).

Nanofillers are added to polymers to further improve their thermal, mechanical and optical properties, depending on the type of filler (Aradhana et al., 2018; Golbang et al., 2020; Mokhtari et al., 2021a). For example, addition of hydroxyapatite particles increases the bioactivity of PEEK for development of cranial implants with improved biocompatibility (Manzoor et al., 2021). Incorporation of expanded graphite (EG) into PEEK via twin-screw compounding and injection moulding, results in significant enhancement of PEEK electrical conductivity (Mokhtari et al., 2021b).

The processing of high-performance polymers is generally more difficult and expensive compared with commodity thermoplastics due to their high melt viscosity and higher melting temperatures (Golbang et al., 2020). Incorporation of fillers into high-performance polymers for improving their performance may further increase melt viscosity thus creating potential problems in achieving sufficient power to process the material and risking thermal/shear degradation of the polymer. Therefore, the type, amount, and size of filler, as well as the processing method should be chosen carefully when developing high-performance nanocomposites (Díez-Pascual et al., 2012; Valino et al., 2019; Golbang et al., 2020; Mokhtari et al., 2021b; Manzoor et al., 2021).

Among the conventional plastics processing techniques, injection moulding is one of the most commonly used methods for production of high-performance polymers/nanocomposites (Shaharuddin and Salit, 2006). Injection moulding enables large volume production with good precision, detail, and repeatability (Goodship, 2004; Shaharuddin and Salit, 2006; Bilewicz et al., 2008; Mokhtari et al., 2021b). When assessing the quality of parts produced via new polymer processing technologies such as additive manufacturing, they are often compared with those made via injection moulding. Additive manufacturing (AM) or 3D printing is becoming popular for producing parts from thermoplastic polymers as it can create complex geometries without the need for sophisticated tooling, resulting in cost-effective and sustainable manufacturing. Although, it should be noted that currently, AM is considered cost-effective for small volumes of production as compared to injection moulding (Dawoud et al., 2016; Koštial et al., 2016; Verdejo de Toro et al., 2020).

3D printing is mostly used for commodity plastics such as acrylonitrile butadiene styrene (ABS), and polylactic acid (PLA), polyvinyl alcohol (PVA), polycaprolactone (PCL), and polyamide (Nylon). However, the thermal and mechanical properties of these polymers are limited, and hence, there is growing demand to adopt AM processes to high-performance polymers for widespread commercial application. In recent years, high performance polymers have been successfully 3D printed via additive manufacturing techniques such as Fused Deposition Modelling (FDM) and High temperature selective laser sintering (HT-SLS). FDM is one of the most user-friendly and cost-effective AM methods for producing complex thermoplastic parts (Liu et al., 2019; Valino et al., 2019; Zanjanijam et al., 2020). However, in comparison with conventional manufacturing methods, such as injection moulding, 3D printing results in lower part mechanical performance. This is mainly due to the weak inter-layer bonding between the deposited layers in FDM and presence of voids. For example, 3D printed Nylon six shows a tensile strength of ~50 MPa as compared with ~80 MPa for the injection moulded parts (Verdejo de Toro et al., 2020). Recently, much research has been conducted to improve the mechanical performance of 3D printed thermoplastics by adjusting and optimizing the printing conditions (i.e., layer thickness, print orientation, infill pattern, nozzle temperature, print bed temperatures, printing speed, etc) or addition of reinforcing particles such as silica, graphite, carbon, or glass fibres (Brucato et al., 1993; Pinto et al., 2015; Yang et al., 2017; Schiavone et al., 2020; Antony Samy et al., 2021). However, addition of fillers to the polymer feedstock is more challenging in FDM due to problems such as clogging of the nozzle, higher melt temperature and low flowability leading to poor chain inter-diffusion and therefore weaker inter-layer bonding as well as delamination. Hence, in order to achieve high quality printed parts, it is important to optimize the printing conditions according to the material flow properties, particle size, and the printer geometrical specification (e.g., nozzle diameter) (Coogan, 2019; Huang et al., 2019; Rostom and Dadmun, 2019; Srinivas et al., 2020; Candal et al., 2021).

To exploit the benefits of additive manufacturing and achieve 3D printed parts comparable with conventional manufacturing techniques such as injection moulding, it is crucial to resolve some of the associated issues with this technology, such as weak interlayer bonding. Hence, this study aims to improve the mechanical properties of 3D printed PEEK through incorporation of IF-WS2 nanoparticles. For this, PEEK nanocomposites with different loadings of IF-WS_2 nanoparticles are produced using two methods: FDM and injection moulding. Then, the thermal and mechanical properties of the developed nanocomposites are evaluated and compared. As mentioned, PEEK is considered as a high-performance polymer with excellent thermal stability (up to 600°C), resistance to chemicals and radiation, as well as biocompatibility which makes it suitable for applications in aerospace, medical and automotive industries. IF-WS_2 nanoparticles are very distinct types of fillers because of their innate mechanical and tribological properties, acting as both reinforcing and lubricating agents. In our previous research, it was shown that incorporation of IF-WS_2 nanoparticles into

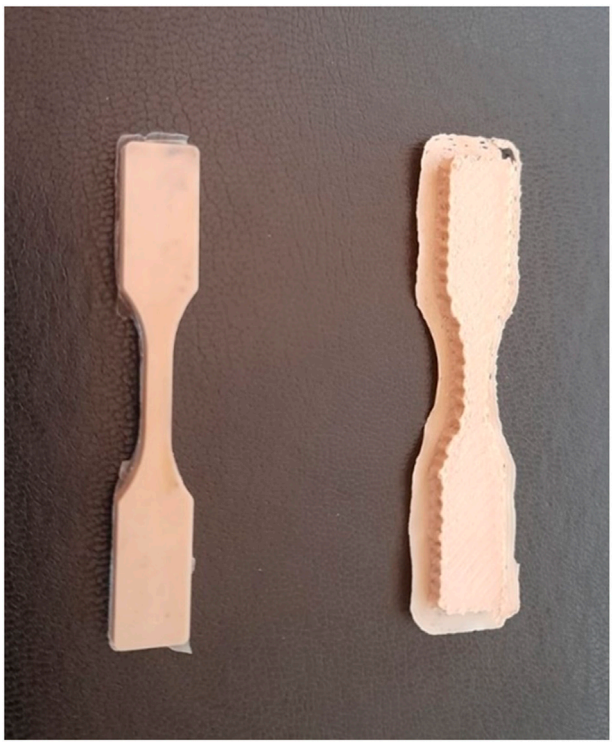

FIGURE 1 | Images of injection moulded and 3D-printed PEEK, from left to right.

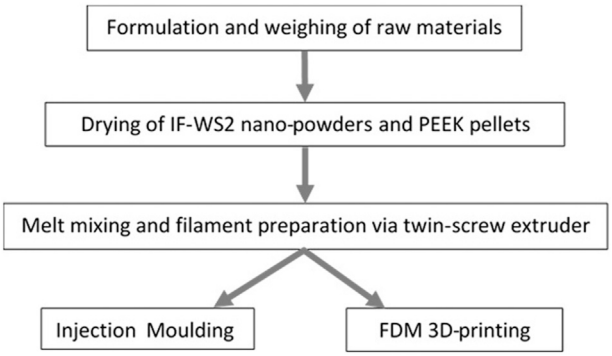

FIGURE 2 | Schematic presentation of the manufacturing process steps.

PEEK via melt compounding leads to reduction of melt viscosity which is favourable for processing without compromising its final mechanical properties (Golbang et al., 2020). It is believed that reduction of viscosity (improved flowability) can increase the bonding between the deposited layers through polymer chain diffusion and therefore improve the mechanical properties of the 3D-printed parts via FDM. Even though, reinforcing fillers generally increase the mechanical properties of the polymer, not all fillers can strengthen the interlayer bonding in FDM printed parts (Pinto et al., 2015; Coogan, 2019; Rostom and Dadmun, 2019; Srinivas et al., 2020). The objective of this study is to reduce the gap between the mechanical properties of the 3D-printed and injection moulded parts using IF-WS_2 nanoparticles to address the low interlayer bonding strength FDM 3D-printed parts, as one of the prominent challenges in additive manufacturing.

METHODOLOGY

Sample Preparation

Inorganic fullerene like Tungsten di-sulfide (IF-WS2) nanoparticles with 80 nm average diameter were prepared by Professor Yanqui Zhu's group at the University of Exeter. Polyether ether ketone (PEEK) 450 G was purchased from Victrex, (Mw ≈ 44,000 g/mol, Tg ≈ 143°C, Tm ≈ 343°C) and used as the matrix. To produce filaments for 3D printing, the IF-WS_2 nanoparticles were melt compounded with PEEK at 0.5, 1, and 2 wt% loading using a twin-screw extruder with 16 mm diameter, length to diameter ratio (L/D) of 40, and screw speed of 30 rpm. The average diameter of filaments was monitored and kept at 1.75 ± 0.15 mm. The screw configuration was designed in a way to enhance nanoparticle dispersion using screw elements consisting of transporting elements for forward conveying of extrudate, kneading elements with 90°, 60°, and 30° twist angles for dispersion, and reverse screw element. The temperatures indicated in each zone of the extruder were: 365 (feeding zone), 400 (melting and compression zone), 385°C (metering zone and die extrusion). The extruded filaments were cooled at room temperature (~25°C).

A modified UM2 + FDM 3D printer was used for to print PEEK nanocomposite specimens which enables extrusion temperatures of up to 420°C (using an all-metal hot end), bed temperature of maximum 350°C (via heating elements embedded under the print bed), and heating lamps for regulation of chamber temperature up to 230°C.

Pellets were cut from the filaments for injection moulding. A Haake MiniJet Pro injection moulding machine was used for production of injection moulded tensile samples, operating at melt temperature of 400°C and mould temperature of 280°C. Specimens with similar dimensions to the injection moulded samples were printed from the extruded filaments using a high temperature Ultimaker. The printing speed, building plate temperature, nozzle temperature and nozzle diameter were set at 40 mm/s, 280°C, 400°C and 2 mm, respectively. A raster orientation of ±45° was applied to produce a uniform morphology. A comparison was made between the mechanical properties of the printed and the injection moulded samples.

Pictures of the 3D-printed and injection moulded samples are presented in **Figure 1**.

The schematic presentation of the sequence of manufacturing process is demonstrated through a flowchart in **Figure 2**.

Characterization

A high resolution FEG SEM (HITACHI), operating at 30 kV and an intensity of 9×10^{-9} was used to observe the gold coated

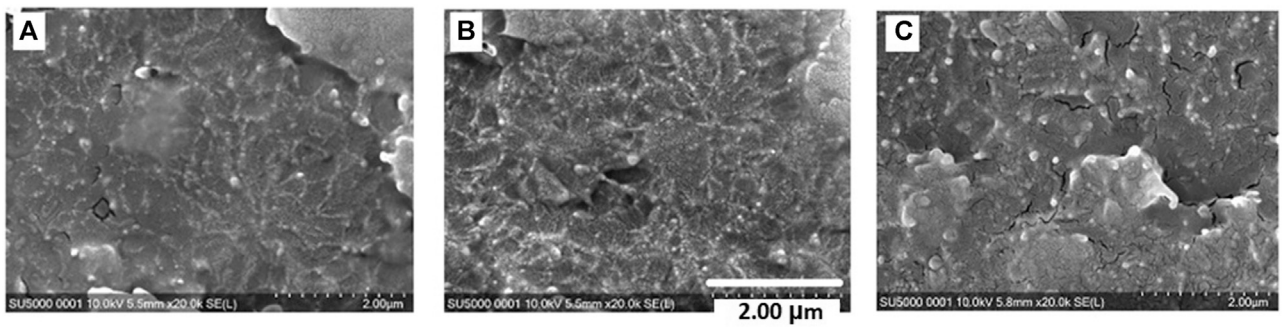

FIGURE 3 | SEM images of PEEK nanocomposites containing **(A)** 0.5 wt%, **(B)** 1 wt%, and **(C)** 2 wt% IF-WS_2 nanoparticles.

fractured surfaces of the filaments to evaluate the dispersion and distribution of IF-WS2 nanoparticles in PEEK.

The thermal properties of the 3D printed and injection moulded nanocomposite samples were measured using a TA-Instrument Q1000 differential scanning calorimeter (DSC). 5 mg samples were sealed in aluminium pans and a standard mode heating-cooling-heating cycle at 10°C/min between 20 and 400°C was applied. The amount of degree of crystallinity (χc) was calculated from the crystallization peak (Golbang et al., 2020).

Tensile testing was performed on both 3D printed and injection moulded samples using an Instron testing machine (Instron 3,344) and following the ISO standard: ISO 527–2 Type 5A. Five specimens (75 mm × 4 mm × 2 mm) were tested for each sample with a crosshead speed of 2.0 mm/min at 20°C and using a 2 kN load cell.

RESULTS AND DISCUSSION

Scanning Electron Microscopy

The SEM images presented in **Figure 3** show the morphology of PEEK nanocomposite filaments with 0.5, 1, and 2 wt% IF-WS_2. Overall, a homogenous distribution of particles is observed in all three loadings. However, there is slightly larger sizes of inclusions present in the 2 wt% and to some extent in the 0.5 wt% samples, indicating some degree of agglomeration in these cases. The higher dispersion degree of particles achieved at 1 wt% IF-WS_2 may be due to the lubricant effect of these nanoparticles. Tendency for agglomeration increases with further increase in the number of particles at the higher loading (2 wt%) (Khare and Burris, 2010; Golbang et al., 2017; Fu et al., 2019; Golbang et al., 2020).

There was no obvious change observed in the distribution and dispersion state of the nanoparticles after the injection moulding and 3D printing process.

Dispersion in a nanocomposite is associated with breaking of agglomerates into smaller sizes and ideally into individual nanoparticles, by overcoming the inter-particle interactions (typically van der Waals forces). The "dispersion state" of nanoparticles is linked to the final properties of the nanocomposite due to the long-range effects of nanoparticle-matrix interface on nearby polymer chains. However, achieving good dispersion is considered as a prominent challenge. The "distribution sate" of particles in a nanocomposite is independent of dispersion state (or the size of inclusions). In a good distribution, the inclusions (e.g., particles, agglomerates, aggregates, ...) are homogeneously distributed in the matrix and isotropic properties are achieved within the nanocomposite. In other words, each inclusion is as far as possible from its nearest neighbour, so that the space is homogeneously filled (Khare and Burris, 2010; Fu et al., 2019).

Thermal Properties

Changes in the crystallinity of the PEEK nanocomposites after extrusion (i.e., filaments), and shaped via 3D printing and injection moulding are shown in **Figure 4**.

Incorporation of IF-WS_2 nanoparticles increases the crystallinity of PEEK in samples up to a loading of 1 wt% which can be attributed to the nucleation effect of these nanoparticles. Reduction of crystallinity with a further increase in IF-WS_2 concentration to 2 wt%, is likely to be due to a reduced nucleation effect of the larger agglomerated IF-WS_2 or a confining effect of the particles that restricts molecular mobility and ability of polymer chains to orient and crystallize (Golbang et al., 2020; Antony Samy et al., 2021).

From **Figure 4**, it can be seen that the overall crystallinity of the 3D printed samples is slightly higher at each filler loading compared with the injection moulded counterparts and filaments. This can be explained by the thermal history experienced in each process. During FDM, the deposited layers are reheated due to the deposition of subsequent layers. This multiple reheating effect contributes to further growth of crystals and higher degrees of crystallinity. During injection moulding, the material is cooled from extrusion temperature (400°C) to the mould temperature (280°C) in less than a minute and then ejected into a room temperature environment. The higher cooling rate in injection moulding compared to that in in FDM, results in a lower degree of crystallinity. The filaments have the lowest degree of crystallinity at each filler loading. This is due to the sudden cool down of the polymer melt to room temperature (Brucato et al., 1993; Yang et al., 2017; Golbang et al., 2020; Schiavone et al., 2020; Antony Samy et al., 2021).

Mechanical Properties

The stress-strain curves of the injection moulded and 3D printed samples are illustrated in **Figures 3**, **4**. The average Young's modulus and ultimate tensile strength are reported in **Table 1**. As seen in

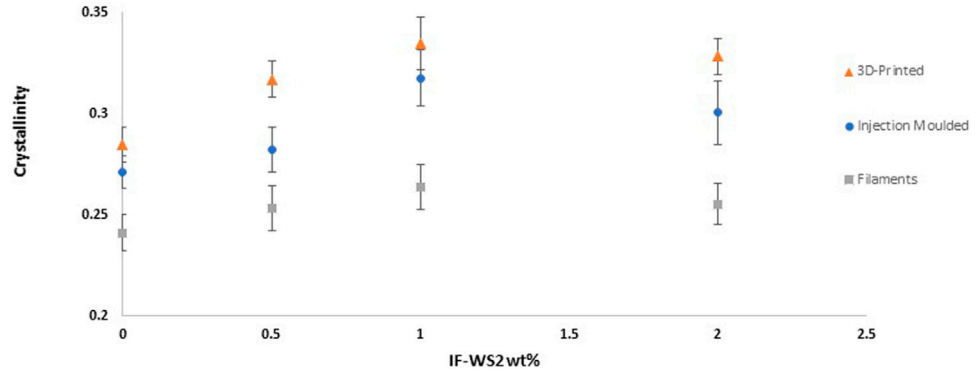

FIGURE 4 | Crystallinity of PEEK nanocomposites processed via extrusion, FDM and injection moulding.

TABLE 1 | Comparison between the mechanical properties of injection moulded and 3D printed PEEK/IF-WS_2 nanocomposite samples.

IF-WS_2 wt%	E_M (GPa)	S_M (MPa)	E_P (GPa)	S_P (MPa)	E_P/E_M (%)	S_P/S_M (%)	$(E- E_{PEEK})/E_{PEEK}$		$(S- S_{PEEK})/S_{PEEK}$	
							M	P	M	P
0	3.6 ± 0.1	92 ± 4	3.0 ± 0.1	63 ± 4	82	68	0	0	0	0%
0.5	3.8 ± 0.2	97 ± 5	3.2 ± 0.2	72 ± 7	84	73	6%	7%	5%	14%
1	4.5 ± 0.1	102 ± 4	3.9 ± 0.1	84 ± 5	87	82	25%	30%	11%	33%
2	4.3 ± 0.3	98 ± 5	3.7 ± 0.2	73 ± 6	86	75	19%	23%	7%	16%

E: Young's modulus, S: Ultimate Tensile Strength, P: 3D-Printed, M: Injection Moulded.

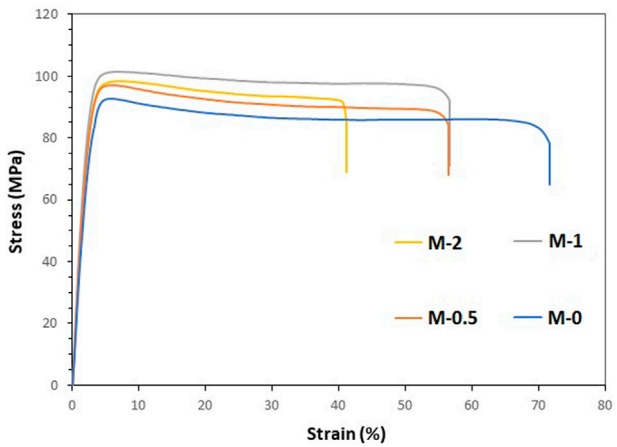

FIGURE 5 | Stress-strain curve for injection moulded PEEK samples containing 0, 0.5, 1, and 2wt% IF-WS_2.

Figures 5, **6**, as well as **Table 1**, the trend of changes in the Young's modulus and tensile strength with addition of IF-WS2 nanoparticles are similar, with the addition of IF-WS2 nanoparticles generally increasing the Young's modulus and tensile strength of PEEK up to a loading of 1 wt%. This increase is due to the presence of the reinforcing filler and the increased crystallinity of these samples. Properties drop off at the 2 wt% loading due to the stress concentration effect of, and lower aspect ratio of, agglomerated IF-WS2, combined with a slightly lower crystallinity. The elongation at break deceases in the injection moulded samples for increasing IF-WS2 which is quite typical when reinforcing fillers are added to a polymer matrix (Pinto et al., 2015; Huang et al., 2019; Rostom and Dadmun, 2019; Golbang et al., 2020). However, the reverse is true for the 3D printed materials with added IF-WS2. Two possible explanations for this improvement are an increase in layer-to-layer bonding due to enhanced thermal conductivity of IF-WS2 containing PEEK and, the lubricating effect of these nanoparticles, contributing to higher molecular mobility and polymer chain inter-diffusion during deposition and therefore better bonding between the layers (Coogan, 2019; Srinivas et al., 2020; Candal et al., 2021).

The 3D printed samples have a lower Young's modulus and tensile strength for each IF-WS_2 loading in comparison to the injection moulded samples, by about 80 and 70%, respectively. There is a very significant reduction in elongation at break for the 3D printed materials compared to those that are injection moulded. These results are expected due to the weaker inter-layer bonding between the layers in 3D printed samples and the presence of voids. Also, the pressure exerted during injection moulding can compress and strengthen the part (Koštial et al., 2016; Verdejo de Toro et al., 2020).

According to the data presented in **Table 1**, the Young's modulus of the 3D printed samples containing 1 wt% IF-WS_2 surpasses that of the injection moulded pure PEEK and the tensile strength is significantly increased to just 7% lower than the unfilled PEEK. Hence, it can be concluded that adding small amounts of IF-WS_2 nanoparticles can overcome the reduced stiffness and tensile strength caused by poor layer adhesion and voids in 3D printed parts.

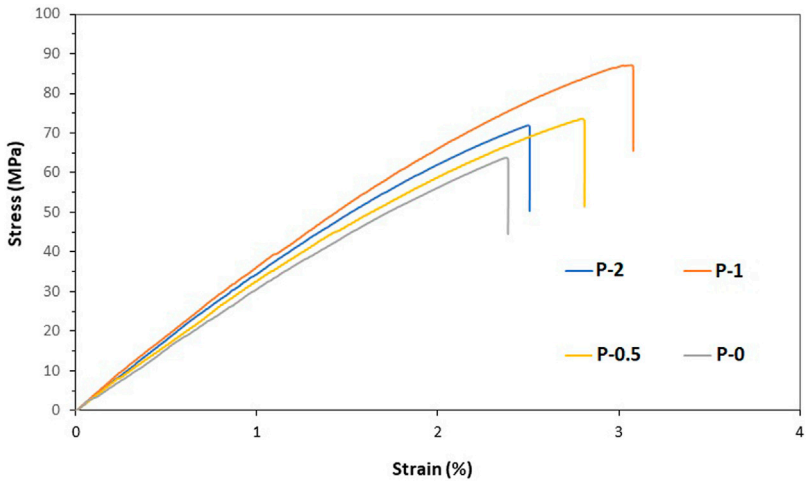

FIGURE 6 | Stress-strain curve for 3D printed PEEK samples containing 0, 0.5, 1, and 2wt% IF-WS_2.

Overall, the increment in the Young's Modulus and tensile strength of PEEK with addition of IF-WS_2 nanoparticles is higher for the 3D printed samples in respect to the injection moulded ones. This is ascribed to the improved bonding between the deposited PEEK layers in the presence of IF-WS_2 nanoparticles.

CONCLUSION

In this work, a comparison was made between the mechanical properties of high-performance PEEK nanocomposites with loadings of 0.5, 1, and 2 wt% IF-WS_2, fabricated by two different methods: injection moulding and 3D printing (FDM). Although the 3D printed samples had slightly higher levels of crystallinity compared with the injection moulded samples, they exhibited lower Young's modulus and tensile strength as expected by about 82–87% and 73–85%, respectively. The lower mechanical properties of the 3D printed samples compared to their injection moulded counterparts is attributed to the lower packing density, poor inter-layer bonding and presence of voids. Overall, addition of IF-WS_2 nanoparticles increases the mechanical properties of PEEK in both 3D printed and injection moulded samples. However, it is worth noting that the presence of IF-WS_2 in PEEK reduces the gap between the mechanical properties of the 3D printed and injection moulded samples which can be ascribed to the simultaneous reinforcing and lubricating effect of these particles, allowing higher molecular inter-diffusion and better bonding between the layers.

DATA AVAILABILITY STATEMENT

The raw data supporting the conclusions of this article will be made available by the authors, without undue reservation.

AUTHOR CONTRIBUTIONS

AG, conceptualization, data curation, formal analysis, investigation, methodology, visualization, writing—original draft, writing—review and editing. MM, investigation, methodology. EA, conceptualization, resources. AM, conceptualization, resources, project administration, financial support. EH, conceptualization, formal analysis, project administration, supervision, funding acquisition, resources, writing—review and editing.

ACKNOWLEDGMENTS

The authors wish to thank the EPSRC for funding for this research under grant reference EP/N034783/1 Novel high performance polymeric composite materials for additive manufacturing of multifunctional components and the North West Centre for Advanced Manufacturing (NW CAM) for their financial contribution.We also wish to thank Professor Yanqui Zhu and Dr Bahareh Yazdani of the University of Exeter for providing the IF-WS_2 nanoparticles.

REFERENCES

Al Christopher, C., da Silva, Í. G., Pangilinan, K. D., Chen, Q., Caldona, E. B., and Advincula, R. C. (2021). High performance polymers for oil and gas applications. *Reactive Funct. Polym.*, 104878.

Antony Samy, A., Golbang, A., Harkin-Jones, E., Archer, E., and McIlhagger, A. (2021). Prediction of part distortion in Fused Deposition Modelling (FDM) of semi-crystalline polymers via COMSOL: Effect of printing conditions. *CIRP J. Manufacturing Sci. Tech.* 33, 443–453. doi:10.1016/j.cirpj.2021.04.012

Aradhana, R., Mohanty, S., and Nayak, S. K. (2018). High performance epoxy nanocomposite adhesive: Effect of nanofillers on adhesive strength, curing and degradation kinetics. *Int. J. Adhes. Adhesives* 84, 238–249. doi:10.1016/j.ijadhadh.2018.03.013

Bilewicz, M., Viana, J. C., and Dobrzański, L. A. (2008). Polymer composite strengthening by developed injection moulding technique. *Arch. Mater. Sci. Eng.* 30 (2), 69–72.

Brucato, V., Piccarolo, S., and Titomanlio, G. (1993). "April. Crystallization kinetics in relation to polymer processing," in *Makromolekulare Chemie. Macromolecular Symposia* (Basel: Hüthig & Wepf Verlag), 68, 245–255. doi:10.1002/masy.19930680119No. 1

Candal, M. V., Calafel, I., Fernández, M., Aranburu, N., Aguirresarobe, R. H., Gerrica-Echevarria, G., et al. (2021). Study of the interlayer adhesion and warping during material extrusion-based additive manufacturing of a carbon nanotube/biobased thermoplastic polyurethane nanocomposite. *Polymer* 224, 123734. doi:10.1016/j.polymer.2021.123734

Coogan, T. J. (2019). *In-Line Monitoring and Prediction of Viscosity, Interlayer Contact, and Strength in the Fused Filament Fabrication Process*. Massachusetts: Doctoral dissertation, University of Massachusetts Lowell.

Dawoud, M., Taha, I., and Ebeid, S. J. (2016). Mechanical behaviour of ABS: An experimental study using FDM and injection moulding techniques. *J. Manufacturing Process.* 21, 39–45. doi:10.1016/j.jmapro.2015.11.002

Díez-Pascual, A. M., Naffakh, M., Marco, C., Ellis, G., and Gómez-Fatou, M. A. (2012). High-performance nanocomposites based on polyetherketones. *Prog. Mater. Sci.* 57 (7), 1106–1190. doi:10.1016/j.pmatsci.2012.03.003

Fu, S., Sun, Z., Huang, P., Li, Y., and Hu, N. (2019). Some basic aspects of polymer nanocomposites: A critical review. *Nano Mater. Sci.* 1 (1), 2–30. doi:10.1016/j.nanoms.2019.02.006

Golbang, A., Famili, M. H. N., and Shirvan, M. M. M. (2017). A method for quantitative characterization of agglomeration degree in nanocomposites. *Composites Sci. Tech.* 145, 181–186. doi:10.1016/j.compscitech.2017.04.013

Golbang, A., Harkin-Jones, E., Wegrzyn, M., Campbell, G., Archer, E., and McIlhagger, A. (2020). Production and characterization of PEEK/IF-WS2 nanocomposites for additive manufacturing: Simultaneous improvement in processing characteristics and material properties. *Additive Manufacturing* 31, 100920. doi:10.1016/j.addma.2019.100920

V. Goodship ed., 2004. *Troubleshooting injection moulding* (Vol. 15). Pielichowski. iSmithers Rapra Publishing.

Huang, B., He, H., Meng, S., and Jia, Y. (2019). Optimizing 3D printing performance of acrylonitrile-butadiene-styrene composites with cellulose nanocrystals/silica nanohybrids. *Polym. Int.* 68 (7), 1351–1360. doi:10.1002/pi.5824

Khare, H. S., and Burris, D. L. (2010). A quantitative method for measuring nanocomposite dispersion. *Polymer* 51 (3), 719–729. doi:10.1016/j.polymer.2009.12.031

Koštial, P., Ružiak, I., Malinarič, S., Jančíková, Z., and Rusnák, V. (2016). "Injection Moulding Versus Rapid Prototyping—Thermal and Mechanical Properties," in *Machining, Joining and Modifications of Advanced Materials* (Singapore: Springer), 121–127.

Liu, P., and Kunc, V. (2020). "Effect of 3D printing conditions on the micro- and macrostructure and properties of high-performance thermoplastic composites," in *Structure and Properties of Additive Manufactured Polymer Components* (UK: Woodhead Publishing), 65–86. doi:10.1016/b978-0-12-819535-2.00003-x

Liu, Z., Wang, Y., Wu, B., Cui, C., Guo, Y., and Yan, C. (2019). A critical review of fused deposition modeling 3D printing technology in manufacturing polylactic acid parts. *Int. J. Adv. Manufacturing Tech.* 102 (9), 2877–2889. doi:10.1007/s00170-019-03332-x

Manzoor, F., Golbang, A., Jindal, S., Dixon, D., McIlhagger, A., Harkin-Jones, E., et al. (2021). 3D printed PEEK/HA composites for bone tissue engineering applications: Effect of material formulation on mechanical performance and bioactive potential. *J. Mech. Behav. Biomed. Mater.* 121, 104601. doi:10.1016/j.jmbbm.2021.104601

Mokhtari, M., Archer, E., Bloomfield, N., Harkin-Jones, E., and McIlhagger, A. (2021). A review of electrically conductive Poly (ether ether ketone) materials. *Polym. Int.*, 1016–1025. doi:10.1002/pi.6176

Mokhtari, M., Archer, E., Bloomfield, N., Harkin-Jones, E., and McIlhagger, A. (2021). High-performance and cost-effective melt blended poly (ether ether ketone)/expanded graphite composites for mass production of antistatic materials. *Polym. Int.*, 1137–1145. doi:10.1002/pi.6226

Pinto, D., Bernardo, L., Amaro, A., and Lopes, S. (2015). Mechanical properties of epoxy nanocomposites using titanium dioxide as reinforcement - A review. *Construction Building Mater.* 95, 506–524. doi:10.1016/j.conbuildmat.2015.07.124

Rostom, S., and Dadmun, M. D. (2019). Improving heat transfer in fused deposition modeling with graphene enhances inter filament bonding. *Polym. Chem.* 10 (44), 5967–5978. doi:10.1039/c9py00832b

Schiavone, N., Verney, V., and Askanian, H. (2020). Effect of 3D printing temperature profile on polymer materials behavior. *3D Printing and Additive Manufacturing* 7 (6), 311–325. doi:10.1089/3dp.2020.0175

Shaharuddin, S. I. S., and Salit, M. S. (2006). A review of the effect of moulding parameters on the performance of polymeric composite injection moulding. *Turkish J. Eng. Environ. Sci.* 30 (1), 23–34.

Srinivas, V., van Hooy-Corstjens, C. S. J., Rastogi, S., and Harings, J. A. W. (2020). Promotion of molecular diffusion and/or crystallization in fused deposition modeled poly(lactide) welds. *Polymer* 202, 122637. doi:10.1016/j.polymer.2020.122637

Valino, A. D., Dizon, J. R. C., Espera, A. H., Jr, Chen, Q., Messman, J., and Advincula, R. C. (2019). Advances in 3D printing of thermoplastic polymer composites and nanocomposites. *Prog. Polym. Sci.* 98, 101162. doi:10.1016/j.progpolymsci.2019.101162

Verdejo de Toro, E., Coello Sobrino, J., Martínez Martínez, A., Miguel Eguía, V., and Ayllón Pérez, J. (2020). Investigation of a short carbon fibre-reinforced polyamide and comparison of two manufacturing processes: Fused Deposition Modelling (FDM) and polymer injection moulding (PIM). *Materials* 13 (3), 672. doi:10.3390/ma13030672

Wiesli, M. G., and Özcan, M. (2015). High-performance polymers and their potential application as medical and oral implant materials: a review. *Implant Dent* 24 (4), 448–457. doi:10.1097/ID.0000000000000285

Yang, C., Tian, X., Li, D., Cao, Y., Zhao, F., and Shi, C. (2017). Influence of thermal processing conditions in 3D printing on the crystallinity and mechanical properties of PEEK material. *J. Mater. Process. Tech.* 248, 1–7. doi:10.1016/j.jmatprotec.2017.04.027

Zanjanijam, A. R., Major, I., Lyons, J. G., Lafont, U., and Devine, D. M. (2020). Fused filament fabrication of peek: A review of process-structure-property relationships. *Polymers* 12 (8), 1665. doi:10.3390/polym12081665

Conflict of Interest: The authors declare that the research was conducted in the absence of any commercial or financial relationships that could be construed as a potential conflict of interest.

Publisher's Note: All claims expressed in this article are solely those of the authors and do not necessarily represent those of their affiliated organizations, or those of the publisher, the editors and the reviewers. Any product that may be evaluated in this article, or claim that may be made by its manufacturer, is not guaranteed or endorsed by the publisher.

frontiers in Materials

ORIGINAL RESEARCH
published: 15 October 2021
doi: 10.3389/fmats.2021.743146

Thermomechanical Characterization of Carbon Black Reinforced Rubbers During Rapid Adiabatic Straining

William Amoako Kyei-Manu[1]*, *Lewis B. Tunnicliffe*[2], *Jan Plagge*[3], *Charles R. Herd*[2], *Keizo Akutagawa*[1], *Nicola M. Pugno*[1,4] *and James J. C. Busfield*[1]

[1]School of Engineering and Materials Science, Queen Mary University of London, London, United Kingdom, [2]Birla Carbon, Marietta, GA, United States, [3]School of Mathematics and Natural Sciences, Bergische Universität Wuppertal, Wuppertal, Germany, [4]Laboratory of Bio-Inspired, Bionic, Nano, Meta Materials & Mechanics, Department of Civil, Environmental and Mechanical Engineering, Università di Trento, Trento, Italy

The thermo-mechanical properties of carbon black reinforced natural and styrene butadiene rubbers are investigated under rapid adiabatic conditions. Eleven carbon black grades with varying surface area and structure properties at 40 parts per hundred (phr) loading are studied and the unreinforced equivalents are included for reference. The results show a strong correlation of the modulus, mechanical hysteresis, temperature rise and calculated crystallinity of the rubbers measured in tensile extension with strain amplification factors. This highlights the influence of matrix overstraining on microstructural deformations of the rubber upon extension. The strain amplification factors are calculated *via* the Guth-Gold equation directly from carbon black type and loading, allowing a correlation of the fundamental morphological properties of carbon black with thermal and mechanical properties of rubbers upon extension. Analysis of the thermal measurements of the rubber compounds upon extension and retraction and contrasting between crystallizing and non-crystallizing rubbers reveals that a substantial irreversible heat generation is present upon extension of the rubber compounds. These irreversible effects most likely originate from microstructural damage mechanisms which have been proposed to account for the Mullins Effect in particle reinforced rubbers.

Keywords: carbon black, strain amplification, thermomechanical characterization, strain induced crytallization, elastomer, Mullins effect, thermography, hysteresis

OPEN ACCESS

Edited by:
Dong Xiang,
Southwest Petroleum University, China

Reviewed by:
Sanjay Mavinkere Rangappa,
King Mongkut's University of Technology North Bangkok, Thailand
Xiaodong Qi,
Southwest Jiaotong University, China

****Correspondence:***
William Amoako Kyei-Manu
w.a.kyei-manu@qmul.ac.uk

Specialty section:
This article was submitted to Polymeric and Composite Materials, a section of the journal Frontiers in Materials

Received: *17 July 2021*
Accepted: *23 September 2021*
Published: *15 October 2021*

Citation:
Kyei-Manu WA, Tunnicliffe LB, Plagge J, Herd CR, Akutagawa K, Pugno NM and Busfield JJC (2021) Thermomechanical Characterization of Carbon Black Reinforced Rubbers During Rapid Adiabatic Straining. Front. Mater. 8:743146. doi: 10.3389/fmats.2021.743146

INTRODUCTION

Particle reinforced rubbers are an important class of materials. Despite their ubiquity, there is still a lack of understanding of the mechanisms controlling their behaviors at both small and large strains. In this article we focus on effects at large strains (strains > ~50%). **Figure 1** illustrates the complex strain and strain history dependence of a typical particle reinforced rubber. The cyclic stress softening and strain history dependence are often referred to as the Mullins effect (Mullins, 1948). In addition, hysteresis and set effects are also present. Despite intensive investigation, the microstructural origins of this large strain behavior and the Mullins Effect are still not entirely clear. Theories to account for the pronounced stiffening (stress upturn) observed at very large strains include approaching the finite extensibility of the rubber network and also the self-reinforcement for rubber materials able to undergo strain induced crystallization. Strain history and hysteresis effects are commonly ascribed to several prosed microstructural damage mechanisms (Diani et al., 2009)

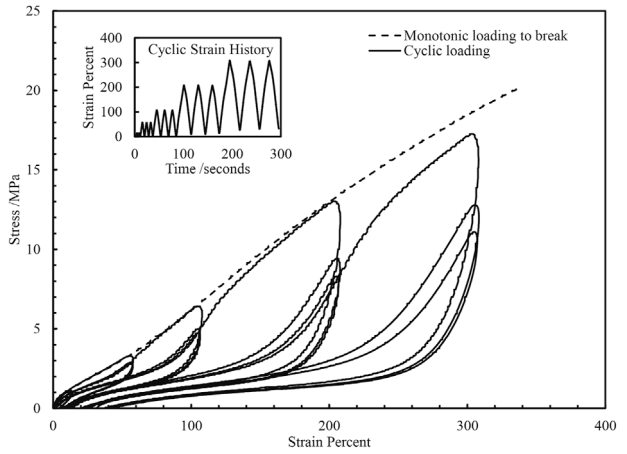

FIGURE 1 | Complex stress-strain behavior observed in 50 parts per hundred (phr) N550 carbon black reinforced natural rubber under cyclic tensile extension. Tests were done at a rate of 500 mm/min at room temperature.

which include: chain breakage at the interface between the rubber and reinforcing particulates, slippage of rubber macromolecules at the particle interface leading to a stress redistribution to neighbouring molecules, rupture of flocculated clusters of reinforcing particulates, progressive chain disentanglements, covalent bond scission and crosslink rupture (Clough et al., 2016) and yielding and rebirth of glass-like immobilized bridges between adjacent particles (Merabia et al., 2008) A common feature of all these proposed damage mechanisms is that they are associated with dissipation of strain energy in the form of heat.

When particulate reinforced rubbers are deformed in uniaxial tension, the heat evolved (Gough, 1805; Joule, 1859) can be attributed, to various degrees, to the intrinsic entropic elasticity (Meyer and Ferri, 1935; Anthony et al., 1942) and viscoelasticity (Payne and Whittaker, 1972) of the rubber matrix and to the hysteretic breakdown of the particulate network within the rubber (Grosch et al., 1967). Where rubbers are amenable to strain induced crystallization (SIC), the heat of fusion of the crystallites at high global strains may also contribute substantially to the observed evolution of heat from the specimen. These effects are strain and strain rate dependent (Tosaka, 2007; Brüning et al., 2015).

More recent numerical (Behnke et al., 2016; Dhawan and Chawla 2019) and experimental (Samaca Martinez et al., 2013; Samaca Martinez et al., 2014; Spratte et al., 2017) thermomechanical studies have expanded on these concepts. Akutagawa et al. (2015) concluded that temperature changes during stretching and retraction of rubber can be reduced to two processes: reversible and irreversible processes. Entropy elasticity and SIC are reversible processes whereas the hysteretic breakdown of the particulate network (particle-particle and particle-polymer breakdown) are irreversible. Le et al. (2020) conducted thermo-mechanical experiments on rubber and developed a quantitative model for the temperature variation caused by isentropic, entropic and viscous dissipation effects under steady state uniaxial tensile cyclic loading. Le Cam et al. (2015) used a calorimetric approach to characterize several important effects such as entropic elasticity, reinforcement by particulates, strain-induced crystallization and Mullins effect of filled and unfilled natural rubber (NR) and styrene butadiene rubber (SBR). Similarly, Le Saux et al. (2013) used a calorimetric approach to detect the onset strains for SIC and correlated this with data from X-ray measurements in literature.

SIC significantly enhances a number of mechanical properties of rubber compounds including crack growth resistance and tear resistance and tensile failure properties. These improvements in compound properties are traced back to a retardation of catastrophic and/or incremental crack growth due to crystallization of a portion of the highly strained rubber ahead of a crack tip (Brüning et al., 2013). NR exhibits SIC because close to 100% of its poly-isoprene chains have *cis*-configuration (Huneau, 2011; Gent, 2012). This stereo-regular structure of NR enables the polymer chains to crystallize either at low temperatures and/or at high strains, leading to a pronounced self-reinforcement. Despite this intrinsic reinforcement mechanism, unfilled NR compounds are unable to provide sufficient mechanical reinforcement, notably abrasion resistance, to be of practical use in many engineering applications and is therefore further reinforced by incorporating fine particulates such as carbon black (CB). Both SIC and the inclusion of CB play critical roles in the reinforcement of rubber products.

Various researchers have investigated the effect of CB on SIC in NR. Lee and Donovan (1987) showed that the inclusion of CB facilitates SIC and increases the size of the crystallized zone at the stressed crack tip. Trabelsi et al. (2003) demonstrated that in NR reinforced with 50 parts per hundred rubber (phr) CB, the onset strain for SIC was 100%, versus 300% for unreinforced NR. This reduction in global onset strains for SIC was attributed to matrix strain amplification due to the presence of rigid CB within the rubber. This process was first proposed by Mullins and Tobin (1966) to explain the stiffening effect that reinforcing particles such as CB had on rubbers. The presence of rigid particles within the rubber causes local overstraining of the rubber matrix when compared with the applied macroscopic strain level. Trabelsi et al. (2003) observed two different regions of strain amplification: a lower strain region where SIC has not occurred and in which the strain amplification factor is independent of applied global strains and a region where SIC has occurred and strain amplification is weakly dependent on applied global strain. The reduction in onset strain of SIC due to the inclusion of reinforcing particulates was also observed by Chenal et al. (2007) who found that the extent of SIC and onset strain required for SIC also depends on the cyclic strain history of the reinforced rubber. Rault et al. (2006) studied SIC and reinforcement in CB reinforced rubbers in relation to strain amplification factors. From their analysis of the strain amplification factors, they observed that in rubbers that do not undergo SIC, reinforcement in filled rubbers has two causes: overstraining/strain amplification of the chains due to a purely geometrical effect and particles acting as new effective crosslinks within the rubber. The latter point of view is shared by Plagge

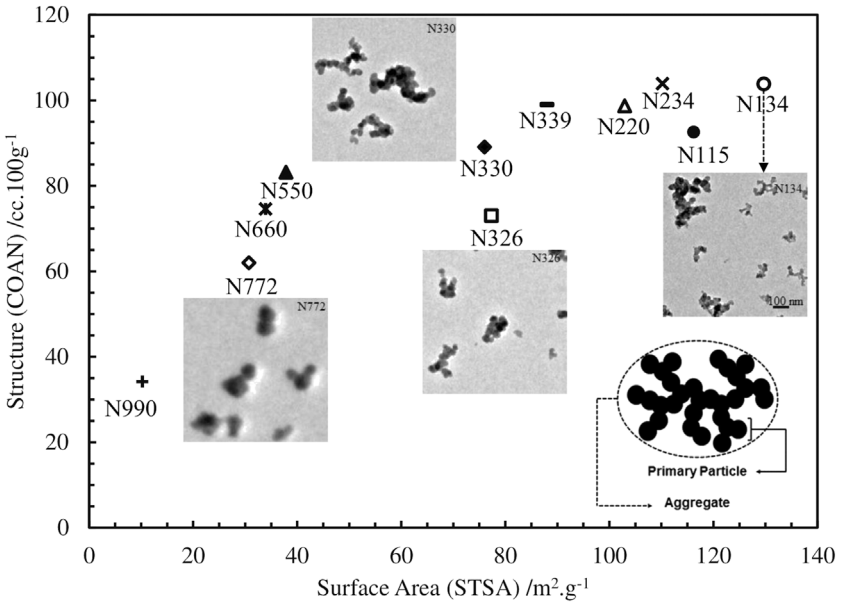

FIGURE 2 | Colloidal plot of carbon blacks studied in this article. A measure of the structure (COAN) is plotted against a measure of the surface area (STSA). Insert: Schematic of the primary particle-aggregate hierarchical structure of carbon black and representative TEM images of N772, N326, N330 and N134.

and Lang (2021) who related the large-strain stiffening to the physicochemical compatibility of carbon black and rubber. When the samples crystallize, the crystallites act as giant cross-links causing the stress to increase drastically with macroscopic extension. Rault et al. (2006) also observed that the addition of small amounts (20 phr) of CB strongly decreases the onset strains required for SIC. They hypothesize that this is due to the CB particles acting as crystal nucleation sites. This point of view is supported by a recent work by Sotta and Albouy (2020), where the SIC-related hysteresis of NR is traced back to nucleation-limited crystallization during stretching.

Many of these aforementioned studies have utilized X-ray scattering techniques to directly study SIC. Recently, two research groups, M. Klüppel and co-workers (Plagge and Klüppel, 2018) and J. B. Le Cam and co-workers (Le Cam et al., 2020), have lead efforts to measure SIC from the increase in temperature upon extension of rubber. While such thermographic techniques do not necessarily provide details on the structure of the crystallites formed, it might potentially provide a much more accessible way to determine the degree of crystallization in stretched rubber. For the case of particle reinforced rubbers, thermal characterization during extension also captures the heat generated from non-SIC related mechanisms (particle network breakdown, polymer-particle de-cohesion etc.).

Furthermore, although there have been numerous previous studies on the effect of CB on mechanical and thermal properties of rubber, there has been limited effort to correlate these effects with the fundamental size and morphological properties of carbon black. This is an important step to make, since these CB properties are already extensively utilized by rubber compound designers to engineer various properties of their compounds to meet end user requirements. Further quantitative understanding of their effects on SIC and other thermomechanical properties of rubbers offer potential for enhancement of rubber product performance.

This study evaluates the evolution of mechanical and thermal properties of NR and SBR compounds reinforced with different types of CB subjected to rapid adiabatic cyclic stretching and retraction. The mechanical results are analyzed in the context of the well-established strain amplification model. The temperature changes during stretching and retraction are similarly analyzed and extraction of information on the crystallization process is attempted. By contrasting NR compounds which are amenable to SIC to those which are not–Styrene Butadiene Rubber (SBR), various contributions to the observed stress and temperature changes upon extension and retraction are qualitatively evaluated.

MATERIALS AND METHODS

Materials

Compounds of SMR CV60 NR reinforced with eleven different CB grades at 40 parts per hundred rubber (phr) loading were prepared. An unreinforced NR counterpart was also included in the tests. The range of CBs used in this study was selected to cover a broad range of surface area and structure space as shown in **Figure 2**. The insert in **Figure 2** shows a schematic representation of an aggregate of CB and representative images from TEM for N772, N330, N326 and N134 CBs using the same scale bar of 100 nm. The aggregate is comprised of a fused assembly of para-crystalline primary particles. The size of the primary particles is the key parameter determining the surface area of the CB while the number and spatial arrangement of the primary particles

TABLE 1 | Composition of tested compounds.

Component	Loading/parts per hundred (phr)	
	Natural rubber	Styrene butadiene rubber
NR SMR CV (60)	100	NA
SBR 1502	NA	100
Carbon black	40	40
Zinc oxide	5	3
Stearic acid	3	1
Sulphur	2	1.75
TBBS[a]	1	1

[a]*N-Tertiarybutyl-2-benzothiazole sulfenamide.*

defines the structure level of CB. The surface area of carbon black is typically determined using nitrogen gas adsorption methods such as the nitrogen surface area (NSA) and statistical thickness surface area (STSA) methods (ASTM International, 2019) The structure level of CB is determined by measuring the amount of oil that is absorbed by a specific amount of carbon black-Oil absorption number (OAN) and compressed oil absorption number (COAN) methods (ASTM International, 2019; ASTM International, 2019).

Unreinforced emulsion SBR 1502 and SBR reinforced with N220 and N772 CBs at 40 phr were also prepared. These compounds were included to contrast with the NR compounds as SBR, unlike NR, does not undergo SIC. **Table 1** shows the compositions of the various compounds used in this study. **Table 2** gives the compound properties such as densities measured using a pycnometer and specific heat capacities measured using a differential scanning calorimeter. Interferometric microscope (IFM) dispersion index values are given in **Table 2**. IFM dispersion characterizes the level of incorporation of the CB into the rubber compounds on the macroscale and is a quantification of undispersed carbon black at a length scale greater than 5 μm diameter. Values of DI greater than 90 indicate an excellent dispersion. IFM DI measurements were performed according to ASTM D2663-14 (2019) method D.

Table 2 also presents the surface area (NSA, STSA) and structure (OAN, COAN) properties of the CBs in the compounds. Compounds were prepared by Birla Carbon (Marietta, GA, United States) using a 1.6 L capacity Banbury mixer and vulcanized sheets measuring 11 mm × 11 mm × ~2 mm were prepared by compression molding at 150°C for NR samples and 160°C for SBR samples to a time of T_{90}+5mins where T_{90} (time taken at 150°C/160°C for the specimen to reach 90% of maximum torque) was measured using an Alpha Technologies moving die rheometer (MDR). The mixing procedure is included in the supplemental information.

Experimental Method

Dumbbells for uniaxial extension and retraction experiments were cut from vulcanized sheets using a hydraulic die press. The dumbbells had approximate gauge length, width and thickness of 45, 6 and 2 mm respectively. To investigate thermal responses under adiabatic conditions, the samples were deformed using an Instron 8801 hydraulic mechanical testing machine equipped with a 1 kN load cell. The tests were run in a position-control mode with the lower grip moving to the targeted position(s). The specimens were extended to target uniaxial strains of 150, 250 and 350% at speeds of 20,000 mm/min giving a strain rate of about 7.40 s^{-1} and a stretching time of 0.5 s for the maximum strain of 350%. For contrast, Candau et al. (2012) determined the time needed for NR to crystallize once samples are elongated above the critical elongation for SIC as 0.02 s during cyclic tensile tests at high strain rates from 8 s^{-1} to 280 s^{-1}. After straining, the samples were held at the maximum

TABLE 2 | Colloidal[a] and compound properties and calculated strain amplification of tested compounds.

Carbon black type	Carbon black properties				Compound properties			Strain amplification factor
	NSA/ $m^2.g^{-1}$	STSA/ $m^2.g^{-1}$	OAN/ $cc.100g^{-1}$	COAN/ $cc.100g^{-1}$	Density,ρ /$g.cm^{-3}$	Heat capacity, $c_p/Jg^{-1}K^{-1}$	Dispersion index	
Natural rubber compounds								
N234	116	110	126	104	1.119	1.314	92	3.102
N134	140	130	125	104	1.120	1.406	91	3.100
N339	91	88	121	99	1.108	1.301	98	2.998
N220	110	103	113	99	1.104	1.348	97	2.991
N115	131	116	112	93	1.111	1.350	94	2.865
N330	76	76	102	89	1.111	1.374	97	2.794
N550	38	38	121	83	1.113	1.303	99	2.678
N660	35	34	93	75	1.106	1.308	95	2.515
N326	77	77	73	73	1.115	1.370	92	2.485
N772	32	31	69	62	1.114	1.351	78	2.290
N990	11	10	34	34	1.114	1.296	96	1.853
Unfilled	NA	NA	NA	NA	0.976	1.564	NA	1.000
Styrene Butadiene Rubber Compounds								
N220	110	103	113	99	1.119	1.292	98	2.991
N772	32	31	69	62	1.122	1.314	93	2.290
Unfilled	NA	NA	NA	NA	0.976	1.635	NA	1.000

[a]*NSA is nitrogen surface area, STSA is statistical thickness surface area, OAN is oil absorption number and COAN is compressed oil absorption number.*

strain for 2 min to regain thermal equilibrium before being rapidly retracted to zero strain at the same strain rate. This process was repeated 10 times for each specimen with three specimens being measured for each compound.

The specimen temperature was measured using a FLIR A35 (focal length = 9 mm) infrared camera. The camera has a thermal sensitivity/noise equivalent temperature difference (NETD) of <0.05°C at +30°C/50 mK and an IR resolution of 320 × 250 pixels. The camera was turned on 2 h prior to the measurements to ensure the internal temperature of the camera was stabilized. The acquisition frequency was set to the maximum rate of 60 Hz. The mean average temperature of a rectangle covering a pixel area of about 225 pixels was used to track and measure the temperature in the center of the specimen during straining and retraction using the FLIR Research IR software. The emissivity was set to 0.95 which is a reasonable approximation for CB reinforced rubber (Browne and Wickliffe, 1979; Luukkonen et al., 2009). The ambient room temperature was measured by placing a black body in the view of the camera and this was verified with a standard thermocouple.

The mechanical and temperature data were recorded on the 1st, 5th and 10th loading and unloading cycles to investigate the effect of Mullins softening on mechanical properties and temperature evolution. However, due to the high permanent set of the filled samples, particularly at high strains, the samples at 350% were re-gripped prior to the 5th and 10th cycles.

Strain Amplification

The results obtained from the thermomechanical experiments are quantitatively discussed using strain amplification factors, X. It is therefore necessary to discuss how these are calculated for the purpose of this paper. Mullins and Tobin (1966) proposed the general concept that when rigid particles are introduced into a rubber matrix they cause greater average deformation on the local scale, ε_{local} versus the globally applied strain level, ε_{global}.

$$\varepsilon_{local} = X\varepsilon_{global}$$

X is therefore a strain amplification factor that quantifies the degree to which the applied global strain is amplified on average at the local scale level. Models with varying levels of sophistication can be used for calculating the strain amplification factor (Huber and Vilgis 1999; Klüppel 2003; Allegra et al., 2008; Domurath et al., 2012), with each having distinct advantages and limitations.

In this paper, we use the simple and widely used Guth-Gold equation which predicts the strain amplification in the compound from the effective volume fraction of particulates in the composite.

$$X = 1 + 2.5\varphi_{eff} + 14.1\varphi_{eff}^2$$

The Guth-Gold equation was developed for spherical particles at low to moderate volume fractions (Mullins and Tobin 1966). The Guth-Gold equation does not account for any substantial networking of particulates within the rubber-which commonly occurs at small to moderate strains-nor any breakdown of the particle-particle network or de-cohesion of the particle-rubber interface. This assumes therefore that X is independent of applied strain level.

The effective volume fraction of CB in each compound, φ_{eff}, is defined as the volume fraction of the carbon black in the rubber plus the volume fraction of rubber occluded from global strain by the CB aggregate structure. In practice it is calculated using the actual volume fraction of CB, φ and the compressed oil absorption number (COAN) which is a measure of the structure of carbon black aggregates. This approach is based on the method initially developed by Medalia (1972) and later modified by Wang et al. (1993). They considered the end point of absorption titration of CB with a specific volume of oil and de-convoluted the intra-aggregate and inter-aggregate oil volumes in the oil/CB cake at the end of the test. The permeated equivalent sphere volume and inter-aggregate oil volume are calculated by assuming that the equivalent spheres pack randomly at a volume fraction of 0.63. The effective volume fraction in a rubber compound, φ_{eff} is then given by the following equation where V_p is the permeated volume of equivalent spheres, V_f is the volume of filler, V_v is the volume between the permeated equivalent spheres, and ρ_{CB} is the density of the CB.

$$\varphi_{eff} = \varphi\left(\frac{1+e}{1+\epsilon}\right)$$

$$e = \frac{(V_p - V_f) + V_v}{V_f} = \frac{\rho_{CB}\mathrm{COAN}}{100}$$

$$\epsilon = \frac{V_v}{V_p} = \frac{0.37}{1-0.37}$$

$$\varphi_{eff} = \varphi\left(\frac{0.0181\mathrm{COAN}+1}{1.59}\right)$$

$$\varphi = \frac{\left(\frac{\text{phr CB}}{\rho_{CB}}\right)}{\left(\frac{\text{phr CB}}{\rho_{CB}}\right) + \left(\frac{\text{phr NR}}{\rho_{NR}}\right)}$$

″phr CB″ and ″phr NR″ are the filler loadings of carbon black and natural rubber respectively in the compound. ρ_{CB} and ρ_{NR} are the densities of carbon black and natural rubber which are taken as 1.81 $\frac{g}{cm^3}$ and 0.92 $\frac{g}{cm^3}$ respectively based on Birla Carbon datasheets.

Tunnicliffe (2021a) recently demonstrated that the Guth-Gold strain amplification factor can be used to scale fatigue crack growth resistance of CB reinforced NR and showed good correlations between calculated strain amplification factors and the state of strain immediately ahead of crack tips in NR Liu et al., 2015. Trabelsi et al. (2003) also showed that experimentally measured strain amplification factors were in good agreement with the Guth-Gold equation. The calculated strain amplification factors of the tested specimen are listed in **Table 2**.

Calculating the Extent of Crystallinity from Thermal Measurements

The methods for calculating crystallinity directly from temperature measurements are described in detail in Plagge and Klüppel (2018) and Le Cam et al. (2020). Le Cam's method is a four step approach that is based on quantitative

calorimetry and temperature measurements. To date it currently has not been applied to reinforced rubber materials and will be the objective of subsequent studies. Plagge and Klüppel's method depends on an energy balance process where the mechanical energy input δW, is balanced with the internal energy, $\mathrm{d}U$, and heat exchange with the environment, δQ. The internal energy is split into a kinetic part which measures microscopic excitations such as vibration, translation and rotation in terms of the heat capacity, C_p, density, ρ, and change in sample temperature and energy gain from crystallization which is labelled as U_c. It is assumed here that all the energy gained is due to crystallization and ignores non-reversible energy dissipation mechanisms in filled rubber such as particle-particle and particle-polymer breakdown. The calculated crystallinity is therefore very likely over estimated by this calculation.

The resulting equation is similar to the first law of thermodynamics (written per volume) as follows:

$$\mathrm{d}U = \delta Q + \delta W$$
$$C_p \rho \mathrm{d}T - \mathrm{d}U_c = \delta Q + \delta W$$
$$U_c = \text{Energy for Crystallization} = \int \left(C_p \rho \mathrm{d}T - \delta W - \delta Q\right)$$

The greatest uncertainty in using this approach is how to determine the amount of heat, δQ exchanged with the environment through convection and radiation. It requires using an algorithm to optimize functions that smoothly vary with time. Rapid extension and retraction rates minimize heat exchange with the environment as discussed in *Heat Exchange Characterization* Section, and this allows us to assume adiabatic conditions and ignore this contribution. The total energy and index of crystallization is therefore simply calculated without δQ as:

$$U_c = \text{Energy for Crystallization} = \int \left(C_p \rho \mathrm{d}T - \delta W\right)$$
$$K = Apparent\ Crystallinity\ Percentage$$
$$= \frac{U_c}{\left(1 - \varphi_{filler}\right)\Delta H} \times 100\%$$

where K which is the percentage of the rubber that is crystalline is calculated from the enthalpy of fusion of the pure polymer, ΔH, which is estimated to be about 61 J cm^{-3} for NR. For the filled compounds, K is normalized by taking into account the filler volume fraction, φ_{filler}.

Heat Exchange Characterization

A fundamental solution to the heat diffusion equation (Plagge and Klüppel, 2018) is:

$$T(x,t) = \frac{1}{\sqrt{4\pi\kappa t}} e^{-\left(\frac{x^2}{4\kappa t}\right)}$$

where x is the thickness of the specimen, κ is the thermal diffusivity and t is time elapsed. From the exponent, the timescale of heat diffusion therefore scales as

$$\tau = \frac{x^2}{4\kappa}$$

For rubber, $\kappa \approx 1.5 \times 10^{-7} \frac{\mathrm{m}^2}{\mathrm{s}}$ and for our samples, $x \approx \frac{\text{sample thickness}}{2} = \frac{2 \times 10^{-3}\ \mathrm{m}}{2} = 1 \times 10^{-3}$ m and hence $\tau \approx 1.7\ s$.

This implies that an inhomogeneous temperature field within the rubber strip (size = 2 mm) will equilibrate in approximately 2 s. Due to the rapid extension and retraction, the timescale of the experiments are of the order of milliseconds; well within the timescale of heat diffusion. The temperature measurements are therefore more likely the real localized temperature of the samples instead of an averaged one due to diffusion.

To characterize the adiabatic nature of the current experimental set up, a specimen similar to those used in the main experiments of this work was heated in an oven for about 3 h at 60°C to ensure a homogenous temperature distribution. The specimen was then quickly gripped in the testing machine and the natural return to room temperature was recorded as a function of time. A heat exchange equation (based on a best fit line with an R^2 value of 0.97, see **Supplemental Data sheet**) which considers the experimental set up and environment was obtained from this graph as

$$T = 17.02\ e^{-\frac{\Delta t}{100}}$$

where T is the temperature variation and t is the time elapsed. The maximum time for extension/retraction in our experiments is about 0.5 s, which produces a 0.08°C temperature variation to the environment. This drop is very close to the smallest temperature resolution of <0.05°C at +30°C/50 mK of the infrared camera.

RESULTS

Mechanical Properties

Stress-Strain and Mooney-Rivlin Curves

Figures 3A–C shows the stress-strain curves for the 1st, 5th and 10th cycles of CB reinforced and unreinforced NR specimens when extended to 350% strain and retracted following a 2 min hold. There is a clear distinction between the initial extension curves depending on the CB types. The CBs with higher strain amplification factors, which is the result of higher structure level of the CB, have a higher incremental modulus response versus CBs with lower strain amplification factors and hence a lower structure. This is illustrated in **Figure 3D** where the measured stress at 300% strain is plotted versus the compound strain amplification factor. Strong linear correlations between the stress value at 300% and strain amplification factors are observed for each cycle level (R^2 values are indicated in the Figure). Upon retraction of the specimens however, there is minimal distinction between the stress-strain curves of the different compounds. This is an interesting observation which requires additional investigation, including a further analysis of the polymer and CB-related stress relaxation occurring during the 2 min hold period. Subsequent papers, would attempt to decompose the contribution of the stress relaxation resulting from strain induced crystallization and post-stretch relaxation based on a model proposed by Tosaka et al. (2006).

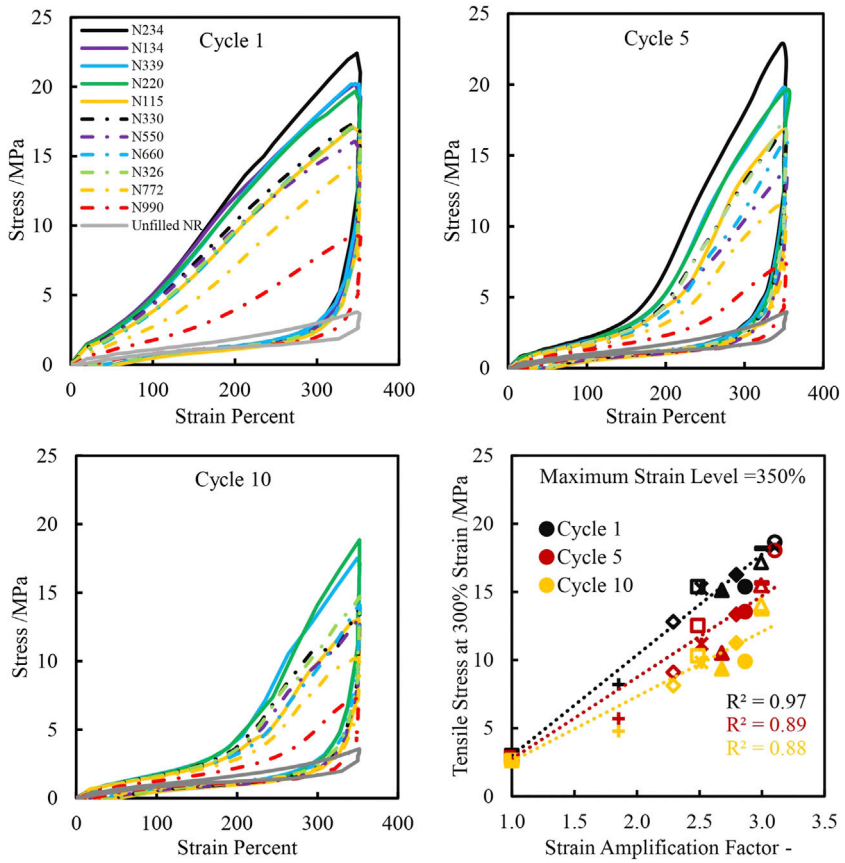

FIGURE 3 | Stress-strain plots of carbon black reinforced and unreinforced natural rubber extended to 350% strain and retracted after a 2 min hold on cycles 1, 5 and 10. Tensile stress at 300% strain as a function of strain amplification factor for cycles 1, 5 and 10.

It has been shown by different authors (Mullins and Tobin 1966; Mark and Erman 2007) that the Mooney-Rivlin relation can be used to describe the stress-strain behavior of rubber at finite extensions. Typically stress-strain data plotted according to the Mooney-Rivlin model show a large and abrupt increase in modulus at high elongations which corresponds to a significant stiffening of the rubber. The molecular origin for this upturn is widely debated. Most attribute it to the limit of the finite extensibility of the network chain (Treloar 1975). Others have attributed it to crystallization upon stretching since experiments in NR showed the upturns diminish with increase in temperature and swelling (Su and Mark, 1977). The reduced stress is calculated and plotted as a function of the inverse of extension ratio in **Figure 4** for cycles 1, 5 and 10.

$$\text{Reduced Stress} = \frac{\sigma}{2\left(\lambda - \frac{1}{\lambda^2}\right)} = C_1 + \frac{C_2}{\lambda}$$

where σ is the engineering stress and λ is the extension ratio. C_1 and C_2 are constants where C_2 is the straight line portion of the graph and $C_1 + C_2$ is the intercept on the vertical axis (Mooney 1940; Rivlin 1948; Treloar 1975)

The qualitative shapes of the stress-strain extension curves and Mooney-Rivlin curves differ between different cycles. Cycles 5 and 10 have a more distinct sigmoid shape with an upward inflection of the curve at strains greater than about 150% for the extension curves. The Mooney-Rivlin curves also show an upturn in stress on cycles 5 and 10 at higher strain values. This stress upturn is due to the progressive crystallization of the NR which stiffens the specimen and/or from the rubber macromolecules approaching finite extensibility. On the 1st cycle of the stress strain curve, however, this upturn is not as distinct. The upturn in stress on the 1st cycle is almost gradual and starts at lower strains compared to cycles 5 and 10 for the Mooney-Rivlin curves as well. These differences are likely due to the differences in microstructural damage history between the 1st and subsequent cycles. As discussed in the introduction, such "damage" could be the result of CB aggregate-aggregate network breakdown, polymer-particle de-cohesion and sliding, and disentanglement of the rubber network (Toki et al., 2013).

Mechanical Hysteresis

The hysteresis losses in rubber are an important factor influencing the rubber's fracture properties. Hysteresis losses dissipate energy input into the rubber thereby increasing the threshold required for fracture. The mechanical hysteresis is calculated as the difference between the area under the loading and unloading curves and plotted as functions of the strain

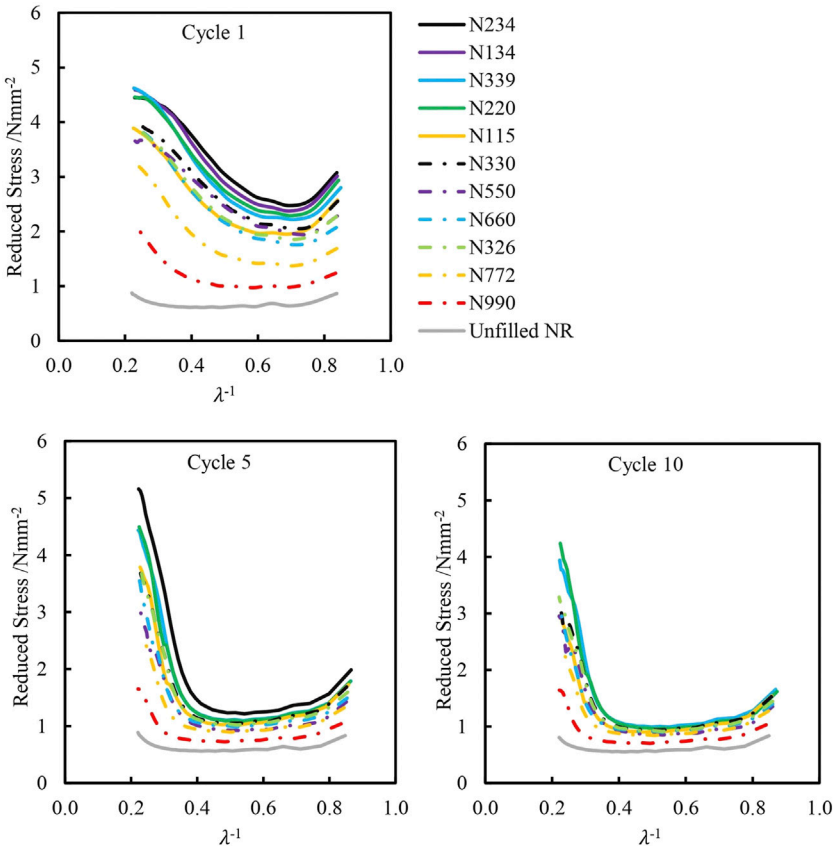

FIGURE 4 | Mooney-Rivlin plots of carbon black reinforced and unreinforced natural rubber extended to 350% strain on cycles 1, 5 and 10.

amplification factor in **Figure 5**. Similar to the tensile stress at 300%, the mechanical hysteresis strongly scales with the strain amplification factor. This observation indicates that selection of CB structure level is important in determining the moduli and mechanical hysteresis of the rubber compound at finite strains. Note that this contrasts with the effect of CB on hysteresis at small to medium strains (the strain range under consideration when examining the Payne Effect), where the surface area of the carbon black generally dictates the levels of hysteresis (Fröhlich et al., 2005, Tunnicliffe (2021b).

Temperature Measurements

Figure 6 is the temperature, stress and strain as a function of time for the 1st cycle of the N234 CB reinforced NR strained to 350%, held for about 2 min and retracted. The significantly slower rate of cooling during the 2 min hold in comparison to the timescale of heating and cooling during extension and retraction highlights that the thermal measurements are conducted under adiabatic conditions. The stress drops significantly in the first few seconds of the 2 min hold, another interesting observation, which a further analysis of the polymer and CB-related stress relaxation during the 2 min hold period will help explain.

The rise and drop in temperature of the specimens extended to 350% and then retracted are plotted in **Figure 7** for the first cycle. Analogous to the mechanical data, there is a clear distinction between the temperature rises upon extension depending on CB type, but minimal differences between the samples upon retraction. Processes such as breakdown of the CB network and strain-induced crystallization dissipate energy during extension causing the observed temperature rise.

$$\text{Temperature Rise} = \text{Temperature}_{\text{final}} - \text{Temperature}_{\text{initial}}$$

$$\text{Temperature Drop} = \text{Temperature}_{\text{final}} - \text{Temperature}_{\text{after2minhold}}$$

The change in temperature for each compound is plotted as a function of the calculated strain amplification factor for strains of 350% (black), 250% (yellow) and 150% (red) for cycles 1, 5 and 10 in **Figure 8**. The data above Temperature Change = 0°C show a rise in temperature and those below 0°C reflect a drop in temperature. From the graph there is a strong correlation of the rise in temperature with strain amplification factor–mirroring the observation for the corresponding mechanical data. As strain amplification increases, the rise in temperature increases, as does the measured stress at a given strain level. There seems to be no apparent correlation with drop in temperature upon retraction. Again this is an area for further investigation. During repeated cycling of the materials, the maximum achieved temperature change upon extension is reduced–most notably between the 1st and 5th cycles. Conversely, the magnitude of temperature change upon retraction appears to be broadly unaffected by cycle number.

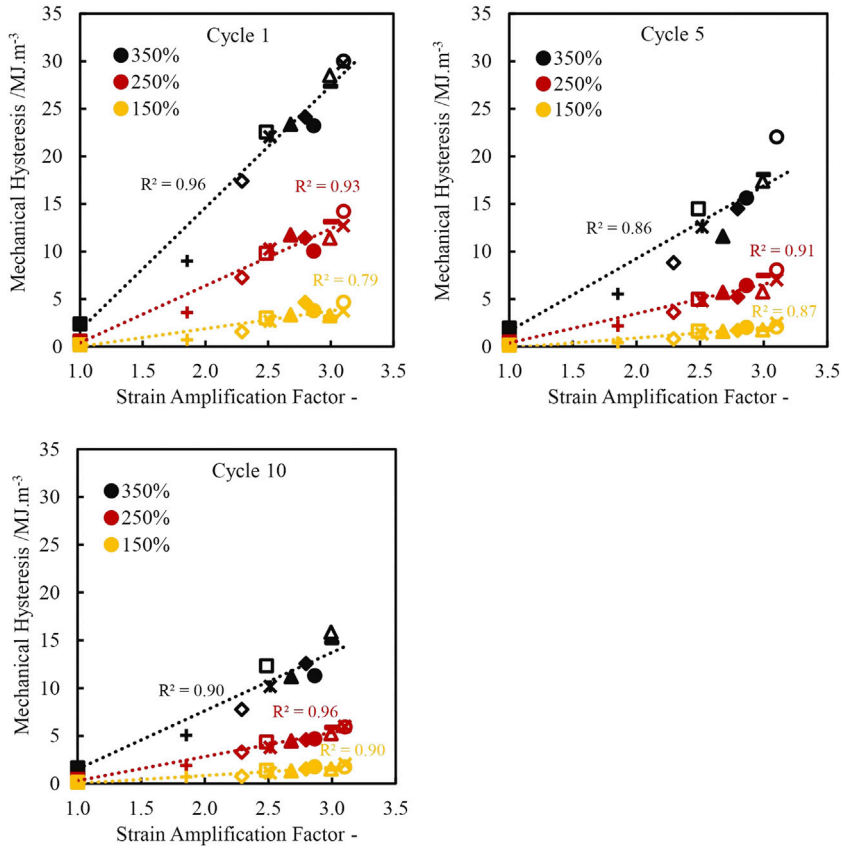

FIGURE 5 | Mechanical hysteresis on cycles 1, 5 and 10 as a function of strain amplification factor of natural rubber samples extended to 350% strain.

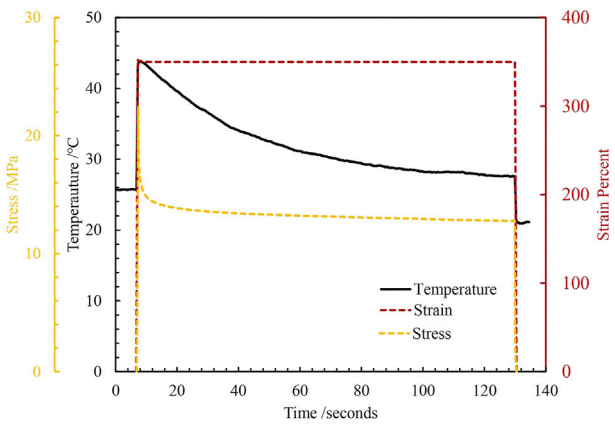

FIGURE 6 | Temperature profile, stress and strain as a function of test time for N234 reinforced natural rubber rapidly extended to 350% strain, held for 2 min and rapidly retracted.

Figure 9 plots the peak stress upon extension and the corresponding temperature rise upon extension for all strains and cycles for all NR compounds. All the points collapse on a master curve with reasonable correlation (R^2 = 0.89), independent of the cycle number, strain level or CB type, suggesting the CB structure controls the maximum stress and corresponding temperature rise.

Strain Induced Crystallization Estimations

Using the approach detailed in *Calculating the Extent of Crystallinity from Thermal Measurements* Section, the apparent crystallinity percentage was estimated for NR specimens after the 1st, 5th and 10th cycles. **Figures 10A,B** show the graphs of the calculated apparent crystallinity percentage upon extension and retraction respectively to and from 350% strain on the 1st cycle. Mirroring the stress-strain and temperature change graphs discussed in *Mechanical Properties* Section *and Temperature Measurements* Section, there is a clear distinction between the calculated apparent crystallinity percentages formed upon extension dependent on the type of CB, but the extent of percentage crystallinity change upon retraction is largely indistinguishable between compounds. **Figures 11A–C** plots the peak apparent crystallinity for each compound at 150, 250 and 350% extension, for the 1st, 5th and 10th cycles, as a function of strain amplification factor. The calculated crystallinity extent correlates well with the strain amplification factors, with a higher strain amplification factor leading generally to a higher crystallinity value, as would be anticipated from a simple consideration of matrix overstraining. The calculated crystallinity extents are observed to decrease successively on

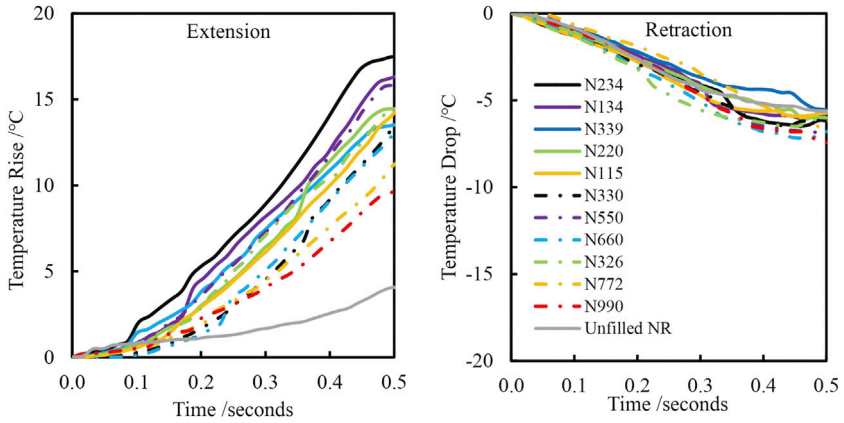

FIGURE 7 | Temperature rise and temperature drop of carbon black reinforced and unreinforced natural rubber extended to 350% strain and retracted after a 2 min hold for 1st cycle.

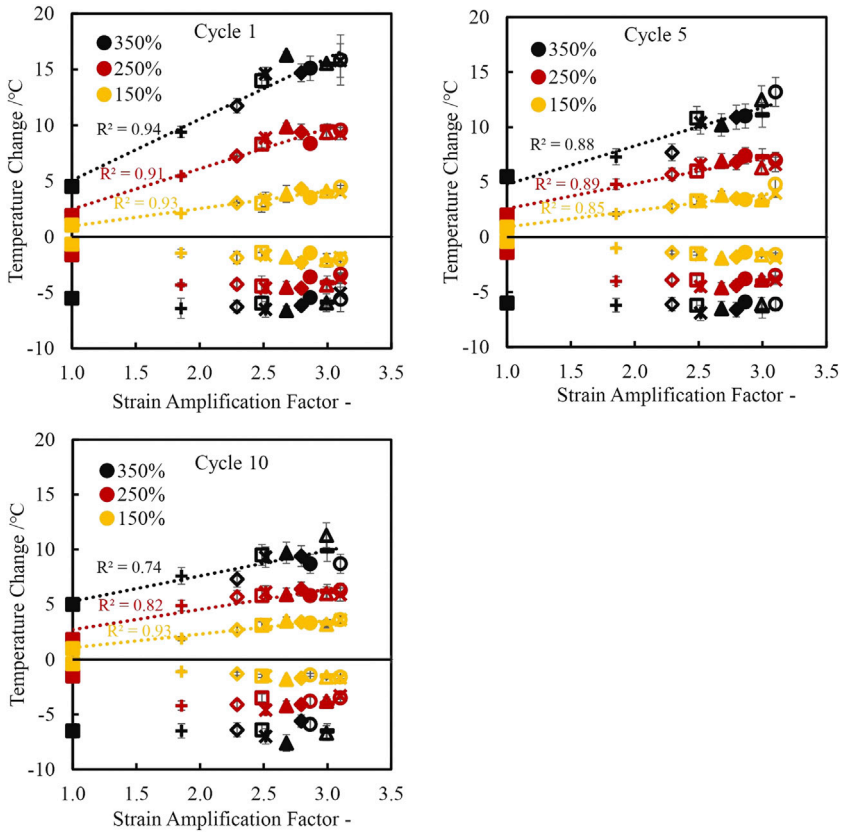

FIGURE 8 | Temperature change as a function of strain amplification factor of carbon black reinforced and unreinforced natural rubber extended on cycles 1, 5 and 10. Positive values are the temperature rise upon extension and negative values are the corresponding temperature drop upon retraction.

each cycle. For contrast, *in situ* Wide Angle X-ray synchrotron (WAXS) experiments conducted on 45 phr N234 reinforced NR extended at a strain rate of 0.25 min^{-1}(~0.0042 s^{-1}) produced similar decreasing crystallinity values upon successive cycles with maximum crystallinities of about 28, 22 and 21% on the first, second and third cycles at a peak strain of ~250% (Chenal et al., 2007).

Figure 11D shows the onset strain percent for crystallite formation for each compound also plotted as a function of the strain amplification factor. Higher strain amplification generally

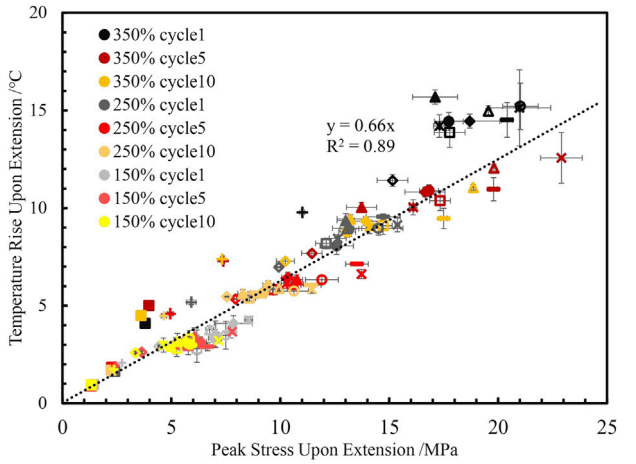

FIGURE 9 | Master-line relating peak stress upon extension and corresponding temperature rise at all tested strain percent and cycles.

leads to an earlier onset of the crystallinity. The onset strain percent for crystallinity also shows a slight increase (shift to higher strains) after the first cycle-similar to that reported by Chenal et al. (2007) who observed an increase in onset strain percent until a stable value is reached typically after three to five cycles.

It appears from **Figure 10** that not all crystals formed upon extension are melted during retraction. The maximum percentage change in crystallinity upon retraction is always significantly lower than the maximum percentage change in crystallinity during extension. These findings are problematic for the following reasons: 1) even when accounting for the fact that crystallinity is known to persist for a while during retraction (Treloar 1975), the values in **Figures 10A,B** imply that the majority of crystallites persist in the fully relaxed state following full retraction. 2) while the crystallization extent upon extension appears to strongly depend on the type of CB, this dependence is lost in the retraction data, despite the fact that the final levels of crystallinity achieved upon maximum extension should persist or even increase during the 2 min hold period as the material progresses towards an equilibrium level of crystallinity (Tosaka, 2007).

Although the data reported in **Figure 10A**, and **Figures 11A–C** are in reasonable agreement with literature for direct measurements of SIC from X-ray scattering techniques, the inconsistency of the retraction data sets with known phenomenological behavior of SIC implies that additional thermal effects both upon extension and retraction are likely influencing the crystallinity values obtained here. For filled rubber samples, it is challenging to use thermography alone to accurately measure the extent of crystallinity due to the irreversible heat generating mechanisms such as particle-particle and particle-polymer breakdown during extension which are difficult to de-convolute from reversible SIC effects.

Styrene Butadiene Rubber Samples

SBR is a non-crystallizing rubber and provides a useful contrast to the NR materials. **Figures 12A,B** show the stress-strain curves and Mooney-Rivlin plots for the SBR compounds strained to 350% for cycles 1, 5 and 10. Similar to the NR stress-strain data, the reinforced SBR compounds show a sigmoid-like curve with distinct stress upturns at high strains, which is especially noticeable for cycles 5 and 10, despite the absence of SIC for SBR. This highlights the pronounced reinforcement effects of CB in non-crystallizing rubbers. Also note that the modulus/stress builds for the SBR compounds scale as expected according to strain amplification factors (with N220 being greater than N772).

The unreinforced SBR does not exhibit any stress upturn. It is also worth noting that the unreinforced SBR specimens failed during the 2 min hold period after initial extension and hence, there is no retraction data for this compound. In comparison, the unreinforced NR displays a moderate stress upturn (**Figure 2**), and did not fail during the 2 min hold period, again highlighting the intrinsic reinforcing effects of SIC in NR.

The Mooney-Rivlin plots also display similar trends to those observed in the NR compounds. On the 1st cycle, the upturn in reduced stress is observed at relatively low strain levels (~100%). However, the stress upturn shifts to higher strains (~200%) after

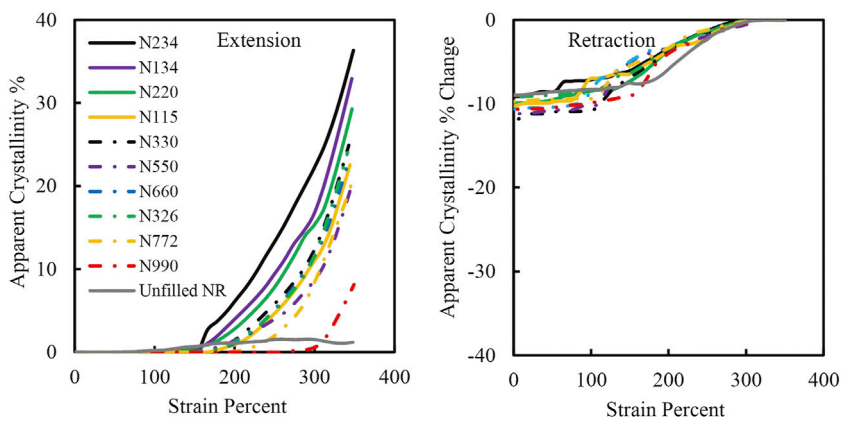

FIGURE 10 | Apparent crystallinity percent of carbon black reinforced and unreinforced natural rubber extended and retracted at 350% strain during cycle 1.

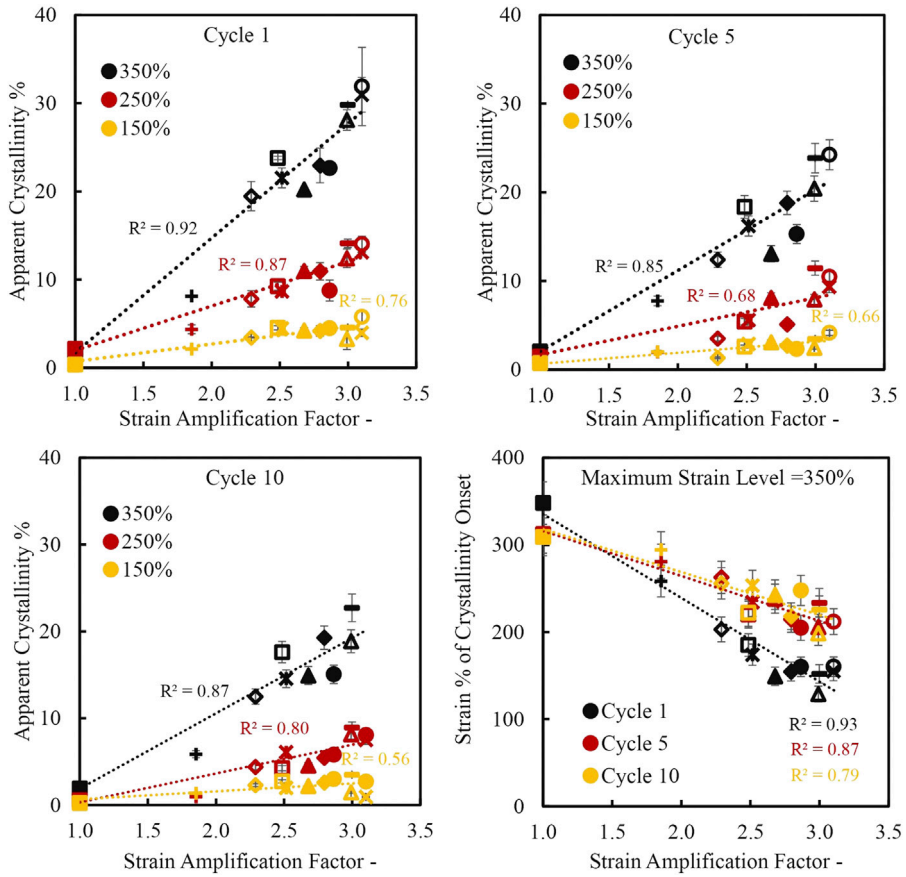

FIGURE 11 | Apparent crystallinity percent and onset of crystallinity as a function of strain amplification factor of carbon black reinforced and unreinforced natural rubber extended on cycles 1, 5 and 10.

cycles 5 and 10. The unreinforced SBR shows no stress upturn even at higher strains unlike the unreinforced NR specimen at 350% strain. Since the stress-strain and Mooney-Rivlin plots of reinforced styrene butadiene rubber specimens show similar behavior to the particulate reinforced NR specimens, it is difficult to conclusively attribute the upturn in stress and reduced stress observed in the NR specimens solely to the onset of SIC. Effects of particle-particle and particle-polymer interactions are clearly influencing the stiffening of the materials examined here.

Figures 12C,D show the temperature rise and drop for the SBR compounds. Again the observed temperature rise mirrors the evolution of stress during extension. The maximum observed temperature rise is ~13°C for the SBR compounds, which cannot be attributed to SIC but rather to entropic elasticity and particle-particle and particle-polymer mechanisms. When comparing analogous SBR and NR materials head to head as shown in **Figures 13A–C**, the NR specimens consistently show a higher change in temperature versus the SBR specimens. The temperature rise of N220 reinforced NR extended to 350% strain on the 1st cycle is ~16°C while the temperature rise of the N220 reinforced SBR is ~13°C. The drops in temperature when retracted from 350% strain on the 1st cycle is ~6°C and 4°C for the N220 reinforced NR and SBR respectively. While the temperature drops of the SBR specimens are lower compared to the NR specimens, it is worth highlighting the temperature drops of the SBR specimens which are entirely due to entropic elasticity are still relatively large. The difference in temperature evolution between the NR and SBR specimens may be due to the additional contribution from SIC in the NR compounds, but it is not possible to quantitatively attribute this difference in the temperature between the two analogous compounds directly to SIC due to inherent differences in polymer molecular architectures, viscoelasticity and crosslink densities. Nevertheless, these results demonstrate that entropic elasticity and particle-particle and particle-polymer mechanisms can contribute substantially to thermal evolution in strained rubbers and would need to be appropriately incorporated into quantitative evaluations of SIC from thermal measurements in reinforced NR compounds.

DISCUSSION

The tensile extension moduli of both the NR and SBR compounds scale linearly with strain amplification factors. This is due to

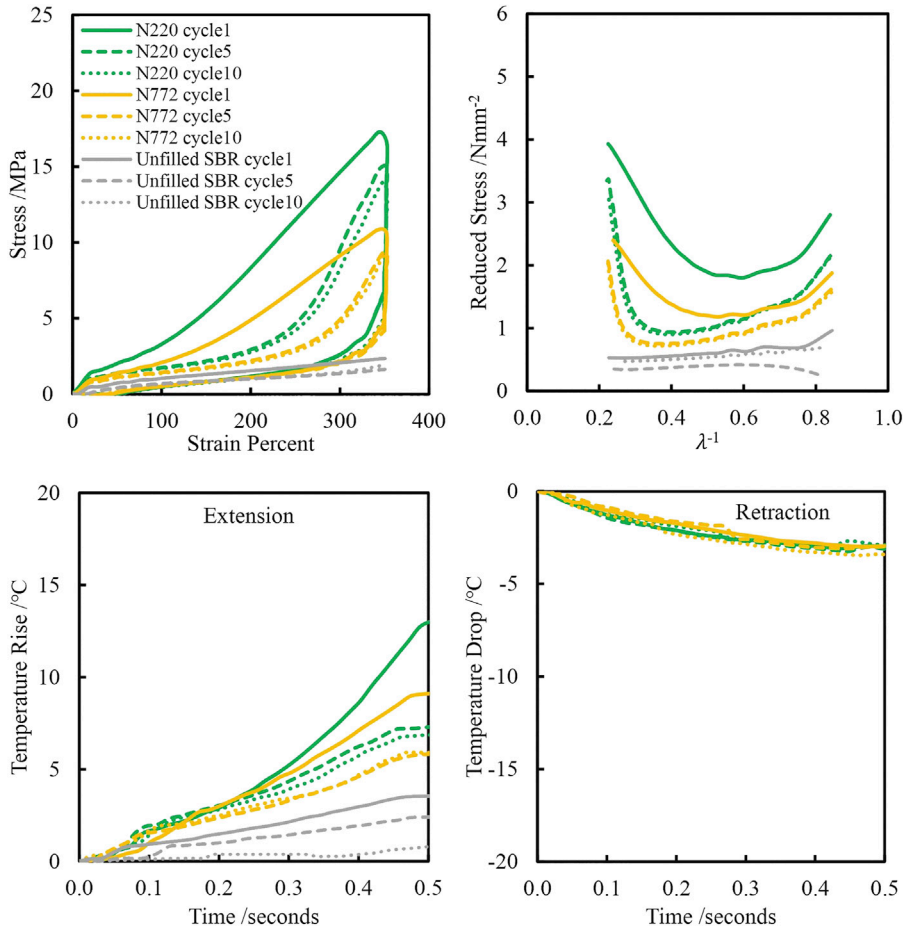

FIGURE 12 | Stress-strain, Mooney-Rivlin and temperature change plots of reinforced and unreinforced styrene butadiene rubber extended to 350% strain.

matrix overstrain effects; with the CBs with higher aggregate structure enhancing the local strain levels. The mechanical retraction data following the 2 min hold collapse onto each other-independent of the type of CB. This requires further investigation but it may be due to particle-particle and particle-polymer breakdown effects during extension and the 2 min hold which are absent upon retraction. Further analysis to de-convolute the contributions to the stress relaxation during the 2 min hold will provide more insight into this.

Mechanical hysteresis scales with strain amplification factors as well, which is most likely a reflection of these experiments being strain controlled, therefore a stiffer compound naturally gives higher hysteresis at fixed strain.

The thermal data for the NR compounds mirrors the mechanical data with the temperature rise upon extension scaling linearly with the strain amplification factor. Similar to the mechanical data, this is due to matrix overstrain effects where the carbon black aggregates with higher structure CBs enhance microstructural heat dissipation process such as the particle-particle and particle-polymer breakdown and SIC for the NR compounds during extension. The peak stress upon extension scales linearly with the corresponding temperature rise independent of cycle number, strain level and CB type. Upon retraction, the temperature drops show similar values, independent of the CB type.

The temperature data of the non-crystallizing SBR suggests that significant temperature generation upon extension must be related to reversible heat generation from entropic elasticity as well as particle-particle and particle-polymer irreversible heat generation. Substantial temperature drops upon retraction for the SBR compounds is related primarily to entropy elasticity and the values of the temperature drop is also very similar between the unreinforced and reinforced SBR compounds.

The calculation of the SIC extent of the NR compounds using the Plagge-Klüppel method shows some consistency with literature data for direct measurement of SIC from X-ray scattering but also produces some crucial differences. The lack of agreement between calculated crystallinity extents upon extension and then retraction, implies that additional, irreversible thermal effects arising from the inclusion of reinforcing particles are as important or maybe even dominate over the SIC contribution to heat evolution upon extension at these high strain rates. Further studies at varied strain rates could help to characterize the rate dependent nature of this dissipation

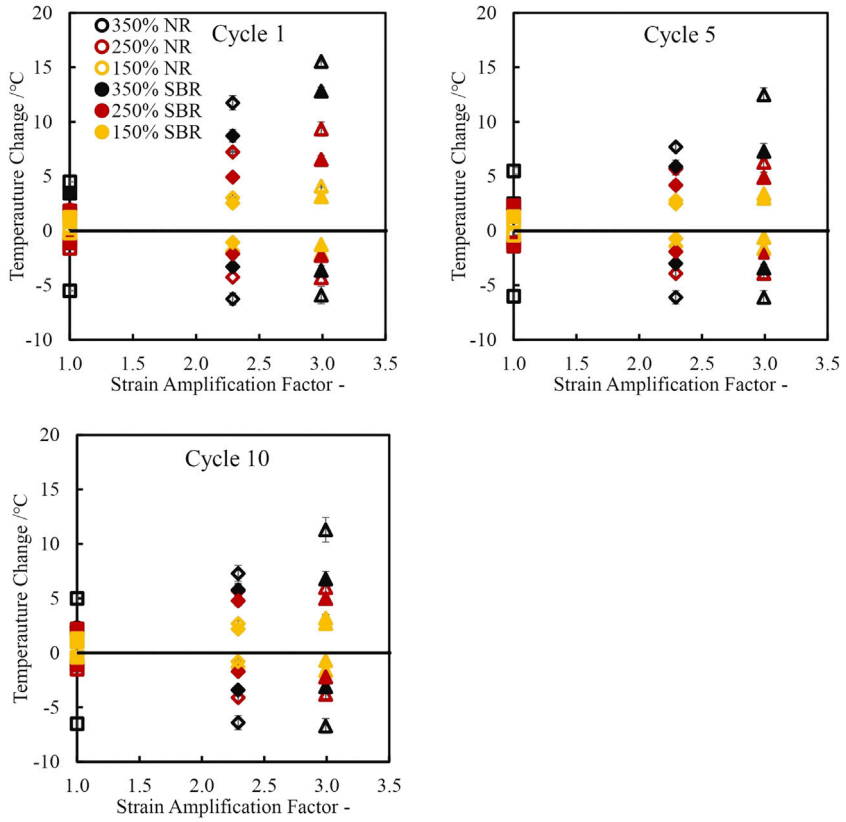

FIGURE 13 | Temperature change as a function of strain amplification factor comparing SBR (filled shapes) and NR (unfilled shapes) extended to 350% (black), 250% (red) and 150% (yellow) and retracted after 2 min.

in non-strain crystallizing rubbers. For particle reinforced rubbers, it will be necessary to quantitatively account for all these different effects in the future analysis of thermal data sets. Direct measurement of the SIC by X-ray scattering is planned to help de-convolute these thermal effects.

CONCLUSION

The thermomechanical properties of CB reinforced and unreinforced rubber compounds at large strains were characterized under adiabatic conditions. Two major conclusions can be drawn from the experiments:

1) Matrix overstrain effects play a significant role on microstructure mechanisms such as entropy elasticity, particle-particle and particle-polymer breakdown and SIC during extension. The modulus and temperature rise of the compounds during extension correlated well with calculated strain amplification factors for the various compounds. The calculated strain amplification factors were derived from the morphological properties of CB and based on our results show that the CB aggregate structure influences these microstructural mechanisms at large strain deformations.
2) Observed thermal effects upon extension are influenced and maybe even dominated by irreversible particle-particle and particle-polymer damage effects based on comparison of the results from non-crystallizing SBR and NR. This makes it difficult to accurately decompose the reversible contribution of SIC from the thermal measurements alone. Direct measurements of SIC by X-Ray scattering are planned as a next step in this work.

From a practical standpoint, the correlation of the mechanical and thermal effects with morphological properties of CB is significant since it can be a useful tool in the design of rubber compounds for engineering applications.

DATA AVAILABILITY STATEMENT

The original contributions presented in the study are included in the article/**Supplementary Material**, further inquiries can be directed to the corresponding author.

AUTHOR CONTRIBUTIONS

WK-M conducted the experiments, analyzed the results and contributed to the preparation of the manuscript. LT, JP, CH,

KA, NP, and JB provided significant intellectual input and guidance in conducting the experiments, analyzing and interpreting the results and contributed to the preparation of the manuscript.

FUNDING

The PhD project for which this research work was conducted is sponsored by Birla Carbon. NP is supported by the European Union within the project LIFE19 ENV/IT/000213–LIFE GREEN VULCAN.

ACKNOWLEDGMENTS

The authors would like to thank Birla Carbon for funding and providing the materials studied in this article.

SUPPLEMENTARY MATERIAL

The Supplementary Material for this article can be found online at: https://www.frontiersin.org/articles/10.3389/fmats.2021.743146/full#supplementary-material

REFERENCES

Akutagawa, K., Hamatani, S., and Nashi, T. (2015). The New Interpretation for the Heat Build-Up Phenomena of Rubbery Materials during Deformation. *Polymer* 66 (1), 201–209. doi:10.1016/j.polymer.2015.04.040

Allegra, G., Raos, G., and Vacatello, M. (2008). Theories and Simulations of Polymer-Based Nanocomposites: From Chain Statistics to Reinforcement. *Prog. Polym. Sci.* 33 (7), 683–731. doi:10.1016/j.progpolymsci.2008.02.003

Anthony, R. L., Caston, R. H., and Guth, E. (1942). Equations of State for Natural and Synthetic Rubber-like Materials. I. Unaccelerated Natural Soft Rubber. *J. Phys. Chem.* 46 (8), 826–840. doi:10.1021/j150422a005

ASTM D2663-14 (2019). "Standard Test Methods for Carbon Black—Dispersion in Rubber," in *Annual Book of ASTM Standard*.

ASTM International (2019). "ASTM Standard D2414-19," in *Standard Test Method for Carbon Black–Oil Absorption Number (OAN)*. (West Conshohocken, Pennsylvania: Annu. Book ASTM Stand. 09.01.

ASTM International (2019). "ASTM Standard D3493-19a," in *Standard Test Method for Carbon Black–Oil Absorption Number of Compressed Sample (COAN)*. (West Conshohocken, Pennsylvania: Annu. Book ASTM Stand. 09.01.

ASTM International (2019). "ASTM Standard D6556-19a," in *Standard Test Method for Carbon Black—Total and External Surface Area by Nitrogen*. (West Conshohocken, Pennsylvania: Annu. Book ASTM Stand. 09.01.

Behnke, R., Kaliske, M., and Klüppel, M. (2016). Thermo-mechanical Analysis of Cyclically Loaded Particle-Reinforced Elastomer Components: Experiment and Finite Element Simulation. *Rubber Chem. Techn.* 89, 154–176. doi:10.5254/rct.15.84852

Browne, A. L., and Wickliffe, L. E. (1979). Rubber Emissivity and the Thermal State of Tires. *Tire Sci. Techn.* 7 (3), 71–89. doi:10.2346/1.2151015

Brüning, K., Schneider, K., Roth, S. V., and Heinrich, G. (2015). Kinetics of Strain-Induced Crystallization in Natural Rubber: A Diffusion-Controlled Rate Law. *Polymer* 72, 52–58. doi:10.1016/j.polymer.2015.07.011

Brüning, K., Schneider, K., Roth, S. V., and Heinrich, G. (2013). Strain-induced Crystallization Around a Crack Tip in Natural Rubber under Dynamic Load. *Polymer* 54, 6200–6205. doi:10.1016/j.polymer.2013.08.045

Candau, N., Chazeau, L., Chenal, J.-M., Gauthier, C., Ferreira, J., Munch, E., et al. (2012). Characteristic Time of Strain Induced Crystallization of Crosslinked Natural Rubber. *Polymer* 53, 2540–2543. doi:10.1016/j.polymer.2012.04.027

Chenal, J.-M., Gauthier, C., Chazeau, L., Guy, L., and Bomal, Y. (2007). Parameters Governing Strain Induced Crystallization in Filled Natural Rubber. *Polymer* 48, 6893–6901. doi:10.1016/j.polymer.2007.09.023

Clough, J. M., Creton, C., Craig, S. L., and Sijbesma, R. P. (2016). Covalent Bond Scission in the Mullins Effect of a Filled Elastomer: Real-Time Visualization with Mechanoluminescence. *Adv. Funct. Mater.* 26, 9063–9074. doi:10.1002/adfm.201602490

Dhawan, M., and Chawla, R. (2019). A Computational Study on Thermo-Mechanical Characterization of Carbon Nanotube Reinforced Natural Rubber. *MRS Adv.* 4, 1161–1166. doi:10.1557/adv.2018.680

Diani, J., Fayolle, B., and Gilormini, P. (2009). A Review on the Mullins Effect. *Eur. Polym. J.* 45, 601–612. doi:10.1016/j.eurpolymj.2008.11.017

Domurath, J., Saphiannikova, M., Ausias, G., and Heinrich, G. (2012). Modelling of stress and strain amplification effects in filled polymer melts. *J. Nonnewton Fluid. Mech.* 171–172, 8–16. doi:10.1016/j.jnnfm.2012.01.001

Fröhlich, J., Niedermeier, W., and Luginsland, H.-D. (2005). The Effect of Filler-Filler and Filler-Elastomer Interaction on Rubber Reinforcement. *Compos. A: Appl. Sci. Manuf.* 36, 449–460. doi:10.1016/j.compositesa.2004.10.004

Gent, A. N. (2012). *Engineering with Rubber: How to Design Rubber Components*. Cincinnati, Munich: Hanser.

Gough, J. (1805). A Description of a Property of Caoutchouc, or Indian Rubber. *Mem. Literaci Philos. Soc. Manch.* 1, 288–295.

Grosch, K., Harwood, J. A. C., and Payne, A. R. (1967). Breaking Energy of Rubbers. *Rubber Chem. Techn.* 40 (3), 815–816. doi:10.5254/1.3539096

Houwink, R. (1956). Slipping of Molecules during the Deformation of Reinforced Rubber. *Rubber Chem. Techn.* 29 (3), 888–893. doi:10.5254/1.3542602

Huber, G., and Vilgis, T. (1999). Universal Properties of Filled Rubbers: Mechanisms for Reinforcement on Different Length Scales. *Kautschuk Gummi Kunststoffe* 52, 102–107.

Huneau, B. (2011). Strain-induced Crystallization of Natural Rubber: A Review of X-Ray Diffraction Investigations. *Rubber Chem. Technol.* 84, 425–452. doi:10.5254/1.3601131

Joule, J. (1859). V. On Some Thermo-Dynamic Properties of Solids. *Phil. Trans. R. Soc.* 149, 91–131. doi:10.1098/rstl.1859.0005

Klüppel, M. (2003). The Role of Disorder in Filler Reinforcement of Elastomers on Various Length Scales. *Adv. Polym. Sci.* 164, 1–86. doi:10.1007/b11054

Le Cam, J.-B., Albouy, P.-A., and Charlès, S. (2020). Comparison between X-ray Diffraction and Quantitative Surface Calorimetry Based on Infrared Thermography to Evaluate Strain-Induced Crystallinity in Natural Rubber. *Rev. Scientific Instr.* 91, 044902. doi:10.1063/1.5141851

Le Cam, J.-B., Samaca Martinez, J. R., Balandraud, X., Toussaint, E., and Caillard, J. (2015). Thermomechanical Analysis of the Singular Behavior of Rubber: Entropic Elasticity, Reinforcement by Fillers, Strain-Induced Crystallization and the Mullins Effect. *Exp. Mech.* 55, 771–782. doi:10.1007/s11340-014-9908-9

Le Saux, V., Marco, Y., Calloch, S., and Charrier, P. (2013). Contribution of Accurate thermal Measurements to the Characterisation of Thermomechanical Properties of Rubber-like Materials. *Plast. Rubber Compos.* 41 (7), 277–284. doi:10.1179/1743289812Y.0000000015

Le, T. H., Yoshikawa, T., Kurokawa, Y., and Inoue, H. (2020). A Quantitative Study on Temperature Variation of Rubber under Steady State Uniaxial Tensile Cyclic Loading. *Mech. Mater.* 148, 103523. doi:10.1016/j.mechmat.2020.103523

Lee, D. J., and Donovan, J. A. (1987). Microstructural Changes in the Crack Tip Region of Carbon-Black-Filled Natural Rubber. *Rubber Chem. Techn.* 60, 910–923. doi:10.5254/1.3536164

Liu, C., Dong, B., Zhang, L.-Q., Zheng, Q., and Wu, Y.-P. (2015). Influence of Strain Amplification Near Crack Tip on the Fracture Resistance of Carbon Black-Filled SBR. *Rubber Chem. Techn.* 88 (2), 276–288. doi:10.5254/rct.15.85956

Luukkonen, A., Sarlin, E., Villman, V., Hoikkanen, M., Vippola, M., Kallio, M., et al. (2009). Heat Generation in Dynamic Loading of Hybrid Rubber-Steel Composite Structure. In ICCM17 Conference Proceedings. (Edinburgh: International Conference on Composite Materials.)

Mark, J. E., and Erman, B. (2007). "Strain-induced Crystallization and Ultimate Properties," in *Rubberlike Elasticity: A Molecular Primer*. Editors J. E. Mark and B. Erman. 2nd ed. (Cambridge: Cambridge University Press), 117–130. doi:10.1017/CBO9780511541322.014

Medalia, A. I. (1972). Effective Degree of Immobilization of Rubber Occluded within Carbon Black Aggregates. *Rubber Chem. Techn.* 45 (5), 1171–1194. doi:10.5254/1.3544731

Merabia, S., Sotta, P., and Long, D. R. (2008). A Microscopic Model for the Reinforcement and the Nonlinear Behavior of Filled Elastomers and Thermoplastic Elastomers (Payne and Mullins Effects). *Macromolecules* 41, 8252–8266. doi:10.1021/ma8014728

Meyer, K. H., and Ferri, C. (1935). The Elasticity of Rubber. *Rubber Chem. Techn.* 8, 319–334. doi:10.5254/1.3539443

Mooney, M. (1940). A Theory of Large Elastic Deformation. *J. Appl. Phys.* 11 (9), 582–592. doi:10.1063/1.1712836

Mullins, L. (1948). Effect of Stretching on the Properties of Rubber. *Rubber Chem. Techn.* 21, 281–300. doi:10.5254/1.3546914

Mullins, L., and Tobin, N. R. (1966). Stress Softening in Rubber Vulcanizates. Part I. Use of a Strain Amplification Factor to Describe Elastic Behavior of Filler-Reinforced Vulcanized Rubber. *Rubber Chem. Techn.* 39 (4), 799–813. doi:10.5254/1.3547144

Payne, A. R., Whittaker, R. E., and Smith, J. F. (1972). Effect of Vulcanization on the Low-Strain Dynamic Properties of Filled Rubbers. *J. Appl. Polym. Sci.* 16, 1191–1212. doi:10.1002/app.1972.070160513

Plagge, J., and Klüppel, M. (2018). Determining Strain-Induced Crystallization of Natural Rubber Composites by Combined Thermography and Stress-Strain Measurements. *Polym. Test.* 66, 87–93. doi:10.1016/j.polymertesting.2017.12.021

Plagge, J., and Lang, A. (2021). Filler-polymer Interaction Investigated Using Graphitized Carbon Blacks: Another Attempt to Explain Reinforcement. *Polymer* 218, 123513. doi:10.1016/j.polymer.2021.123513

Rault, J., Marchal, J., Judeinstein, P., and Albouy, P. A. (2006). Stress-Induced Crystallization and Reinforcement in Filled Natural Rubbers: 2H NMR Study. *Macromolecules* 39, 8356–8368. doi:10.1021/ma0608424

Rivlin, R. (1948). Large Elastic Deformations of Isotropic Materials IV. Further Developments of the General Theory. *Phil. Trans. R. Soc. Lond. A.* 241 (835), 379–397. doi:10.1098/rsta.1948.0024

Samaca Martinez, J. R., Balandraud, X., Toussaint, E., Le Cam, J.-B., and Berghezan, D. (2014). Thermomechanical Analysis of the Crack Tip Zone in Stretched Crystallizable Natural Rubber by Using Infrared Thermography and Digital Image Correlation. *Polymer* 55, 6345–6353. doi:10.1016/j.polymer.2014.10.010

Samaca Martinez, J. R., Le Cam, J.-B., Balandraud, X., Toussaint, E., and Caillard, J. (2013). Mechanisms of Deformation in Crystallizable Natural Rubber. Part 1: Thermal Characterization. *Polymer* 54, 2717–2726. doi:10.1016/j.polymer.2013.03.011

Sotta, P., and Albouy, P.-A. (2020). Strain-Induced Crystallization in Natural Rubber: Flory's Theory Revisited. *Macromolecules* 53 (8), 3097–3109. doi:10.1021/acs.macromol.0c00515

Spratte, T., Plagge, J., Wunde, M., and Klüppel, M. (2017). Investigation of Strain-Induced Crystallization of Carbon Black and Silica Filled Natural Rubber Composites Based on Mechanical and Temperature Measurements. *Polymer* 115, 12–20. doi:10.1016/j.polymer.2017.03.019

Su, T.-K., and Mark, J. E. (1977). Effect of Strain-Induced Crystallization on the Elastomeric Properties of Cis-1,4-Polybutadiene Networks. *Macromolecules* 10 (1), 120–125. doi:10.1021/ma60055a025

Toki, S., Che, J., Rong, L., Hsiao, B. S., Amnuaypornsri, S., Nimpaiboon, A., et al. (2013). Entanglements and Networks to Strain-Induced Crystallization and Stress-Strain Relations in Natural Rubber and Synthetic Polyisoprene at Various Temperatures. *Macromolecules* 46, 5238–5248. doi:10.1021/ma400504k

Tosaka, M., Kawakami, D., Senoo, K., Kohjiya, S., Ikeda, Y., Toki, S., et al. (2006). Crystallization and Stress Relaxation in Highly Stretched Samples of Natural Rubber and its Synthetic Analogue. *Macromolecules* 39, 5100–5105. doi:10.1021/ma060407

Tosaka, M. (2007). Strain-Induced Crystallization of Crosslinked Natural Rubber as Revealed by X-ray Diffraction Using Synchrotron Radiation. *Polym. J.* 39 (12), 1207–1220. doi:10.1295/polymj.PJ2007059

Trabelsi, S., Albouy, P.-A., and Rault, J. (2003). Effective Local Deformation in Stretched Filled Rubber. *Macromolecules* 36, 9093–9099. doi:10.1021/ma0303566

Treloar, L. (1975). *The Physics of Rubber Elasticity*. New York: Oxford University Press.

Tunnicliffe, L. B. (2021a). Fatigue Crack Growth Behavor of Carbon Black-Reinforced Natural Rubber. *Rubber Chem. Techn* 94 (3), 494–514. doi:10.5254/rct.21.79935

Tunnicliffe, L. B. (2021b). Thixotropic Flocculation Effects in Carbon Black-Reinforced Rubber: Kinetics and Thermal Activation. *Rubber Chem. Techn.* 94, 298–323. doi:10.5254/rct.21.79896

Wang, M.-J., Wolff, S., and Tan, E.-H. (1993). Filler-Elastomer Interactions. Part VIII. The Role of the Distance between Filler Aggregates in the Dynamic Properties of Filled Vulcanizates. *Rubber Chem. Techn.* 66, 178–195. doi:10.5254/1.3538305

Conflict of Interest: Authors LT and CH were employed by company Birla Carbon, United States.

The remaining authors declare that the research was conducted in the absence of any commercial or financial relationships that could be construed as a potential conflict of interest.

Publisher's Note: All claims expressed in this article are solely those of the authors and do not necessarily represent those of their affiliated organizations, or those of the publisher, the editors and the reviewers. Any product that may be evaluated in this article, or claim that may be made by its manufacturer, is not guaranteed or endorsed by the publisher.

frontiers in Materials

REVIEW
published: 19 October 2021
doi: 10.3389/fmats.2021.774843

Progress on Polymer Composites With Low Dielectric Constant and Low Dielectric Loss for High-Frequency Signal Transmission

Lu Wang, Jing Yang, Wenhua Cheng, Jiajia Zou and Dan Zhao*

China Electronics Technology Group Corporation No. 38 Research Institute, Hefei, China

The development of information transmission technology towards high-frequency microwaves and highly integrated and multi-functional electronic devices has been the mainstream direction of the current communication technology. During signal transmission, resistance-capacitance time delay, crosstalk, energy consumption increase and impedance mismatch restrict the high density and miniaturization of Printed circuit board (PCB). In order to achieve high fidelity and low delay characteristics of high-frequency signal transmission, the development of interlayer dielectric materials with low dielectric constant (Dk) and low dielectric loss factor (Df) has become the focus of researchers. This review introduces the dielectric loss mechanism of polymer composites and the resin matrix commonly used in several high-frequency copper-clad laminates, and mainly describes how to reduce the dielectric constant and dielectric loss of materials from the level of molecular structure design, as well as the effect of fillers on the dielectric properties of polymer substrates. As a kind of potential functional fillers for dielectric polymeric composites, the carbon nanofillers are used to tailor the dielectric properties of their composites *via* different dimensions and loadings, as well as their proper preparation methods. This review finally summarizes the interface bonding failure mechanism and a feasible idea to optimize the dielectric properties of polymer matrix composites is also proposed.

Keywords: dielectric constant, dielectric loss, high frequency, polymer composites, carbon nanofillers

OPEN ACCESS

Edited by:
Dong Xiang,
Southwest Petroleum University, China

Reviewed by:
Wei Zhou,
Beijing Institute of Radiation Medicine, Beijing, China
Xianlong Zhang,
Sichuan University, China

****Correspondence:***
Lu Wang
42278010@qq.com

Specialty section:
This article was submitted to Polymeric and Composite Materials, a section of the journal Frontiers in Materials

Received: *13 September 2021*
Accepted: *28 September 2021*
Published: *19 October 2021*

Citation:
Wang L, Yang J, Cheng W, Zou J and Zhao D (2021) Progress on Polymer Composites With Low Dielectric Constant and Low Dielectric Loss for High-Frequency Signal Transmission. Front. Mater. 8:774843. doi: 10.3389/fmats.2021.774843

INTRODUCTION

In recent years, the rapid development of information transmission technology has led to the gradual development of electronic devices in the direction of thin and light, high performance, high frequency and high speed. Owing to the development of high density and miniaturization of PCB, the core component of high frequency microwave communication, microwave signal transmission between integrated circuits and microstrip lines in the system is prone to mutual interference, resulting in the delay of resistance and capacitance (RC), crosstalk and increase of energy consumption. The copper clad laminate (CCL) is the carrier of the printed circuit board and plays a major role in its conductivity, insulation and support, largely determining the performance, quality, manufacturing costs and long-term reliability of PCB. Therefore, the fabrication of copper clad laminates for use at high frequencies has become the focus of researchers.

TABLE 1 | The ε' and tanδ of Representative Polymers.

Polymer	ε'	Tanδ
Polytetrafluoroethylene	2.1	1×10^{-4}
Polypropylene (isotactic)	2.2	1×10^{-4}
Cycloolefin polymer	2.3	2×10^{-4}
Polybutadiene	2.5–2.8	5×10^{-3}
Poly(methyl methacrylate)	2.6	8×10^{-3}
Polyphenylene Oxide (PPE)	3.5	2×10^{-3}
Thermosetting cyanate resin	3.45–3.55	4×10^{-3}–5×10^{-3}
bismaleimide-triazine resin	4.1–4.3	4×10^{-3}–8×10^{-3}

According to the signal transmission rate formula, the relationship between high frequency signal transmission speed V and signal transmission loss and interlayer dielectric resin can be expressed as follows:

$$V = \frac{kc}{\sqrt{\varepsilon_r}}$$

Where V (m/s) and c (m/s) are the signal propagation speed and the speed of light in a vacuum. Where k is a Constant and ε_r is the dielectric constant of the substrate. It can be seen that the lower the dielectric constant of the substrate, the faster the signal propagation speed will be. In high frequency circuits, the dielectric loss of the substrate is also a problem to be considered by the signal propagation loss formula：

$$\alpha = k' f \sqrt{\varepsilon_r} \tan\delta$$

Where α (dB/m) and ε_r are the signal transmission loss and the dielectric constant of the substrate. Where $\tan\delta$ is the dielectric loss factor of the substrate and f is frequency. The smaller the dielectric loss factor of the substrate is, the smaller the attenuation of signal propagation will be. Since the signal propagation speed and propagation efficiency are largely affected by the dielectric properties of copper-clad laminates, the research and development of high performance substrate materials with low dielectric constant and low dielectric loss is the premise of high frequency application of PCB.

Compared to the inorganic dielectric material silicon dioxide (SiO_2), organic polymer materials as interlayer dielectric (ILD) generally have lower dielectric constants due to their smaller material density and lower single-bond polarizability. In addition, they show obvious advantages in the ease of chemical and geometric structure design. Resin matrix, as an important part of CCL, plays a decisive role in the dielectric properties of CCL. In order to ensure no void electroplating deposition during copper metallization, in addition to composition stability at high temperatures, organic polymers must also have very high glass transition temperatures: minimum temperature above 300°C and ideal temperature above 400°C (Shamiryan et al., 2004). In order to solve the high fidelity, low delay, and impedance matching of signal transmission, these interlayer dielectric resins must have an extremely low dielectric constant and dielectric loss, The dielectric properties of common resins are shown in **Table 1**.

DIELECTRIC LOSS MECHANISM

Dielectric loss is caused by the failure of the molecular polarization process to keep pace with the rate of change of the oscillating applied electric field. When the relaxation time (τ) in the polymer is less than or equal to the rate of the oscillating electric field, there is no or minimum loss. However, when the oscillating speed of the electric field is much greater than the relaxation time, the polarization cannot change with the oscillation frequency, resulting in energy absorption and heat dissipation. When the dipole polarization is completely out of sync with the frequency of the applied oscillating electric field, the dielectric loss is also minimal.

The relative permittivity can be expressed by the following complex equation:

$$\varepsilon^* = \varepsilon' - j\varepsilon''$$

It consists of the real part of the dielectric constant (ε') and the imaginary part of dielectric loss (ε''). The ratio of dielectric loss to dielectric constant is the value of tanα :

$$\tan\alpha = \frac{\varepsilon''}{\varepsilon'}$$

Among them, dielectric materials have five types of polarization: interface polarization, ion polarization, dipole (orientation) polarization, atomic (vibration) polarization, and electron polarization. Each polarization is related to the dielectric loss at a particular frequency (**Figure 1**). These five types of polarization can be divided into two states: relaxation and resonance. Relaxation includes interfacial polarization, ion polarization, and dipole (oriented) polarization. For a multicomponent polymer system, Maxwell--Wagner effect generates interfacial and interfacial polarization. For polymers containing ions, whether impurity ions or ions in polymer electrolytes and polyelectrolytes, ion polarization occurs below a few hundred Hertz. If the polymer is polar and contains permanent dipoles, these permanent dipoles may respond to the external field by rotation, resulting in dipole (orientation) polarization in the polymer. There are two types of dipole relaxation: dipole segment relaxation (relaxation associated with micro-brownian motion of the entire chain, called α relaxation) and dipole group relaxation (i.e., relaxation associated with local motion of molecules and small chain units, called β and γ relaxation) (Prateek et al., 2016). The activation energy required for α relaxation is greater than that for β and γ relaxation, and the increase rate of α relaxation is higher when it is close to a glassy state. γ relaxation occurs at lower temperatures and is associated with the movement of small units of the main or side chain. Depending on their nature (amorphous or crystalline) and temperature, these dipoles relax between 10 Hz and a few GHz, covering the power and radio ranges (**Figures 2**–**6**).

For polymer materials, resonance includes electron polarization and atomic (vibrational) polarization. Both types of polarization exist in polymers, whether polar or nonpolar, amorphous or crystalline. Because their dielectric losses are in the

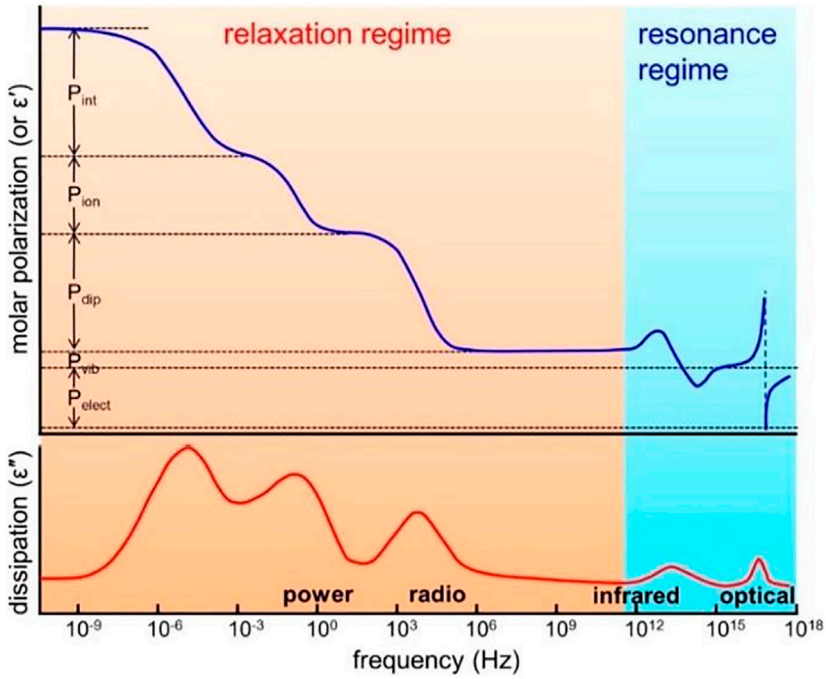

FIGURE 1 | Different types of polarization as a function of frequency in polymers. P_{elect}, electronic polarization; P_{at}, atomic polarization; P_{dip}, (dipolar) orientational polarization; P_{ion}, ionic polarization; P_{int}, interfacial polarization. The top panel shows the molar polarization (or the real part of permittivity), and the bottom panel shows the dissipation factor (the imaginary part of permittivity). Reprinted with permission from Prateek et al. (2016). Copyright© 2016 American Chemical Society.

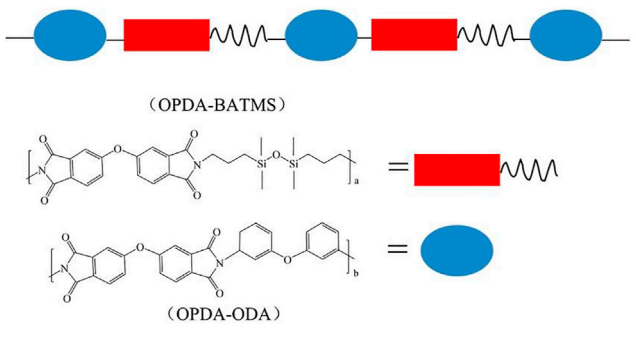

FIGURE 2 | Use of Disiloxane-Linked Diamine BATMS in Preparing Poly(imide siloxane) Films PI-χ.

infrared and optical ranges, they are not seen in power and radiofrequency. As can be seen from **Figure 1**, in the field of 10^{-6}–10^{12} Hz radio wave communication, in the low-frequency range, the more polarization types, the higher the dielectric constant, and the higher the dielectric loss. As the frequency moves towards the high frequency until within 10^{12} Hz, various polarization response times gradually lag behind the change of electric field frequency, and the dielectric constant decreases gradually. Therefore, for the composites with dipole polarization and interfacial polarization, the dielectric constant of the composites decreases with the increase of frequency. In the high frequency region (10^{2}–10^{6} Hz), the dielectric constants of the composites have little difference, and the difference is mainly reflected in the low frequency region (10^{-1}–10^{2} Hz).

POLYMER COMPOSITES FOR HIGH-SPEED SIGNAL TRANSMISSION

Commonly Used Resin Matrix for High Frequency Copper Laminates

The molecular structure of the polymer plays a major role in the dielectric and adhesive properties. However, the requirements for low dielectric constant, dielectric loss and strong adhesion of polymer materials are often contradictory. On the one hand, the strong adhesion to the microstrip conductor requires that the polymer chain contains polar functional groups such as amino, cycloxyl, and isocyanate, which can enhance the interfacial forces between polymer chains and microstrip conductors (usually copper foil) by electrostatic interaction, thereby improving the durability and reliability of integrated circuit boards. On the other hand, the orientation polarization of the intrinsic dipole moments combined with the dipole polarization of polar functional groups decisively causes a large increase in the dielectric loss; so, optimizing the dielectric properties (especially low dielectric loss) requires that polymer chains contain nonpolar functional groups. Besides, the position of the polar functional group is also very important: if the polar group is on the side chain of the polymer, especially the flexible polar group, which has strong mobility, it will have a greater impact on the dielectric properties;

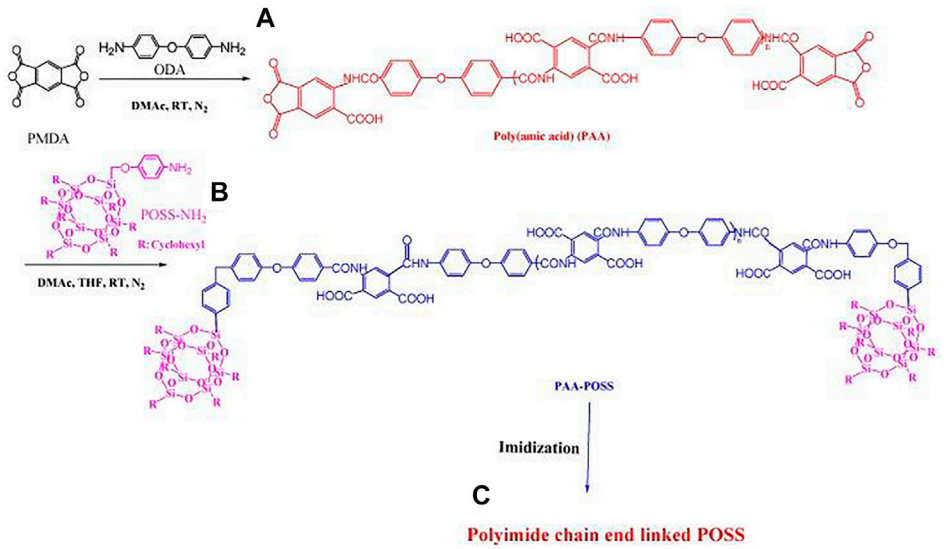

FIGURE 3 | Preparation of **(A)** poly(amic acid) (PAA); **(B)** PAA/POSS nanocomposites; and **(C)** PI linked through its chain ends to POSS. Reprinted with permission from (Leu et al., 2003b). Copyright© 2003 American Chemical Society.

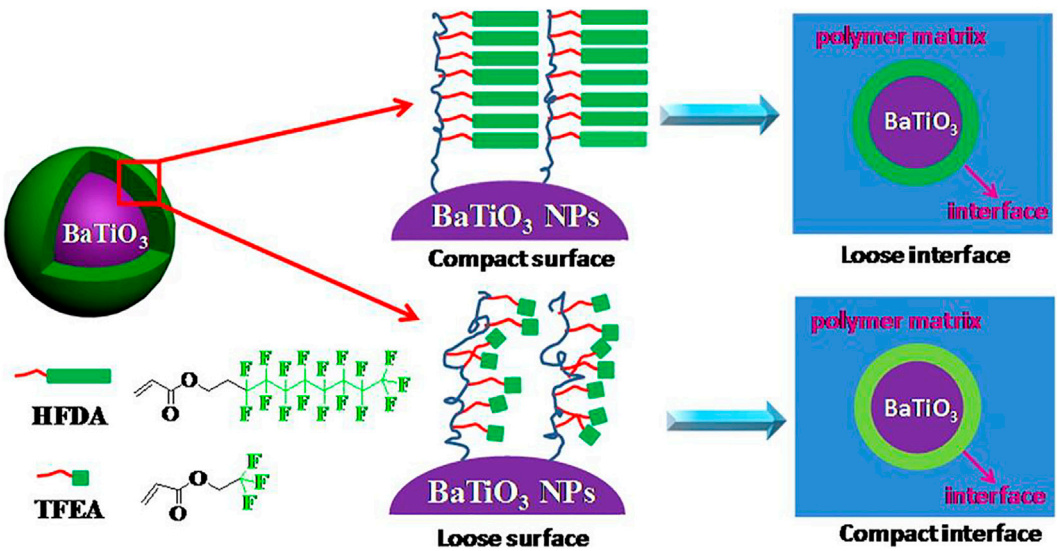

FIGURE 4 | Schematic illustration for the fluoro-polymer@BT nanoparticles and the interfacial region within the nanocomposites. Reprinted with permission from Yang el al. (2013). Copyright© 2013 American Chemical Society.

Polar groups have little effect if they are in the polymer backbone. The branching, cross-linking and orientation stretching of macromolecules also have an impact on the dielectric properties.

Polytetrafluoroethylene [-(CF_2–CF_2)$_n$-] is a non-polar linear polymer with highly symmetrical structure, composed of two elements: carbon and fluorine. Due to the lack of active polar groups, high crystallinity, high electronegativity of fluorine atom and high dissociation energy of C-F bond, it has lower surface energy and higher surface hydrophobicity, making it hard affected by frequency, temperature and humidity. Except for compound modification and molecular structure design, the surface of PTFE can be directly treated to improve the adhesion performance of PTFE without reducing the bulk performance. PTFE is an available candidate for the high-frequency application in CCL, but its low inferior adhesion to substrates and poor processability, high coefficient of thermal expansion restrict its practical application. At present, sodium naphthalene, ion irradiation and plasma treatment are mostly used for its surface modification. Particularly, plasma

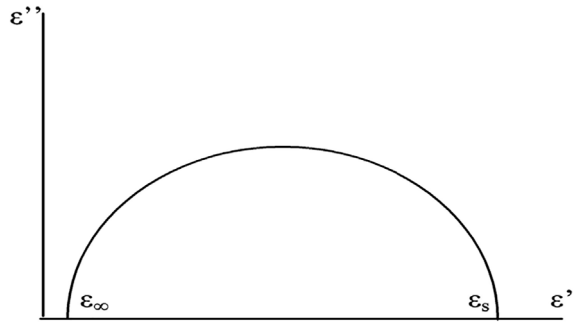

FIGURE 5 | Cole-Cole Plot showing the relationship between dielectric constant and dielectric loss.

modified the surface of PTFE without affecting the overall physical and chemical properties of PTFE.

Polyimide (PI) is a polymer with rigid chain of imide heterocycle, which is composed of binary amine and binary acid/anhydride with large free volume. Due to its excellent overall properties, such as thermal oxidation stability, unique electrical property and high mechanical strength, it is used as a polymer matrix for aerospace and microelectronics. In order to facilitate the processing of polyimide, many researchers have developed soluble polyimide. The main purpose of improving solubility is to reduce the interaction between polymer chains and the stiffness of polymer structure by introducing non coplanar, flexible and kink elements. For thermosetting polyimide, the molecular weight can be turned by the ratio of anhydride to amine group, and the polymer meeting the performance requirements can be obtained by crosslinking. The introduction of asymmetric dianhydride and diamine can not only limit the stacking of main chain and charge transfer electron polarization interaction, but also make polyimide have high Tg and thermal properties. Therefore, polyimides based on molecular or geometric asymmetry exhibit higher solubility, low melt viscosity and other required properties (Yu et al., 2018).

Epoxy resins are used as substrates or adhesives for copper-clad laminates due to its excellent properties, such as good moisture resistance, solvent resistance and chemical resistance, low shrinkage after curing, excellent electrical and mechanical properties, and good adhesion to many substrates. Taking bisphenol A diglycidyl ether epoxy resin as an example, the polar groups in the molecular chain such as ether bond and hydroxyl group are conducive to improve the adhesion between epoxy resin and copper foil. Rigid groups such as benzene ring in the molecular chain are beneficial to improve the rigidity and heat resistance of epoxy resin. The ether bond in the molecular chain endows the epoxy resin with good alkali resistance and flexibility. As a thermosetting resin, epoxy resin has good processability and reactivity, but the application of epoxy resins is limited by its brittleness, high dielectric loss and high dielectric constant. Generally, higher crosslinking degree will make it difficult to orient polar groups, so it will reduce the dielectric constant, but it is unfavorable to the mechanical properties. The crosslinking density and polar group concentration can be reduced by grafting flexible chains or blending with reactive functional groups.

Olefin polymers are carbon chain polymers without any polar groups, which endow dielectric materials with excellent dielectric properties. The common hydrocarbon resins include styrene-butadiene copolymer, styrene-butadiene-divinylbenzene copolymer, butadiene homopolymer and so on, only composed of C and H elements. Due to the small electronic polarizability of C-C and C-H, olefin polymers exhibit low dielectric constant and ultralow dielectric loss over wide frequency and temperature ranges. which are the ideal candidates for high-frequency CCL (Zhang, 2019). Among them, polybutadiene e.g. cis-1,4- polybutadiene, trans-1,4-polybutadiene, 1,2-polybutadiene and polybutadiene with different contents can be synthesized through different polymerization conditions and methods. The side chain of high 1,2-polybutadiene contains many double bonds (with a high degree of unsaturation) and is an amorphous structure, mainly used as an adhesive and sealant. Peroxide decomposed at different temperatures can be selected as crosslinking agent to control the curing temperature of crosslinking reaction. The absence of polar groups limits its application range to a certain extent. For low molecular weight non-vulcanized polybutadiene liquid rubber, the characteristic of easy-creeping makes it difficult to form a stable coating film at room temperature. Up to now, researches on polybutadiene utilized in CCL are relatively less. Other dielectric polymers also include polyphenylene ether (PPO), cyanate ester (CE), Poly (arylene ether nitrile) (Tong et al., 2019), parylene, polynaphthalene, polybenzoxazole resin, polynorbornene, Polyaryl ether, polyarylene, SiLK resin, polyquinoline, polyquinoxaline, polybenzocyclobutene, porous polymer materials (Volksen et al., 2010).

%1.2 Principles and examples of molecular structure design.

According to the Clausius-Mossotti formula：

$$\varepsilon = \frac{1 + 2\left(\frac{p_m}{v_m}\right)}{1 - \left(\frac{p_m}{v_m}\right)}$$

Where k is dielectric constant, Pm is molar polarizability and Vm is molar free volume fraction. It can be seen from the formula decreasing the molecular molar polarization and increasing the

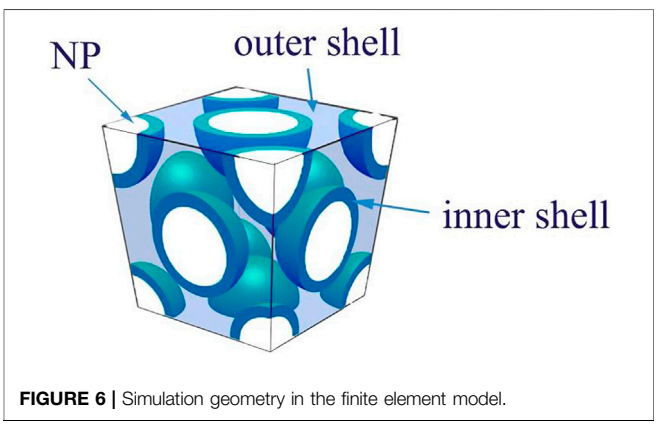

FIGURE 6 | Simulation geometry in the finite element model.

free volume of the polymer are the main ways to reduce the dielectric constant.

The reduction of dielectric constant and dielectric loss by polymer molecular structure design is usually achieved by several key methods. *1*) Introducing C-F and C-C chemical bonds composed of chemical elements with low polarizability. *2*) Introducing asymmetric, rigid non-planar conjugated structure or flexible structure into the polymer main chain through copolymerization and block polymerization to reduce the molar polarizability. *3*) Adding space-occupying groups such as methyl, ethyl and phenyl to the dielectric material to increase the free volume in the polymer structure.

Reduce Molecular Polarizability

First, the chemical elements involved in the preparation of low dielectric constant polymer materials can be appropriately selected to reduce the polarizability of the molecules. Bonding the precursors of atoms with appropriate electronegativity in an appropriate configuration can reduce the molecular polarizability. The incorporation of fluorine atoms is a good way to reduce the dielectric constant of polymers. The C-F bond has the lowest electronic susceptibility and dipole moment, making fluorination a potential candidate for low dielectric constant applications. On the one hand, fluorine atoms possess the strongest electronegativity and can better fix electrons, so the doping of fluorine atoms is particularly effective in reducing the electron and ion polarizability (Dhara and Banerjee, 2010). On the other hand, the bond energy of the C-F bond is very strong, and the fluorine-containing group contains a larger free volume.

Except for C and F, the thermal motion ability and orientation polarization ability of the segment units are different. Compared with aliphatic segment units, silicon is larger than carbon atoms, silicon-oxygen bonds are more flexible than carbon-carbon bonds, and siloxane (Si-O-Si) possesses a low dielectric constant. Therefore, the bulky silicone resin unit has relatively small mobility, which reduces the efficiency of the dipole's response to changes in polarity at alternating frequencies. Haixia Qi et al. prepared a polyimide siloxane film by copolymerizing the synthesized disiloxane diamine (BATMS) with ODA and ODPA (Qi et al., 2019). Among them, the segments of ODPA-BATMS and ODPA-ODA are randomly distributed along the main chain of the copolymer, but the segments of ODPA-BATMS are alternately composed of disiloxane alkyl and imide rings (**Figure 2**). The flexible, high-temperature resistant disiloxane segment increases the molecular chain spacing and inhibits the charge transfer complex (CTC). The interaction between polymer chains is reduced, which helps to reduce chain accumulation and charge transfer electron polarization interactions. When the molar ratio of BATMS reaches 75%, the free volume and hydrophobic properties increase, and the molar polarization is significantly reduced. The dielectric constant of the copolymer film PI-75 is as low as 2.48 (1 MHz, 25°C). In addition, there exists the inherent non-polarization of the disiloxane segment and the change of the aggregation state of the copolymer film. The molar volume of the siloxane segment unit increases and the unit molar polarizability of the segment decreases. On the one hand, the introduction of asymmetric monomers or large side groups increases the free volume of PI molecules and disrupts the formation of effective CTCs. On the other hand, this reduces the interaction between polymer chains and the rigid structure of the polymer, which can improve the melt processability of the polymer or the solubility in organic solvents.

Polyhedral oligomeric silsesquioxane (POSS) with empirical formula ($RSiO_{1.5}$) is the smallest silica nanoparticle (NP), where R can be an organic functional group (such as amine, alkyl, alkylene, epoxide unit, acrylate, hydroxyl) or hydrogen atom. According to the number of R and the preparation method of nanocomposites, Mohamed et al. classified it as a blend of non-functional POSS nanocomposites and polyimide, and a chain of monofunctional POSS nanocomposites and polyimide (Mohamed and Kuo, 2019), and the covalent connection of the end or side chain, the covalent bonding of the bifunctional POSS nanocomposite material and the polyimide main chain, and the formation of the polyimide thermal crosslinking structure of the multifunctional POSS nanocomposite material. Among them, POSS molecules are usually stable at temperatures as high as 400°C, which is higher than the thermal degradation temperature of most polymers. Incorporating them into some polymers leads to improved thermal stability and mechanical properties (Leu et al., 2003a). Wei et al. synthesized POSS-diamine monomer, and synthesized nano-polyimide composites with an adjustable dielectric constant by controlling the molar ratio of POSS-diamine monomer, PMDA, and ODA (Leu et al., 2003b). At the same time, POSS can be used as a large steric hindrance substituent group, the lowest dielectric constant of this composite material is 2.3, and the mechanical properties are controllable.

Leu et al. used pyromellitic dianhydride (PMDA) react with 4,4'-oxydiphenylamine (ODA) in DMAc under N_2 atmosphere at room temperature to form PAA (Leu et al., 2003a). Then, POSS-NH_2 reacts with PAA in DMAc to obtain PAA/POSS nanocomposite (**Figure 3**). After the PAA/POSS nanocomposite is thermally imidized at 300°C, its chain end is connected with POSS nanoparticles to obtain PI. Upon addition of 2.5 mol% of POSS units, the dielectric constant of the resulting polyimide POSS nanocomposite decreased from 3.40 to 3.09 for the pure PI without any decrease in mechanical strength. POSS cage-like siloxane structure is currently a better silicon-containing group for modified PI, which can overcome the disadvantages of reduced mechanical properties and high cost due to dependence on fluorine-modified materials.

Xiangxiu Chen et al. synthesized trapezoidal multifunctional polysiloxane (PN-PSQ) with a large number of amino groups and phenanthrene phosphide structures so as to improve the heat and fire resistance, dimensional stability and dielectric properties of BMI resin (Chen et al., 2014). On the one hand, PN-PSQ resin with phosphide-phenanthryl group has larger benzene side groups and non-coplanar structure; on the other hand, the–NH_2 group of PN-PSQ resin shortens the distance between curing crosslinking points of BMI resin which to a certain extent increased the crosslinking density of BMI resin, so the orientation and relaxation of dipoles which accompanying

the movement of polymer segments is limited, and finally the dielectric properties (the dielectric constant and loss at 1 MHz are 3.01 and 0.008, which are only 88 and 80% of that of BMI resin, respectively) are optimized. While there are polar reactive groups in PN-PSQ, their good symmetry has little effect on the dielectric constant and loss of the resin.

Devaraju et al. blended glycidyl terminated hyperbranched polysiloxane (HPSiE) with different percentages into diglycidyl ether bisphenol A (DGEBA) resin, and added curing agent diaminodiphenylmethane (DDM) (Devaraju et al., 2013). With the increase of HPSiE composition, the flexible polysiloxane bonding arising more porous voids, compared with pure DGEBA resin (the dielectric constant is 4.5), the dielectric constant can reach 3.5 at 15 wt%. Owing to the chemical interaction between HPSiE and DGEBA and the existence of Si-O-Si hydrophobic bond in the composites, the contact angle and water resistance are enhanced. Jie Dong et al. make amino-functionalized hyperbranched polysiloxane (NH_2-HBPSi) graft onto PI chain by *in-situ* polymerization (Dong et al., 2017). The large bulk of HBPSi enhances the free volume and dielectric confinement effect, the dielectric constant of 16 wt% NH_2-HBPSi/PI can be as low as 2.2, and the dielectric loss is about 0.01 at 10^8 Hz.

Increase the Free Volume of Polymer

Chen, Jiangbin et al. designed and synthesized a benzoxazine resin with high frequency, low dielectric constant (<3) and very low dielectric loss (tan<0.005) (Chen et al., 2019). The large -$C(CH_3)_3$ group was introduced into the end of benzoxazine copolymer, which effectively increased the free volume of the polymer and reduced the molecular polarity of it. Both alicyclic and aliphatic units have lower molar polarizability and molecular chain packing density, which can destroy the planarity of molecular chains and inhibit the charge transfer interaction within chains and/or between chains at the same time, and it is beneficial to improve the solubility of materials, reduce the dielectric constant and improve the optical transparency (Zhuang et al., 2019). In addition, the alicyclic structure can improve the hydrophobicity of the material and keep the dielectric properties of the film stable. Takashi Tasaki et al. developed a soluble polyimide with benign heat resistance and low dielectric properties (Dk is 2.85, Df is 0.0056 at 10 GHz) by optimizing the composition ratio of aliphatic, alicyclic and aromatic groups in the main chain of polyimide (Tasaki, 2018). In addition, polyimide adhesive shows good adhesion to common polyimide film and copper foil, and can be used in three-layer flexible copper-clad laminate (FCCL). The FCCL shows a transmission loss similar to that of liquid crystal polymer (LCP) FCCL at a frequency less than 20 GHz.

Ping Yu et al. used 3,4'-diaminodiphenyl ether (3,4'-ODA), 2,3,3',4'-biphenyl tetracarboxylic dianhydride (a-BPDA) and 2,3,3',4'-Oxydiphthalicanhydride (a-ODPA) as raw materials, synthesizing a new asymmetric bismaleimide oligomers with different molecular weights and dianhydride (Yu et al., 2019). Oligomers have high solubility and solubility stability in common organic solvents. Low molecular weight OD-BMI-1 and BP-BMI-1 oligomers have lower melt viscosity and wider processing window.

Others

Introducing air holes or nano foam materials, blending inorganic low dielectric materials, forming hyperbranched structures (Lei et al., 2016; Dong et al., 2017) and the use of cross-link interpenetrating network structure (Song et al., 2019) can be beneficial to reduce the orientation of dipole and improve the comprehensive properties of polymer. For nano-porous composites, the structure, size and size distribution of pores will have a vital impact on the uniformity of material properties, which is not conducive to the preparation process of large-scale production. In addition, the introduction of the hole structure will significantly reduce the mechanical properties and air tightness of the material, therefore, the material has low mechanical strength and poor barrier performance, which cannot meet the requirements of practical application.

The Influence of Fillers on the Dielectric Properties of Polymer Matrix

The morphology of inorganic particles includes zero-dimensional nanofillers (spherical nanoparticles, nanocubes and nanoparticles with irregular morphology), one-dimensional nanofillers (nanowires, nanofibers, nanotubes, such as carbon nanotubes CNT) and two-dimensional nanofillers (including nanosheets and nanoplates, such as graphene and nanoclay). Among them, it is often used Al_2O_3 (Yao et al., 2015) SiO_2、TiO_2、h-BN (Yang et al., 2017; Ge et al., 2019)、AlN (Wang et al., 2019) and $ZrTi_2O_6$ to improve the dielectric and mechanical properties. Because of the hydrophilicity of ceramic filler surface and the hydrophobicity of polymer, there is interface incompatibility, which leads to the aggregation of nanoparticles (Mittal et al., 2018). The difference of dielectric constant and conductivity between ceramic filler and polymer does not match at the interface, which leads to the accumulation of charge and local redistribution of electric field, and produces Maxwell-Wagner interface polarization (Murugaraj et al., 2005). Compared with zero-dimensional nano-filler, one-dimensional ceramic filler is easier to permeate, which leads to higher relative dielectric constant and heat conductivity coefficient. At the same time, large dipole moment is beneficial to the dielectric enhancement of polymer composites under low load. The zero-dimensional nano filler is easy to agglomerate because of its high surface area and volume effect, and is difficult to form monodisperse nanoparticles in polymer matrix, so it is necessary to modify the surface of inorganic particles (Kango et al., 2013). In order to obtain the strong interaction between polymer and nano-filler, the dispersibility of nano-filler and its compatibility with polymer are of vital importance. The filler dispersion of polymer/nanofiller composites (PNC) which is prepared by solution intercalation, *in-situ* intercalation, melt intercalation and other methods can be improved to a varying extent. The surface treatment of nano-filler, among which the surface modification can obtain good dispersibility and/or compatibility with polymer of nano-filler, and improve Tg of composite material.

Carbon nanotubes (CNTs) and graphene nanoplatelets (GnPs) are respectively typical one-dimensional and two-dimensional carbon nanofillers, which are commonly used in

polymeric composites with dielectric properties (He et al., 2017; Zhao et al., 2019). It is well known that a sudden increase in the dielectric permittivity with one or several orders of magnitude is presented when the loading of conductive fillers reaches a critical value (Xu et al., 2015), *i.e.*, the percolation threshold. However, when the content of the conductive filler is very close to or above the percolation threshold, conductive networks are generated and, thus, significant dielectric loss caused by leakage conduction loss from the capacitors would occur (Huang and Terentjev, 2010). On this basis, the dielectric behavior of polymeric composites can be tailored by tuning the conductive network structures, such as by compounding appropriate contents of carbon fillers in polymer matrix, as well as controlling the agglomeration situation of conductive nanofillers.

Li et al. studied the dielectric properties of polyamide 11(PA11)/CNT and PA11/Polypropylene (PP)/CNT composites, and the dielectric constant of all systems enhances significantly when the loading of CNTs approaches the conductively percolative threshold (Li et al., 2019). As for the PA11/CNT system, when the content of CNTs reaches up to 0.1 wt%, it shows an obvious increase of the dielectric constant from 6 to 50 at 100 Hz. The AC conductivity of the exceeded loading of 2 wt% CNTs shows a typical frequency-independence within the low frequency range, presenting a typical transition from insulation to conduction. In terms of PA11/PP/CNT composites, a lower percolative loading on 0.05 wt% of CNTs was presented (A9P1C0.05) when the dielectric constant underwent its sharp increase, arising from the segregated conductive structure of CNTs in the PA11/PP blend. For the possible reason, the author proposed the effect of "barrier medium" PP in the segregated CNT network on the dielectric property. They thought the PP long chain can diffuse into the CNT bundles with the incorporation of polar PP-g-MAH, enhancing interfacial interaction between CNTs and PP. As a result, the charge accumulation under electric field would be enhanced *via* interfacial polarization. The mini-capacitor network with CNTs as electrodes and a very thin PP layer as dielectric can be formed in the composites near the percolative threshold, which is correlated with the increment of dielectric constant. In addition, the PP in between CNTs can hinder the connection of CNTs and the current leakage, finally resulting in the suppressed increase of dielectric loss. (Re. Constructing a segregated carbon nanotube network in polyamide-based composites towards high dielectric constant and low loss).

As is mentioned above, nanofiller is easy to agglomerate because of its high surface area and volume effect. According to the micro-capacitor model (Prateek et al., 2016), a better dispersion of conductive particles in an insulating polymer matrix is capable of generating more micro-capacitors, which is benefit for achieving higher polarization effect. Zhu et al. reported CNT/PVDF dielectric composites dielectric composites, in which CNT was modified by coating with the polydopamine (PDA) (Zhu et al., 2017). In this study, the coating layer was controlled by changing the concentration of dopamine monomers, and this PDA coating, playing roles of constructing the barrier layer and hindering CNTs aggregation, benefiting the dispersion of CNT in the PVDF matrix. It is exhibited that both of the dielectric permittivity and loss factor of the composites gradually decrease accompanied with the thickening of PDA coatings, which can be ascribed to the weakened interfacial polarization between conducting particles and polymeric matrix.

The influence of interface on the dielectric properties of nanocomposites has been widely studied and can be described from two aspects (Zhang et al., 2018). On one hand, the interface structure characteristics (such as inorganic/organic compatibility, polymer/filler interaction, polymer chain configuration and particle surface state) can determine the final dispersion or aggregation of ceramic nanoparticles in polymer matrix. On the other hand, abnormal local interface electrical/dielectric properties (e.g. interface electronic state and effects on traps or scattering points, charge density, charge redistribution and electric field) can adjust the dielectric and breakdown behavior of nanocomposites and the overall performance of polymer and ceramic fillers. Polymer-filler particle interface model, such as dielectric bilayer model (LEWIS, 1994), multi-core model (Tanaka et al., 2005) and interphase power law model (Todd and Shi, 2005), phase field model (Shen et al., 2018) etc., the development of these model can explain the influence of interface effect on electrical and dielectric properties of nanocomposites. The model makes idealized assumptions on the size and shape of micro/nano-particles, and a single theory or model cannot explain the interaction between interfaces. According to the volume fraction, shape and direction of particles in the filler, the ratio of dielectric constant between filler and matrix and the interaction between filler and matrix, the geometric shape, size, concentration and size-to-dielectric constant of composite materials can be predicted through one or more equations in the model.

The change of polymer molecular structure (free volume fraction, mobility, crystallinity and polymer chain configuration) from interface to matrix caused by interface will affect the way of charge transport and the dielectric properties of polymer matrix. Generally, it is proved that the dielectric constant of the interface region surrounded by filler is lower than that of the bulk polymer matrix (Anandraj and Joshi, 2018). Theoretically, nanoparticles with larger surface area and higher interface strength can effectively limit the orientation and movement of dipoles in the interface region. Although interfacial polarization increases the dielectric constant to a certain extent, interfacial inhibition plays a major role in affecting the dielectric constant of composites. The bonding between filler and matrix also helps to reduce dipole polarity, the decreasing of mobility of polymer chain and the charge transfers lead the dielectric loss decreases simultaneously. However, in fact, nano-materials have a larger surface area than micron-materials (higher dielectric constant and loss due to higher interfacial polarization), which leads to easy aggregation of materials in the matrix (especially at higher load, aggregation of nanofillers and its poor compatibility with polymers will lead to induced voids and matrix density decreases). Aggregation of nanofillers and poor compatibility with polymers will lead to weak interaction between nanofillers and polymers, it means that there is more free volume at the interface between filler and polymer, which makes it cannot effectively limit the mobility of polymer

chain. At the same time, the ceramic filler is hydrophilic in nature, if the particle surface is not coupled with silane coupling agent, its hygroscopicity will increase, resulting in a decrease in dielectric properties. In addition, if silane coupling agent is used for surface modification, the introduction of polar groups may increase the dielectric constant. It should be understood that silane coupling agent improves the interface adhesion.

Wu et al. used silica (SiO_2) to coat multi-walled carbon nanotubes (MWCNTs) to form a core-shell structure (SiO_2@MWCNTs) and organically modified montmorillonite (O-MMT) synergistically modified Reinforce epoxy resin (Wu et al., 2017). Under the lower filling of nanometer materials, the firm interface between the filler and the polymer and the entanglement of EP molecular chains are conducive to restricting the movement of charge carriers, and contributing to the reduction of dielectric constant and dielectric loss. On the one hand, its surface has abundant polar groups (-OH), which produces higher interface strength with the polymer. On the other hand, the one-dimensional filler carbon nanotubes (CNT) with high aspect ratio has a relatively low surface area, which helps to reduce the surface energy, thereby preventing filler agglomeration (Huang et al., 2019a). In addition, the conductive percolation threshold of most CNT/polymer conductive nanocomposites is less than 1 wt%. Therefore, higher interface strength and larger surface area can effectively limit the orientation of the dipole and the movement at the interface. At the same time, the SiO_2 layer can effectively inhibit the electron transfer and accumulation of the composite. However, under the filling of higher nanomaterials, the aggregation of CNTs will reduce the area of the interface region. Compared with epoxy resin, carbon nanotubes have a higher dielectric constant. At this time, the interface polarization is dominant, so the dielectric constant increases instead.

Graphene oxide acts as an insulator, and its oxygen atoms are randomly attached to the graphene. The sp^2–hybridized carbon atoms are converted into the sp^3–hybridized carbon in GO, which reduces the conjugation and limits the π electrons, and loses the graphene's conductivity. In view of the homogeneity of GO is not as high as that of graphene, and the electron mobility is much lower. The dielectric constant of the film is determined by the dielectric constant of the PI matrix and the impedance of GO. Jen-Yu Wang prepared two low dielectric constant and ultra-high strength graphene oxide (GO)/polyimide composite films (PI-GO and PI-ODA-GO films) through solution blending and *in-situ* polymerization (Wang et al., 2011). As the GO content increases, the dielectric constant (Dk) decreases to 2.0. Moreover, the uniform dispersion of ODA-GO in the PI-ODA-GO composite film prepared by *in-situ* polymerization leads to an increase in the dielectric constant. In addition to the introduction of ODA-GO can increase the free volume in the PI matrix, at the same time the partially reduced GO sheet evenly dispersed in the PI can also form many heterojunctions, limiting the movement of electrons in the PI, that is, limiting The electrons in PI are polarized, thereby reducing its dielectric constant. On the one hand, if the GO surface has many polar functional groups, the molecular polarization of PI is increased. On the other hand, many tiny incompatible interfaces are formed between PI and GO, and the interaction force is weak, which is equivalent to introducing a large amount of interface polarization to produce interface polarization.

Yang et al. synthesized core-shell fluoropolymer@$BaTiO_3$ hybrid nanoparticles with different shell thicknesses or different shell structures through reversible addition-fragmentation chain transfer (RAFT) polymerization (Yang et al., 2013). The encapsulated shell polymer is chosen to be more insulating to maintain high resistivity and low loss. Using this hybrid nanoparticle as a filler, a solution blending method was used to prepare an energy storage nanocomposite based on polyvinylidene fluoride-hexafluoropropylene copolymer [P(VDF-HFP)] (**Figure 4**). Among them, the BT-PTFEA hybrid nanoparticles with shorter side groups have a higher graft density, and the interface formed by the close packing limits the mobility of the macromolecular chains of the matrix polymer, resulting in the lowest dielectric loss [from Pure (VDF-HFP) 0.032 is reduced to the lowest 0.016].

Among them, the dielectric loss of dielectric materials usually comes from three different factors: direct current (DC) conduction, space charge transfer (interface polarization) and the movement of molecular dipoles (dipole loss). Generally speaking, a decrease in polymer content will result in a decrease in molecular dipoles, which means a decrease in dipole loss; $BaTiO_3$ nanoparticles are covered by a stable and dense fluoropolymer shell, the formation of an insulating layer outside the dielectric nanofiller limits the transfer and accumulation of space charges in the nanocomposite material. Surface modification by fluoropolymer improves the dispersibility of BT nanoparticles and enhances the interfacial adhesion of nanocomposites, which may further limit the movement of molecular dipoles.

Interface Design of Polymer Composite Material and Metal Microstrip Wire

The interface not only exists between polymer-filler particles, polymer-polymer, and filler particles-filler particles. For copper-clad laminates, the interface between polymer composites and metal microstrip wires has an impact on the performance of the final product. important influence. In order to manufacture very fine copper circuits with line widths and pitches less than 1 micron, it is necessary to maintain the dielectric properties of the printed circuit board while improving the adhesion between the copper and the dielectric substrate.

In high-speed signal transmission, there are two factors that cause transmission loss due to signal propagation loss on printed circuit boards: conductor loss and dielectric (insulating material) loss (Kondo et al., 2016):

$$\boldsymbol{\alpha = \alpha_C + \alpha_d}$$

Conductor loss can be divided into scattering loss caused by surface roughness and skin effect loss (Okubo et al., 2013):

$$\boldsymbol{\alpha_C = \alpha_H + \alpha_S}$$

Among them, α_H is the loss caused by the skin effect, and α_S is the scattering loss. The skin effect is a phenomenon called the skin effect that AC signals mainly flow near the surface of the

conductor, rather than the entire cross-section of the conductor. The general way to reduce conductor loss is to make the surface of the circuit smooth. However, smoothing the surface of copper circuits will weaken the adhesion between them and insulating materials. Therefore, it is difficult to manufacture a copper circuit with a smooth surface and good adhesion to insulating materials. Silica nanofillers include spherical, amorphous, fused, crystalline, and synthetic silica. Hisao Kondo et al. used uniform spherical SiO_2 as a filler to make the insulating material and the substrate have a similar coefficient of thermal expansion (Kondo et al., 2016). Compared with the conductor surface that is usually micro-etched or roughened in the past, the film has a smooth surface to reduce the conductor loss.

In addition, the surface of dielectric materials can be treated by plasma treatment, ultraviolet light, γ-ray, ion radiation, and chemical modification (Baklanov et al., 2013). Polar functional groups are introduced on the surface to increase the polarity and polarity of the material surface. Surface tension can avoid the introduction of a large number of polar functional groups in the body, thereby avoiding poor dielectric properties when improving adhesion performance. Oxygen-containing polar functional groups at the interface have strong electronic polarization and atomic polarization, resulting in high dielectric constant and dielectric loss. In particular, while the interface adhesion is improved, when the peel strength of the polymer-metal interface exceeds a certain value, the failure mode of the polymer and copper foil after surface modification is essentially cohesive failure. There is no point in increasing the interface bonding at this point.

In dielectric bonded films, the adhesive force is related to the dielectric properties of the substances involved, so that the dielectric constant, conductivity, dipole moment and refractive index can also be used to determine the general adhesive tendency. IWAMOTO, NE et al. state that the adhesive force is the sum of the forces acting between metal-polymer, polymer-polymer and any intermediate layers (e.g. metal-oxide and oxide-polymer) (Iwamoto, 1995). For the general interfacial interaction energy, this can be qualitatively summarised by the following expression：

$$W \propto \sum f\left(\varepsilon, \frac{A}{d}, \rho, \omega, R\right)_{metal-dielectric} + \sum f(\mu, R)_{dielectric-dielectric}$$

The metal-polymer interface is analogous to a capacitive circuit, where A is the surface area of the capacitor; d is the distance between the capacitor poles. ε is the dielectric constant, ρ is the resistivity, ω is the frequency, R is the electric field induced by the dipole in the interaction and μ is the dipole moment. However, it cannot be ignored that the structure and geometry of the dielectric bonding film interface, plastic deformation has an influence on the measured structure of the experiment, but this complicates the model.

Product Structure Design

Copper-clad laminates (CCL) are the dominant base material for the manufacture of PCBs. Copper-clad laminates include double-layer flexible copper-clad laminates (FCCL) made of insulating film and copper or triple-layer flexible copper-clad laminates (3-FCCL) with additional adhesive. Most of the existing commonly used high temperature resistant adhesives are epoxy resin adhesives, which are widely used as adhesives due to their strong bonding properties, chemical resistance, good insulating properties, low curing shrinkage and other excellent properties. The different molecular weights of epoxy resins affect their bonding properties because the number of epoxy groups in the molecule decreases as the average molecular weight increases; the distance between the crosslinking points then increases after curing, which leads to a reduction in crosslink density. Due to the severe stress concentration, the mechanical properties of the cured product will decrease as the crosslinking density decreases. This coupled with the fact that internal stresses are difficult to relieve as the crosslink density increases, will result in a non-uniform network structure and reduced mechanical properties. To solve this problem, some researchers have tried to blend two or more epoxy resins with different molecular weights to obtain products with medium crosslinking density.

Many add rubber elastomers to epoxy resins to overcome their brittleness, and phenolic resins and modified polyimides are receiving increasing attention as an ideal class of high temperature resistant adhesives. Polyimides can be divided into two categories, thermosetting and thermoplastic. In recent years, thermosetting PI resins have been valued and developed significantly for their excellent heat resistance. The curing process requires appropriate pressurisation to remove air bubbles due to moisture and solvent evaporation.

Lee et al. designed a three-layer composite structure of polyimide (PI) film as a core layer with low dielectric bonding layers on both sides for a high frequency bonding layer (HFBP) film with a Dk of about 2.80 and a Df of about 0.006 at 10 GHz and a peel strength of more than 1.2 kgf/cm (Lee and Du, 2016). By adjusting the thickness of the core layer, it can be used as a bonding sheet in a copper-clad laminate (CCL) It can also be used together with copper foil for the preparation of high frequency single/dual sided substrates. HFBP films offer better performance than LCP films in terms of workability and thickness tolerance.

Takashi Tasaki et al. developed solvent soluble polyimide with good heat resistance and low dielectric constant (Dk)/dissipation factor (Df) characteristics by optimising the composition ratio of aliphatic, alicyclic and aromatic groups present in the polyimide backbone (Tasaki, 2018). Using this PI binder, a low-profile copper foil and a plain PI film, a three-layer FCCL was developed which showed similar transmission losses to the LCP FCCL at frequencies less than 20 GHz.

INTERFACIAL BONDING DAMAGE MECHANISMS

In addition to properties such as low dielectric constant, low hygroscopicity and high Tg, materials used as insulating layers in microelectronic applications are expected to exhibit high adhesive adhesion to metals used as interconnecting wires. Bond damage

can occur either within the bonding layer or at the interface between the bonding layer and the surface to be bonded. The former refers to cohesive failure, where the adhesive ends up on both surfaces. The latter refers to interfacial bond failure, where the damage occurs at the interface between the bonding layer and the surface to be bonded (Barcia et al., 2004). The peel strength of the adhesive is determined by the interactions between the internal adhesive layer and the bonding interface (van der Waals interactions, electrostatic forces and hydrogen bonding) as well as the deformability and fluidity of the adhesive (mechanical coupling forces). In the case of microstrip copper conductors, the interactions during bonding originate directly from the oxide of copper and the polar groups of the polymer, and possible coordination interactions at the interface also have an impact on the bond strength.

Before introducing the mechanism of bond breakage, we first introduce four mechanisms that explain adhesion. *1*) Mechanical interlocking theory: Mechanical interlocking refers to the existence of unevenness or hollows and cavities on the surface of the substrate, where the adhesive flows, diffuses, penetrates and solidifies to form something like a "hook bond," "nail bond," "anchor bond," like glue being locked into a rough, unruly wood surface. *2*) Diffusion theory: The molecular chains of the adhesive in close contact with the surface molecules of the substrate penetrate each other and fuse at the interface. Compared to other bonding theories, this theory does not require molecular interactions to achieve excellent bond strength, but diffusion theory is only applicable to the adhesion of compatible polymers and the bonding of thermoplastics. *3*) Electronic theory: There is an electrostatic attraction between the interface of the adhesive and the substrate, i.e. positive and negative charges are attracted to each other. In this theory, the adhesion force is due to electrostatic interaction between the partially charged adhesive and the bonded object. However, the contribution of electrostatics to the adhesion force is usually small. *4*) Adsorption theory: This theory of adhesion is probably the most generally accepted, where adhesives and adhered substances can adhere by forces acting between atoms in the interfacial region when sufficiently tight intermolecular contact is achieved at the interface. The interactions between the adhesive and the adhered can be divided into two categories, namely primary and secondary valence bonds. Primary valence bonds lead to chemisorption and include covalent, ionic and metallic bonds; secondary valence bonds lead to physical adsorption and include van der Waals forces, hydrogen bonds and acid-base interactions. There is debate as to which type of bond is more important for adhesion, with primary bonds having a fairly high interaction energy (15–250 kcal/mol) compared to secondary bonds, which are typically less than 10 kcal/mol. Of the primary valence bonds, ionic and metallic bonds are relatively undirected because the ions in ionic and metallic bonds are approximately spherical, whereas covalent bonds are strongly oriented because the orbitals involved are usually non-spherical. In practice, mixtures of these bond types occur frequently, and many adsorption systems should include bonding properties similar to more than one type. The theory of adsorption adhesion based on the formation of secondary valence bonds is of broad utility because secondary valence bonds have few directional constraints, are applicable to many systems, and are less dependent on surface morphology than primary valence bonds.

Spherical particles have a higher packing density and uniform stress distribution than laminated particles, which when filled into the resin increases fluidity, resulting in better mechanical and adhesive properties of CCL.

SPECIFIC EXAMPLES OF DIELECTRIC LOSS MECHANISMS AND SIGNAL TRANSMISSION SIMULATIONS

According to the Debye relaxation model, the real and imaginary parts of the dielectric constant can be expressed by the following equation：

$$\varepsilon' = 1 + \frac{\varepsilon_0 - \varepsilon_\infty}{1 + \omega^2\tau^2} \quad \varepsilon'' = \frac{\varepsilon_0 - \varepsilon_\infty}{1 + \omega^2\tau^2}\,\omega\tau$$

The model relates the dielectric properties to the relaxation time. The relationship between ε' and ε'' can be expressed by eliminating the parameter ωτ as：

$$\left(\varepsilon' - \frac{\varepsilon_s + \varepsilon_\infty}{2}\right)^2 + \varepsilon''^2 = \left(\frac{\varepsilon_s + \varepsilon_\infty}{2}\right)^2$$

This is a form of the hemispherical diagram, often referred to as the Cole-Cole diagram (**Figure 5**). Where ε_∞ is the dielectric constant at frequency infinity ε_0 and ε_s are the dielectric constants at rest, ω is the angular frequency, and τ is the relaxation time.

Todd et al. used the dielectric constants of the filler component, matrix component and interphase region and their respective volume fractions to determine the effective dielectric constants of the composite system (Todd and Shi, 2005). In contrast to hybrid models such as Power-law, Maxwell-Garnett and Bruggeman, the interphase power law (IPL) model takes into account the interaction forces at the composite interface and determines the real and imaginary parts of the complex dielectric constant of the composite system.

$$\varepsilon_i = \varepsilon_i' + i\varepsilon_i''$$

The IPL model is applicable to any random, homogeneous dispersion of filler particles in the matrix. The model takes into account interphase permittivity, interphase volume fraction, interphase overlap and filler shape/orientation effects.

$$\varepsilon_c^\beta = \varnothing_1\varepsilon_1^\beta + \varnothing_2\varepsilon_2^\beta + \varnothing_3\varepsilon_3^\beta$$

Where, $\varnothing_1$, $\varnothing_2$, $\varnothing_3$ represent the volume fraction of the filler, interphase region and matrix of the composite, respectively, ε_1, ε_2, ε_3 represent the dielectric constant of the composite, and the dielectric constants of the filler, interphase region and matrix in the composite, respectively. β is a dimensionless parameter describing the shape and orientation of the filler particles in the composite. $\varnothing_2$ is related to the filler volume fraction, the

surface area of the filler and the thickness of the interphase region surrounding each filler particle.

On the one hand, experiments provide an intuitive understanding of physical and chemical processes from a qualitative or quantitative perspective, and the simulation method can even further quantitatively evaluate the microstructure and properties of polymeric materials systematically (Huang et al., 2019b). Based on molecular dynamics (MD), Subramanian et al. studied the relationship between regular sequence, structure and properties of model polymers, such as polypropylene (PP) and polymethyl-methacrylate (PMMA) (Subramanian et al., 2001). By using the density functional theory (DFT), Bai et al. quantitatively analyzed the charge density and the dipole moment of PIs with two different molecular structures (Bai et al., 2000). In particular, reactive molecular dynamics (ReaxFF MD), combined with advantages of the DFT and the MD, could iteratively calculate the distribution of electrons in each atom (Van Duin et al., 2001). It could also effectively simulate interactions of both intramolecular chemical bonds and intermolecular non-bonded, and on this basis, it could study the influence of intramolecular characteristic groups on the model dipole moments. The dipole moment could directly measure the polarization of dielectrics. Xu wei Huang et al. 2014applied the ReaxFF MD simulation to the polyimide model, and calculated the effect of different phenyl sulfide contents on molecular stacking and polarization characteristics of modified polyimide by clarifying the change of the intermolecular interaction with the intermolecular distance and the electron distribution (Huang et al., 2019a).

On the basis of MD, Lina Si et al. analyzed the nanoporous amorphous silica (n-a-SiO_2) with different porosities and mechanical properties of the films, as well as the interfacial adhesion strength of silica (Si et al., 2014). The relationship between the increasing in porosity of n-a-SiO_2 and its decreasing on dielectric constant were predicted by using Lorentz-Lorenz, Rayleigh, Parallel model and Clausius-Mossotti equation. To study the interfacial adhesion strengths of n-a-SiO_2, SiOCH films and silica, the interfacial adhesion interaction (E_{int}) between low-k films and silica was calculated by using the following equation:

$$E_{int} = E_{tot} - (E_{low-k} + E_{silica})$$

Where E_{tot} is the total internal energy of the low-k films/silica system, $E_{\text{low-}k}$ is the energy of the individual low-k film, and E_{silica} is the energy of silica. In the Accelrys MD software, the unit of interaction energy is kcal/mol, where "mol" means a mole number of system molecules in the periodic condition. Therefore, the area of the interface is a mole number of interface in a single system with a thickness of 10.697 Å and the unit of the interaction energy becomes Joules per square meter (J/m^2). Therefore, the following equation is used to calculate the interaction energy in simulations:

$$E_{int-area} = \frac{[E_{tot} - (E_{low-k} + E_{silica})]}{surface - area}$$

If the interaction energy is negative, there is an attractive force between the objects, such as adhesion; if it is positive, there is a repulsive force. The interfacial strength of n-a-SiO_2/SiO_2 decreases with the increase of the porosity, and the introduction of -CH_2 groups in SiOCH improves its bonding strength.

Tao Pang et al. used furfurylamine (FU), aniline (AN) and bisphenol A to prepare furfural-based thermosetting benzoxazine resins by using toluene as a non-polar solvent (Pang et al., 2019). Based on the crosslink density (ρ) equation and Debye formula, they analyzed the influence of different ratios of FU and AN on the T_g and dielectric properties of benzoxazine resins. Compared with most polybenzoxazines whose k value normally was about 3.50, furfural-based polybenzoxazines had a lower dielectric constant (2.60, 5 GHz; 2.71, 10 GHz) and ultra-low dielectric loss (0.007, 5 GHz; 0.006 10 GHz). By increasing FU content, the cross-linking density and reactivity of polybenzoxazines were gradually improved. As the FU/AN molar ratio increased from 1: 2 to 1:1, the Tg value changed from 278 to 294°C due to the increasing in cross-linking density and hydrogen bonding. However, as the FU/AN molar ratio was further increased from 1:1 to 2:1, under the condition of that the increasing in free volume induced by benzene was ignored, such a partially replacement of AN by FU not only reduced the molecular aromaticity of obtained polybenzoxazines, but also reduced the rigidity of polymer segments. Therefore, the Tg value did not increase significantly.

The elastic modulus of the crosslink density (ρ) of the thermoset material in the rubber region can be estimated by the following equation (Ran et al., 2010):

$$\rho = \frac{E'}{3\varnothing RT}$$

Where ρ is the number of moles of network chains per unit volume of the cured polymer, ∅ is the front factor and equals to 1, E′ is the storage modulus of the sample at the Tg plus 40°C, R and T are the gas constant and the absolute temperature, respectively. This equation is strictly valid only for lightly crosslinked polymers.

In addition, the concentration of cross-linking per unit volume (X_{density}) can be used to define the cross-linking density, using the following semi-empirical equation (Shen et al., 2018):

$$\log_{10} G' = 7 + 293 X_{density}$$

In the formula, G' is the storage modulus of cured resins in the rubber platform area where the temperature is higher than glass transition temperature (Tg). In this work, G' is the modulus at absolute temperature T, which is 40°C higher than Tg. The possible cause of this phenomenon can be analyzed through the following Debye formula (Volksen et al., 2010).

$$\frac{K-1}{K+2} = \frac{4\pi}{3} N\left(a_e + a_d + \frac{u^2}{3k_bT}\right)$$

Where k_b is Boltzmann's constant, N is the number density of dipoles, a_e stands for the electric polarization, a_d stands for the distortion polarization, u is orientation polarization related to dipole moment, T and k respectively are temperature constant and dielectric constant.

In the signal transmission, the chemical structure of furan without benzene ring is conducive to the reduction of dielectric constant and dielectric loss factor. Firstly, after AN with the phenyl in high polarizability being replaced by FU, a reduction in polar functional groups occurred in polybenzoxazines, leading to the reduction of N and a_e. Secondly, FU increased the cross-linking density of the polymer and thus limited chains mobility, resulting in decreasing in N and a_d to a certain extent. Finally, for amorphous polymers in low anisotropy, the value of u for cured films was low. Theoretically, the dielectric loss factor is related to the polarization and the cross-linking density of polymer network. However, at high frequencies, dipole polarization fails to respond to external frequencies in time, which indicates the dielectric loss factor is more sensitive to the cross-link density. As the content of FU increases, the cross-linking density increases linearly, but the dielectric loss factor decreases linearly. In addition, as the degree of curing increases, the cross-linking density increases, and the polymer gradually transitions from the rubbery state to the glassy state, and the maximum dielectric loss shifts to the low-frequency direction.

Yanhui (Huang et al., 2014) conducted a two-dimensional finite element analysis on the image of on the surface of silica (Yan et al., 2014). The resulting TEM images retained the volume fraction, dispersion and geometric shape (simplifying SiO_2 to an ellipse) of the filler in the matrix through the conversion algorithm.

Due to the inherent structural heterogeneity of polymers, it can be described by the superposition of Debye functions with different relaxation time:

$$\varepsilon'_{(\omega)=}\varepsilon_{\infty}+\sum_{i=1}^{n}\frac{\Delta\varepsilon_i}{1+(\omega\tau_i)^2}$$

$$\varepsilon''_{(\omega)=}\sum_{i-1}^{n}\frac{\Delta\varepsilon_i\omega^r r_i}{1+(\omega\tau_i)^2}$$

$\varepsilon'_{(\omega)}$ and, $\varepsilon''_{(\omega)}$ respectively represent the real and imaginary parts of the dielectric constant, and taking n as 25 is to accurately simulate the shape of curves. The direct current conductivity is about 10^{-18}, S/m $\Delta\varepsilon_i$ and τ_i are the dielectric relaxation strength and relaxation time of each Debye component, and ε_{∞} is the dielectric constant at infinite frequency. To obtain the dielectric spectrum of epoxy resins matrix, the experimental dielectric spectrum of pure epoxy resin is fitted and modeled according to the above formula by Prony series algorithm. The dielectric constant of silica was taken as a frequency-independent constant of 3.9. However, the above formulas do not consider the filler/matrix interaction. This interaction can enhance or limit the mobility of polymer chains in interface regions, thereby changing the relaxation time. It is necessary to further adjust the additional tuning parameters in the formula of matrix to achieve the relaxation behavior of interface regions. The matrix-filler interface region is represented by a single phase with uniform thickness surrounding nanofillers and this thickness is assumed to be 60 nm:

$$\varepsilon'_{int\,(\omega)=}\varepsilon_{\infty}+c+M_{\alpha}\sum_{\tau_i>\tau_0}\frac{\Delta\varepsilon_i}{1+(S_{\alpha}\omega\tau_i)^2}+M_{\beta}\sum_{\tau_i<\tau_0}\frac{\Delta\varepsilon_i}{1+\left(S_{\beta}\omega\tau_i\right)^2}$$

$$\varepsilon''_{int\,(\omega)=}M_{\alpha}\sum_{\tau_i>\tau_0}\frac{S_{\alpha}\omega\tau_i\Delta\varepsilon_i}{1+(S_{\alpha}\omega\tau_i)^2}+M_{\beta}\sum_{\tau_i<\tau_0}\frac{S_{\beta}\omega\tau_i\Delta\varepsilon_i}{1+\left(S_{\beta}\omega\tau_i\right)^2}$$

α and β represent the relaxations of different structures in the interface region. α relaxation is the micro-Brownian motion of entire chain segment, and β relaxation is the rotation of polar groups. τ_i is higher than τ_0 when α is relaxed, and τ_i is lower τ_0 when β is relaxed. M, S and c respectively are tuning parameters under the corresponding relaxation obtained by matching the simulation output and the experimental data, the relaxation time and effects of dipole, ion and electronic polarization. The increase in dielectric loss at low frequencies is attributed to the α relaxation caused by the movement of polymer main chains, while the peak around 10^4 Hz is attributed to β relaxation caused by the movement of polar groups on side chains. It shows that the horizontal moving of S_{α} and S_{β} in the curve reflect the change of the relaxation time of α and β in interface area, and the vertical displacement of M_{α} and M_{β} in the curve reflect the change of the degree of polarization. The tuning parameter c reflects the change of dielectric constant over 10^6 Hz under effects of dipolarization, ion polarization and electronic polarization. For the tested system, S is usually less than 1 and M is greater than 1, which indicates that the chain segment at the interface has greater mobility and polarizability than that in the matrix. At the same time, the interface area of the composite may have stronger chain mobility and polarization in the frequency range measured. The change in polarization at higher frequencies may be attributed to short functional groups such as short-chain molecules (i.e. p-thiophene and ferrocene). It should be noted that only unimodal PGMA nano-dielectric material (M_{α} = 4) cannot reflect the change of polarization degree very well, which is caused by relatively poor fitting of its loss curve.

Furthermore, Yanhui Huang et al. used three-dimensional finite element analysis again to analyze a series of core@single-shell/double-shell nanocomposites (NP) (**Figure 6**) (Huang et al., 2016). In order to effectively control the thickness of each polymer shell, atom transfer radical polymerization (ATRP) was initiated on the surface of barium titanate ($BaTiO_3$) to graft one or more acrylic polymers to form spherical nanoparticles. Then, the polymer (shell) will deform to a certain extent to fill the gaps between the spherical NPs to form a close-packed structure by direct compression. Assuming that the free polymer PMMA and PHEMA have the same imaginary part permittivity (the methacrylic acid skeleton and the relaxation mode strength of the ester group are same), the direct current conductivity of PHEMA can be collected from the fictitious permittivity spectrum of PHEMA to obtain Fitted PHEMA DC conductivity. First, the experimental dielectric spectra of free polymers without barium titanate (PMMA, PHEMA, and PANa) were used as the input dielectric constant of each polymer shell, and the geometric information was clearly captured for two-dimensional finite element simulation and simulation.

For BT@PMMA, at low BT content (16 vol% BT), the simulated dielectric spectrum of the longer graft chain matches the experimental data very well. At high BT content (40 vol% BT), the short graft chain would induce the elimination of the volume effect, and the polymer chains near the particle surface are more easily stretched and tightly packed. At this time, the filler/matrix interface interaction cannot be ignored. Compared to free polymer,

this produces an interfacial region with a slower relaxation time and reduced strength. Since the simulation is assuming that the grafted polymer has the same relaxation behavior as the free polymer, the difference between the simulated dielectric spectrum and the experimental dielectric spectrum may be related to the grafted polymer having an interface area with the free polymer. As the geometry and interface are considered in the simulation, the interface relaxation behavior is clearly included in the simulated dielectric spectrum, which is different from the two-dimensional finite element analysis.

Since the grafted polymer and the free polymer have different relaxation behaviors, the dielectric spectrum of the free polymer initiated without barium titanate is decomposed into a superposition of 20 Debye relaxation functions, and the tuning parameters M, S is used as the offset factor of relaxation strength and relaxation time to inversely calculate the interface relaxation:

$$\varepsilon^* = \varepsilon_\infty + M_\alpha \sum_{n=20} \frac{\Delta\varepsilon_i}{1 + i\omega(S\tau_i)}$$

Similarly, ε_∞ is the dielectric constant when the frequency is infinite. $\Delta\varepsilon_i$ and τ_i are the dielectric relaxation strength and the DC conductivity is extracted from the PHEMA fictional permittivity spectrum. When the thickness is 10 nm, the values of M and S are 0.6 and 5, respectively. According to the above principles, it shows that the chain segment at the interface has a reduced relaxation strength and an increased relaxation time of the interface region than the body, which means a smaller mobility and a weakened polarization rate.

CONCLUSION AND PERSPECTIVE

The strong adhesion and excellent dielectric properties of polymer materials are often contradictory. It has been proved difficult to accurately predict the dielectric properties. Understanding the mechanism of interface adhesion failure and the mechanism of high-frequency dielectric response is an important step in the design to meet the requirements of high-speed and high-frequency signal transmission. Due to the inherent multi-variable problem of adhesion, the morphological factors of different chemical structures and the bonding strength of elements to copper will affect the results of the peeling test between copper and polymer. The method of surface modification improves the bonding strength (addition of functional groups that promote adhesion into the polymer/metal interface), which can avoid the introduction of a large number of polar groups in the body of the adhesive film, but this lacks the specificity of the groups to improve the adhesion. At the same time, the surface treatment conditions, such as the pre-curing of the polymer and the surface treatment, affect the interface roughness and mechanical strength, and ultimately determine the adhesion and dielectric properties.

As a non-polar liquid rubber, polybutadiene has a low dielectric constant and loss due to its extremely weak polarity, making it very suitable for high insulation materials. There have been studies on the modification of polybutadiene with functional groups and epoxy resins, for example, HTPB (hydroxy-terminated polybutadiene), EHTPB (epoxidized hydroxy-terminated polybutadiene), CTPB (carboxyl-terminated polybutadiene) Polybutadiene), NCOTPB (isocyanate terminated polybutadiene) to modify and toughen epoxy resin. However, the interface bonding strength between non-polar polybutadiene and copper foil is poor, and it is very challenging to improve the interface bonding strength as much as possible without damaging the dielectric properties. In terms of low dielectric constant, since the dielectric constant of the filler particles is much higher than the dielectric constant of the polymer, the filler particles are the main factor that affects the dielectric constant of the dielectric bonding film material. How to control the dielectric constant of the filler particles to achieve the low thermal expansion coefficient and low dielectric constant of the dielectric bonding film material has important theoretical significance and engineering application value.

Ceramic particles are often used to reduce the thermal expansion coefficient of the polymer matrix material and adjust the dielectric constant of the adhesive film material. Compared with layered particles, spherical particles have higher bulk density and uniform stress distribution, and can increase fluidity when filled into resin, so that CCL has better mechanical properties and adhesion properties. SiO_2 is the most common surface modifier and filler used in CCL. Due to its excellent performance, many literature reports that the spherical SiO_2 used in electronic equipment can improve dielectric properties, increase heat resistance, improve drilling processability and reduce costs. In addition to the molecular structure design of the polymer, attention should be paid to the influence of nano-filler particles on the dielectric properties of the composite material. The higher interface area of the nano-composite material effectively improves the polarization effect. The improvement of the chemical or physical bonding between the polymer matrix and the filler helps to reduce the conduction loss and the dielectric loss caused by the interface polarization. Therefore, the surface modification of nano-filler particles such as SiO_2 can be carried out. For example, functional groups (such as γ-APS, γ-aminopropyltriethoxysilane) are introduced after treatment with the coupling agent and take advantage of the synergistic effect between different types of filler particles (such as multi-component polydisperse fillers and core-shell fillers) to give composite materials more excellent comprehensive properties. At the same time, a theoretical model of the relationship between the structure of the functional filler and the dielectric properties is established to provide new ideas for the development of high-performance dielectric materials. In addition to directly introducing nano-filler particles SiO_2 (or POSS-NH_2 with functional groups), tetraethoxysilane can be used to prepare multiple composite films through a sol-gel process. Through the modification and adjustment of the composite system, the performance of the hybrid multi-element composite material and its relationship with the composition could be studied, and the thermal expansion coefficient of the composite material would be optimized. Thus, its complementary effect would improve the weakness of the single or binary system.

AUTHOR CONTRIBUTIONS

LW: article framework design and writing; JY: literature review and summary of relevant conclusions; WC: picture editing and related copyright acquisition; JZ: form editing and correction; DZ: Reference editing and correction.

REFERENCES

Anandraj, J., and Joshi, G. M. (2018). Fabrication, Performance and Applications of Integrated Nanodielectric Properties of Materials - A Review. *Compos. Inter.* 25 (5-7), 455–489. doi:10.1080/09276440.2017.1361717

Bai, X., Zhang, Z., Feng, J., Xie, G., and Chen, J. (2000). Studies on Charge Transfer of Polyimide Rings. *Chem. J. Chin. Univ-chin* 21 (9), 1455–1458.

Baklanov, M. R., De Marneffe, J.-F., Shamiryan, D., Urbanowicz, A. M., Shi, H., Rakhimova, T. V., et al. (2013). Plasma Processing of Low-K Dielectrics. *J. Appl. Phys.* 113 (4), 041101. doi:10.1063/1.4765297

Barcia, F. L., Soares, B. G., and Sampaio, E. (2004). Adhesive Properties of Epoxy Resin Modified by End-Functionalized Liquid Polybutadiene. *J. Appl. Polym. Sci.* 93 (5), 2370–2378. doi:10.1002/app.20739

Chen, J., Zeng, M., Feng, Z., Pang, T., Huang, Y., and Xu, Q. (2019). Design and Preparation of Benzoxazine Resin with High-Frequency Low Dielectric Constants and Ultralow Dielectric Losses. *ACS Appl. Polym. Mater.* 1 (4), 625–630. doi:10.1021/acsapm.8b00083

Chen, X., Ye, J., Yuan, L., Liang, G., and Gu, A. (2014). Multi-functional Ladderlike Polysiloxane: Synthesis, Characterization and its High Performance Flame Retarding Bismaleimide Resins with Simultaneously Improved thermal Resistance, Dimensional Stability and Dielectric Properties. *J. Mater. Chem. A.* 2 (20), 7491–7501. doi:10.1039/c4ta01292e

Devaraju, S., Vengatesan, M. R., Selvi, M., Song, J. K., and Alagar, M. (2013). Hyperbranched Polysiloxane-Based Diglycidyl Ether of Bisphenol a Epoxy Composite for Low K Dielectric Application. *Polym. Compos.* 34 (6), 904–911. doi:10.1002/pc.22496

Dhara, M. G., and Banerjee, S. (2010). Fluorinated High-Performance Polymers: Poly(arylene Ether)s and Aromatic Polyimides Containing Trifluoromethyl Groups. *Prog. Polym. Sci.* 35 (8), 1022–1077. doi:10.1016/j.progpolymsci.2010.04.003

Dong, J., Yang, C., Cheng, Y., Wu, T., Zhao, X., and Zhang, Q. (2017). Facile Method for Fabricating Low Dielectric Constant Polyimide Fibers with Hyperbranched Polysiloxane. *J. Mater. Chem. C* 5 (11), 2818–2825. doi:10.1039/c7tc00196g

Ge, M., Zhang, J., Zhao, C., Lu, C., and Du, G. (2019). Effect of Hexagonal boron Nitride on the thermal and Dielectric Properties of Polyphenylene Ether Resin for High-Frequency Copper Clad Laminates. *Mater. Des.* 182, 108028. doi:10.1016/j.matdes.2019.108028

He, D., Wang, Y., Song, S., Liu, S., and Deng, Y. (2017). Significantly Enhanced Dielectric Performances and High Thermal Conductivity in Poly(vinylidene Fluoride)-Based Composites Enabled by SiC@SiO2 Core-Shell Whiskers Alignment. *ACS Appl. Mater. Inter.* 9 (51), 44839–44846. doi:10.1021/acsami.7b14751

Huang, X., Sun, B., Zhu, Y., Li, S., and Jiang, P. (2019a). High-k Polymer Nanocomposites with 1D Filler for Dielectric and Energy Storage Applications. *Prog. Mater. Sci.* 100, 187–225. doi:10.1016/j.pmatsci.2018.10.003

Huang, X., Wang, J., Li, Q., Lin, J., and Wang, Z. (2019b). Impact of the Phenyl Thioether Contents on the High Frequency Dielectric Loss Characteristics of the Modified Polyimide Films. *Surf. Coat. Technology* 360, 205–212. doi:10.1016/j.surfcoat.2018.12.111

Huang, Y., Huang, X., Schadler, L. S., He, J., and Jiang, P. (2016). Core@Double-Shell Structured Nanocomposites: A Route to High Dielectric Constant and Low Loss Material. *ACS Appl. Mater. Inter.* 8 (38), 25496–25507. doi:10.1021/acsami.6b06650

Huang, Y., Krentz, T. M., Nelson, J. K., Schadler, L. S., Li, Y., Zhao, H., Brinson, L. C., Bell, M., Benicewicz, B., Wu, K., and Breneman, C. M. (2014). "Prediction of Interface Dielectric Relaxations in Bimodal brush Functionalized Epoxy Nanodielectrics by Finite Element Analysis Method," in IEEE Conference on Electrical Insulation and Dielectric Phenomena, (Des Moines, IA: CEIDP), 748–751. doi:10.1109/CEIDP.2014.6995897

Huang, Y. Y., and Terentjev, E. M. (2010). Tailoring the Electrical Properties of Carbon Nanotube-Polymer Composites. *Adv. Funct. Mater.* 20 (23), 4062–4068. doi:10.1002/adfm.201000861

Iwamoto, N. E. (1995). Comparisons of Experimental Data to Indices of Adhesion Derived from Dielectric Models. *Polym. Eng. Sci.* 35 (22), 1811–1817. doi:10.1002/pen.760352211

Kango, S., Kalia, S., Celli, A., Njuguna, J., Habibi, Y., and Kumar, R. (2013). Surface Modification of Inorganic Nanoparticles for Development of Organic-Inorganic Nanocomposites-A Review. *Prog. Polym. Sci.* 38 (8), 1232–1261. doi:10.1016/j.progpolymsci.2013.02.003

Kondo, H., Yoshida, M., Kusama, M., and Teraki, S. (2016). High Performance Insulating Adhesive Film for High-Frequency Applications. *Int. Conf. Electronics Packaging (Icep)*, 35–38. doi:10.1109/ICEP.2016.7486777

Lee, W.-C., and Du, B.-S. (2016). "A Composite Structure of High Frequency Low Dielectric Film and the Application in Flexible Printed Circuit (FPC)," in International Microsystems, Packaging, Assembly, and Circuits Technology Conference, IMPACT, Taipei, Taiwan, October 26–28, 2016 (IEEE), 389–392. doi:10.1109/IMPACT.2016.7800019

Lei, X., Chen, Y., Qiao, M., Tian, L., and Zhang, Q. (2016). Hyperbranched Polysiloxane (HBPSi)-Based Polyimide Films with Ultralow Dielectric Permittivity, Desirable Mechanical and thermal Properties. *J. Mater. Chem. C* 4 (11), 2134–2146. doi:10.1039/c5tc03391h

Leu, C.-M., Chang, Y.-T., and Wei, K.-H. (2003a). Synthesis and Dielectric Properties of Polyimide-Tethered Polyhedral Oligomeric Silsesquioxane (POSS) Nanocomposites via POSS-Diamine. *Macromolecules* 36 (24), 9122–9127. doi:10.1021/ma034743r

Leu, C.-M., Reddy, G. M., Wei, K.-H., and Shu, C.-F. (2003b). Synthesis and Dielectric Properties of Polyimide-Chain-End Tethered Polyhedral Oligomeric Silsesquioxane Nanocomposites. *Chem. Mater.* 15 (11), 2261–2265. doi:10.1021/cm0208408

Lewis, T. J. (1994). Nanometric Dielectrics. *IEEE Trans. Dielect. Electr. Insul.* 1 (5), 812–825. doi:10.1109/TDEI.2013.6451377

Li, W., Wang, M., Huang, T., Zhang, N., Yang, J., and Wang, Y. (2019). Constructing a Segregated Carbon Nanotube Network in Polyamide-Based Composites towards High Dielectric Constant and Low Loss. *Mater. Lett.* 245, 204–207. doi:10.1016/j.matlet.2019.03.004

Mittal, G., Rhee, K. Y., Mišković-Stanković, V., and Hui, D. (2018). Reinforcements in Multi-Scale Polymer Composites: Processing, Properties, and Applications. *Composites B: Eng.* 138, 122–139. doi:10.1016/j.compositesb.2017.11.028

Mohamed, M., and Kuo, S. (2019). Functional Polyimide/polyhedral Oligomeric Silsesquioxane Nanocomposites. *Polymers* 11 (1), 26. doi:10.3390/polym11010026

Murugaraj, P., Mainwaring, D., and Mora-Huertas, N. (2005). Dielectric Enhancement in Polymer-Nanoparticle Composites through Interphase Polarizability. *J. Appl. Phys.* 98 (5), 054304. doi:10.1063/1.2034654

Okubo, T., Sudo, T., Hosoi, T., Tsuyoshi, H., and Kuwako, F. (2013). "Signal Transmission Loss on Printed Circuit Board in GHz Frequency Region," in 2013 IEEE Electrical Design of Advanced Packaging Systems Symposium, Nara, Japan, December 12–15, 2013, 112–115. doi:10.1109/EDAPS.2013.6724402\

Pang, T., Zeng, M., Feng, Z., Chen, J., Huang, Y., and Xu, Q. (2019). A Facile Method for the Preparation of Furfurylamine Based Benzoxazine Resin with High-Frequency Low Dielectric Constants and Ultra-low Dielectric Losses. *J. Mater. Sci. Mater. Electron.* 30 (9), 8358–8370. doi:10.1007/s10854-019-01153-y

Prateek, Thakur, V. K., and Gupta, R. K. (2016). Recent Progress on Ferroelectric Polymer-Based Nanocomposites for High Energy Density Capacitors: Synthesis, Dielectric Properties, and Future Aspects. *Chem. Rev.* 116 (7), 4260–4317. doi:10.1021/acs.chemrev.5b00495

Qi, H., Wang, X., Zhu, T., Li, J., Xiong, L., and Liu, F. (2019). Low Dielectric Poly(imide Siloxane) Films Enabled by a Well-Defined Disiloxane-Linked Alkyl Diamine. *ACS Omega* 4 (26), 22143–22151. doi:10.1021/acsomega.9b03302

Ran, Q.-c., Tian, Q., Li, C., and Gu, Y. (2010). Investigation of Processing, Thermal, and Mechanical Properties of a New Composite Matrix-Benzoxazine Containing Aldehyde Group. *Polym. Adv. Technol.* 21 (3), 170–176. doi:10.1002/pat.1412

Shamiryan, D., Abell, T., Iacopi, F., and Maex, K. (2004). Low-k Dielectric Materials. *Mater. Today* 7 (1), 34–39. doi:10.1016/S1369-7021(04)00053-7

Shen, Z. H., Wang, J. J., Jiang, J. Y., Lin, Y. H., Nan, C. W., Chen, L. Q., et al. (2018). Phase-Field Model of Electrothermal Breakdown in Flexible High-Temperature Nanocomposites Under Extreme Conditions. *Adv. Energ. Mater.* 8 (20), 1800509. doi:10.1002/aenm.201800509

Si, L., Guo, D., Xie, G., and Luo, J. (2014). Mechanical Properties and Interface Characteristics of Nanoporous Low-K Materials. *ACS Appl. Mater. Inter.* 6 (16), 13850–13858. doi:10.1021/am503236m

Song, N., Yao, H., Ma, T., Wang, T., Shi, K., Tian, Y., et al. (2019). Decreasing the Dielectric Constant and Water Uptake by Introducing Hydrophobic Cross-Linked Networks into Co-polyimide Films. *Appl. Surf. Sci.* 480, 990–997. doi:10.1016/j.apsusc.2019.02.141

Subramanian, V., Samuel Asirvatham, P., Balakrishnan, R., and Ramasami, T. (2001). Molecular Mechanics Studies on Polypropylene and Polymethylmethacrylate Polymers. *Chem. Phys. Lett.* 342 (5), 603–609. doi:10.1016/S0009-2614(01)00620-0

Tanaka, T., Kozako, M., Fuse, N., and Ohki, Y. (2005). Proposal of a Multi-Core Model for Polymer Nanocomposite Dielectrics. *IEEE Trans. Dielect. Electr. Insul.* 12 (4), 669–681. doi:10.1109/TDEI.2005.1511092

Tasaki, T. (2018). "Low Transmission Loss Polyimides Substrates: A Novel Alternative to Liquid Crystal Polymers," in 2018 IEEE 20th Electronics Packaging Technology Conference, Singapore, December 04–07, 2018 (Irvine, CA: EPTC), 237–240. doi:10.1109/EPTC.2018.8654331

Todd, M. G., and Shi, F. G. (2005). Complex Permittivity of Composite Systems: A Comprehensive Interphase Approach. *IEEE Trans. Dielect. Electr. Insul.* 12 (3), 601–611. doi:10.1109/TDEI.2005.1453466

Tong, L., Lei, X., Yang, G., and Liu, X. (2019). Self-toughening and Self-Enhancement Poly(arylene Ether Nitrile) with Low Dielectric Constant by Solid Crosslinking Reaction. *Polymers* 11 (9), 1403. doi:10.3390/polym11091403

Van Duin, A. C. T., Dasgupta, S., Lorant, F., and Goddard, W. A. (2001). ReaxFF: A Reactive Force Field for Hydrocarbons. *J. Phys. Chem. A.* 105 (41), 9396–9409. doi:10.1021/jp004368u

Volksen, W., Miller, R. D., and Dubois, G. (2010). Low Dielectric Constant Materials. *Chem. Rev.* 110 (1), 56–110. doi:10.1021/cr9002819

Wang, H., Yuan, Y., Chi, Z., Yang, Z., Li, E., and Tang, B. (2019). Researches on Silane Coupling Agent Treated AlN Ceramic Powder and Fabrication of AlN/PTFE Composites for Microwave Substrate Applications. *J. Mater. Sci. Mater. Electronmaterials Electronics* 30 (22), 20189–20197. doi:10.1007/s10854-019-02402-w

Wang, J.-Y., Yang, S.-Y., Huang, Y.-L., Tien, H.-W., Chin, W.-K., and Ma, C.-C. M. (2011). Preparation and Properties of Graphene Oxide/polyimide Composite Films with Low Dielectric Constant and Ultrahigh Strength via In Situ Polymerization. *J. Mater. Chem.* 21 (35), 13569–13575. doi:10.1039/c1jm11766a

Wu, Z., Gao, S., Chen, L., Jiang, D., Shao, Q., Zhang, B., et al. (2017). Electrically Insulated Epoxy Nanocomposites Reinforced with Synergistic Core-Shell SiO2 @MWCNTs and Montmorillonite Bifillers. *Macromol. Chem. Phys.* 218 (23), 1700357. doi:10.1002/macp.201700357

Xu, N., Hu, L., Zhang, Q., Xiao, X., Yang, H., and Yu, E. (2015). Significantly Enhanced Dielectric Performance of Poly(vinylidene Fluoride-Co-Hexafluoropylene)-Based Composites Filled with Hierarchical Flower-like TiO2 Particles. *ACS Appl. Mater. Inter.* 7 (49), 27373–27381. doi:10.1021/acsami.5b08987

Yang, K., Huang, X., Huang, Y., Xie, L., and Jiang, P. (2013). Fluoro-Polymer@BaTiO3 Hybrid Nanoparticles Prepared via RAFT Polymerization: Toward Ferroelectric Polymer Nanocomposites with High Dielectric Constant and Low Dielectric Loss for Energy Storage Application. *Chem. Mater.* 25 (11), 2327–2338. doi:10.1021/cm4010486

Yang, X., Tang, L., Guo, Y., Liang, C., Zhang, Q., Kou, K., et al. (2017). Improvement of Thermal Conductivities for PPS Dielectric Nanocomposites via Incorporating NH2-POSS Functionalized nBN Fillers. *Composites A: Appl. Sci. Manufacturing* 101, 237–242. doi:10.1016/j.compositesa.2017.06.005

Yao, Y., Zeng, X., Guo, K., Sun, R., and Xu, J.-b. (2015). The Effect of Interfacial State on the thermal Conductivity of Functionalized Al2O3 Filled Glass Fibers Reinforced Polymer Composites. *Composites Part A: Appl. Sci. Manufacturing* 69, 49–55. doi:10.1016/j.compositesa.2014.10.027

Yu, P., Wang, Y., Yu, J., Zhu, J., and Hu, Z. (2018). Influence of Different Ratios of A-ODPA/a-BPDA on the Properties of Phenylethynyl Terminated Polyimide. *J. Polym. Res.* 25 (5), 1–11. doi:10.1007/s10965-018-1508-4

Yu, P., Zhang, Y. l., Yang, X., Pan, L. j., Dai, Z. y., Xue, M. z., et al. (2019). Synthesis and Characterization of Asymmetric Bismaleimide Oligomers with Improved Processability and Thermal/mechanical Properties. *Polym. Eng. Sci.* 59 (11), 2265–2272. doi:10.1002/pen.25229

Zhang, F. (2019). *Study of the Effect of SiO2 Morphology and Particle Size on the Dielectric Properties of Polyolefin Composite Resins*. Master's thesis. Chengdu, China: University of Electronic Science and Technology.

Zhang, X., Li, B.-W., Dong, L., Liu, H., Chen, W., Shen, Y., et al. (2018). Superior Energy Storage Performances of Polymer Nanocomposites via Modification of Filler/Polymer Interfaces. *Adv. Mater. Inter.* 5 (11), 1800096. doi:10.1002/admi.201800096

Zhao, B., Hamidinejad, M., Zhao, C., Li, R., Wang, S., Kazemi, Y., et al. (2019). A Versatile Foaming Platform to Fabricate Polymer/carbon Composites with High Dielectric Permittivity and Ultra-low Dielectric Loss. *J. Mater. Chem. A.* 7 (1), 133–140. doi:10.1039/c8ta05556d

Zhu, J., Ji, X., Yin, M., Guo, S., and Shen, J. (2017). Poly (Vinylidene Fluoride) Based Percolative Dielectrics with Tunable Coating of Polydopamine on Carbon Nanotubes: Toward High Permittivity and Low Dielectric Loss. *Composites Sci. Technology* 144, 79–88. doi:10.1016/j.compscitech.2017.03.017

Zhuang, Y., Seong, J. G., and Lee, Y. M. (2019). Polyimides Containing Aliphatic/alicyclic Segments in the Main Chains. *Prog. Polym. Sci.* 92, 35–88. doi:10.1016/j.progpolymsci.2019.01.004

Conflict of Interest: Authors LW, JY, WC, JZ, and DZ were employed by the company China Electronics Technology Group Corporation No. 38 Research Institute.

Publisher's Note: All claims expressed in this article are solely those of the authors and do not necessarily represent those of their affiliated organizations, or those of the publisher, the editors and the reviewers. Any product that may be evaluated in this article, or claim that may be made by its manufacturer, is not guaranteed or endorsed by the publisher.

frontiers in Materials

ORIGINAL RESEARCH
published: 21 October 2021
doi: 10.3389/fmats.2021.741541

The Nail Penetration Behaviour of Carbon Nanotube Composite Electrodes for Energy Storage

*Evangelos Koliolios, Daniel G. Mills, James J. C. Busfield and Wei Tan**

School of Engineering and Materials Science, Queen Mary University of London, London, United Kingdom

The high surface area, electrical and mechanical properties of carbon nanotube (CNT) composites has rendered them promising candidates for structural power composites. Nevertheless, it is important to understand their mechanical behaviour before they are applied in energy storage devices amid the safety concerns. This work explores the nail penetration behaviours of supercapacitor specimens consisting of CNT electrodes and pseudocapacitor specimens with carbon nanotube-polyaniline (CNT/PANI) electrodes. Specimens with and without electrolyte were tested. The dry cells without electrolyte follow a power law behaviour, while the wet cells with the electrolyte exhibit a piece-wise nonlinear relationship. The force, voltage and temperature of the supercapacitor were recorded during the nail penetration test. No temperature change or overheating was observed after short-circuit. Moreover, electrochemical testing is performed before and after the specimen penetration. The cyclic voltammetry shows the dramatic loss of capacitance, changing the cell behaviour from capacitor to resistor-like manner. Johnson-Cook model was used to predict the nail penetration behaviour. The coefficients of Johnson-Cook model are calibrated from the experimental load-displacement curves. The finite element model predictions are in a good agreement with the experimental results.

Keywords: nail penetration, carbon nanotube, composites, energy storage, supercapacitors, electrochemical performance

OPEN ACCESS

Edited by:
Dong Xiang,
Southwest Petroleum University, China

Reviewed by:
Yun Huang,
Southwest Petroleum University, China
Jin Zhou,
Xi'an Jiaotong University, China

****Correspondence:***
Wei Tan
wei.tan@qmul.ac.uk

Specialty section:
This article was submitted to Polymeric and Composite Materials, a section of the journal Frontiers in Materials

Received: *14 July 2021*
Accepted: *27 September 2021*
Published: *21 October 2021*

Citation:
Koliolios E, Mills DG, Busfield JJC and Tan W (2021) The Nail Penetration Behaviour of Carbon Nanotube Composite Electrodes for Energy Storage. Front. Mater. 8:741541. doi: 10.3389/fmats.2021.741541

1 INTRODUCTION

Battery perforation and internal short circuiting is likely to occur in the event of a collision involving electric vehicles or hybrid vehicles. Nail penetration testing is one of the widely-used methods to evaluate the damage tolerance, internal short circuit behaviour and fire safety of lithium ion batteries. As the energy density of supercapacitors increases and their use becomes more widespread, understanding their failure behavior is also critical to aid the proliferation of their use in efficient, low emission vehicles.

Regarding the safety standards of commercial supercapacitors, a review was conducted by Walden et al. (2011) where nail penetration and overcharging for devices with supercapacitors were suggested as potential safety tests, which are similar to the tests conducted for commercial lithium-ion batteries.

Abbreviations: ν, Poisson's Ratio; σ, Stress; E, Young's Modulus; G_c, Fracture Toughness; r, Coefficient of determination; ϵ, Strain; ϵ_p, Plastic Strain.

Currently there are specific IEC (International Electrochemical Commission) standards that commercial supercapacitors need to follow depending on their application such as IEC 62576 IEC (2018), which relates to the application of supercapacitors on hybrid electric vehicles. Nevertheless, the current IEC standards for supercapacitors do not include any mechanical testing standards. In this study nail penetration testing was selected to be conducted as extreme failure of the specimen can be observed and the risk created by such an experiment can be evaluated accordingly.

This investigation draws inspiration from Tan et al. (2021), where the electrochemical properties of a CNT/PANI specimen are discussed. However, the CNT/PANI supercapacitor mechanical properties must also be assessed to ensure that there are no hazards if such a specimen is used in industrial applications, such as regenerative braking. Nevertheless, there is a gap of scientific investigations, regarding the mechanical abuse testing of supercapacitors. Qiu et al. (2019) and Qiu et al. (2020) have performed bending tests on alkaline supercapacitors and on a supercapacitor whose electrolyte is based on biomass respectively, to observe how bending affects the charging and discharging on the device. However mechanical abuse tests that lead to failure of the specimen have not been addressed. Therefore the methodology followed is similar to that of pouch battery mechanical abuse testing, where an extensive literature is available. The study of Sahraei et al. (2012) and Greve and Fehrenbach (2012) provide a basis on the approach of both experimental testing and modelling of mechanical abuse in batteries. The modelling procedure involves assuming a homogenized specimen, and using either power law or piece-wise functions to approximate the experimental behaviour of the battery jellyroll, which is similar to the methodology carried out during the modelling of the supercapacitor.

Additionally, a more in depth analysis on general indentation has also been performed by Sahraei et al. (2014), where the effect of different indentor shapes is highlighted. Different indentor shapes can be further used to not only evaluate the durability of the specimen but to also validate the mechanical model of the supercapacitor. In this investigation however, only a nail indentor was used to penetrate the cell, while observing not only mechanical but also electrochemical and thermal behaviour of the specimen. This is similar to the approach of Zhang et al. (2015b), where quasi-static indentation is performed and multiphysical parameters are observed. However multiphysical modelling will involve future work for this investigation as it involves further experimentation and understanding of the short-circuit mechanisms.

The scope of this study is to therefore investigate the behaviour of both a CNT and a CNT/PANI supercapacitor under nail penetration, which involves the mechanical, electrical and thermal behaviour during puncture and the mechanical modelling of the nail penetration process. It aims to fill in the gap on mechanical abuse testing of supercapacitor and pave the road for further experimental and numerical investigations on similar specimens. Additionally, this investigation aims to highlight the durability of CNT electrodes, compared to traditional active carbon electrodes. This study also evaluates the safety of the specimen after puncture and to observe whether the specimen can still store electrical energy after failure.

2 MATERIALS AND METHODS

2.1 Material Preparation

The CNT mats used in this study were supplied by Tortech Nano Fibers Ltd. These CNT mats were manufactured by a floating-catalyst chemical vapour deposition (FCCVD) process. Then CNT mat samples of width 50 mm, length 60 mm and 50 μm thickness were used as the electrode materials. Three-electrode electrodeposition system was used to coat the PANI materials on the CNT mats. The detail of electrodeposition procedure can be found in Tan et al. (2021). In brief, the CNT mat and a platinum mesh were used as the working electrode and the counter electrode respectively, while a saturated calomel electrode was employed as a reference electrode. The electrodeposition solution is made of 1 M sulphuirc acid and 0.05 M aniline. A constant current of 1 mA/1 cm^2 was applied on the CNT mat samples to deposit PANI. Detailed microstructures can be found in the SEM images presented in Tan et al. (2021).

2.2 Mechanical Testing

The samples presented in **Figure 1**, were tested using an INSTRON 5967 with a 1 kN load cell held with the sample stage presented in **Figures 2**, **3** under displacement control and atmospheric conditions. The indentation tip shown in **Figure 4** was lowered onto the sample prior to testing until the load cell read a positive load, all the testing took place at a displacement rate of 0.8 mm/min. In order to perform the penetration testing on the supercapacitor samples and its constituent parts a sample stage was designed and fabricated. Commercial products are available for puncture testing, however this investigation specifically required for the cells to lie horizontally flat during testing to evenly distribute the electrolyte throughout. To allow for the nail to pass completely through the samples unobstructed and to collect any harmful H_2SO_4 electrolyte that may spill out during testing, the sample stage was elevated with the use of a cup. The samples needed to be secured with enough pressure that they would not be drawn out during penetration testing and so a top pressure plate with four 5 mm bolts, (one in each corner) was used to fix the samples in place. There is also a need to ensure that the nail would repeatedly make contact at exactly the centre of the exposed part of the sample during each test repeat, this required an aligner to centre the sample stage in the INSTRON machine. This was not a structural part and so could be manufactured *via* additive manufacturing out of PLA while the cup, base plate and pressure plate were machined from aluminum, the CAD model of the sample testing apparatus can be seen in **Figure 2**. Three penetration tests were performed on a pseudocapacitor cell for which the CNT electrode had been electrodeposited with PANI, a test was performed on an identical cell without the PANI for comparison. Images of the failed specimen and the experimental setup can be observed in **Figure 5**. The direct spun CNT mat consists of multi-walled carbon nanotubes. The mat has a

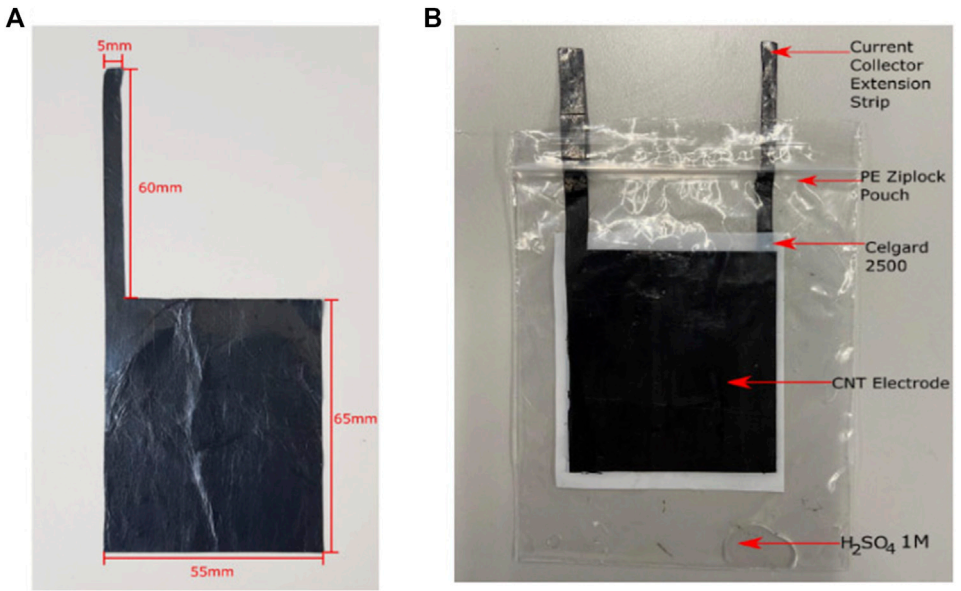

FIGURE 1 | (A) Electrode Dimensions and **(B)** Supercapacitor Specimen Configuration.

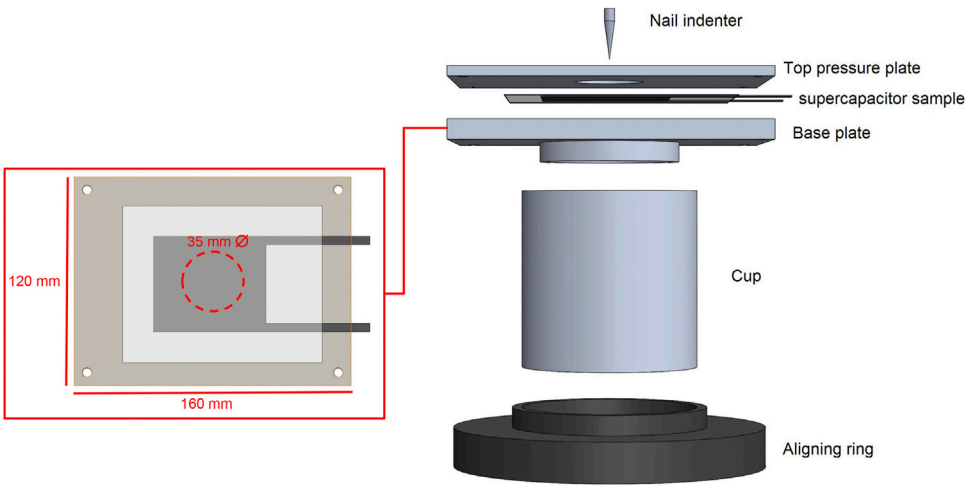

FIGURE 2 | Base plate dimensions and the effective area of unsupported specimen and CAD model of the bespoke nail penetration test rig.

nominal thickness of 60 μm and an areal mat density of 0.0234 kg/m^2, and the volumetric mat density is 390 kg/m^3. The direct-spun mat has a 6 wt% of Fe content, using a thermo-gravimetric analyser. A bundle density of 1560 kg/m^3 was determined by helium pycnometry (Tan et al., 2019; Stallard et al., 2018). The diameters of individual carbon nanotube bundles range from 30 to 100 nm, confirmed by SEM and TEM images (Tan et al., 2021). The measurements of the individual CNTs within the CNT mats have shown a length up to 1 mm (Koziol et al., 2007). Penetration tests were also performed on dry cells that had no electrolyte to assess if prolonged exposure to 1 M H_2SO_4 electrolyte had an effect on the mechanical properties of the cells.

2.3 Electrochemical Testing

Cyclic voltammetry can be used to analyse qualitative details of electrochemical processes under different conditions such as the presence of intermediates in oxidation reduction reactions and the reversibility of reactions. CV can also be used to evaluate the stoichiometry of the device, the diffusion coefficient of the chemical constituents, the capacitance and the cycle life of the capacitor (Gamry, 2012). Capacitors can only work inside the voltage window of both the upper and lower voltage limits where the voltages outside the window can cause the system to be damaged by electrolyte decomposition. Although aqueous electrolytes such as the diluted sulphuric acid solution are usually safer and simpler to use, non-aqueous electrolyte

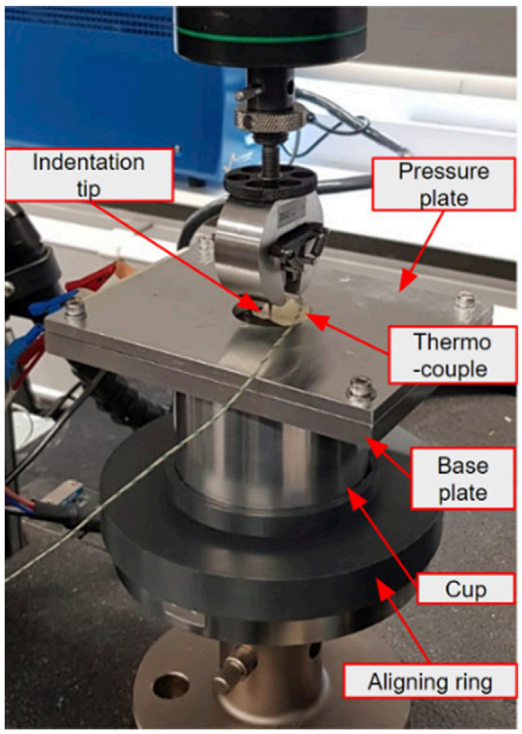

FIGURE 3 | Annotated picture of the nail penetration testing set up.

capacitors may have a much larger voltage window (Gamry, 2012). To test the upper and lower voltage limits, we use the cyclic voltammetry. This is a procedure that plots the current flowing through the electrochemical cell and voltage is varied between a set voltage range, this is also called a linear voltage ramp. A CV test often sweeps the voltage between the two limit potentials repetitively in opposite directions resulting in a complete cycle.

2.4 Mechanical Modelling

Mathematical models are of utmost importance when trying to approximate the behaviour of a specimen. As mentioned in the previous section, the EDLC and PANI pesudocapacitor exhibit a hardening behaviour under nail penetration/indentation. This hardening behaviour is similar to the one observed in the battery jellyroll and that it follows the power law as discussed by Greve and Fehrenbach (2012) and the power law is of the form:

$$\sigma = A + B\epsilon^n \tag{1}$$

where σ is stress, ϵ is strain and A, B and n are constants. The physical meaning of A is yield strength, B and n are constants that predict the hardening behaviour of the specimen according to the Johnson-Cook plastic behaviour (Johnson and Cook, 1983). A is the initial yield strength of the material at a quasi-static strain rate, B and n represents the flow stress on strain hardening behavior at quasi-static strain rate (Johnson and Cook, 1983; Nam et al., 2014). The approach of investigations studying the hardening behaviour of energy storage devices, like batteries in the case of Xu et al. (2016), is to obtain the power curve constants through experiments, as the equation is purely empirical. Therefore for the region before fracture for the Dry Cell 1 experiment and the PANI-1 experiment (**Figure 6**), a best-fit power law curve code was generated with Python. In order to obtain the Nominal Stress vs Nominal Strain data however, the force was divided by the tip surface area approximated equal to $A_{tip}=7.069 \times 10^{-4} mm^2$, assuming that the area at the tip area is a flat punch with a diameter of 0.03 mm. The nominal strain was obtained by dividing the displacement with the thickness of the specimen which was 0.25 mm before indentation [similar to the approach of Xu et al. (2016)] the best fit curve, the equation of the best fit curves as well as the coefficient of determination are presented in **Figure A1**.

A sample of experimental data were plotted, as this improved the clarity of the best fit curve, however all the data were used for the optimisation process of the best fit line performed by Python. The EDLC hardening behaviour follows the hardening law perfectly, with a nearly ideal coefficient of determination value of $r^2 = 0.9998$. The PANI hardening behaviour however, does not abide exactly by the power law, as the constant A is negative and this is not a physically possible value for yield strength. Other similar investigations such as Sahraei et al. (2012), Lai et al. (2014) and Zhang et al. (2015a), observed that the behaviour of the components and thus of a homogenized wet bare cell attains piece-wise behaviour, therefore this approach should be followed for the PANI-1 experiment. The behaviour of a wet bare cell was assumed non-linear before plasticity and linear after plasticity was reached. The piece-wise relationship between stress and strain are presented below (Sahraei et al., 2012; Lai et al., 2014; Zhang et al., 2015a):

FIGURE 4 | Conical indentation tip with an internal angle of 9.5° and a tip radius of 250 μm.

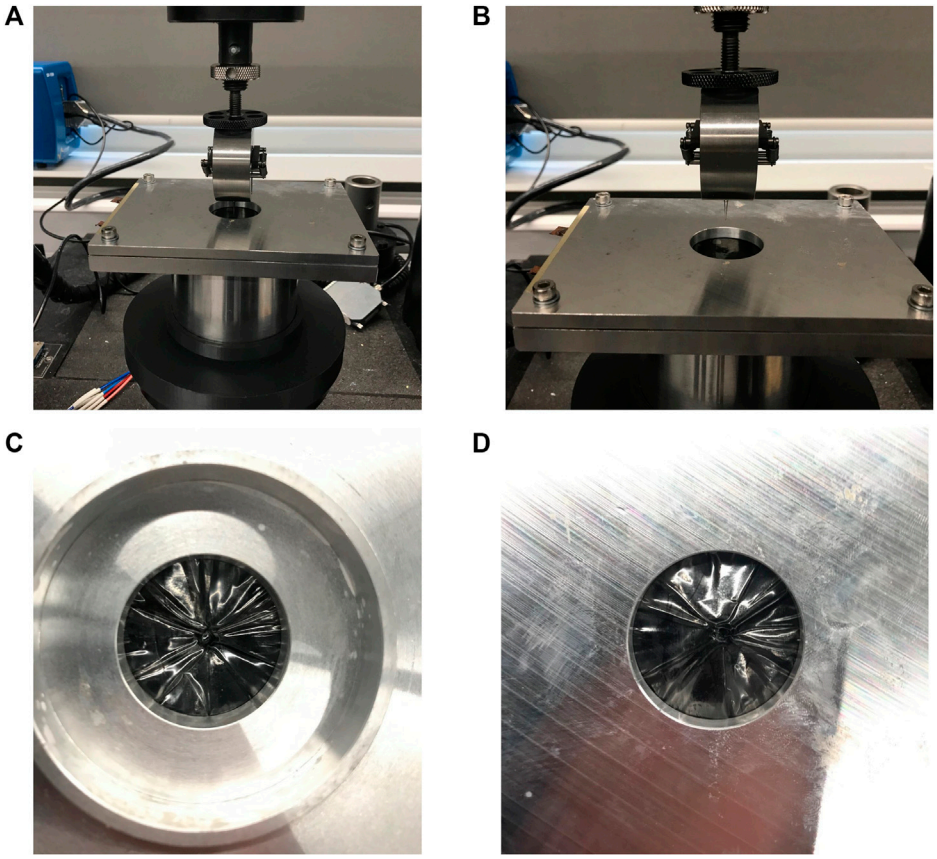

FIGURE 5 | Test setup **(A)** before and **(B)** after nail penetration. **(C)** The penetrated specimen from the top view **(D)** from the bottom view.

$$\sigma_n = \begin{cases} E_{max}\,(e^{c\epsilon_n} - 1)/ce^{c\epsilon_p} & \epsilon_n < \epsilon_p \\ E_{max}\,(1 - e^{c\epsilon_p})/c + E_{max}\,(\epsilon_n - \epsilon_p) & \epsilon_n \geq \epsilon_p \end{cases} \quad (2)$$

Where E_{max} is the maximum Young's Modulus Value, ϵ_p is the plastic strain and c is a fitting parameter. By applying the above function and fitting it to the experimental data of PANI 1 and wet EDLC 1, which also does not abide the power law curve, are presented in **Figure A2** and the coefficients in **Table 1** respectively. By using the piece-wise equation, the coefficient of determination becomes more idealised, which will result in a better simulated value. The wet cells therefore, follow a different behaviour under indentation, due to an electrolyte being contained inside the PE pouch which fills the pores of the electrodes and the separator. In order to provide a better approximation of the difference between the behaviour CNT and PANI approximations, the values of constants for the dry CNT specimen that will be used during modelling are given as follows $A = 5.737$ MPa, $B = 25.245$ MPa and $n = 2.20$.

During indentation, the maximum Modulus achieved by the wet CNT EDLC is significantly larger than that achieved by PANI, and therefore the coating CNT with PANI results in a less stiff specimen, which also fails at larger nominal strain values. The value of the constant c, is a measure of how fast the modulus increases with strain, a smaller value of c indicates a larger increase in modulus over strain Zhang et al. (2015a), and in this case even though the wet PANI specimen has a smaller modulus, it increases at a greater rate over strain. It is also important to comment that the coefficient of variation value is closer to $r^2 = 1$ for PANI and therefore the approximation can be more accurate. Finally, the parameters of the piece-wise formula can be integrated into ABAQUS and construct a subroutine to create a model which gives appropriate results, even for wet cells which is extremely important as these cells will experience indentation in service. At this point it must also be noted that several experiments were conducted and using the values of constants generated from one experiment will not provide a complete image of the nail indentation. The simulation procedure is greatly affected by the results being non-repeatable, as different critical values are observed for similar specimen. Nevertheless, by conducting a greater number of experiments, the statistical significance of the modelling constants and material properties used in this article can be determined.

3 RESULTS AND DISCUSSION

3.1 Mechanical Testing

Regarding the puncture force of each material, the Celgard separator (**Figure 6B**) provided the lowest resistance to

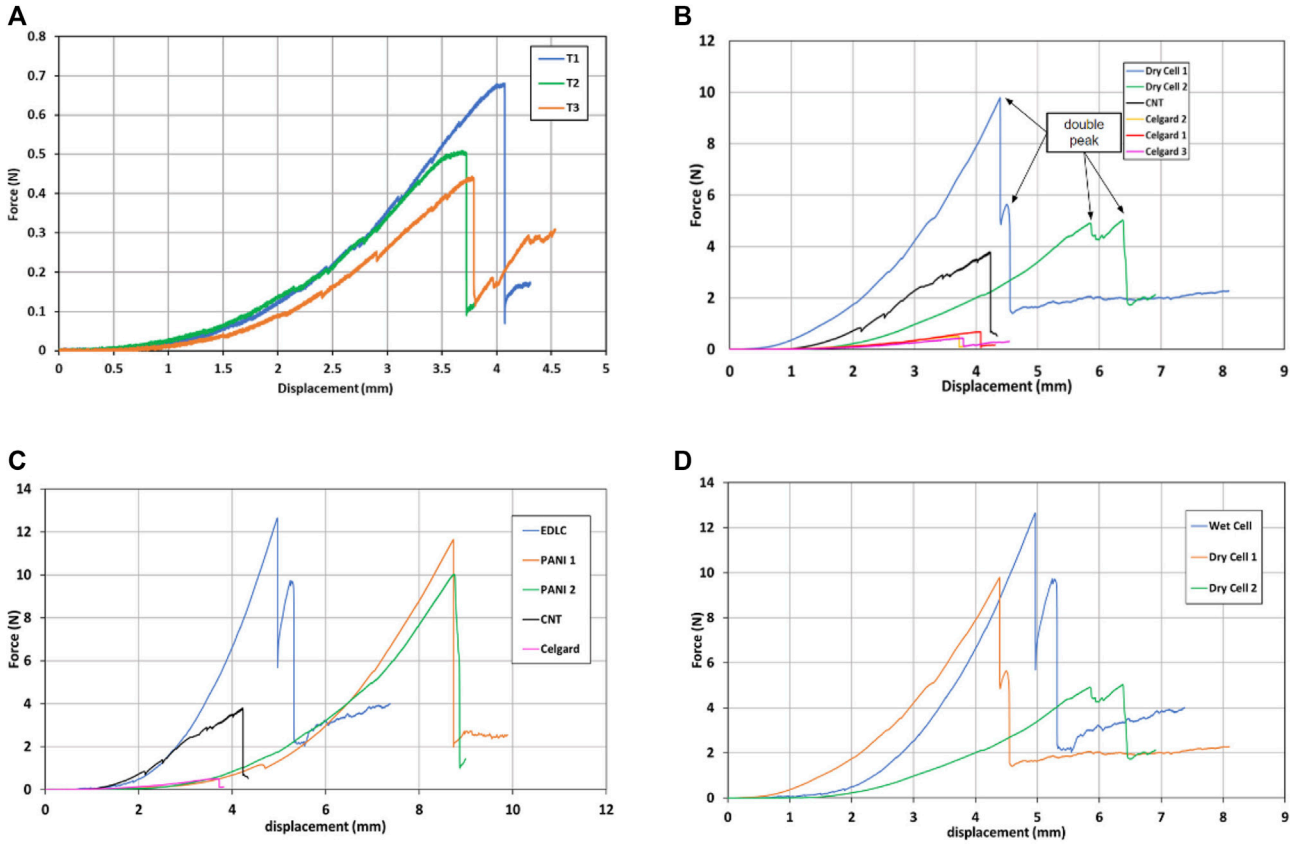

FIGURE 6 | (A) Force-displacement plot for nail penetration of Celgard 2500 separator, **(B)** Force-displacement plot comparing behavior of Celgard 2500 separator, a dry EDLC cell and a single CNT electrode, **(C)** Force-displacement plot comparing behavior of the Carbon Nanotube Mat (CNT), Celgard 2500 separator (Celgard), an electrolyte soaked EDLC cell (EDLC) and PANI-coated CNT pseudocapacitor electrode cells (PANI 1 and PANI 2), **(D)** Force-displacement plot comparing behavior of dry and wet electrolyte soaked cells.

puncture with an average puncture force of 0.54 N, however unlike during tensile testing there is a relatively low scatter in displacement or strain to failure. This is likely caused by the fact that a much smaller volume of the separator is under stress during puncture testing and due to the fact that the failure of the separator is initiated by the inherent slit-like pores in the material there is less variability in the flaw sizes in the volume of material experiencing maximum stress. Moghim et al. (2020) performed puncture strength testing on Celgard 2400 a very similar separator to 2500 and found that the two different failure modes, occurred simultaneously during puncture testing as axisymmetric stress is being applied to an anisotropic material. Prior to the puncture point, the stick-slip behaviour can be clearly seen in T3 of **Figure 6A** where there is force relaxation and then subsequent increase, indicating the separator has yielded in the transverse direction (TD). The "saw-tooth" uneven rise in force again seen in all samples after sample failure and complete nail penetration is caused by the widening of the hole the nail has made due to its conical shape.

The same saw-tooth behaviour can be seen from the force-displacement plot for the single CNT electrode in **Figure 6B**, this can likely be attributed to the puncture and subsequent delamination of the various sub-layers of nonwoven CNT that make up the bulk of the CNT mat as is described by Tan et al. (2019) when discussing the hierarchical microstructure of direct-spun CNT mats. The puncture force from the CNT electrode was measured to be 3.31 N, almost an order of magnitude higher than the Celgard and so displaying much more dominant behaviour as can be seen in **Figures 6B,C**. The dominant CNT behaviour coupled with fluctuations in force produced by the CNT mats make it difficult to interpret the points of failure for specific cell components. However a feature noted in **Figure 6B** and which can also be seen in **Figures 6C,D**, is the "double peak" phenomenon. Each peak may be caused by the sequential failure of the top and then the bottom CNT electrode. Curiously this behaviour is only seen in samples in which pure CNT electrodes were used (labeled EDLC in the figures below), the cells that used electrodes deposited with PANI do not have a double peak when failing, possibly due to the fact that both CNT layers fail simultaneously. The reason for this behaviour in PANI deposited electrodes is unclear, possibly due to the reduction of fracture toughness in CNT/PANI electrodes in contrast to bare CNT mats.

It can also be seen in **Figure 6C** the cells that use pure CNT electrodes (EDLC) have a lower displacement to failure and show a higher stiffness than both the PANI coated electrode samples. Tan et al. (2021) reported the in-plane tensile mechanical properties of CNT-PANI composites electrodes. The composite has a PANI volume fraction of 8.7% Tan et al. (2021), similar to that of the CNT/PANI electrodes used in this study at 6.65%. The modulus of the CNT mat rose from 3.5 to 6 GPa. Penetration testing however applies stress in the out of plane direction that either cause some delamination or fracture of the CNT mat. Although, it is worth mentioning that another study by the same authors Tan et al. (2019) found the delamination toughness of the direct-spun CNT mats to be 5.4 J/m^2 as compared to an in plane toughness of 22 kJ/m^2, a difference of four orders of magnitude. Another possible explanation for the anomalous loss in stiffness may be caused by the PANI on the CNT bundles absorbing water through prolonged exposure to the aqueous H_2SO_4 electrolyte, weakening the entire electrode. The effects of water absorption by polymers such as nylon is well documented Reimschuessel (1978) with stiffness decreasing as water is absorbed. PANI transitions between its three oxidation states during charging and discharging, emeraldine being one of these three oxidation states and work by Casanovas et al. (2012) shows that this type of PANI is hydrophilic and irreversibly absorbs water which organise into nanodrops within the polymer network. Polymers absorbing solvents also leads to a phenomenon known as swelling in which they will expand in volume (Buckley and Berger, 1962b; Buckley and Berger, 1962a). In the case of the PANI coated CNT mat this swelling may force apart the coated nanotube bundles and weaken the entire structure of the electrode. It is feasible that the modulus of PANI being reduced by the absorption of water, in combination with the polymer swelling, can explain the reduction in stiffness, the higher displacement to failure and the lack of "double peaks" seen in the PANI coated electrode samples. However there is no literature to date investigating the effects of water absorption on the mechanical properties of PANI nor its volumetric effects.

Figure 6B highlights the different phases that the sample cells go through during indentation tests, where the force displacement curve can be split into two distinct stages. Tan et al. (2019) found the volume fraction of the CNT mat used in this study to be only 0.187 equaling a void fraction of 0.813, therefore the initial stiffening stage can be attributed to the porosity of the CNT mat decreasing with compressive loading as shown in **Figure 7**, similar results are described by Zhang et al. (2015a) during nail penetration testing of single lithium ion cells, attributing the stiffening to void volume reduction in the electrode material.

At first glance the stiffening behaviour of the entire force-displacement curve may look to follow a power law, however in reality the second linear stage is actually constituted of regions of different hookean behavior each with successively increasing stiffness. In the linear stage stiffening events can be seen taking place in which distinct gradient changes occur as explained in the mechanical modelling part.

To assess the effects of poroelastic interactions between the CNT mat, the separator and the electrolyte dry cells were constructed that used pure uncoated CNT mats as electrodes, the results of which can be seen in **Figure 6D** The most noticeable result of this test is the fact that all the samples produced a double peak upon failure, highlighting the fact that only the PANI samples lacked them. Apart from this there seems no discernible difference between the behaviour of a wet and a dry cell at the strain rates used in this test Gor et al. (2014) and Cannarella et al. (2014) tested the mechanical properties of a PP Celgard separator both dry and immersed in both water and DMC to investigate the poroelastic behaviour. They found that under compressive testing, for both dry and wet separators, stiffness increases linearly with strain rate, at lower strain rates, then the stiffening of the wet separator sharply rose becoming far more pronounced at higher strain rates, above 10^{-3} s^{-1}. Under tensile loading the authors again saw stiffness increase with strain rate however saw a reduction in stiffness for separator immersed in DMC, indicating that the softening effects due to polymer solvent interactions are far more pronounced in tension than in compression.

From the results shown it is clear that CNT is far more dominant in the behavior of the supercapacitor cells compared to the Celgard separator. In **Figures 6B,C** the force-displacement curve for the EDLCs and CNT are closely aligned, showing similar initial stiffening and then liner stiffening.

In the force displacement curve of the PANI 2 sample in **Figure 6C** a small drop in force is seen after 4 mm displacement before it continues to rise again, this is likely due to the outer PE pouch being pierced by the indentation tip and then being subsequently met by the first CNT electrode. The reason for the small, but present, distance between the two is due to the fact that as force was applied by the pressure plate to affix the samples in place, the pressure inside the cell would cause the part of the cell exposed through the hole to inflate with excess electrolyte, separating the two layers.

Figure 8 depicts temperature, voltage and penetration force with respect to time, up until the point of mechanical failure. It can be seen that neither electrical nor mechanical failure has an effect on cell temperature with the observed periodic temperature fluctuations observed probably arising from the oscillation of an adjacent air conditioning unit. The lack of any rise in temperature of the cell upon failure is to be expected due to the small amount of energy stored in the cell, insufficient to cause any joule heating when the cell internally short circuits. It is well reported in the literature that when performing penetration and indentation testing of batteries, the drop in current or voltage output of the battery coincides with the sudden drop in penetration/indentation force (Zhang et al., 2015b; Sahraei et al., 2012). This is due to the fact that in the construction of a modern lithium ion cell, the electrode material has the worst mechanical properties compared to the other major components, namely the current collector, the separator and the pouch. The electrodes in batteries are not symmetrical and are either made of graphite for the anode or inorganic lithium compounds as cathode material. In both cases they are sponge, foam like materials that contribute very little to the structural properties of the batteries themselves

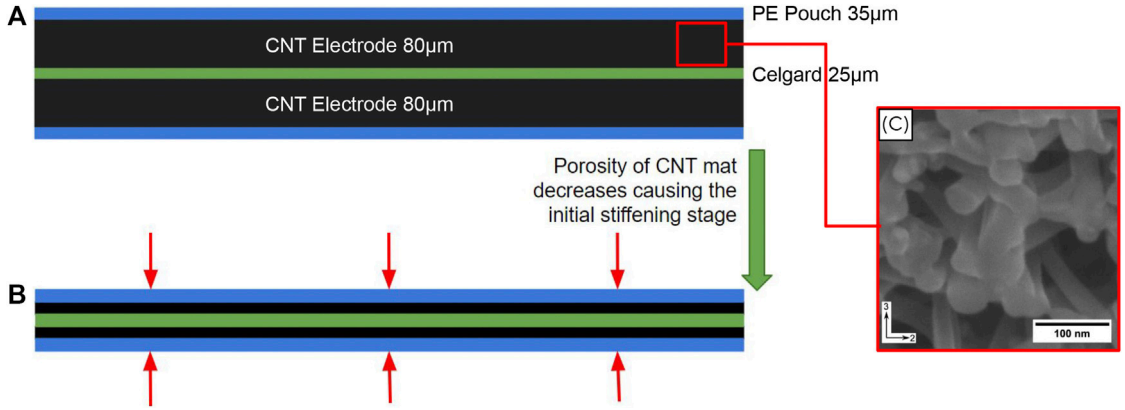

FIGURE 7 | Schematic showing **(A)** the layer thickness of a pure CNT EDLC cell used in nail penetration testing, **(B)** the compression and densification of the CNT mat reducing the pore volume fraction resulting in the initial stiffening stage of the force-displacement curve and **(C)** an SEM image taken side on to the CNT mat showing its porosity [Tan et al. (2019)].

with yield and tensile strengths of < 10 MPa Wang et al. (2018), Pan et al. (2020). Due to this the cell will fail when either the nail or indentation head has passed through or crushed the first electrode it encounters and punctures the separator allowing current to flow through one electrode to the other. In complete contrast to this, the CNT mats in the capacitor cells tested in this study have the most dominant effect over the mechanical strength of the whole cell, possessing the highest modulus, yield, tensile strength and strain to failure, and as a result during penetration testing the separator fails before the electrodes which is the reason for a drop in cell voltage is seen in **Figure 8** before total mechanical failure. Upon failure of the first electrode, the nail then draws CNT fiber bundles from one electrode, through the punctured separator into the second electrode. **Figure 9** shows optical microscope image of two separator samples from a failed cell, indicating CNT fiber residue left around the puncture hole. The current is drawn around the separator after structural failure of the separator as the two electrodes come in contact, a slight contact will draw the current away for the separator and towards the easiest path of current. Due to the fact that these fibers are extremely thin (< 1 μm), in the event of a short circuit in an industrial sized cell, even with a low charge level, the current density would exceed many thousands of A/m^2, causing sufficient Joule heating to cause thermal degradation and in cell that uses ionic liquids suspended in an organic volatile solvent, a combustion and thermal runaway.

3.2 Electrochemical Testing

The electrochemical tests were conducted for the samples before and after the nail penetration. A two-electrode system was used for the electrochemical characterisation. Cyclic voltammetry were conducted by applying a triangular voltage waveform between −0.2 and 0.8 V. The indentation clamping grip is cleaned from any loose electrolytes as well as the nail to not transport any electrolytes to the next sample. After the nail penetration test, the sample is left in the bespoke rig to allow for excess electrolytes to leave the punctured pouch and to collect in the basin of the cup.

Figure 10 shows the resulting CV curves of both EDLC and CNT/PANI pseudocapacitors before and after the nail penetration tests. The area under the CV curves indicates the capacitance of these supercapacitors. From the results shown it is clear the penetration largely affects the performance of both capacitors as the capacitor is unable to store the electrochemical energy after testing. The linear lines in **Figure 10** indicate that penetrated supercapacitor essentially forms a resistor due to short circuit, as the area under curves becomes almost zero. The gradient of these linear lines gives the resistance of these resistor-like cells. The spike in the current may be due to the influence of the movement of electrolytes as it leaves the pouch and in contact with the plates. The resistance is 0.2Ω for the CNT/PANI pseudocapacitor and 0.15Ω for the EDLC supercapacitor. The CNT/PANI capacitor shows there is still some energy storage capability left due to the larger area shown in the voltammogram. The capacitor is close to complete failure like the CNT/PANI capacitor as the current is very high, any further fracture would have the same result for both supercapacitors.

3.3 Mechanical Modelling

For this mechanical model, the Johnson-Cook hardening model was implemented in ABAQUS explicit. The supercapacitor was treated as homogeneous, in order to reduce computation time and complexity. Far-field encastre boundary conditions on the specimen are assumed to sufficiently to simulate the effect of the holders. Additionally, biased mesh was used where mesh becomes finer towards the center of the specimen to smooth the contact with the indentor. It was also ensured that at least 4 elements were in initial contact with the indentor since indentation contact is highly mesh dependent. The friction also assumes the value of a minimal coefficient of 0.1 as a study of friction between the indentor and the supercapacitor specimens are beyond the scope of this article.

Since the specimen is treated as homogeneous, different material properties are also assumed, a process which involved a large amount of trial and error calibration, as testing was not

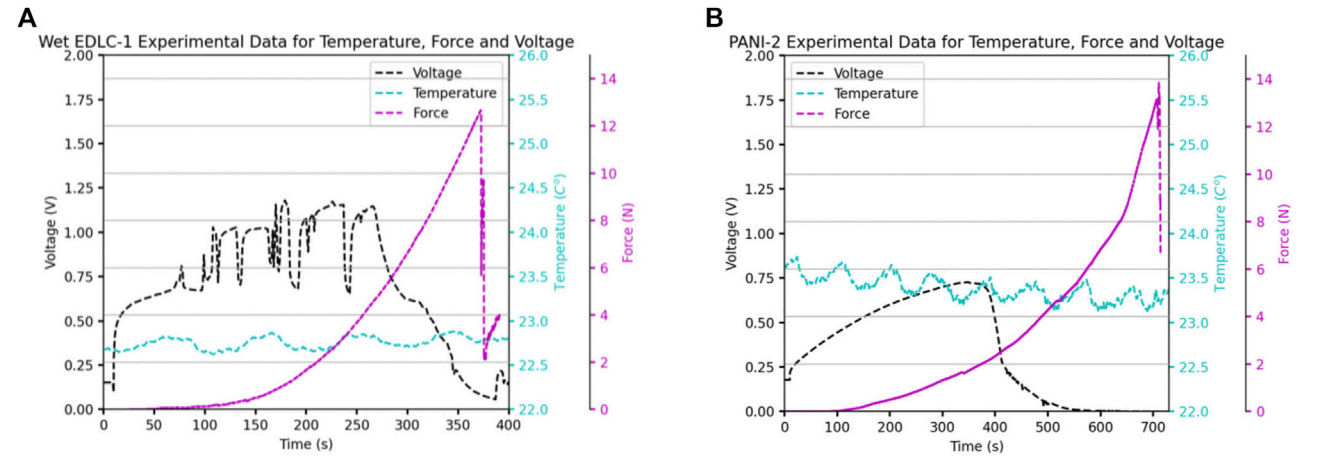

FIGURE 8 | Four axis graph depicting the measured voltage, temperature and force with respect to time for the penetration test of a pure CNT EDLC and CNT/PANI sample.

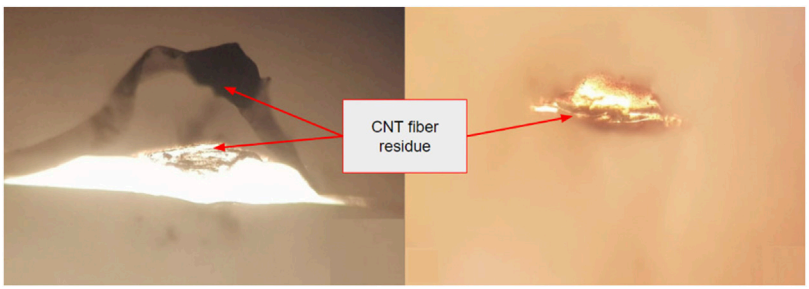

FIGURE 9 | Optical microscope images of the separator from failed test cells showing CNT fiber residue on the puncture hole.

possible at this time. Initially, the Johnson-Cook parameters of the supercapacitor were obtained by performing power law curve fitting. All the values of constants that were not included in the discussion were assumed to be equal to zero, as this is not a temperature and strain-rate dependent model. The indentor velocity used was the same as the experiment and equal to 0.8 mm/min and this is equivalent to a strain rate of $3.2min^{-1}$ experienced by the specimen. The homogenised specimen will initially be modelled as isotropic as it will require further testing to obtain material parameters for each loading direction. The Young's Modulus and Poisson's ratio values that are used in this model are E = 500 MPa and $\nu = 0.3$. Several values of the Poisson's ratio were tested for this specimen to determine its sensitivity on the load-displacement behaviours, as shown in **Figure 11**.

Results shows the Johnson-Cook model captures the hardening behaviour, however exhibiting certain fluctuations due to the nature of a contact problem. The effect of Poisson's ratio on the predicted load-displacement response is minor. The prediction with Poisson's ratio of $\nu = 0.3$, has a larger peak at the start of indentation and overestimates the force, but it is more accurate at higher displacements. The peak that is initially observed during the start of the indentation can be accounted to numerical error. This is due to the computations that occur at the start of the contact, creating a large force when the indentor first comes into contact with the specimen, however this can be potentially resolved by reducing the time step of calculation or by

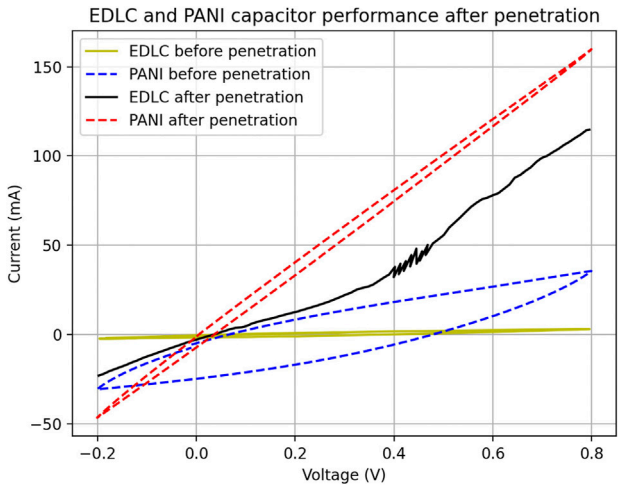

FIGURE 10 | Current vs. Voltage for supercapacitors before penetration and after penetration.

TABLE 1 | Optimised Piece-wise model constants.

Property	Wet PANI1 specimen	Wet EDLC specimen
E_{max} (MPa)	1239	1977
C	0.160	0.280
ϵ_p	28	14.6

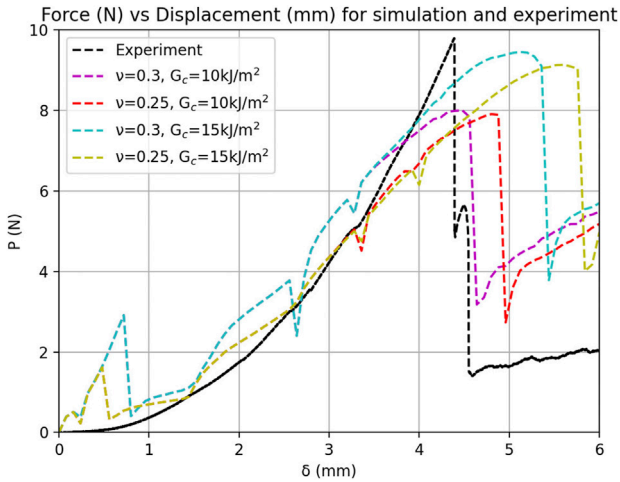

FIGURE 11 | Experimental vs. Calibrated Simulated results for Dry EDLC for different Poisson's Ratio and Fracture Energy values, with incorporated fracture effect.

increasing the mesh density. Overall, the hardening curve is approximated with a good accuracy, and the simulations can further increase in accuracy by refining the mesh. Also, the model includes the fracture behaviour observed by the specimen during the experiment. The fracture is modelled as ductile damage and the damage evolution is defined as fracture energy with linear softening and multiplicative degradation criterion. Linear softening is not accurate in this case as fracture is similar to brittle fracture, but it could be effectively used to simulate the model in this case. The predicted load-displacement curves with different fracture toughness G_c values are presented in **Figure 11**. It is distinguishable that the sharp peak attained before fracture is not replicated by the model. The $\nu = 0.3$ simulations appear to be more accurate in the approximation of the displacement at which failure occurs. The $\nu = 0.25$ simulation appears to attain a steeper peak at failure, however it does not accurately predict the displacement at failure nor the double peak that is observed in the experiment. Incorporating a higher fracture energy increases the area under the curve of the force-displacement graph, resulting in higher force at failure, but smaller displacements at failure and less steep peaks. This implies that further calibration of both fracture energy and strain at fracture could potentially provide a higher accuracy in both force at failure and displacement at failure. Another approach would be introducing a different damage model which could both capture the steep peak and capture exactly the displacement.

In order to observe the differences between experimental and simulated fracture, **Figure 12** are presented. The experimental fracture in **Figure 12D**, is similar to **Figure 12C**, as both show the deformation around the fracture hole. This behaviour is modelled by Johnson-Cook Plasticity in the case of the simulation, which creates similar deformation as the experiment, where the resultant punctured specimen exhibits a well-like geometry as the deformed elements do not recover. Observing the bottom view image, the plastic deformation of the elements is also evident around the puncture hole. The above observation indicates that

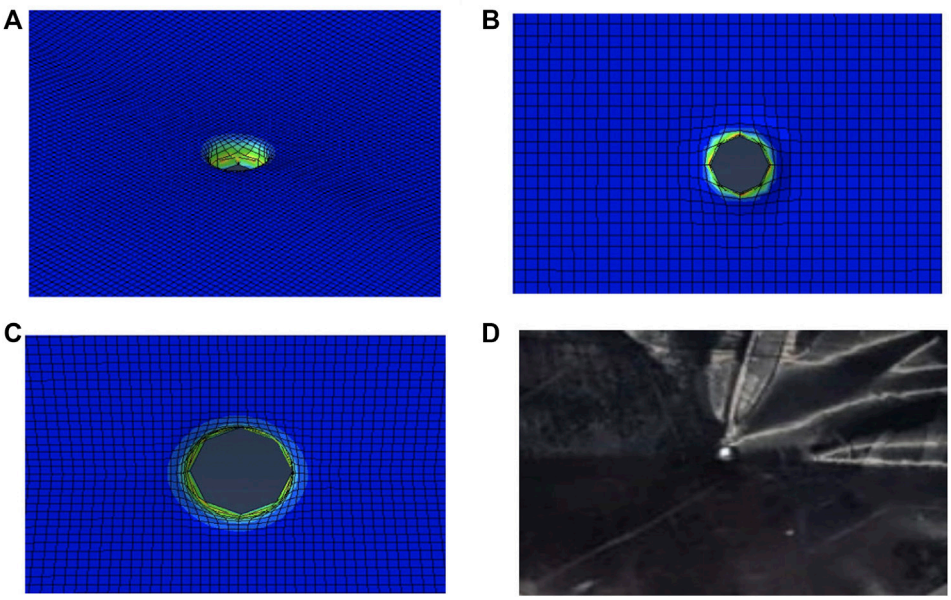

FIGURE 12 | Simulated fracture from **(A)** Perspective view **(B)** Bottom View **(C)** Top view compared to **(D)** sample after nail penetration.

the simulation is effective at replicating similar puncture behaviour and deformation behaviour as in the experiment, even though the specimen is homogenized.

At this point it is important to comment that, the behaviour of the dry EDLC, provided the challenges in modelling it, is accurately approximated. A larger number of elements and more experimental measurements could further help to refine the simulation and increase confidence in the model under compression and indentation loading.

4 CONCLUSIONS AND FUTURE WORK

To summarise the main findings of this investigation, this study discusses the different penetration behaviours observed between CNT/PANI supercapacitors and pure CNT supercapacitors. Additionally it also investigates the difference in the behaviour of dry and wet supercapacitors and how models can be effectively employed to simulate the nail penetration of a specimen. A Johnson-Cook model captures the behaviour of pure CNT supercapacitors under nail penetration with an excellent accuracy. Finally, the electrochemical testing of both CNT/PANI and pure CNT specimens after nail penetration indicates that there is a short-circuit and as a result the punctured specimen cannot store energy and act as resistors. Nevertheless, the penetration testing of the supercapacitor cells in this study were much safer with no noticeable temperature change, due to the low energy storage and the absence of flammable materials.

This study opens up a clear avenue for future investigation, such as investigating the solvent induced swell behaviour of PANI both in terms of mechanical and volumetric effects. Our study suggests that stronger and tougher separators should be used to improve the crashworthiness of supercapacitors. Additionally, the supercapacitor could also be model as heterogeneous, which could potentially allow the model to capture more failure behaviours in the experiment. Electrical modelling could be coupled with the mechanical and thermal modelling to provide a complete simulation on the supercapacitor Zhang et al. (2015a). Further investigation would also involve including a larger amount of supercacitors stacked together, which will be similar to a real world application.

DATA AVAILABILITY STATEMENT

The original contributions presented in the study are included in the article/Supplementary Material, further inquiries can be directed to the corresponding author.

AUTHOR CONTRIBUTIONS

EK: Conceptualisation, methodology, software, verification, investigation, writing–original draft, writing–review and editing, visualization, software. DM: Conceptualisation, writing-review and editing, software, formal analysis, investigation, visualization. JB: Conceptualisation, Investigation, methodology, writing–review and editing. WT: Conceptualisation, writing–review and editing, supervision, project administration, funding acquisition, resources, methodology, validation.

FUNDING

WT acknowledges financial support from the EPSRC (grant EP/V049259/1) and European Commission Graphene Flagship Core Project 3 (GrapheneCore3) under grant No. 881603.

ACKNOWLEDGMENTS

The authors would like to acknowledge Erica Di Federico, for her valuable help during mechanical testing. The authors would also like to thank Dennis Ife, for his help in the design and manufacturing of the sample stage used during nail penetration testing. We also thank Tortech Nano Fibers Ltd for providing the CNT mats used in experiment.

REFERENCES

Buckley, D. J., Berger, M., and Poller, D. (1962a). The Swelling of Polymer Systems in Solvents. I. Method for Obtaining Complete Swelling-Time Curves. *J. Polym. Sci.* 56, 163–174. doi:10.1002/pol.1962.1205616314

Buckley, D. J., and Berger, M. (1962b). The Swelling of Polymer Systems in Solvents. Ii. Mathematics of Diffusion. *J. Polym. Sci.* 56, 175–188. doi:10.1002/pol.1962.1205616315

Cannarella, J., Liu, X., Leng, C. Z., Sinko, P. D., Gor, G. Y., and Arnold, C. B. (2014). Mechanical Properties of a Battery Separator under Compression and Tension. *J. Electrochem. Soc.* 161, F3117–F3122. doi:10.1149/2.0191411jes

Casanovas, J., Canales, M., Fabregat, G., Meneguzzi, A., and Alemán, C. (2012). Water Absorbed by Polyaniline Emeraldine Tends to Organize, Forming Nanodrops. *J. Phys. Chem. B* 116, 7342–7350. doi:10.1021/jp300426b

Gamry (2012). *Testing Electrochemical Capacitors Part 1- Cyclic Voltammetry and Leakage Current. Part 1*. Warminster, PA: Gamry Instruments inc.

Gor, G. Y., Cannarella, J., Prévost, J. H., and Arnold, C. B. (2014). A Model for the Behavior of Battery Separators in Compression at Different Strain/charge Rates. *J. Electrochem. Soc.* 161, F3065–F3071. doi:10.1149/2.0111411jes

Greve, L., and Fehrenbach, C. (2012). Mechanical Testing and Macro-Mechanical Finite Element Simulation of the Deformation, Fracture, and Short Circuit Initiation of Cylindrical Lithium Ion Battery Cells. *J. Power Sourc.* 214, 377–385. doi:10.1016/j.jpowsour.2012.04.055

IEC (2018). *IEC 62576, Electric Double-Layer Capacitors for Use in Hybrid Electric Vehicles - Test Methods for Electrical Characteristics*. Geneva, Switzerland: International Standard.

Johnson, G., and Cook, W. (1983). "A Constitutive Model and Data for Metals Subjected to Large Strains, High Strain Rates, and High Temperatures," in Proceedings 7th International Symposium on Ballistics, the Hague, April 19-21, 1983 541–547.

Koziol, K., Vilatela, J., Moisala, A., Motta, M., Cunniff, P., Sennett, M., et al. (2007). High-performance Carbon Nanotube Fiber. *Science* 318, 1892–1895. doi:10.1126/science.1147635

Lai, W.-J., Ali, M. Y., and Pan, J. (2014). Mechanical Behavior of Representative Volume Elements of Lithium-Ion Battery Cells under Compressive Loading Conditions. *J. Power Sourc.* 245, 609–623. doi:10.1016/j.jpowsour.2013.06.134

Moghim, M. H., Nahvi Bayani, A., and Eqra, R. (2020). Strain-rate-dependent Mechanical Properties of Polypropylene Separator for Lithium-ion Batteries. *Polym. Int.* 69, 545–551. doi:10.1002/pi.5986

Nam, H. S., Han, J. J., Kim, J. W., and Kim, J. S. (2014). Ductile Fracture Simulation for A106 gr.B Carbon Steel under High Strain Rate Loading Condition. *Recent Adv. Struct. Integrity Anal. Proc. Int. Congress* APCF/SIF-2014, 37–41. doi:10.1533/9780081002254.37

Pan, Z., Sedlatschek, T., and Xia, Y. (2020). Effect of State-Of-Charge and Air Exposure on Tensile Mechanical Properties of Lithium-Ion Battery Electrodes. *J. Electrochem. Soc.* 167, 090517. doi:10.1149/1945-7111/ab8804

Qiu, F., Huang, Y., Hu, X., Li, B., Zhang, X., Luo, C., et al. (2019). An Ecofriendly Gel Polymer Electrolyte Based on Natural Lignocellulose with Ultrahigh Electrolyte Uptake and Excellent Ionic Conductivity for Alkaline Supercapacitors. *ACS Appl. Energ. Mater.* 2, 6031–6042. doi:10.1021/acsaem.9b01150

Qiu, F., Huang, Y., Luo, C., Li, X., Wang, M., and Cao, H. (2020). An Acid-Resistant Gel Polymer Electrolyte Based on Lignocellulose of Natural Biomass for Supercapacitors. *Energy Technol.* 8, 2000009. doi:10.1002/ente.202000009

Reimschuessel, H. K. (1978). Relationships on the Effect of Water on Glass Transition Temperature and Young's Modulus of Nylon 6. *J. Polym. Sci. Polym. Chem. Ed.* 16, 1229–1236. doi:10.1002/pol.1978.170160606

Sahraei, E., Hill, R., and Wierzbicki, T. (2012). Calibration and Finite Element Simulation of Pouch Lithium-Ion Batteries for Mechanical Integrity. *J. Power Sourc.* 201, 307–321. doi:10.1016/j.jpowsour.2011.10.094

Sahraei, E., Meier, J., and Wierzbicki, T. (2014). Characterizing and Modeling Mechanical Properties and Onset of Short Circuit for Three Types of Lithium-Ion Pouch Cells. *J. Power Sourc.* 247, 503–516. doi:10.1016/j.jpowsour.2013.08.056

Stallard, J. C., Tan, W., Smail, F. R., Gspann, T. S., Boies, A. M., and Fleck, N. A. (2018). The Mechanical and Electrical Properties of Direct-Spun Carbon Nanotube Mats. *Extreme Mech. Lett.* 21, 65–75. doi:10.1016/j.eml.2018.03.003

Tan, W., Stallard, J. C., Smail, F. R., Boies, A. M., and Fleck, N. A. (2019). The Mechanical and Electrical Properties of Direct-Spun Carbon Nanotube Mat-Epoxy Composites. *Carbon* 150, 489–504. doi:10.1016/j.carbon.2019.04.118

Tan, W., Stallard, J. C., Jo, C., De Volder, M. F. L., and Fleck, N. A. (2021). The Mechanical and Electrochemical Properties of Polyaniline-Coated Carbon Nanotube Mat. *J. Energ. Storage* 41, 102757. doi:10.1016/j.est.2021.102757

Walden, G., Stepan, J., and Mikolajczak, C. (2011). "Safety Considerations when Designing Portable Electronics with Electric Double-Layer Capacitors (Supercapacitors)," in 2011 IEEE Symposium on Product Compliance Engineering Proceedings, San Diego, CA, October 10-12, 2011 1–5. doi:10.1109/PSES.2011.6088259

Wang, L., Yin, S., Zhang, C., Huan, Y., and Xu, J. (2018). Mechanical Characterization and Modeling for Anodes and Cathodes in Lithium-Ion Batteries. *J. Power Sourc.* 392, 265–273. doi:10.1016/j.jpowsour.2018.05.007

Xu, J., Liu, B., Wang, X., and Hu, D. (2016). Computational Model of 18650 Lithium-Ion Battery with Coupled Strain Rate and Soc Dependencies. *Appl. Energ.* 172, 180–189. doi:10.1016/j.apenergy.2016.03.108

Zhang, C., Santhanagopalan, S., Sprague, M. A., and Pesaran, A. A. (2015a). Coupled Mechanical-Electrical-thermal Modeling for Short-Circuit Prediction in a Lithium-Ion Cell under Mechanical Abuse. *J. Power Sourc.* 290, 102–113. doi:10.1016/j.jpowsour.2015.04.162

Zhang, C., Santhanagopalan, S., Sprague, M. A., and Pesaran, A. A. (2015b). A Representative-sandwich Model for Simultaneously Coupled Mechanical-Electrical-thermal Simulation of a Lithium-Ion Cell under Quasi-Static Indentation Tests. *J. Power Sourc.* 298, 309–321. doi:10.1016/j.jpowsour.2015.08.049

Conflict of Interest: The authors declare that the research was conducted in the absence of any commercial or financial relationships that could be construed as a potential conflict of interest.

Publisher's Note: All claims expressed in this article are solely those of the authors and do not necessarily represent those of their affiliated organizations, or those of the publisher, the editors and the reviewers. Any product that may be evaluated in this article, or claim that may be made by its manufacturer, is not guaranteed or endorsed by the publisher.

5 APPENDIX

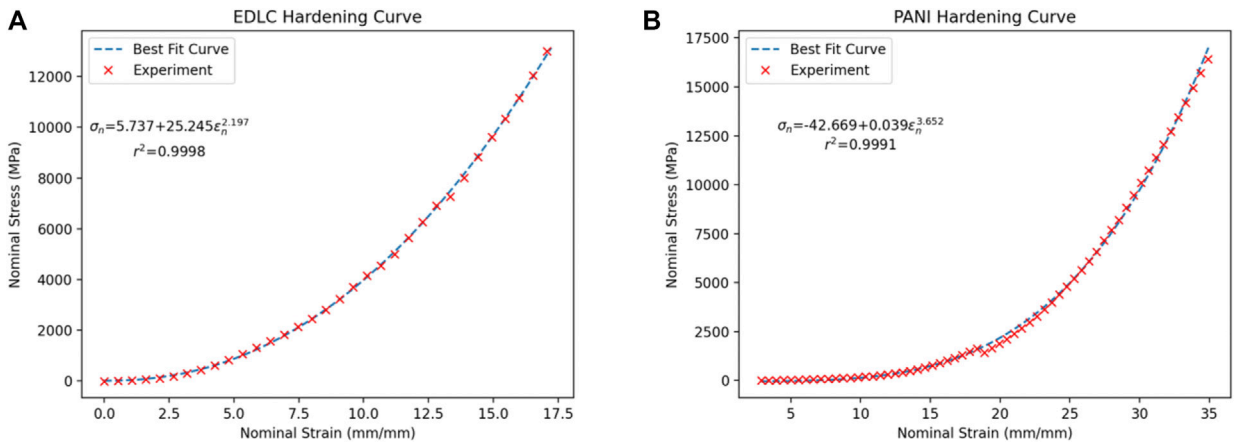

FIGURE A1 | (A) Best fit curve for the hardening region of the Dry Cell 1 EDLC nail penetration **(B)** Best fit curve for the hardening region of the PANI-1, CNT/PANI-coated pseudocapacitor nail penetration.

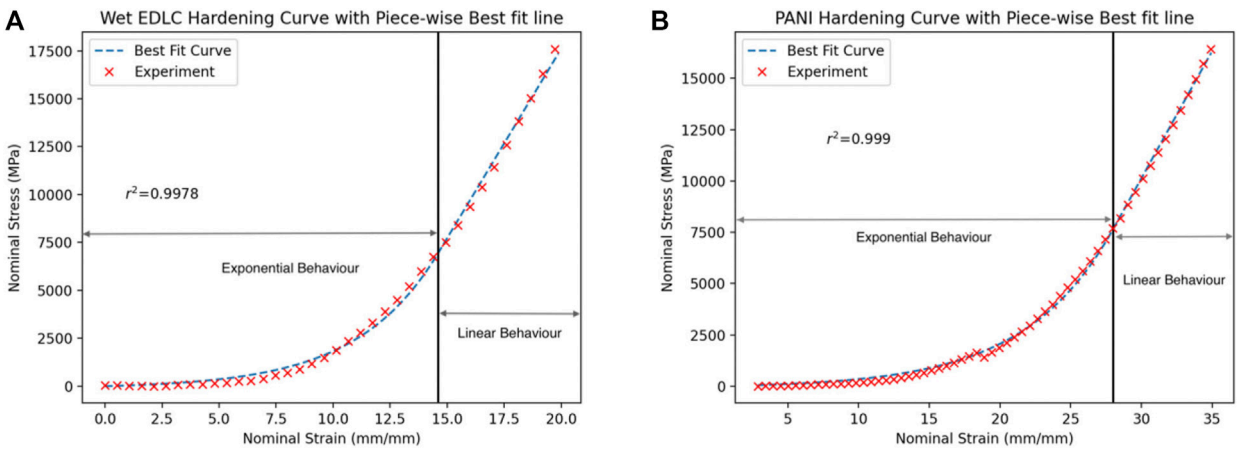

FIGURE A2 | (A) Piece-wise best fitting curve for PANI-1, wet PANI pseudocapacitor **(B)** Piece-wise best fitting curve for wet EDLC-1.

frontiers in Materials

ORIGINAL RESEARCH
published: 16 November 2021
doi: 10.3389/fmats.2021.773343

Fabrication and Mechanical Performance of Graphene Nanoplatelet/Glass Fiber Reinforced Polymer Hybrid Composites

Xudan Yao, Ian A. Kinloch and Mark A. Bissett**

Department of Materials, Henry Royce Institute and National Graphene Institute, University of Manchester, Manchester, United Kingdom

Glass fiber reinforced polymer (GFRP) composites are promising alternatives for the traditional carbon steel pipes used in the oil and gas industry due to their corrosion and chemical resistance. However, the out-of-plane mechanical properties of GFRPs still need further improvement to achieve this goal. Hence, in this work, two methods combining either vacuum mixing or spray coating with vacuum-assisted resin infusion were studied to fabricate graphene nanoplatelet (GNP)/GFRP hybrid composites. The former method resulted in a severe filtering effect, where the GNPs were not evenly distributed throughout the final composite, whereas the latter process resulted in a uniform GNP distribution on the glass fabrics. The addition of GNPs showed no modest contribution to the tensile performance of the GFRP composites due to the relatively high volume and in-plane alignment of the glass fibers. However, the GNPs did improve the flexural properties of GFRP with an optimal loading of 0.15 wt% GNPs, resulting in flexural strength and modulus increases of 6.8 and 1.6%, respectively. This work indicates how GNPs can be advantageous for out-of-plane mechanical reinforcement in fiber-reinforced composites.

Keywords: Graphene nanoplatelets, glass fiber composites, nanocomposites, mechanical properties, composite production

OPEN ACCESS

Edited by:
Dong Xiang,
Southwest Petroleum University, China

Reviewed by:
Sandeep Kumar,
University of Warwick, United Kingdom
Jin Zhou,
Xi'an Jiaotong University, China

****Correspondence:***
Xudan Yao
xudan.yao@manchester.ac.uk
Mark A. Bissett
mark.bissett@manchester.ac.uk

Specialty section:
This article was submitted to Polymeric and Composite Materials, a section of the journal Frontiers in Materials

Received: *09 September 2021*
Accepted: *20 October 2021*
Published: *16 November 2021*

Citation:
Yao X, Kinloch IA and Bissett MA (2021) Fabrication and Mechanical Performance of Graphene Nanoplatelet/Glass Fiber Reinforced Polymer Hybrid Composites. Front. Mater. 8:773343. doi: 10.3389/fmats.2021.773343

INTRODUCTION

Glass fiber reinforced polymer (GFRP) composite has been increasingly investigated as an alternative piping material to carbon steel for oil and gas industry applications, owing to its lightweight, high specific strength and stiffness, good chemical and thermal resistance, ease of transportation, installation, and minimal maintenance (Edwards, 1998; Rafiee, 2016; Al-Samhan et al., 2017). In particular, the recent requirement of moving the offshore oil and gas industry from shallow coast to "deep water" production (Hale et al., 2000) challenged the traditional steel tether design: larger platforms are needed to withstand high axial tension mechanics for works deeper than 1500 m. As a result, lightweight materials, such as nonmetallic composites, are urgently needed for "deep water" applications (Ochoa and Salama, 2005), as well as other applications in demanding environments.

The curvature and flexibility of these composite pipelines lead to flexural and bend stresses, trigging the failure of composite laminates (Omrani et al., 2015; Seretis et al., 2017). To improve the bending properties of the composites, nanomaterials have been introduced to strengthen the matrix and interface. Graphene and its derivatives have been extensively studied since its first isolation in

2004 (Novoselov et al., 2004) and widely applied into fiber-reinforced polymer composites (Kamar et al., 2015; Qin et al., 2015; Wang et al., 2016a; Wang et al., 2016b; Mahmood et al., 2016; Monfared Zanjani et al., 2016; Pathak et al., 2016; Du et al., 2017; Jiang et al., 2017; Kwon et al., 2017; Prusty et al., 2017; Wang et al., 2017; Zhang et al., 2017; Umer, 2018; Yao et al., 2018; Jena et al., 2020; Topkaya et al., 2020; Vigneshwaran et al., 2020; Turaka et al., 2021), owing to their outstanding mechanical, electrical, and thermal properties. In particular, graphene nanoplatelets (GNPs), which are comprised of 10s of graphene layers, can be mass-produced by various techniques, including ball-milling, chemical exfoliation, thermal exfoliation, etc. (Jang and Zhamu, 2008; Young et al., 2012; Cataldi et al., 2018).

To introduce nanomaterials into the composite laminates, two primary methods have been used based on the vacuum assisted resin infusion (VARI) (Kamar et al., 2015). One is initially mixing the nanomaterials with epoxy resin, followed by VARI; another is coating/sizing the fibers with nanomaterials, followed by VARI (Kamar et al., 2015). Seretis et al. (2017) previously mixed GNPs with epoxy resin by mechanical stirring, followed by a hand layup procedure. With increasing GNP content, the flexural strength of the composites increased initially and then reached a plateau, followed by a reduction with the GNP content increasing further (Seretis et al., 2017). Wang et al. (2016b) combined sonication, a calendaring technique, and high-speed shear mixing to combine GNPs with epoxy and then used a hand layup technique for composite preparation. The flexural strength of the GFRP composites increased initially, followed by a decrease with adding GNPs (Wang et al., 2016b). Eaton et al. (2014) plasma functionalized carbon nanofillers and then mixed them with resin by three roll mill, followed by resin infusion, claiming that it could be used to make the hybrid composites. Zhang et al. (2015, 2017) studied the filtration effect of GNPs during resin infusion of nano-engineered hierarchical composites and claimed that the effect is related to filler dimensions, fiber volume fractions, and flow length. In addition, a spray-coating method was proposed to avoid the potential filtration effect when introducing GNPs into composite laminates (Zhang et al., 2015; Zhang et al., 2017).

In this work, both methods combining either vacuum mixing or spray coating with VARI were studied for GNP/GFRP hybrid composite fabrication. Afterward, the latter was selected for preparing GFRP composites with various GNP loadings [0–5 wt% relative to the coated glass fabric (GF)], owing to its uniform distribution. Before the final pipeline applications, the effects of GNPs on GFRP composite panels were discussed in this work, with dry woven GF selected to simulate the structure of braided pipes. Tensile and four-point bending tests were performed on all samples, which verified the potential of spray-coating GNPs onto GF to improve the bending properties of GFRP composites.

MATERIALS AND METHODS

Materials

The GNPs were purchased from First Graphene (UK) Ltd, with an average particle diameter of ~10 μm and tapped density of 0.124 g cm^{-3}. Plain weave woven GF, with an areal weight of 299 g m^{-2}, was purchased from Easy Composites (UK). Low viscosity Araldite epoxy resin and Aradur hardener were purchased from Huntsman (United States). Ethanol was purchased from Fisher Scientific (United Kingdom).

TABLE 1 | Vacuum mixing parameters.

	Stage 1	Stage 2	Stage 3
Speed (1/min)	0	800	2,000
Vacuum (mbar)	5	5	5
Time for first mixing (min)	2	3	5
Time for final mixing (min)	1	1.5	2.5

Vacuum Mixing of GNP/Epoxy

To disperse the GNPs into the epoxy resin uniformly, high-speed vacuum mixing was applied using the SpeedMixer (DAC 600.2 CM51) under the conditions summarized in **Table 1**. GNPs were mixed initially with either epoxy resin or hardener, after which the other component was added. Scanning electron microscope (SEM) analysis of the brittle fracture surfaces was then undertaken to assess the GNP distribution and toughing mechanisms, as shown in **Figure 1**. All images show river lines caused by the brittle fracture of the thermoset resin (Hull, 1999; Olowojoba et al., 2017), with the crack deflection and pull-out contributed by the embedded GNPs (Johnsen et al., 2007; Bindu et al., 2014; Eqra et al., 2015; Domun et al., 2017; Hu et al., 2020), which are beneficial to the composite toughening. No difference was observed whether the GNPs were mixed into the resin or hardener first. Hence, as the weight ratio of the epoxy and hardener was 100:35, the GNPs were initially added to the epoxy for high-loading GNPs to be used.

Filtering Effect

Once the epoxy–GNP formulation was prepared (**Figure 2A**), VARI was used to fabricate the composites (**Figure 2B**), followed by the cure cycle suggested by the supplier (80°C 2 h +140°C 8 h). After demoulding, it was visually observed that few GNPs had penetrated into the laminate, with most of them being filtered and remaining in the infusion mesh. This severe degree of filtering in the mesh suggests that the direct VARI method is not suitable for the GNP-loaded epoxy (**Figure 2C**).

Spray Coating

To solve the GNP distribution problem, a spray-coating method was developed. Initially, GNPs were dispersed in ethanol, with the concentration of ~5 mg ml^{-1}, by ultra-sonication for 40 min. Eight layers of plain weave GF with a quasi-isotropic layup $([0/90]/[\pm45])_{2s}$ were selected for the sample preparation. All internal surfaces were spray-coated with the dispersed GNPs (**Figure 3A**), using a Paasche VL airbrush system connected with an Iwata Power Jet Lite compressor. After being left overnight to evaporate all the solvent, the VARI method was used to fabricate the composites. Samples with the GF spray-coated with 0, 0.1, 0.5, 2, and 5 wt% of the GNPs (relative to the fabric) were prepared, where a 0 wt% sample was spray-coated with pure ethanol as a

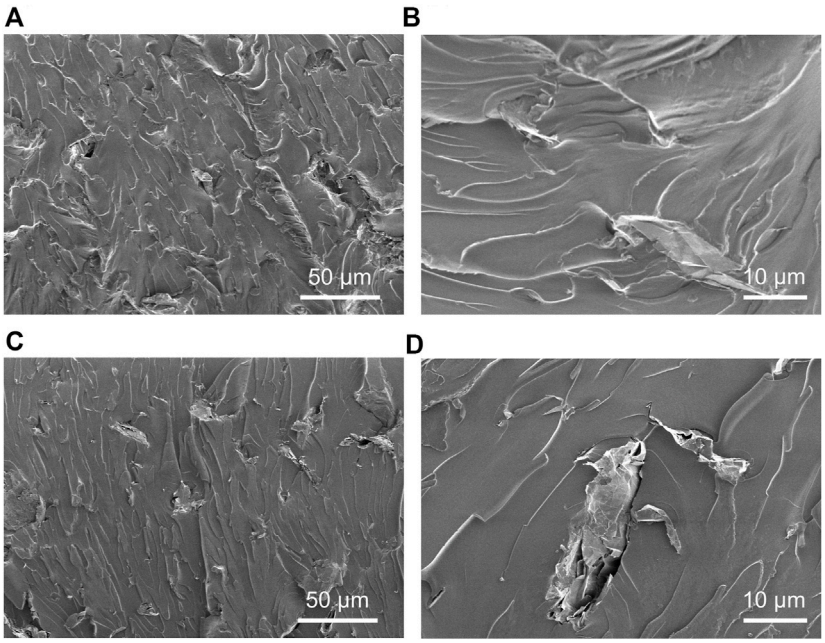

FIGURE 1 | SEM images of fracture surfaces of **(A, B)** GNPs first mixed with epoxy resin followed by adding hardener and **(C, D)** GNPs first mixed with hardener followed by adding epoxy resin.

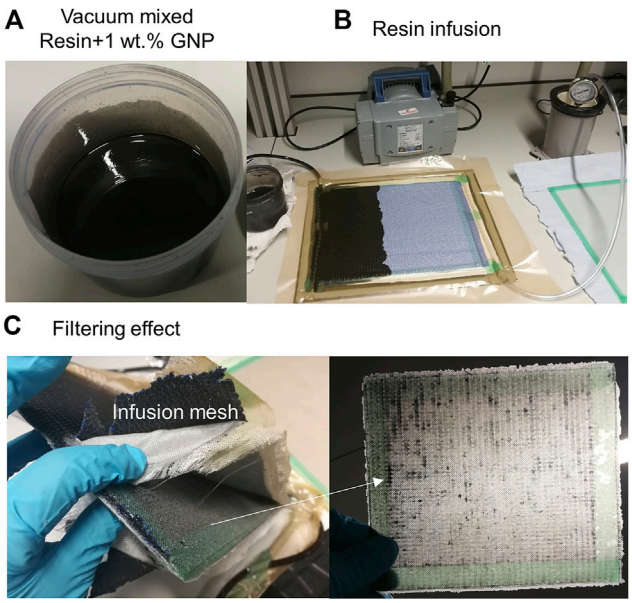

FIGURE 2 | (A) Vacuum mixed epoxy resin with 1 wt% GNP, **(B)** vacuum-assisted resin infusion procedure, and **(C)** cured panel with a large amount of GNPs filtered and left in infusion mesh, rather than penetrate into glass fiber composites.

control to ensure this did not affect the mechanical properties of the fibers. **Figures 3B, C** represent the GF before and after the spray coating, where GNPs spread uniformly on the surface of the fabric. To check the final mass of GNPs, the fabric was weighed before and after the coating procedure, with the values summarized in **Table 2**. It suggests that there are weight losses caused by overspray and other mechanisms during the spray-coating procedure, and the final GNP loadings were found to be 0, 0.03, 0.15, 0.49, and 1.11 wt% relative to the fabric.

Characterization

Field emission SEM, SU5000, and TESCAN MIRA3 SC were used to observe the morphology of the GNPs, GF, and composites. An FEI Tecnai G2 20 (LaB_6) transmission electron microscopy (TEM) was used to evaluate the GNPs using bright-field images and diffraction patterns. A Renishaw InVia Raman system was applied to obtain the Raman spectroscopy of the GNPs, using the 633-nm laser. A Thermo Scientific Nicolet iS50-IR with a diamond ATR crystal was used to conduct the Fourier transform infrared (FTIR) spectroscopy. The density of the composites was measured by a Sartorius YDK03 Density Kit through liquid buoyancy, using isopropyl alcohol as the liquid, based on the standard ASTM D792. A NETZSCH STA 449 F5 Jupiter was used for the thermogravimetry analysis.

Mechanical Testing

The mechanical performance of the composites was evaluated through tensile and four-point bending tests, each test with three specimens, according to ASTM D3039 and ASTM D7264 standards. The specimen sizes of 250 × 25 × 2 mm and 100 × 12.7 × 2 mm were selected for the tensile and flexural tests, respectively, following the recommendation from the standards. The tests were undertaken in the environmental lab with a constant temperature of 23°C and relative humidity of 50%.

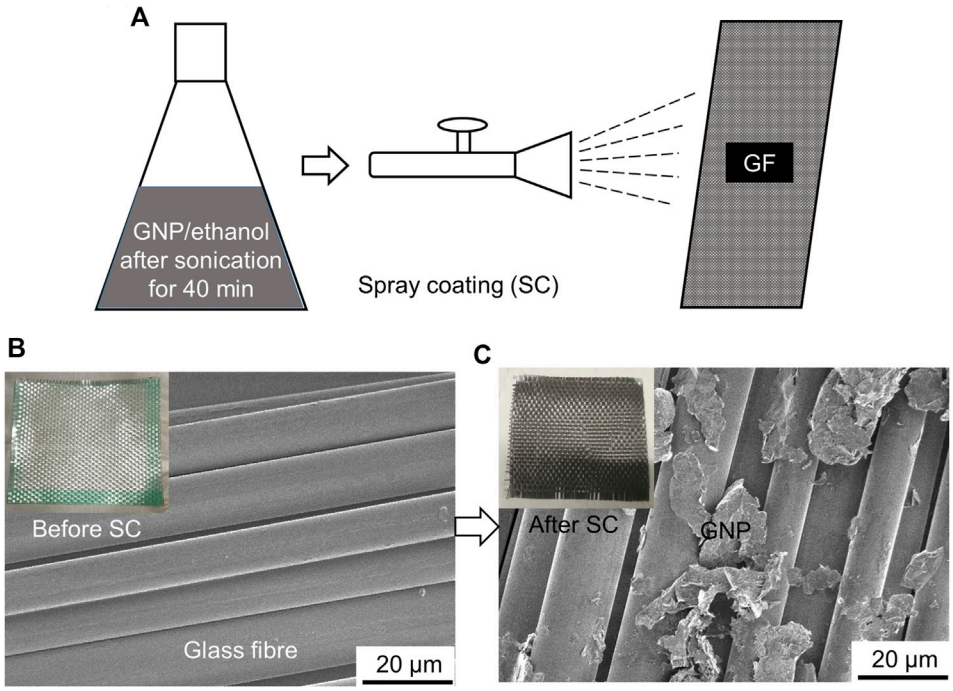

FIGURE 3 | (A) Schematic of the spray-coating process. SEM images of glass fabric **(B)** before and **(C)** after spray-coated with GNPs. Embedded images are optical photos.

TABLE 2 | Weight of glass fabric before and after spray coating (SC), GNP dispersed in ethanol and final amount spray-coated (SCed) onto fabric.

Sample (%)	Before SC/g	Dispersed GNP/g	After SC/g	SCed GNP/g	Final wt%
0.1	145.02	0.15	145.07	0.05	0.03
0.5	145.20	0.73	145.42	0.22	0.15
2	142.59	2.85	143.29	0.7	0.49
5	143.01	7.15	144.6	1.59	1.11

Regarding the tensile tests, the gauge length was calibrated at 50 mm, with a testing rate of 2 mm min^{-1}. During the flexural tests, the support and load span were set at 67.2 and 33.6 mm, respectively, with the testing rate (Y, 3.59 mm/min) calculated based on **Equation 1** (ASTM D6272):

$$Y = 0.167ZL^2/d \quad (1)$$

where L is the support span (mm), d is the depth (thickness) of the beam (mm), and Z is the straining rate of the outer fibers (0.01 mm/mm min).

RESULTS AND DISCUSSION

Morphology and Structure

The representative Raman spectrum, SEM image, TEM image, and its selected area electron diffraction pattern of the GNPs used are shown in **Figure 4**. Characteristic G (~1,581 cm^{-1}), 2D (~2,672 cm^{-1}), and D (~1,332 cm^{-1}) bands of graphitic materials are shown in the Raman spectrum (**Figure 4A**). Here, the G band represents the C-C sp^2 network (Lin et al., 2015), the broad and asymmetric 2D band suggests the GNP consists of graphene with many layers (Lin et al., 2015; Ferrari et al., 2006), and the D band indicates the structural defects related to the zone-boundary phonons (Ferrari et al., 2006). In addition, FTIR was used to identify functional groups of the GNP flakes. As shown in **Figure 4B**, the representative C=C stretching band (~1,586 cm^{-1}), hydroxyl band (C-OH, ~1,200 cm^{-1}), epoxy vibrational band (C-O-C, ~1,107 cm^{-1}), and carboxyl band (C=O, ~1,700 cm^{-1}) are clearly observed (Ţucureanu et al., 2016; Coates, 2006; Li et al., 2018; Li et al., 2013). The existence of these functional groups paves the path for improving interfacial connections through reacting with epoxy matrix. The SEM image and TEM bright-field image (**Figures 4C, D**) illustrate the GNP flake structure with the lateral size varies from a few to ~15 microns. **Figure 4E** shows the corresponding selected area electron diffraction pattern of the GNP in **Figure 4D**. It indicates the crystalline structure of the GNP, which has many layers of graphene with highly ordered

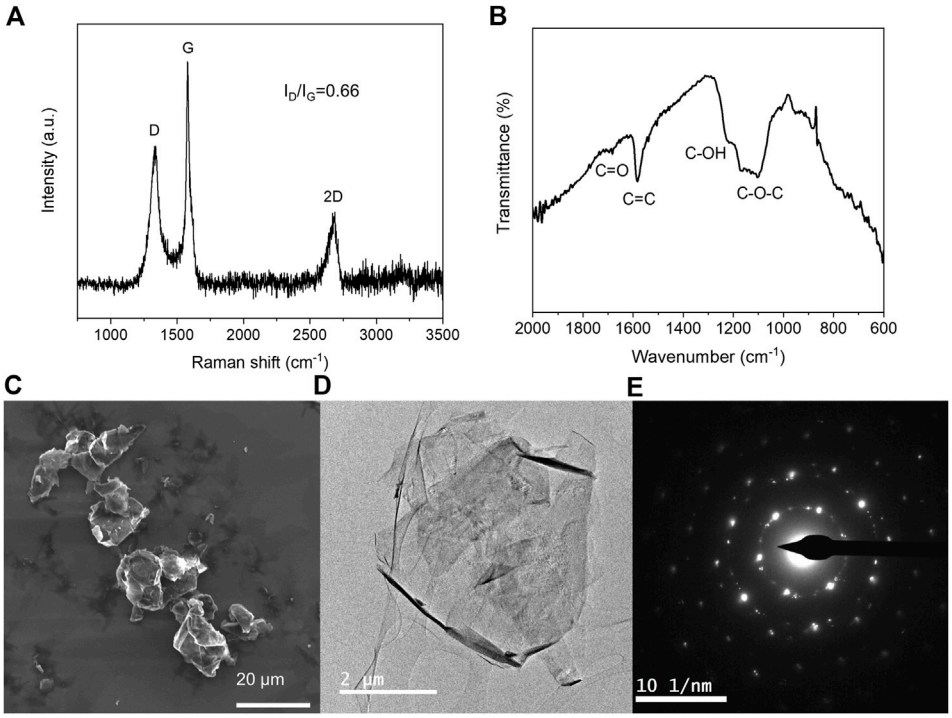

FIGURE 4 | (A) Raman spectrum, **(B)** FTIR spectrum, **(C)** SEM image, **(D)** TEM bright field image and **(E)** corresponding selected area electron diffraction pattern of the GNP.

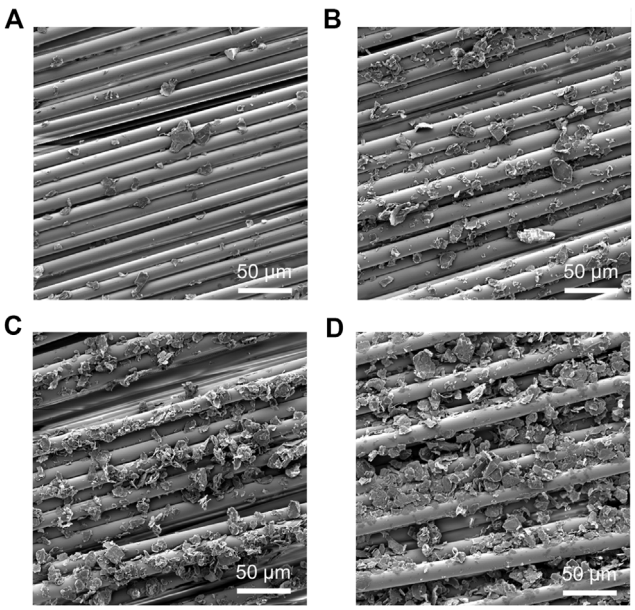

FIGURE 5 | SEM images of glass fibres spray-coated with **(A–D)** 0.03, 0.15, 0.49, and 1.11 wt% GNPs.

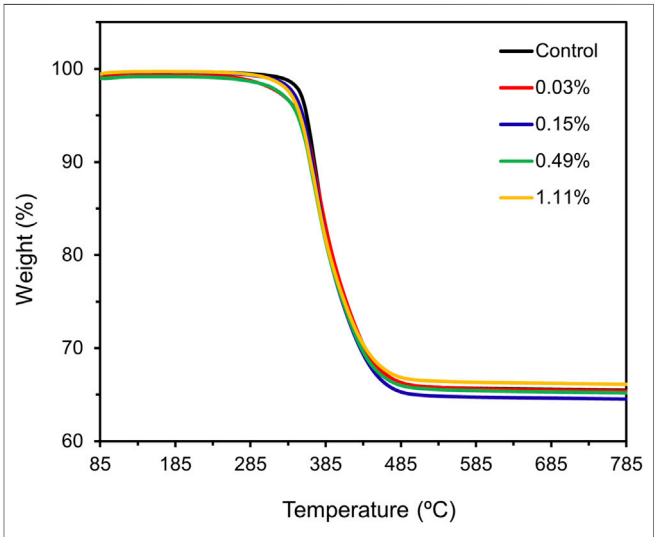

FIGURE 6 | Thermogravimetric analysis for GFRP composites with different GNP loadings.

hexagonal arrangements of carbon atoms (Venturi and Hussain, 2020).

Figure 5 shows the SEM images of GFs spray-coated with 0.03, 0.15, 0.49, and 1.11 wt% GNPs. With the increasing loading, more and more GNPs are seen to be connected with each other and form continuous networks. The surface coverage of GNPs was assessed using ImageJ, and it was found that the GNP areal coverage increased from 7.2 to 22.6, 42.1, and 59.9% at 0.03, 0.15, 0.49, and 1.11 wt% GNPs, respectively. This may have significant effects on the interfacial connections and thus mechanical properties of the composites.

TABLE 3 | Density, fiber weight/volume fraction, and void content of composites with different GNP loadings.

Sample	Density, ρ_c/g cm^{-3}	Resin weight fraction/%	GNP weight fraction/%	Fibre weight fraction/%	Fibre volume fraction/%	Void content/%
Control	1.81	34.7	0	65.3	46.5	0.7
0.03%	1.80	34.8	0.02	65.2	46.2	1.1
0.15%	1.80	35.6	0.1	64.3	45.6	0.5
0.49%	1.78	35	0.3	64.7	45.3	2.1
1.11%	1.77	34	0.7	65.3	45.5	3.4

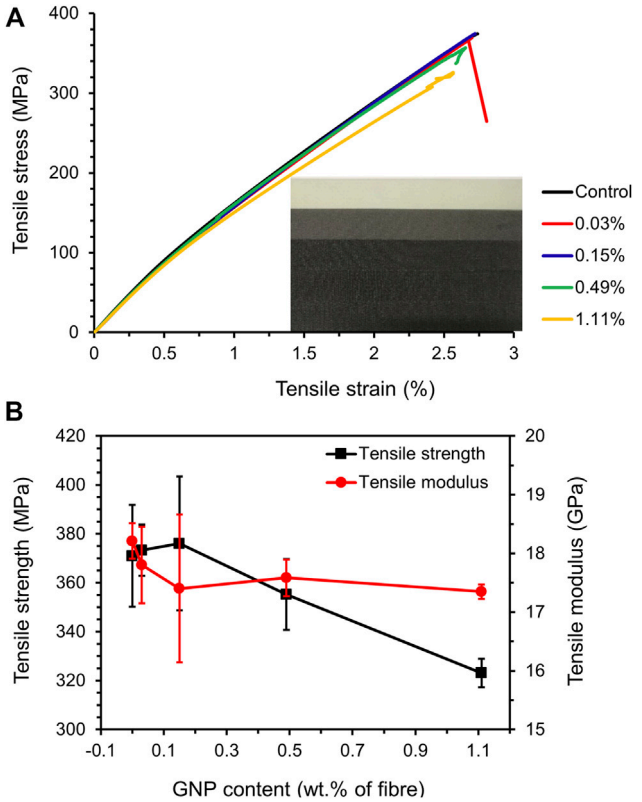

FIGURE 7 | (A) Representative tensile stress–strain curves embedded with photos of samples with different GNP loadings. **(B)** Tensile strength and modulus of the composites.

Fibre Volume Fraction

To check the fiber volume fraction and void content of the composites, thermogravimetry analysis was used with nitrogen as the atmosphere and temperature ranging from room temperature to 800°C. The results are summarized in **Figure 6**, from which the weight percentage of the resin can be obtained as 34.7, 34.8, 35.6, 35, and 34% for control, 0.03, 0.15, 0.49, and 1.11% samples, respectively. The residual weight includes both glass fibers (GFs) and GNPs, which can be differentiated as mentioned in **Section 2.4**. Afterward, the fiber volume fraction (V_f) could be calculated by:

$$V_f = W_f \times \left(\rho_c/\rho_f\right) \tag{2}$$

whereas the void content (V_v) could be obtained based on ASTM D2734:

$$V_v = 100 - \rho_c \times \left(\frac{W_r}{\rho_r} + \frac{W_f}{\rho_f} + \frac{W_g}{\rho_g}\right) \tag{3}$$

where ρ is the density, W is the weight fraction, and V is the volume fraction. The subscript symbols f, c, v, r, and g represent the glass fiber, composite, void, resin, and GNP, respecctively. The density of the composite was measured by a Sartorius YDK03 Density Kit, whereas densities of the fiber (2.54 g/cm^3), GNP (2.2 g/cm^3), and resin (1.19 g/cm^3) are constant. All corresponding results are summarized in **Table 3**.

The results suggest that with the GNP loading increasing, the fiber volume fraction decreased gradually, and void content tends to increase, particularly at high GNP loadings (0.49 and 1.11%). This could be attributed to the 2D layered structure of the GNPs, which led to more voids trapped between the flakes.

Tensile Properties

The representative stress–strain curves of the composites with different GNP loadings under tension are shown in **Figure 7A**. The embedded photo of the samples indicates the uniform distribution of the GNPs. All composites exhibited linear behavior during the tensile tests. In particular, all curves overlapped at the initial stage (0–0.5% strain), where the tensile modulus was determined using the strain range between 0.1 and 0.3%. Hence, with the GNP loading increasing, the tensile modulus, which represents the elastic properties, remained unchanged with the values sitting within error bars, as shown in **Figure 7B**. However, with the strain further increasing, the curve of the sample with the highest GNP loading (1.11 wt%) separated with all other curves due to the formed continuous GNP networks (**Figure 5D**), which hindered the stress transfer and triggered the occurrence of the delamination (Kamar et al., 2015; Umer, 2018). As a result, the tensile strength, which is dominated by the fiber reinforcements rather than GNP fillers (Kumar et al., 2020), kept constant with the GNP addition until the loading reached 1.11 wt %, where the strength decreased by 12.9% (**Figure 7B** and **Table 4**).

Flexural Properties

Compared with the tensile properties of the composites, which are governed by the reinforcing GF, flexural properties typically consist of a combination of the fabric, GNPs, matrix, and their interfacial connections (Wang et al., 2016b). **Figure 8** shows the flexural stress–strain curves, strength, and modulus for all the composite laminates. All the curves showed linear behavior, indicating elastic

TABLE 4 | Tensile and flexural properties of GFRP composites with different GNP loadings.

Sample	Tensile strength, σ_t (MPa)	$\Delta\sigma_t$ (%)	Tensile modulus, E_t (GPa)	ΔE_t (%)	Flexural strength, σ_f (MPa)	$\Delta\sigma_f$ (%)	Flexural modulus, E_f (GPa)	ΔE_f (%)
Control	371.0 ± 20.9		18.2 ± 0.3		425.4 ± 10.8		23.1 ± 0.8	
0.03%	373.3 ± 10.4	0.6	17.8 ± 0.7	−2.2	443.1 ± 14.9	4.2	23.3 ± 0.7	0.8
0.15%	376.1 ± 27.3	1.4	17.4 ± 1.3	−4.4	454.5 ± 3.1	6.8	23.4 ± 0.6	1.6
0.49%	355.2 ± 14.5	−4.3	17.6 ± 0.3	−3.4	313.4 ± 14.3	−26.3	19.8 ± 1.0	−14.2
1.11%	323.1 ± 5.8	−12.9	17.3 ± 0.1	−4.7	350.6 ± 26.5	−17.6	21.2 ± 1.0	−8.2

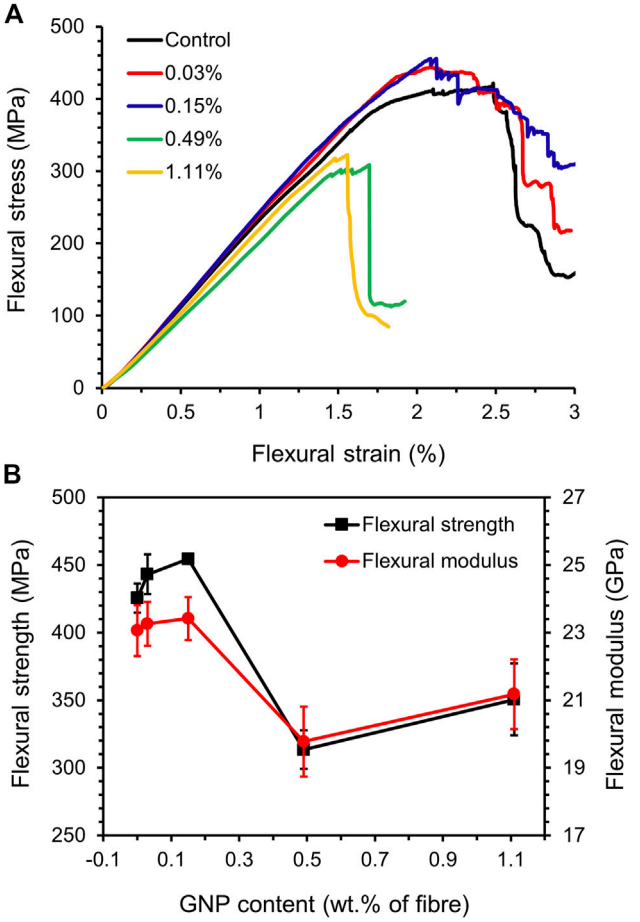

FIGURE 8 | (A) Stress–strain curves of GFRP composites with different GNP loadings under four-point bending. **(B)** Flexural strength and modulus of the composites.

deformation, with the slope increasing with loadings up to an optimum loading of 0.15 wt%, above which the properties began to decrease. Accordingly, the trend of both flexural strength and modulus (obtained from the 0.1 to 0.3% strain) initially increased, followed by a decrease with the GNP loading increasing. Both inflection points sit at 0.15 wt%, where the strength and modulus increased by 6.8 and 1.6%, respectively, as shown in **Figure 8B** and **Table 4**. This improvement was attributed to the strengthened interfacial connections, consisting of chemical bonding, mechanical anchoring, and interlocking, which can occur between the GNPs and matrix, which, as a result, prevented the crack initiation and increased the crack propagation path. Among them, the chemical bonding was contributed by the functional groups on the GNPs, such as hydroxyl, epoxy, and carboxyl, as evidenced by the FTIR (**Figure 4B**), which could interact more strongly with the epoxy matrix.

Other groups have also reported similar behaviors (Seretis et al., 2017; Wang et al., 2016b; Topkaya et al., 2020; Jena et al., 2020; Turaka et al., 2021); namely, the flexural properties got improved, followed by weakened with increasing GNP additions, as a small amount of GNPs could contribute to chemical bonding, mechanical anchoring, and interlocking between the interfaces (Pathak et al., 2016; Moaseri et al., 2014), which strengthened the composites under bending. However, the formation of GNP networks under high loadings (**Figure 5D**) accelerated the delamination and decreased the stress transfer efficiency (Kamar et al., 2015; Umer, 2018), thus weakening the composite performance.

CONCLUSION

This work studied two different methods for GNP/GFRP hybrid composite fabrication, firstly in which vacuum mixing was accompanied by direct VARI, resulting in a severe filtering effect of the GNPs. In comparison, spray coating of the GNPs onto the fiber surface followed by the VARI method of resin infusion resulted in a uniform GNP distribution in the composites. This process is flexible, allowing for a wide variety of shapes of the structure (e.g., pipes) to be achieved and can be applied onto any fibers and different fillers, which could also be easily scaled up for industrial applications.

With different GNP loadings applied, the tensile properties of the composite laminates, which are governed predominantly by the GFs, showed no obvious change until the loading increased up to 1.11 wt%. In contrast, the flexural properties were improved at low loadings of GNP (0.03 and 0.15 wt%), as a result of strengthened interfacial properties, and then weakened with the loading increased further (0.49 and 1.11 wt%) due to accelerated delamination and decreased stress transfer efficiency. In particular, with 0.15 wt% GNPs spray-coated onto the GF, flexural strength and modulus of the composite increased by 6.8 and 1.6%, respectively. Overall, the 0.15 wt% sample performed the best in this work, with the flexural properties being significantly improved. Understanding the mechanical properties of these GFRP materials is vital for many industrial applications where they would be expected to

undergo flexural strain. In the future, different chemical functionalization could be applied to the fillers and matrix to strengthen the interfacial connection between the different constituent materials by chemical bonding and improve the mechanical performance further.

DATA AVAILABILITY STATEMENT

The original contributions presented in the study are included in the article further inquiries can be directed to the corresponding authors.

AUTHOR CONTRIBUTIONS

XY conducted the experiments and wrote the article draft, and MB and IK supervised the project. All authors contributed to the results discussion, analysis, and revision of the article.

FUNDING

This work was funded by PETRONAS in collaboration with the University of Manchester.

REFERENCES

Al-Samhan, M., Al-Enezi, S., Al-Banna, A., and Yussuf, A. (2017). Effect of Crude Oil and Well Stream Chemical on Glass Fiber Epoxy Composite Pipes. *Sci. Eng. Compos. Mater.* 24 (6), 893–899. doi:10.1515/secm-2015-0183

Bindu, B. S., Nair, A. B., Abraham, B. T., Beegum, P. M. S., and Thachil, E. T. (2014). Microwave Exfoliated Reduced Graphene Oxide Epoxy Nanocomposites for High Performance Applications. *Polymer* 55 (16), 3614–3627. doi:10.1016/j.polymer.2014.05.032

Cataldi, P., Athanassiou, A., and Bayer, I. S. (2018). Graphene Nanoplatelets-Based Advanced Materials and Recent Progress in Sustainable Applications. *Appl. Sci.* 8 (9), 1438. doi:10.3390/app8091438

Coates, J. (2006). "Interpretation of Infrared Spectra, A Practical Approach," in *Encyclopedia of Analytical Chemistry*, Chichester: John Wiley 8 Sons Ltd.1–23. doi:10.1002/9780470027318.a5606

Domun, N., Hadavinia, H., Zhang, T., Liaghat, G., Vahid, S., Spacie, C., et al. (2017). Improving the Fracture Toughness Properties of Epoxy Using Graphene Nanoplatelets at Low Filler Content. *Nanocomposites* 3 (3), 85–96. doi:10.1080/20550324.2017.1365414

Du, X., Zhou, H., Sun, W., Liu, H.-Y., Zhou, G., Zhou, H., et al. (2017). Graphene/epoxy Interleaves for Delamination Toughening and Monitoring of Crack Damage in Carbon Fibre/epoxy Composite Laminates. *Composites Sci. Tech.* 140, 123–133. doi:10.1016/j.compscitech.2016.12.028

Eaton, M. J., Ayre, W., Williams, M., Pullin, R., and Evans, S. L. (2014). "Nano-reinforcement of Resin Infused Carbon Fibre Laminates Reinforced Using Carbon Nano-Tubes and Graphene," in 16th International Conference on Experimental Mechanics, Cambridge, United Kingdom, July 7, 2014, 1–3.

Edwards, K. L. (1998). An Overview of the Technology of Fibre-Reinforced Plastics for Design Purposes. *Mater. Des.* 19 (1–2), 1–10. doi:10.1016/s0261-3069(98)00007-7

Eqra, R., Janghorban, K., and Daneshmanesh, H. (2015). Mechanical Properties and Toughening Mechanisms of Epoxy/graphene Nanocomposites. *J. Polym. Eng.* 35 (3), 257–266. doi:10.1515/polyeng-2014-0134

Ferrari, A. C., Meyer, J. C., Scardaci, V., Casiraghi, C., Lazzeri, M., Mauri, F., et al. (2006). Raman Spectrum of Graphene and Graphene Layers. *Phys. Rev. Lett.* 97 (18), 187401–187404. doi:10.1103/PhysRevLett.97.187401

Hale, J. M., Shaw, B. A., Speake, S. D., and Gibson, A. G. (2000). High Temperature Failure Envelopes for Thermosetting Composite Pipes in Water. *Plastics, Rubber and Composites* 29 (10), 539–548. doi:10.1179/146580100101540752

Hu, B., Conghua, Y.-h., Zhang, B.-y., Zhang, L., Shen, Y., and Huangzhou, H.-z. (2020). Enhancement of Thermal and Mechanical Performances of Epoxy Nanocomposite Materials Based on Graphene Oxide Grafted by Liquid Crystalline Monomer with Schiff Base. *J. Mater. Sci.* 55 (8), 3712–3727. doi:10.1007/s10853-019-04273-2

Hull, D. (1999). *Fractography: Observing, Measuring and Interpreting Fracture Surface Topography*. Cambridge, UK: Cambridge University Press.

Jang, B. Z., and Zhamu, A. (2008). Processing of Nanographene Platelets (NGPs) and NGP Nanocomposites: A Review. *J. Mater. Sci.* 43 (15), 5092–5101. doi:10.1007/s10853-008-2755-2

Jena, A., ShubhamPrusty, R. K., and Ray, B. C. (2020). Mechanical and Thermal Behaviour of Multi-Layer Graphene and Nanosilica Reinforced Glass Fiber/Epoxy Composites. *Mater. Today Proc.* 33, 5184–5189. doi:10.1016/j.matpr.2020.02.879

Jiang, J., Yao, X., Xu, C., Su, Y., Zhou, L., and Deng, C. (2017). Influence of Electrochemical Oxidation of Carbon Fiber on the Mechanical Properties of Carbon Fiber/graphene Oxide/epoxy Composites. *Composites A: Appl. Sci. Manufacturing* 95, 248–256. doi:10.1016/j.compositesa.2017.02.004

Johnsen, B. B., Kinloch, A. J., Mohammed, R. D., Taylor, A. C., and Sprenger, S. (2007). Toughening Mechanisms of Nanoparticle-Modified Epoxy Polymers. *Polymer* 48 (2), 530–541. doi:10.1016/j.polymer.2006.11.038

Kamar, N. T., Hossain, M. M., Khomenko, A., Haq, M., Drzal, L. T., and Loos, A. (2015). Interlaminar Reinforcement of Glass Fiber/epoxy Composites with Graphene Nanoplatelets. *Composites Part A: Appl. Sci. Manufacturing* 70, 82–92. doi:10.1016/j.compositesa.2014.12.010

Kumar, S., Singh, K. K., and Ramkumar, J. (2020). Comparative Study of the Influence of Graphene Nanoplatelets Filler on the Mechanical and Tribological Behavior of Glass Fabric-reinforced Epoxy Composites. *Polym. Composites* 41 (12), 5403–5417. doi:10.1002/pc.25804

Kwon, Y. J., Kim, Y., Jeon, H., Cho, S., Lee, W., and Lee, J. U. (2017). Graphene/carbon Nanotube Hybrid as a Multi-Functional Interfacial Reinforcement for Carbon Fiber-Reinforced Composites. *Composites B: Eng.* 122, 23–30. doi:10.1016/j.compositesb.2017.04.005

Li, Z., Chu, J., Yang, C., Hao, S., Bissett, M. A., Kinloch, I. A., et al. (2018). Effect of Functional Groups on the Agglomeration of Graphene in Nanocomposites. *Composites Sci. Tech.* 163, 116–122. doi:10.1016/j.compscitech.2018.05.016

Li, Z., Young, R. J., Wang, R., Yang, F., Hao, L., Jiao, W., et al. (2013). The Role of Functional Groups on Graphene Oxide in Epoxy Nanocomposites. *Polymer* 54 (21), 5821–5829. doi:10.1016/j.polymer.2013.08.026

Lin, Y.-H., Yang, C.-Y., Lin, S.-F., and Lin, G.-R. (2015). Triturating Versatile Carbon Materials as Saturable Absorptive Nano Powders for Ultrafast Pulsating of Erbium-Doped Fiber Lasers. *Opt. Mater. Express* 5 (2), 236. doi:10.1364/ome.5.000236

Mahmood, H., Tripathi, M., Pugno, N., and Pegoretti, A. (2016). Enhancement of Interfacial Adhesion in Glass Fiber/epoxy Composites by Electrophoretic Deposition of Graphene Oxide on Glass Fibers. *Composites Sci. Tech.* 126, 149–157. doi:10.1016/j.compscitech.2016.02.016

Moaseri, E., Karimi, M., Maghrebi, M., and Baniadam, M. (2014). Fabrication of Multi-Walled Carbon Nanotube-Carbon Fiber Hybrid Material via Electrophoretic Deposition Followed by Pyrolysis Process. *Composites Part A: Appl. Sci. Manufacturing* 60, 8–14. doi:10.1016/j.compositesa.2014.01.009

Monfared Zanjani, J. S., Okan, B. S., Menceloglu, Y. Z., and Yildiz, M. (2016). Nano-engineered Design and Manufacturing of High-Performance Epoxy Matrix Composites with Carbon Fiber/selectively Integrated Graphene as Multi-Scale Reinforcements. *RSC Adv.* 6 (12), 9495–9506. doi:10.1039/c5ra23665g

Novoselov, K. S., Geim, A. K., Morozov, S. V., Jiang, D., Zhang, Y., Dubonos, S. V., et al. (2004). Electric Field Effect in Atomically Thin Carbon Films Supplementary. *Science* 5 (1), 1–12. doi:10.1126/science.1102896

Ochoa, O. O., and Salama, M. M. (2005). Offshore Composites: Transition Barriers to an Enabling Technology. *Compos. Sci. Technol.* 65 (15-16), 2588–2596. doi:10.1016/j.compscitech.2005.05.019

Olowojoba, G. B., Kopsidas, S., Eslava, S., Gutierrez, E. S., Kinloch, A. J., Mattevi, C., et al. (2017). A Facile Way to Produce Epoxy Nanocomposites Having Excellent

Thermal Conductivity with Low Contents of Reduced Graphene Oxide. *J. Mater. Sci.* 52 (12), 7323–7344. doi:10.1007/s10853-017-0969-x

Omrani, E., Barari, B., Dorri Moghadam, A., Rohatgi, P. K., and Pillai, K. M. (2015). Mechanical and Tribological Properties of Self-Lubricating Bio-Based Carbon-Fabric Epoxy Composites Made Using Liquid Composite Molding. *Tribology Int.* 92, 222–232. doi:10.1016/j.triboint.2015.06.007

Pathak, A. K., Borah, M., Gupta, A., Yokozeki, T., and Dhakate, S. R. (2016). Improved Mechanical Properties of Carbon Fiber/graphene Oxide-Epoxy Hybrid Composites. *Composites Sci. Tech.* 135, 28–38. doi:10.1016/j.compscitech.2016.09.007

Prusty, R. K., Ghosh, S. K., Rathore, D. K., and Ray, B. C. (2017). Reinforcement Effect of Graphene Oxide in Glass Fibre/epoxy Composites at In-Situ Elevated Temperature Environments: An Emphasis on Graphene Oxide Content. *Composites Part A: Appl. Sci. Manufacturing* 95, 40–53. doi:10.1016/j.compositesa.2017.01.001

Qin, W., Vautard, F., Drzal, L. T., and Yu, J. (2015). Mechanical and Electrical Properties of Carbon Fiber Composites with Incorporation of Graphene Nanoplatelets at the Fiber-Matrix Interphase. *Composites Part B: Eng.* 69, 335–341. doi:10.1016/j.compositesb.2014.10.014

Rafiee, R. (2016). On the Mechanical Performance of Glass-Fibre-Reinforced Thermosetting-Resin Pipes: A Review. *Compos. Structures* 143, 151–164. doi:10.1016/j.compstruct.2016.02.037

Seretis, G. V., Kouzilos, G., Manolakos, D. E., and Provatidis, C. G. (2017). On the Graphene Nanoplatelets Reinforcement of Hand Lay-Up Glass Fabric/epoxy Laminated Composites. *Composites Part B: Eng.* 118, 26–32. doi:10.1016/j.compositesb.2017.03.015

Topkaya, T., Çelik, Y. H., and Kilickap, E. (2020). Mechanical Properties of Fiber/graphene Epoxy Hybrid Composites. *J. Mech. Sci. Technol.* 34 (11), 4589–4595. doi:10.1007/s12206-020-1016-4

Ţucureanu, V., Matei, A., and Avram, A. M. (2016). FTIR Spectroscopy for Carbon Family Study. *Crit. Rev. Anal. Chem.* 46 (6), 502–520. doi:10.1080/10408347.2016.1157013

Turaka, S., Reddy, K. V. K., Sahu, R. K., and Katiyar, J. K. (2021). Mechanical Properties of MWCNTs and Graphene Nanoparticles Modified Glass Fibre-Reinforced Polymer Nanocomposite. *Bull. Mater. Sci.* 44 (3), 194. doi:10.1007/s12034-021-02444-z

Umer, R. (2018). Manufacturing and Mechanical Properties of Graphene Coated Glass Fabric and Epoxy Composites. *J. Compos. Sci.* 2 (2), 17. doi:10.3390/jcs2020017

Venturi, F., and Hussain, T. (2020). Radial Injection in Suspension High Velocity Oxy-Fuel (S-HVOF) Thermal Spray of Graphene Nanoplatelets for Tribology. *J. Therm. Spray Technol.* 29 (1–2), 255–269. doi:10.1007/s11666-019-00957-y

Vigneshwaran, G. V., Shanmugavel, B. P., Paskaramoorthy, R., and Harish, S. (2020). Tensile, Impact, and Mode-I Behaviour of Glass Fiber-Reinforced Polymer Composite Modified by Graphene Nanoplatelets. *Arch. Civ Mech. Eng.* 20 (3). doi:10.1007/s43452-020-00099-x

Wang, C., Li, J., Sun, S., Li, X., Zhao, F., Jiang, B., et al. (2016). Electrophoretic Deposition of Graphene Oxide on Continuous Carbon Fibers for Reinforcement of Both Tensile and Interfacial Strength. *Composites Sci. Tech.* 135, 46–53. doi:10.1016/j.compscitech.2016.07.009

Wang, C., Li, J., Yu, J., Sun, S., Li, X., Xie, F., et al. (2017). Grafting of Size-Controlled Graphene Oxide Sheets Onto Carbon Fiber for Reinforcement of Carbon Fiber/epoxy Composite Interfacial Strength. *Composites Part A: Appl. Sci. Manufacturing* 101, 511–520. doi:10.1016/j.compositesa.2017.07.015

Wang, F., Drzal, L. T., Qin, Y., and Huang, Z. (2016). Size Effect of Graphene Nanoplatelets on the Morphology and Mechanical Behavior of Glass Fiber/epoxy Composites. *J. Mater. Sci.* 51 (7), 3337–3348. doi:10.1007/s10853-015-9649-x

Yao, X., Gao, X., Jiang, J., Xu, C., Deng, C., and Wang, J. (2018). Comparison of Carbon Nanotubes and Graphene Oxide Coated Carbon Fiber for Improving the Interfacial Properties of Carbon Fiber/epoxy Composites. *Composites Part B: Eng.* 132, 170–177. doi:10.1016/j.compositesb.2017.09.012

Young, R. J., Kinloch, I. A., Gong, L., and Novoselov, K. S. (2012). The Mechanics of Graphene Nanocomposites: A Review. *Composites Sci. Tech.* 72 (12), 1459–1476. doi:10.1016/j.compscitech.2012.05.005

Zhang, H., Liu, Y., Huo, S., Briscoe, J., Tu, W., Picot, O. T., et al. (2017). Filtration Effects of Graphene Nanoplatelets in Resin Infusion Processes: Problems and Possible Solutions. *Composites Sci. Tech.* 139, 138–145. doi:10.1016/j.compscitech.2016.12.020

Zhang, H., Liu, Y., Kuwata, M., Bilotti, E., and Peijs, T. (2015). Improved Fracture Toughness and Integrated Damage Sensing Capability by Spray Coated CNTs on Carbon Fibre Prepreg. *Composites Part A: Appl. Sci. Manufacturing* 70, 102–110. doi:10.1016/j.compositesa.2014.11.029

Conflict of Interest: This study received funding from PETRONAS. The funder had the following involvement with the study: decision to publish. All authors declare no other competing interests.

Publisher's Note: All claims expressed in this article are solely those of the authors and do not necessarily represent those of their affiliated organizations or those of the publisher, the editors, and the reviewers. Any product that may be evaluated in this article, or claim that may be made by its manufacturer, is not guaranteed or endorsed by the publisher.

Advantages of publishing in Frontiers

OPEN ACCESS
Articles are free to read for greatest visibility and readership

FAST PUBLICATION
Around 90 days from submission to decision

HIGH QUALITY PEER-REVIEW
Rigorous, collaborative, and constructive peer-review

TRANSPARENT PEER-REVIEW
Editors and reviewers acknowledged by name on published articles

Frontiers
Avenue du Tribunal-Fédéral 34
1005 Lausanne | Switzerland

Visit us: www.frontiersin.org
Contact us: frontiersin.org/about/contact

REPRODUCIBILITY OF RESEARCH
Support open data and methods to enhance research reproducibility

DIGITAL PUBLISHING
Articles designed for optimal readership across devices

FOLLOW US
@frontiersin

IMPACT METRICS
Advanced article metrics track visibility across digital media

EXTENSIVE PROMOTION
Marketing and promotion of impactful research

LOOP RESEARCH NETWORK
Our network increases your article's readership